Doctoral Dissertation
Doctoral Program in Architectural and Landscape Heritage (31th Cycle)

Hybrid simulation techniques in the structural analysis and testing of architectural heritage

Gaetano Miraglia
* * * * * *

Supervisor
Prof. R., Ceravolo

Doctoral Examination Committee:
Prof. D., Ferretti, Università di Parma
Prof. V., Sarhosis, University of Newcastle

Politecnico di Torino
June, 2019

I hereby declare that, the contents and organisation of this dissertation constitute my own original work and does not compromise in any way the rights of third parties, including those relating to the security of personal data.

Gaetano Miraglia

Turin, April, 2019

Abstract

This thesis examines the development of the concept of structural modelling of architectural heritage, from the first historic experiences on physical models, passing through milestones such as the model corroboration and updating, for finally proposing novel hybrid simulation and testing procedures for use in the field of architectural heritage.

Model corroboration techniques are known to be a powerful tool to adjust a predictor, be it analytical or numerical (e.g. Finite Element Model), so that the outcomes of simulations are as consistent as possible with data available from experimental campaigns. To this aim, several algorithms have been established in the past, with increasing complexity. Sometimes these procedures have given satisfactorily results, in terms of both accuracy and reliability. However, for very complex structures, as those one belonging to the architectural heritage, the application of standard procedures has proven to be not reliable. This is mainly due to the inability of models to consider, in the calibration process, the high uncertainties intrinsic in this type of buildings, as their complex geometry, the material behaviour and the old construction techniques that makes, for example, the connections between the different physical components of an historical building an important unknow factor.

Thus, in this thesis work, an ensemble model corroboration technique is firstly proposed to increase the reliability of the corroboration process, as well as the accuracy of models in a broad sense (i.e. reducing overfitting). The technique is here demonstrated on the typical problem of calibrating a linear dynamical model from results of an experimental modal analysis, however, the same technique can be applied to corroborate nonlinear models, as those addressed in this thesis to identify hysteretic degrading models for masonry structures. In the last part, the thesis establishes a hybrid simulation/testing design procedure to allow the simulation and testing of mass distributed systems with distributed interfaces

between the subcomponents of systems (i.e. if the system is substructured, the interfaces between the components can be represented by at least of lines), very frequent characteristic in structures relating to the architectural heritage. Combining the proposed corroboration technique and the assumed nonlinear identification methods (that consider time-frequency distribution of records coming from real monitored systems), and thanks to the proposed hybrid simulation/testing design procedure, nonlinear corroboration of hybrid models for architectural heritage structures can be carried out, also within a probabilistic framework, as will be stated in the conclusions.

The advantage of using hybrid methods in corroborating models, lies in the fact that the information received from the physical part are used to suppress the high uncertainties of different phenomena, as for example the dependence of material parameters from the load amplitude, typical of masonry structures, without the need to carry out destructive or invasive tests on the real system, thus in full compliance with the deontological guidelines on testing on cultural heritage.

How to read this thesis

Chapter 1 – It introduces the engineering modelling

Chapter 1 introduces the role of models for the structural analysis and preservation of architectural heritage by means of emblematic examples. Firstly, a definition of model is introduced in general terms, then, some relevant contributions of models for architectural heritage and engineering structures are reported thanks to which the main concepts of the engineering modelling are described. The discussion brings to the conclusion that a step forward in modelling can be represented by the synergistic combination of physical and virtual models, which would lead to the definition of those that in the literature are referred to be hybrid models.

Chapter 2 – It highlights the importance of model corroboration

Chapter 2 explains that the corroboration of models can be pursued with data coming from experimental data using different modelling strategies. The first and simply strategy regards the corroboration of linear models. This means that the mathematical tools used to predict the response of structures can be described with linear laws. The second, and more complex strategy, regards the simulation of structures with nonlinear models, e.g. mathematical laws that consider the stresses as a nonlinear function of the strain field and others physical quantities. Then, the corroboration of mathematical models with physical models is examined and the so called hybrid simulation/testing techniques are introduced. The importance of using hybrid techniques relies in the possibility to test the most uncertain part of a building in laboratory, without the need to model it, and to simulate the simplest part with linear or nonlinear mathematical (mostly numerical) models. In this way the overall model, results to be improved in terms

of both accuracy, because the information coming from the test during the dynamic simulation, and efficiency, because the use of linear or nonlinear models for just a part of the emulated building.

Chapter 3 – It proposes a novel technique to corroborate models

Chapter 3 describes a novel approach to the model updating. In fact, the high number of available algorithms makes the choice of the best suitable one for the calibration of a model a very difficult activity. Moreover, very often, there are several algorithms that perform the calibration task in the same way, without any perceptible difference in terms of efficiency, accuracy or precision. But the choice of the best suitable algorithm is not the only difficultness. In fact, each algorithm is characterised by several parameters that should be properly tuned on the model being updated. Finally, for a chosen algorithm, one or more objectives may be pursued, bringing each time to a different result (set of calibrated quantities). For these reasons, the novel approach described in the chapter aims to define the best result of a calibration process among the results that come from different updating algorithms (tuned in different ways), each one characterised by one or more objectives pursued. To do it the optimisation is carried out within the so called rank aggregation problem, i.e. a problem that aims to define the best result among results ranked in different lists. The ensemble technique is applied to a numerical linear model.

Chapter 4 – It proposes a method to corroborate nonlinear models

Chapter 4 proposes an efficient method for the instantaneous identification of nonlinear hysteretic and degrading systems. This represents a next step respect to the linear model updating, being explored in this case also the behaviour of the systems with respect to strong external loads. However the ensemble technique described in Chapter 3 can be still applied. A numerical validation and application of the method on an old monitored masonry structure is presented in the chapter.

Chapter 5 – It proposes a hybrid simulation/testing design procedure

Chapter 5 proposes a hybrid simulation/testing design procedure for mass distributed systems with distributed interfaces, characteristic of structures belonging to the architectural heritage. For these systems, in principle, several actuators should be used to impose the correct boundary conditions to the tested specimen. Thus the procedure aims to reduce the number of actuators necessary to achieve a predetermined coupling accuracy between physical and numerical subdomains. The chapter reports a numerical validation of the procedure.

Chapter 6 – It reports an experimental hybrid simulation campaign

Chapter 6 reports an experimental hybrid simulation campaign applied on a mass distributed system with distributed interface between the physical and numerical subdomain. An advanced technique for the substrucuring and reduction, named Component Mode Synthesis, is implemented. It will be shown that thanks to this technique, combined to the hybrid simulation, some very complex behaviours, such as the variability of vertical loads and stresses in the tested specimen can be accounted. Then, the success of the hybrid test proves the effectiveness of the proposed design procedure.

Chapter 7 – It applies the hybrid testing design procedure on an emulated cultural heritage structure

Chapter 7 applies the procedure proposed in Chapter 5, and validated in Chapter 6, to an emulated cultural heritage structure in order to exemplify the work of the thesis. Both numerical and physical subdomain are simulated through the use of computers. The Regina Montis Regalis, Sanctuary in Vicoforte, is selected as emblematic masonry case study of architectural heritage.

Conclusions and perspectives – It concludes the thesis and describe possible future works

This last part summarizes the main outcomes of the thesis. Then it describes possible future works that can be carried out thanks to the combination of the outcomes of the thesis, mainly focusing on the analysis and conservation of heritage structures.

Acknowledgment

Firstly, I feel the need to thank my family, my father, my mother and my sister for their patience and support.

A special thanks goes to professor Giuseppe Abbiati and professor Rosario Ceravolo, without whom the conclusion of this thesis would have been impossible. In particular, I want to thank Giuseppe for his patience, wisdom and for having hosted me in the ETH laboratories, where the hybrid tests reported in this thesis were conducted. Then, I want to thank Rosario for guiding me through the doctoral program with his profound experience.

I must acknowledge the RELUIS project for sharing some of the experimental data used in this thesis.

Finally, I am grateful to the *Fondazione Cassa di Risparmio di Cuneo - CRC* and the *Amministrazione del Santuario di Vicoforte* for having partially supported my research, and to professor Raimondo Betti who hosted me for a period at Columbia University.

...belief is again another form of conclusion.

Lee B.

Contents

List of Tables

List of Figures

Chapter 1

The role of models for the analysis and preservation of architectural heritage

This chapter introduces the role of models for the structural analysis and preservation of architectural heritage by means of emblematic examples. Firstly, a definition of *model* is introduced in general terms, then, some relevant contributions of models for architectural heritage are reported with a brief discussion on their conceptual importance. Models for structural engineering are discussed next, and the fundamental distinction between *physical* and *mathematical* models is reported. The excursus on modelling of the first part of the chapter concludes with the impossibility to define a clear line of demarcation between the qualitative and quantitative disciplines in their contribution to modelling of a real system belonging the architectural heritage.

Subsequently, more in depth investigations of physical and mathematical, here named *virtual*, models are conducted. Pros and cons of these two approaches are highlighted. If on one hand physical models can compensate for the lack or inadequacy of virtual models, the latter can overcome the limits of reproduction scale, which is intrinsic in the well-known *π-theorem*. The discussion brings to the conclusion that a step forward in modelling can be represented by the synergistic combination of physical and virtual models, which would lead to the definition of those that in the literature are referred to as *hybrid models*.

1.1. Models for architectural heritage

Man, by nature, engage with the surrounding reality in response of what are his perceptions. Although everyone has a different realization of reality, in general this is presented to all of us as a set of complex systems, (Novello, 2013), which

interact each other in a more or less marked way. In turn, a system is defined as a set of interacting elements, that is a set of objects that communicate to keep a regular interaction, or a mutual dependence, in order to achieve a certain purpose, (Hesse, 1980), (Marchis, 1988). This turns into results, which represent inputs and/or outputs of the systems.

Although reality is difficult to represent, in the past, many scientists met this challenge. The result was to represent only pieces of reality, or systems, depending on the outcome the scientist had to reach. Without perceiving it, the man began to realize and use *models* to finalize what the thought could not do. In this frame, a model is defined as, (Novello, 2013): *[…] a schematic construction, purely hypothetical or materially realized, or of intuitive origin, with which the object of a research is represented globally or only partially […]*. All the activities used to define a model are referred as *modelling (modellistica*, in Italian*)*. Since models are used in different fields, modelling activities may differ in turn. In the engineering fields, modelling is defined as a set of theories and methods used for experimentation, being it virtual (e.g. mathematical models), or real world (e.g. physical models).

A model should always contain the essential aspects of the system that seeks to emulate, so as to allow an understanding of the system that is not only complete, but also *exploitable*. To this end, the modelling must be undertaken in distinct phases. The first one is the *analysis*. In this phase, all the possible information on the system are collected and analysed. In the second phase, called *synthesis*, the information is analysed critically so as to minimize the unnecessary one. Then, in the *modelling* phase, the information that have passed the synthesis stage are used to realize the model. Finally, in the last phase, the model is used to extract new information about the system itself, information that could not be collected without the use of the model. This last phase is called *identification*.

Figure 1 shows an example of a model used to study the historic dome, designed by Michelangelo, of the Vaticano's temple, (Cavallari Murat, 1982). The figure is strongly emblematic as it shows how a system (the dome of the temple) can be modelled in two different, equally important, ways. In the first case, (Figure 1a), the model is useful as it allows to recognize in unequivocal way the existence of an equilibrium and therefore the distribution of the system masses. With the second model, (Figure 1b), instead it is possible to perceive the path of the loads that are discharged to the ground according to specific paths.

It is also possible in this way to define the structural elements and differentiate them from those with less structural importance. Thus the models produce two or more exploitable understandings of the system that, as we stated above, is a fundamental characteristic that makes a good model.

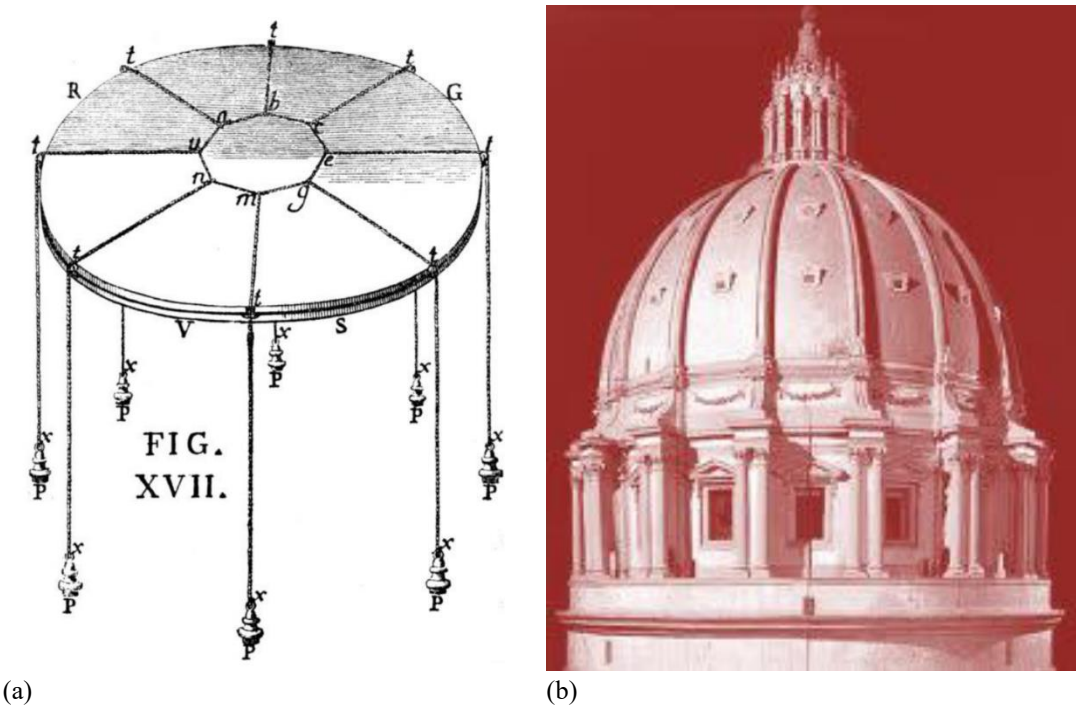

(a) (b)

Figure 1: Models of the Michelangelo's historic dome, in Vaticano, Italy, (Cavallari Murat, 1982): (a) graphical schematization of loads distribution; and (b) physical model.

Figure 2 is another example of model. The model, representing the structure of the Norfolk Scope, Virginia, U.S.A., (Marchis, 2009), was used to assess the strength of the building in presence of high forces due to wind in the wind tunnel of the Polytechnic of Turin, in 1969. This example wants to underline that the ways that a model can give useful information are countless. In this case in fact, in addition to the information coming from a simple observation, the model can be used to extrapolate information on the behaviour of the building in case of rare events, such as a strong storm.

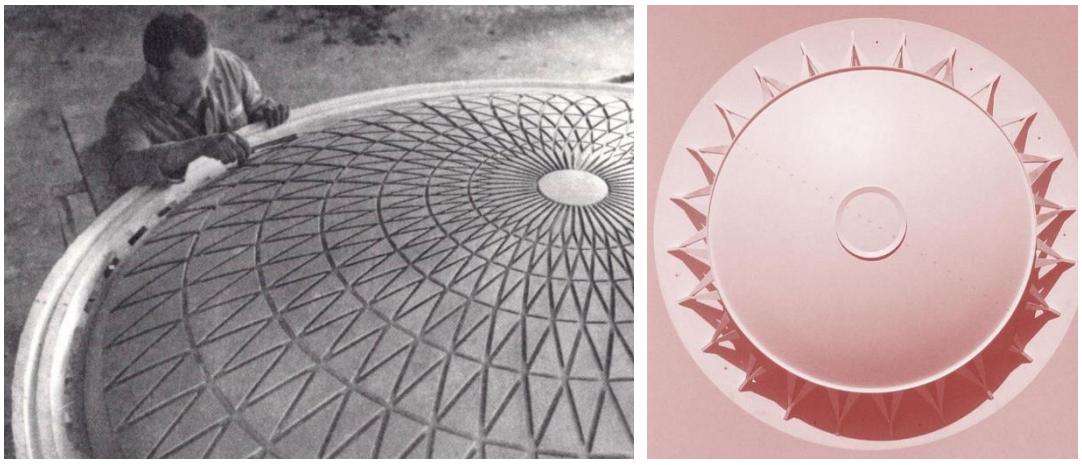

(a) (b)

Figure 2: Model of the Norfolk Scope, Virginia, U.S.A., (Marchis, 2009): (a) during the realization; and (b) final model.

Figure 2a depicts a construction phase of the model, in 1967, in the ISMES laboratories, while Figure 2b shows the final model in scale 1:50.

Figure 3 shows a significative example, (Iori & Poretti, 2007), of how a model can be built to investigate very complex scenarios. The figure reports the model of the *Bridge on Basento*, Potenza, Italy (Figure 3a), and the realized structure (Figure 3b). At that time the available tools to design such structures, with high complex shapes, were very limited. For common structures, the engineers and architects used to follow simplified approaches. However, when they had to contend with unique problems, such as the construction of an architectural work, they knew that these simplified methods could lead to meaningless, or misleading, results. The solution was to adopt models that accurately reproduced the geometry of building, and/or that could aid the most advanced tools of the time. For this reason, in 1967, at the ISMES laboratories, it was decided to carry out the reproduction of the *Bridge on Basento* in a very high scale, i.e. 1:10. This allowed to overcome the problems related to the ability of the model in representing the real system, ability that decreases as the scale of the model decreases.

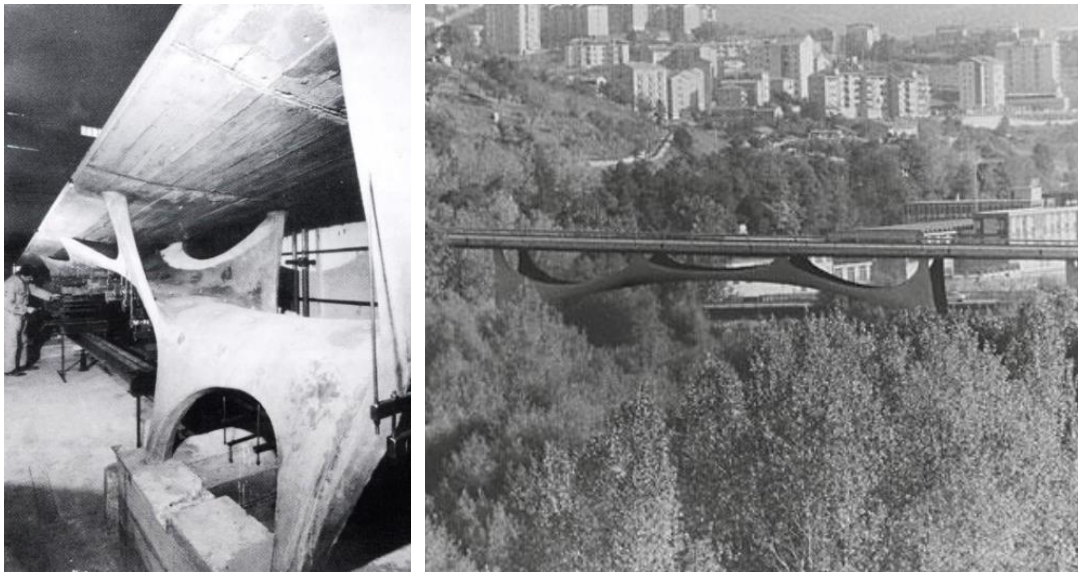

(a) (b)

Figure 3: Bridge on Basento, Potenza, Italy, (Iori & Poretti, 2007): (a) model in laboratory; and (b) real structure.

With the previous example, attention was focused on the shape of the system to be modelled. If one wants to generalize, the form is nothing that the representation of the space filled by a system. Although the process of creating a model should not be confused with actions designed to define its form, it is certainly true that the correct reproduction of the occupied space underlies the conception of any model (physical or not) associated with a system that admits a spatial representation. It is for this reason that research on this subject has gone a long way in history. Starting from the manually graphic reproduction of a system,

we have now arrived at the representation of models using advanced techniques such as the 3D Laser Scanner, e.g. the Laser Imaging Detection and Ranging Laser (LIDAR). The LIDAR is an optical sensing technology, which measure distances by using laser techniques. The LIDAR can capture countless number of points (spatial coordinates) with high accuracy and efficiency. However, the collected points are undifferentiated, this requiring additional treatments before that the model can be useful to produce exploitable information. Figure 4 reports an example of application of LIDAR to an existing dome. The dome is that one of the church of the *SS Trinità*, Turin, Italy. In the figure it is possible to observe the raw points cloud recorded by LIDAR. The accuracy is extremely high in the overall structure (Figure 4a). However, this very high accuracy is not always a pros as it brings noise if the points cloud is used for specific scopes. For example, is very easy to denote the presence of a railing, but if the aim of the points cloud is to be used in a structural analysis the presence of a railing represents noise for the structural problem. This results in a complication of the synthesis phase (the output of the synthesis is showed in Figure 4b), during which the useless information must be eliminated in favour of a greater effectiveness of the final model.

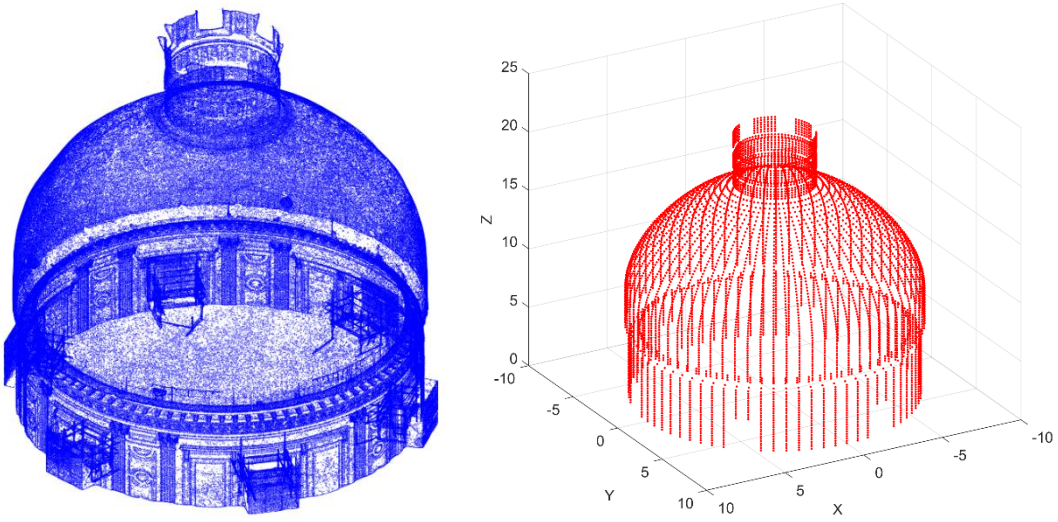

(a) (b)

Figure 4: Points cloud representing the dome of the church of the *holy trinity*, Turin, Italy: (a) before; and (b) after the synthesis phase.

Up to this point, it is possible to appreciate that models are useful to get some kind of information that are very difficult to get without an aid. However, what happen when the purpose for which a model is conceived is reached ? The model is still useful ? These questions are hard to answer and providing the answers is out of the scope of this thesis. Thus, we will limit ourselves to saying that a model can always be useful to those who will be able, through observation, to gather new information and turn them into useful advice for the community. This, especially true for the models of architectural heritage but still valid for any type of model,

introduces the important role covered by the exhibitions of historical models. In this sense, a collection of models is not only a means to preserve the *memory* but, in addition to this function, their exhibition may stimulate people to take cues, enrich their knowledge, make connections that are useful for conceiving of new objects and systems, i.e. new pieces of reality. An impressive collection of architectural models is the one stored at Politecnico di Torino (Politecnico di Torino, 1989), which can be accessed through a virtual museum, (https://areeweb.polito.it/strutture/cemed/museovirtuale/). The museum collects a countless number of model realized in the nineteenth century at the school of applications for engineers in Turin. Still nowadays, strolling down the corridors of the Polytechnic of Turin, it is possible to visit the temporary exhibitions of these models. Figure 5 reports one of these beautiful models, i.e. the model of the Isabella bridge on the Po, in Turin, 1880 (scale 1:50), with the details of the ribs. This example demonstrates the role the models play in teaching, as, with the help of the models, the students can appreciate the different construction phases used for bridges and other architectural works.

In this section the attention was concentrated on the concept of model, with special emphasis on the models employed in the analysis of architectural heritage systems. The next section will more specifically focus on models used to address structural engineering problems, possibly related to architectural heritage.

Figure 5: Model of the Isabella Bridge on the Po, Turin, Italy, (Politecnico di Torino, 1989).

1.2. Models for structural engineering

Structural engineers often recur to idealized models in order to reduce, analyse and predict the behaviour of complex objects and systems. To this aim two categories of models can be used:

- Physical models;
- Mathematical models.

In turn, each aforementioned type can be classified in:

- Models to emulate the inertial or mass properties;
- Models to emulate the constitutive relations.

For physical models, the mass aggregation model is imposed itself by the system geometry. The only distinction that one can be stated is the difference between lumped mass, and distributed mass models. Once the physical model is realized, according to the right rules of the modelling, the aggregation model is univocally defined. In contrast, for mathematical models, the mass aggregation or assembly model is not unique. It is possible to recognize mono-dimensional, bi-dimensional and tri-dimensional formulations where the masses of the system can be idealized as both lumped and distributed, with discrete or continuous formulations. For simple systems, the model can be described by analytical closed form equations. However, in the majority of the cases, the models are built through numerical assembly techniques.

As regards the model to emulate the constitutive relations, for physical models the relations are provided by the nature of materials used to realize the artefact, which are influenced by the scale of the physical model. Then, if the mathematical models used to describe the aggregation between the parts are innumerable, those to describe the constitutive relations are almost infinite. One can assume isotropic vs anisotropic models, with mono-dimensional, bi-dimensional and tri-dimensional formulations.

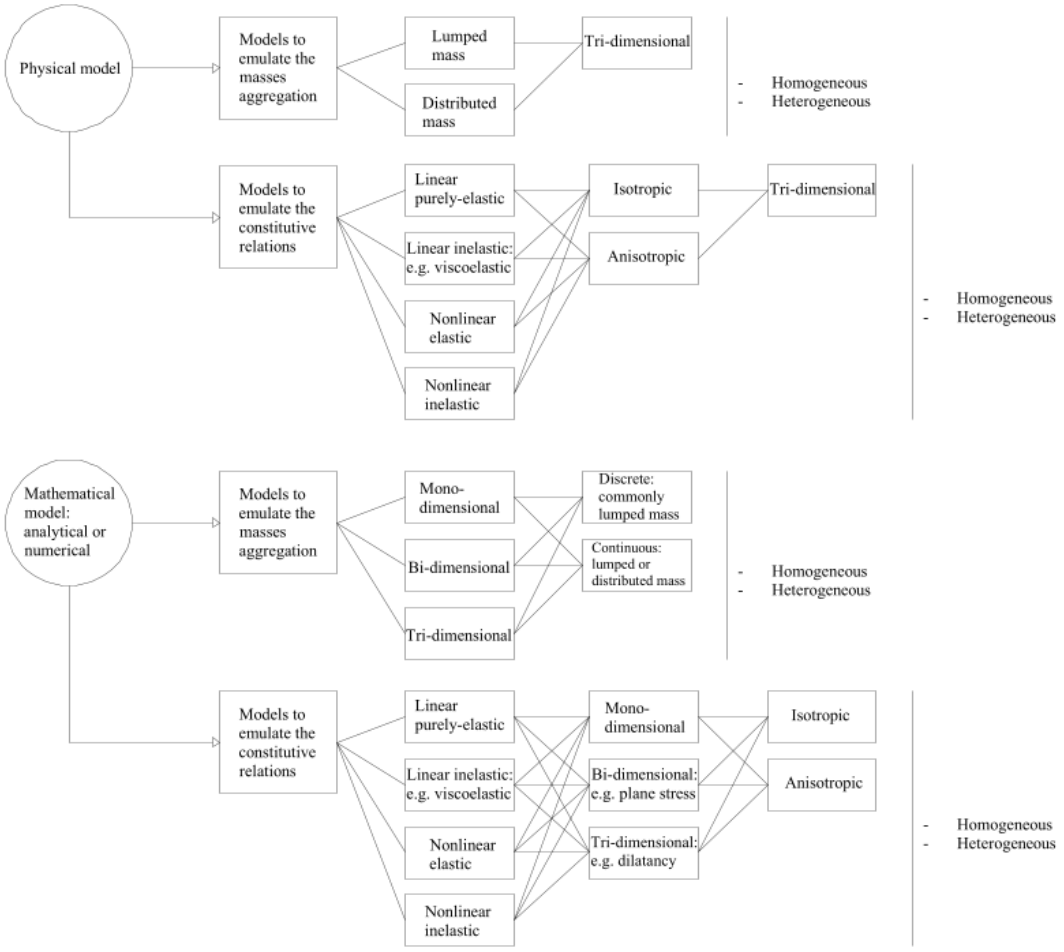

Figure 6: Conceptual map of models available for structural engineering.

If one refers to the constitutive behaviour, it is possible to recognize linear purely-elastic (that obey the Hook's law), linear inelastic (such as linear visco-elastic models), nonlinear elastic (e.g. that obey super elasticity models) and nonlinear inelastic (as models that includes hardening or softening behaviours, with or without memory, etc.) models. For these models both analytical closed equations and numerical techniques can be used to describe the constitutive relations. Finally, it is worth noting that for both physical and numerical models, homogeneous and heterogeneous idealization of the masses aggregation and constitutive relations can be used in the modelling, based on the system to be emulated. Figure 6 reports a conceptual map of models available for structural engineering.

Figure 7 reports two types of scaled physical models. In Figure 7a, (Tang, 2013), it is showed the lumped mass (inverted catenary) model that Antoni Gaudì used to find the optimal shape for La Sagrada di Família. Instead Figure 7b, reports a stunning scaled model of the Beauregard dam realized by ISMES, Bergamo, Italy (Oberti, 1967), where it is possible to recognize the isostatics used to determine the path of the internal loads.

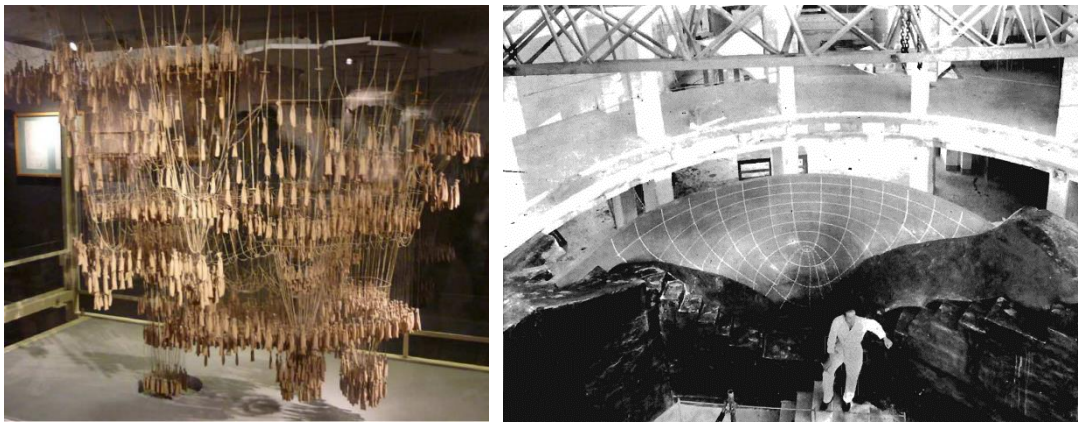

(a) (b)

Figure 7: Physical models: (a) lumped mass, (Tang, 2013); (b) distributed mass, (Oberti, 1967).

Figure 8 reports the use of mathematical models to simulate an arch. In Figure 8a it is possible to recognize just one dimension of the arch, its directrix. The other dimensions are considered by using models that emulates the behaviour of the system along the width and depth of the section. In Figure 8b, the same system is emulated with a tri-dimensional model. Instead of using specific formulations, the behaviour along the width and depth of the section is intrinsic in the virtual model formulation.

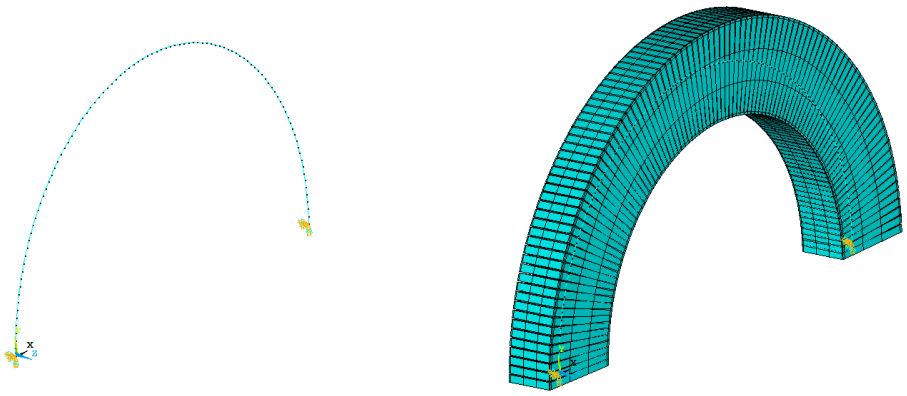

(a) (b)

Figure 8: Mathematical models for an arch: (a) mono-dimensional; and (b) tri-dimensional.

In the next sections some worth of mentioning model for representing real systems are reported for both physical and mathematical, named *virtual*, models.

1.3. Physical models

The theory behind physical models is based on the principle of *similarity*. According to this principle, two systems are said to be physically similar if it is possible to recognize a geometrical and mechanical correspondence between any point of the systems, i.e. if the systems' properties are in a constant ratio in those points, (Oberti, 1967). If all this is simple to say, it is not easy to realize. In fact the similarity between systems and models is a vast science, which bases its rules on Buckingham's theorem. According to this theorem, a system can be described completely by a number of groups of dimensionless variables equal to the differences in the number of physical variables of the system and a number (usually 3) of independent fundamental variables. The importance of the Buckingham's theorem, or *π-theorem*, lies in the fact that if a model is intended to describe a system, it does not need to reproduce all the physical variables of the system, but just a reduced number of dimensionless variables. The difficulty in the application of the theorem, however, is represented by the scale of the model. This because, for some reason, the constancy of the ratio between the properties of the model and the system can be lost if the modelling scales become too small. One clarifying example is that of the glass, which at small scales exhibits a less brittle behaviour. Thus, for some systems, a nonlinearity exists in the transition of the geometrical scale. But if this is true, if the material behaviour differs in a nonlinear way with changing its geometric scale, it means that the type of response of the system due to an applied force is not proportional to the system geometric scale. However any system is continuously subjected to loads because the existence of gravity. Thus, when modelling it is of paramount importance to understand if the volume/mass forces are negligible or not. The smaller the influence of volume/mass forces on the response of the system, the smaller the

scale of the model that can be used. On the contrary, difficulties can arise if the volume forces are not negligible, as in this case it is necessary to use large-scale models, or to use techniques that artificially increase the density of the material.

Oberti proposed the following classification of testing methods on models, (Oberti, 1967):

- Tests to address simple, or modestly complicated, plane problems: they commonly use technologies based on photo-elasticity and work based on the experimental application of the principle of reciprocity. The scale of the model is commonly large because the model focus on a local part of a structure;
- Tests to address simple, or modestly complicated, tri-dimensional problems: with these, entire structures are commonly studied, with small or medium scale (rarely the scale approximates the real dimension of the system), adopting also different materials from those of the system to be emulated;
- Tests to address problems characterized by mild to high complexity: for these problems the theory does not produce satisfactory results, or in some cases the laws to describe these phenomena have not been formulated yet (e.g. the problem to be described is chaotic).

Another important distinction to be made when talking about physical models is that of the testing phases. Commonly two distinct phases can be differentiated:

- Application of serviceability loads;
- Application of collapse loads.

In the first phase, loads with values close to the conditions of similarity are applied, this imposing the equality of the unitary strain between the model and the system. It is important to note that at the first load application, inelastic phenomena of various types can occur (settling, partialization of joints, local plasticization, etc.), which should be deliberately removed with loading and unloading cycles to initialize the model, i.e. the model, from that point onwards, behaves in a linear elastic way for small strain. Then, with the second phase, the model is loaded up to the collapse and the distance (in terms of forces) between collapse and serviceability configurations can be considered as a global safety coefficient. Figure 9 reports the double-sided dam of Hongrin, Switzerland. The physical model, showed in Figure 9a, refers to the end of the test, carried out at ISMES laboratory, that brought the model up to the collapse. The information gathered during the test proved to be of a paramount importance for the understanding of the structural behaviour of the dam and its construction. The structure, still in operation, is showed in Figure 9b.

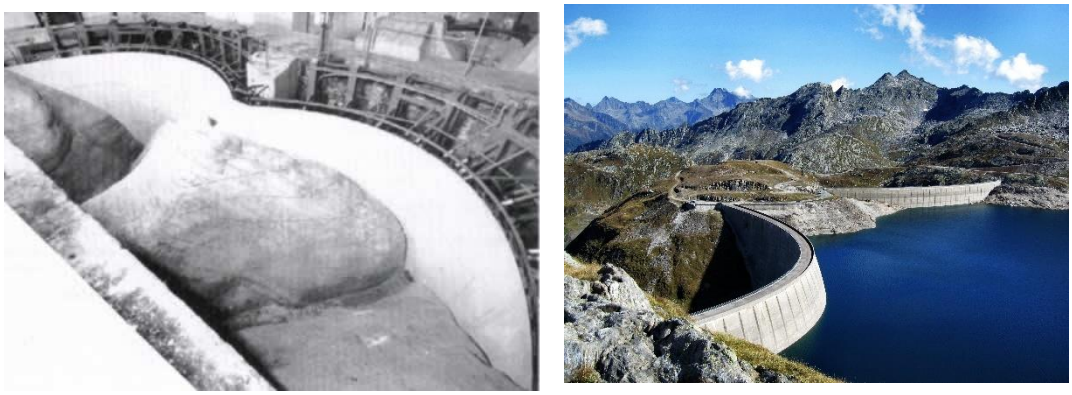

(a) (b)

Figure 9: Hongrin dam, Switzerland: (a) model in laboratory, (http://www.asim.it/ismes/Ismes_It/132.htm); and (b) real structure, (https://commons.wikimedia.org/wiki/File:Naret.jpg).

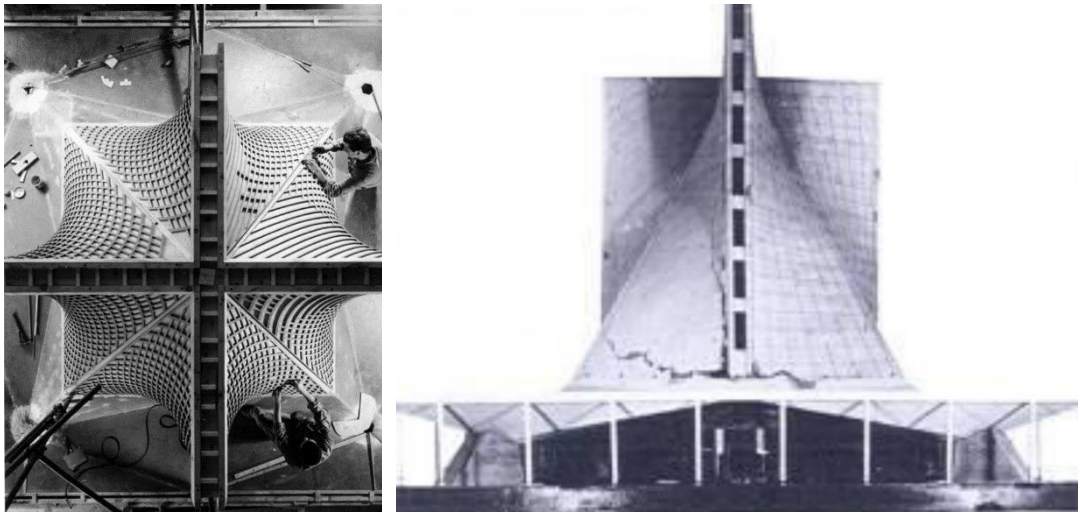

(a) (b)

Figure 10: St. Mary Cathedral, in San Francisco, U.S.A: (a) physical model realized at ISMES, (Hildebrand, 2015); and (b) the same model tested at Politecnico di Torino, (Chiorino. 2017).

Although the principal cases of interest of ISMES were the concrete dams built during the second half of 1900, in the laboratories many architectural building were realized. One example is the St. Mary Cathedral, in San Francisco (1963-71) of Pier Luigi Nervi and collaborators. Figure 10 reports the phases of construction of the physical model, depicted in Figure 10a, (Hildebrand, 2015), and the model after the test carried out in the wind tunnel at Politecnico di Torino (Figure 10b), (Chiorino. 2017). From the model after the collapse it is possible to denote a marked crack pattern at the base of the hyperbolic surface.

Another example of cultural heritage modelling is the physical model realized at ISMES (see Figure 11a) is that of the Cathedral of Milan, (Novello, 2013). In Figure 11a it is reported the elastic model (1:15 scale) of the structural system, lantern, pillars and main spire of the Milan Cathedral, built at ISMES. In Figure 11b, a different model (exhibition model) of the cathedral is instead reported.

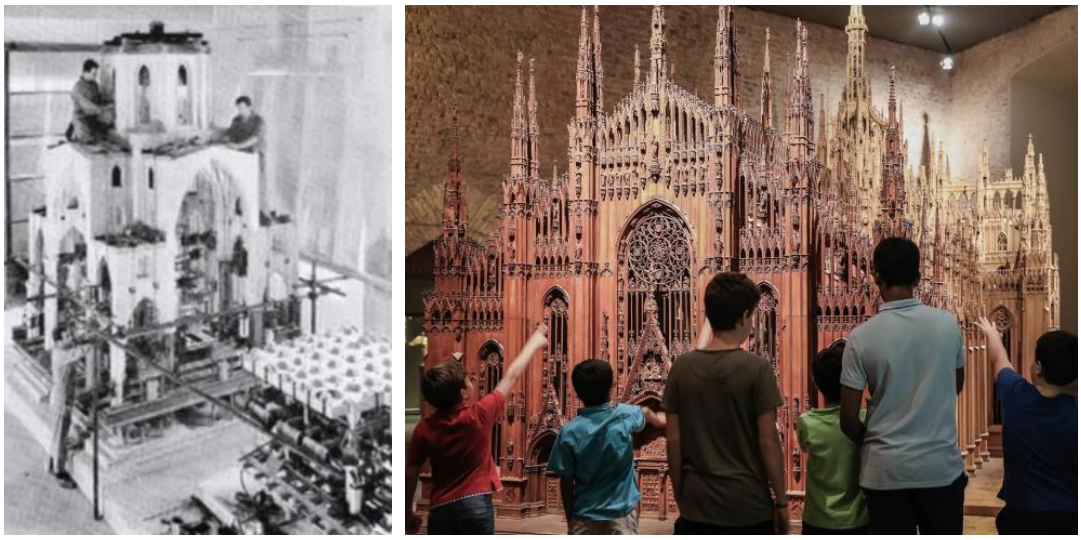

(a) (b)

Figure 11: The Cathedral of Milan: (a) physical model realized at ISEMS, (Novello, 2013); and (b) a different model for exhibition purposes, (https://www.duomomilano.it).

(a) (b)

Figure 12: Physical model of masonry arch bridge, (Ruocci, 2010): (a) model during the construction; and (b) final model.

Although ISMES' models have focused on works with a certain impact on the community, one must not forget that physical models apply to any type of structure, regardless of the opinion the community has on the system to be modelled. A beautiful example of a physical model of a masonry bridge can be found in (Ruocci, 2010). This work concerns the application of Structural Health Monitoring (SHM) methodologies to protect masonry bridges from scour risk, (Ruocci et al., 2009). To validate his work he applies SHM methodologies on the physical model of a masonry bridge, subjected to settlement of a pier. Figure 12 shows the aforementioned masonry arch bridge, (Ruocci, 2010).

To conclude this excursus on physical models, an extract of the words of Professor Guido Oberti, (Oberti, 1967), regarding the tests on physical models to address complex problems (*new methods* hereinafter) is reported below:

[…] The new methods instead, rather than obeying to pre-conceived schematizations, prefer to approach the reality of the single case by reproducing

their peculiar characteristics; thus, one does not hesitate to introduce into the model materials, foundations, constraints, joints and executive modalities in general, which, while making it harder to produce analytical comments and causing a certain dispersion of results in repeated tests (especially around discontinuities), allow for a more realistic and synthetic vision of the problem, and therefore more in keeping with the true aims of the experimental test. […].

If these words reassure the reader on the use of physical models, it must always be remembered that reality is something quite different from a simple, however complex, extrapolation of the results of experimental tests. In this sense, Figure 13 is emblematic. It shows the viaduct on Polcevera, which collapsed at 11.36 am on August 14th, 2018. This case highlights how the reality is constantly evolving, and the results of experimental tests can cease to be valid with time, this because both the system and the surrounding environment undergo continuous changes. For this reason, a model should always be able to change and incorporate new information. Fortunately, physical models are not the only tool a structural analyst can rely on. Another valid tool is represented by mathematical models, or *virtual models* in a broader sense.

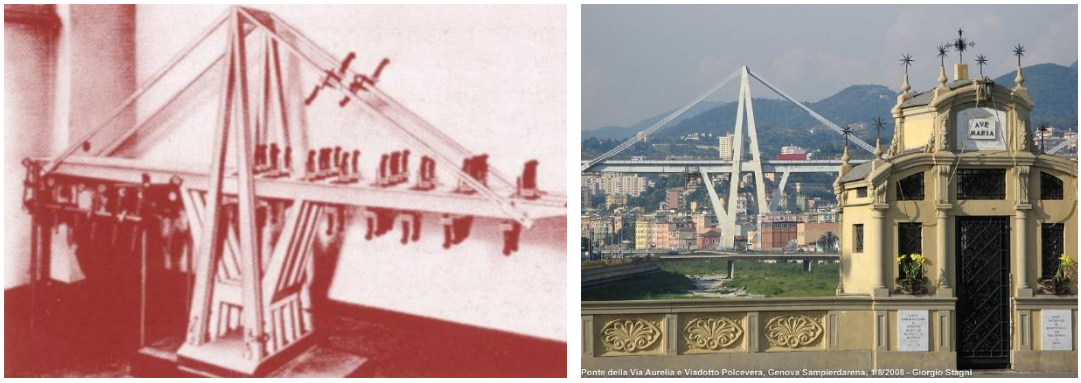

(a) (b)

Figure 13: Viaduct on Polcevera: (a) physical model realized at ISMES, (Novello, 2013); and (b) photo of the viaduct taken in 2008 by Giorgio Stagni, (http://www.stagniweb.it).

1.3.1. From physical to virtual models

With the advent of advanced virtual models, two different views about the analysis of structural systems have taken place, (Hildebrand, 2015):

- Thoughts according to which, although the development of advanced numerical methods, such as the Finite Element Method (FEM), has brought numerous advantages to the analysis of structural systems (as they are quicker and cheaper than the methods needed for a physical modelling), physical modelling cannot be replaced in its entirety by virtual modelling;

- Thoughts according to which physical modelling can be replaced in its entirety by virtual modelling.

Two examples of these thoughts are represented by: (i) the field of *structural assessment*, where laboratory tests on physical models still play an important role on the definition of the safety of a structure, and; (ii) the field of *form-finding*, where computer tools soon proved extraordinarily effective in replacing experimental practices on physical models, such as those conducted by Frei Otto and Heinz Isler.

In the next section, the use of virtual models is described through an illustrative classification of the different types available today. The discussion starts with the description of common models up to arrive to the definition of most advanced methods, which can nowadays be grouped with the term of *digital twin*.

1.4. Virtual models

For virtual models it is possible to recover the classification reported in Figure 6 about the mathematical models used to approximates the mass aggregation of a system. Given a selected geometric representation (mono-, bi- or tri- dimensional) of the system, the following classification holds:

- Discrete model: it is possible to identify, regardless of its size, a finite particle of mass if the matter is broken down;
- Continuous model: it is not possible to identify, a finite particle of mass if the matter is broken down infinitely.

Both discrete and continuous models can be treated analytically or numerically. Well-known discrete models are those developed to describe the *molecular dynamics*. In this case the equations of motion are commonly written starting from the potential of each particle. A gradient applied on the potential, defines the force that the particle exerts on a point of a system. Then, knowing the particle's mass it is easy to get the dynamic response (acceleration, velocity and displacement) of the system in any point by integration. Typical examples of continuous models are those related to the *continuous dynamics*. In this case, the equations of motion are commonly written in terms of two quantities that define the kinetic energy and the elastic potential energy. In addition to these two quantities other physical quantities can be contemplated to represent more complex behaviours of systems, (e.g. nonlinear stiffness terms, etc.). With continuous models, instead of having a force field that connects different mass particles, the masses are connected by continuous portions of matter, having distributed mass and stiffness characteristics. The stiffness in this case is defined by the materials that constitutes the body and the geometry of the system. Figure 14, (Haddad et al., 2016), reports two virtual models of a bi-dimensional plate (system), with a uniformly distributed load applied at the top: on the left the

system is modelled with a discrete approach, while on the right a continuous modelling is adopted.

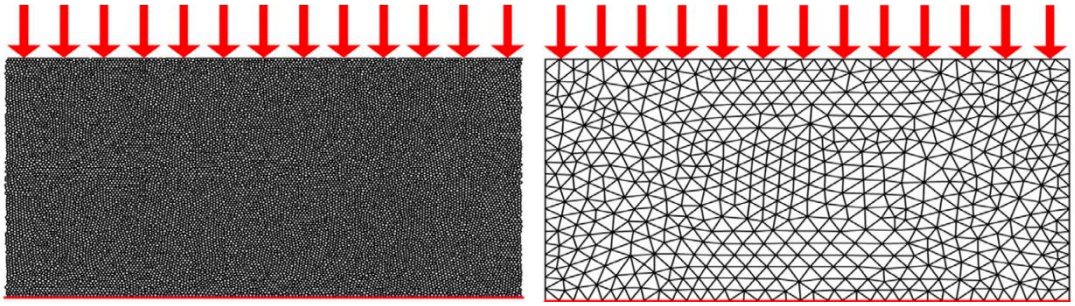

(a) (b)

Figure 14: Models for a bi-dimensional plate, (Haddad et al., 2016): (a) discrete model; (b) continuous model.

Hereinafter some emblematic examples are reported, helping to make a clear distinction between the aforementioned types of models. Among the countless discrete methods available nowadays, the most widely quoted in the structural analysis is the Discrete Element (DE) method, (Cundall et al., 1979). The DE method is known to be very appropriate when the modelled system exhibits large displacements, or in case the continuity of the system may fail during the simulation due to, for example, low tensile strength values of materials. The method is also very suitable for solving problems like friction, rigid kinematics, contact behaviours, etc. Figure 15 shows a typical representation of a DE model for two types of vaults, (Lengyel, 2017).

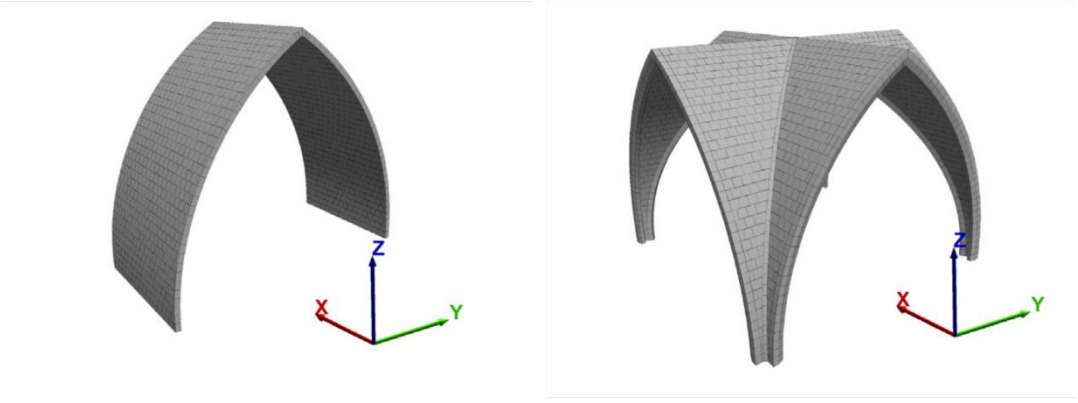

(a) (b)

Figure 15: Vaults modelled with DEM, (Lengyel, 2017): (a) barrel vault; and (b) cross vault.

DE models are extremely useful when dealing with masonry structures. This is related to the low tensile strength of the masonry, due to which the structure of the system may experience disconnections caused by the appearance of concentrated or distributed cracks patterns. Figure 16 reports the numerical response of a vault modelled with DE method, (Bertolesi et al., 2019). In Figure

16a the response is referred to an horizontal movement of the base, while Figure 16b reports the response to a vertical action. From the first picture an *arch-type* collapse is denoted for the vault in X direction, while from the second picture, the collapse is more distributed in the space. Both simulations, however, predict the same vulnerable part, the keystone area of the vault. To reach this conclusion, the structural analyst only needs the visual check of the simulation's results, which unequivocally highlights a detachment of a limited portion of mass from the mass of the system that is still aggregated. The DE method, therefore, in addition to possess the numerous advantages mentioned above, has the virtue of being extremely intuitive, a fact that should never be underestimated when working with virtual models.

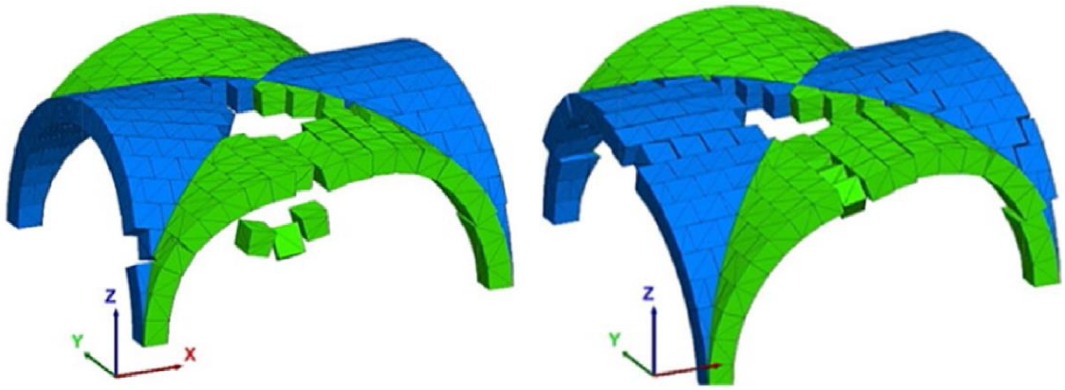

(a) (b)

Figure 16: DEM analysis of vaults, (Bertolesi et al., 2019): (a) horizontal action response; and (b) vertical action response.

It is worth mentioning that although discrete models enjoy many properties, they may be inappropriate if applied to certain types of problems. In particular, big problems that involve very complex systems are difficult to simulate due to computational limitations. This bring, when working with very large systems, to the obligatory choice between an accurate but inefficient model or a not very accurate (raw discretized) but efficient model. Fortunately, discrete models are not the only tool that an engineer can rely on, especially when dealing with huge systems. In fact, if the system to be analysed is very large, the need to study the behaviours between two finite portions of matter becomes expensive and not very useful. Sometimes, one prefers to observe the structural problem at a higher scale. In this way, all micro-behaviours are studied with equivalent, linear or nonlinear models. This is precisely the concept of continuous models. If compared with discrete models, continuum models are commonly (not always) more efficient.

As this thesis focuses on the modelling and analysis of large historical buildings, the virtual models adopted hereinafter fall in the family of continuum methods. Thus, among a countless number of complex behaviours that characterize masonry historical buildings (e.g. nonlinear mechanical behaviour of the materials, construction phases, interaction between the different portions of

the building, etc.), this work will refer to homogenised laws to describe the structural response of continuous mechanical models. This does not implies that other aspects are less important, especially when working with masonry buildings. For this type of buildings, in fact, the formation of cracks, and therefore the dislocation (complete or partial) of subparts of the building is a very common finding. The importance of the interaction between the different portions of the building is also reported by international guidelines and standards on heritage structures (e.g. ICOMOS-ISCARSAH, 2003), which highlight that the acquisition of an appropriate level of knowledge on the construction and its structural details (e.g. the connections between different elements) is of paramount importance for the definition a reliable structural model, especially because a little variation in the nature of these characteristics commonly entails an important variation of the model prediction capability.

In structural engineering the standard method used to emulate a system is represented by the Finite Element (FE) modelling, (Zienkiewicz, 2005). With FE models it is possible to study systems with very complex geometries in a relatively simple way. The geometry, in fact, is divided in different subparts called elements. Then the elements are connected together to form the final virtual model. The method is best suitable for problems where the system to be modelled does not exhibit disconnections in its constitutive parts and can be applied to solve a countless number of physical problems such as structural, thermodynamic, electromagnetic problems, etc. Figure 17a reports a FE model of Hagia Sophia in Istanbul, (Croci et al., 2006). In the picture it is reported the stress field that concern the structure. The stress field can be used to detect the most critical parts of the structure, increasing the level of knowledge on the system, allowing in this way to make more conscious decisions. In Figure 17b a recent photo of the building is reported.

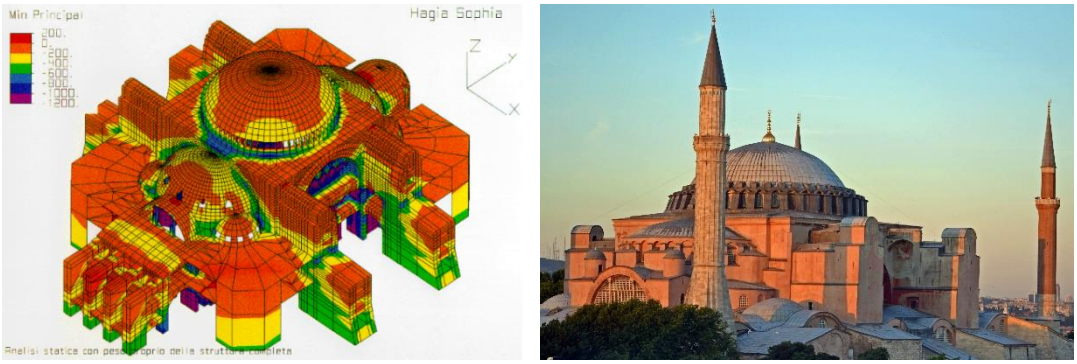

(a) (b)

Figure 17: Hagia Sophia: (a) FE model, (Croci et al., 2006); and (b) recent photo, (https://commons.wikimedia.org/wiki/File:Hagia_Sophia_2017.jpg).

Figure 18 concerns another relevant application of the FE method. In Figure 18a in fact it is reported the model of the Colosseum, (Cerone et al., 2000), while in Figure 18b a recent photo of the monument is showed. This example is

emblematic as it highlights the importance of the aim for which a model is built. The FE model in the picture concerns the entire building, whilst the present structure is the one reported on Figure 18b. In fact the authors in their work explored several configurations of the geometry of the Colosseum.

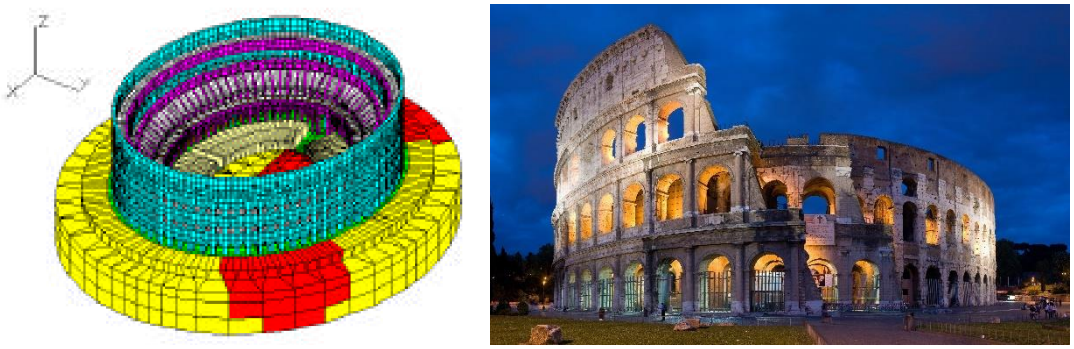

(a) (b)

Figure 18: Colosseum: (a) FE model, (Cerone et al., 2000); and (b) recent photo of the structure, (https://commons.wikimedia.org/wiki/File:Colosseum_in_Rome,_Italy_-_April_2007.jpg).

A real system can evolve in the time due to unpredictable events, and constructing different models that follow the several stages of the real system is a way to understand how the response of the system changed over time, allowing countless of considerations. For example, an important consideration regards the structural and stability assessment of the building (now different from the original conception) in presence of rare actions such as fires, earthquakes, settlements, etc., which, whenever investigated, should be applied in configurations that are different from the present one.

The previous example confirmed that a model should be constructed based on the aim of the simulation. In particular, it is shown that a real system can evolve in the time, thus its schematization must contemplate different models. However not only does the system change its configuration, but also the environment surrounding the system will do, both in the short and long time and both in a temporary or permanent way. To better explain this concept, Figure 19 reports the Sanctuary of Vicoforte, Cuneo, Italy, (Ceravolo et al., 2019). The Sanctuary of Vicoforte, in fact, counts on both static and dynamic monitoring system. The health state monitoring is performed continuously, meaning that a change of the surrounding environment or a change in the system properties can be detected at all times. For example, a change in the environment temperature is commonly reflected in a deviation of the natural frequencies of the system, (Pecorelli et al., 2018). This change is relatively small, in addition it is periodic and persistent. For this reason the phenomenon is said to be a *physiological*. When the virtual model is used to predict a particular response (being it modal or structural) all the physiological behaviours that bring some variability, and thus uncertainty, should be considered in some way, in order to have a reliable comparison between the model prediction and the actual response of the system. If the necessity to

incorporate physiological behaviours of the system in the model is important, including *pathological* ones is fundamental. A pathological behaviour is that due to a temporary or permanent change of an environment condition that produce a permanent change of the structural properties. An example of pathological behaviour is the permanent reduction of the natural frequencies of a system after an earthquake event. When such pathological behaviours occur, they should be considered in virtual models by reinitializing both the constitutive models of materials as well as, if needed, the geometry of the model. These are the reasons that brought the virtual modelling toward a new era, where experimental data and models are connected with continuous or periodic processes, giving life to the concept of *digital twin*.

A digital twin has not a unique definition however it can be defined as, (El Saddik, 2018): […] a digital replica of a living or non-living physical entity. By bridging the physical and the virtual world, data is transmitted seamlessly allowing the virtual entity to exist simultaneously with the physical entity. […] The digital twin is thus a paradigm that relies on Ultra-High-Fidelity (UHF) calibrated computational models against experimental benchmarks and it is shifting the paradigm of design, verification, monitoring and life-cycle assessment, in several industrial and scientific sectors.

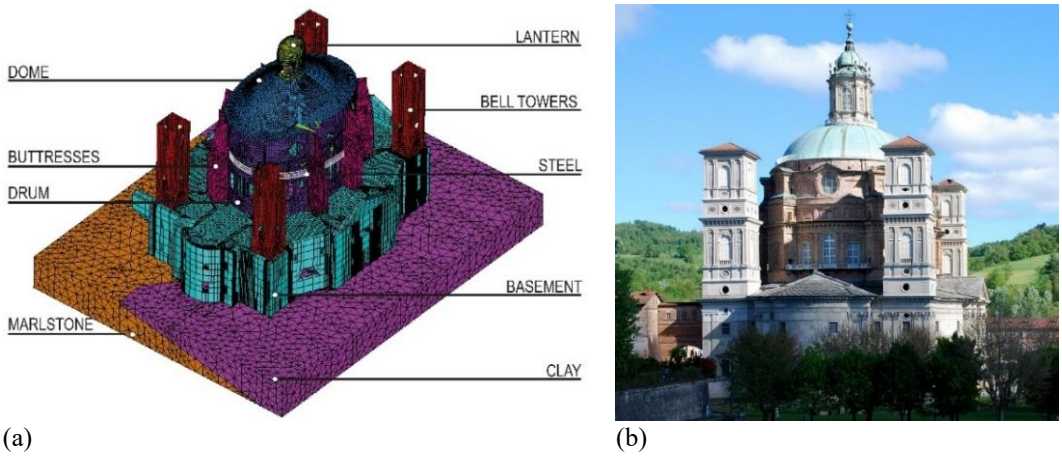

(a) (b)

Figure 19: Sanctuary of Vicoforte, (Ceravolo et al., 2019): (a) FE model; and (b) image of the Sanctuary.

To conclude the discussion on virtual models it is possible to affirm that, in the opposite of physical models, they have the great advantage to be able to incorporate experimental data and thus to change continuously, following the evolution of the real system. However, this is only possible if the mathematical model exists, and even if it does exist, it simulates in a satisfactory manner the physical phenomenon to be emulated.

1.5. The age of hybrid models

Cultural heritage structures intrinsically contain a huge number of uncertainties. These uncertainties, as those one related to the dynamic interaction between disconnected components of the structure, are the cause of the rising of very complex and, at the most, chaotic behaviours. This is what this thesis wants to stress out. The only way that a model has to predict in a reasonable, as long as approximate, way the output of a system that exhibits very complex or chaotic behaviours, is to detect the causes of the complex behaviour and split the modelling in two part: (i) a mathematical/virtual part; and (ii) a physical part. The first one represents a model that is able to reproduce the linear and/or the nonlinear behaviours with available mathematical models. It can be an analytical model (commonly if the system is very simple), but more in general it is represented by a numerical model of the system. For this reason it is often referred as Numerical Substructure (NS). The second part is represented by a physical model that reproduce the part of the system that intrinsically cause the high complexity of the system behaviour. It is commonly a physical reproduction, in natural scale, of a sub-part of the system, and for this reason it is often referred as Physical Substructure (PS). Because the PS is a real, physical artefact, it not need mathematical models to describe its behaviour. Already the PS (and the NS), is part of the *hybrid model* that is used to predict the complex nonlinear behaviour of the analysed system. Figure 20 reports a schematization of the hybrid model.

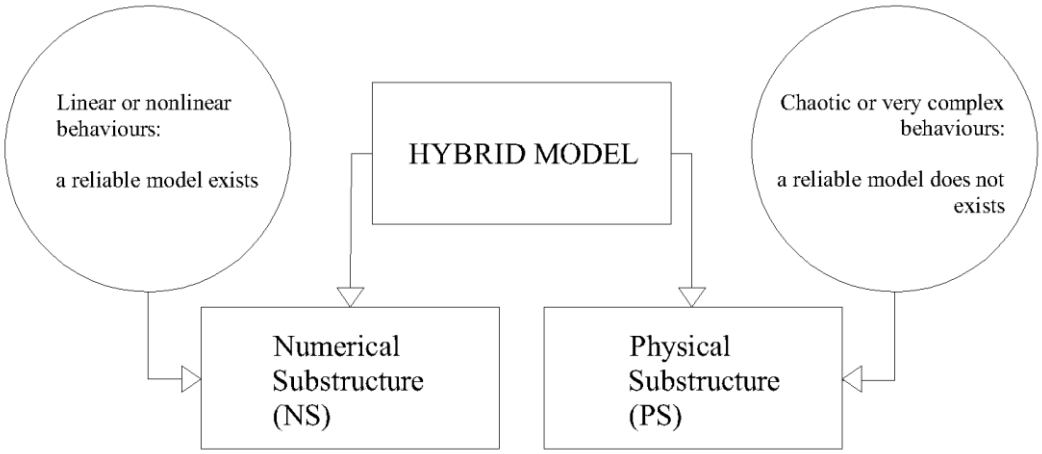

Figure 20: Hybrid model schematization.

Because of the mixed nature of the model, the analysis carried out with this type of models is referred to as Hybrid Simulation/Testing (HS/T). The simulation regards the NS, while the testing regards the PS. The two parts are then interconnected through specific algorithms, but, during simulations and testing, the NS can benefit of all the information coming from the PS, hence the modelling of very complex or chaotic behaviours is avoided.

The advantage of using hybrid models rely in the fact that the two modelling strategies are used in an appropriate way to solve specific problems. If physical models are not suited to represent structural systems when the scale of the reproduction becomes too small, they are very good in representing extremely complex behaviours when reproduced in scale approximately close to the real one. On the opposite, if virtual models are proved to fail when applied to systems with very complex or chaotical behaviours, they are demonstrated to be really good in solving problems where, within the limits of the instrumental or calculation approximations, the theory finds a good matching with the real observation (as the linear elasticity), and this can be done in a relative cheap way. This, results in a synergic effect, which makes hybrid modelling a step forward respect to uncoupled virtual and physical modelling.

The hybrid simulations were introduced for the first time in 1969, in Tokyo, to simulate the seismic response of civil structures. Motohiko Hakuno, Masatoshi Shidawara and Tsukasa Hara of the University of Tokyo, on that they occasion tested a simple cantilever beam (see Figure 21), (Hakuno et al., 1969), loading it with an electro-hydraulic jack. The data were recorded with light-sensitive paper.

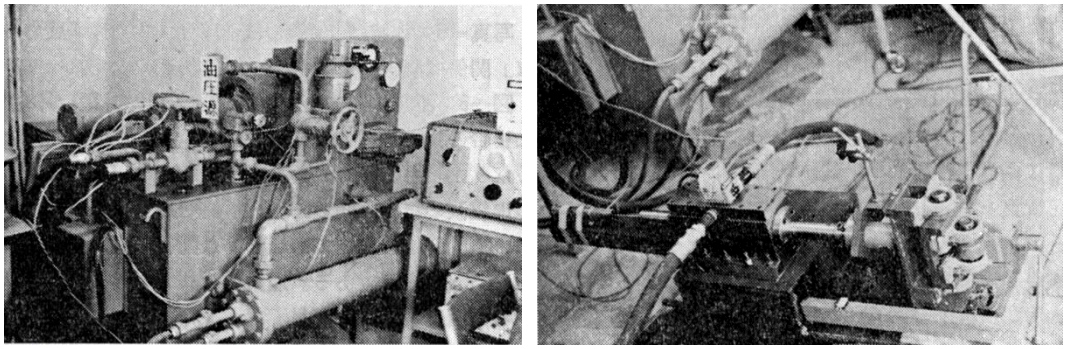

Figure 21: Historical photos of the experimental setup for the cantilever beam system, (Hakuno et al., 1969).

The theoretical bases at that time had not yet been written and the formulation of the theory arrived later, in 1973, with Professor Stephen A. Mahin (University of Berkeley), who began to work on the mathematical basis. Following the works of Mahin, the first real hybrid experiment was carried out in 1974, by a different group of Japanese researchers from the University of Tokyo, who tested a rectangular steel frame, (Okada et al., 1980). From 1969 to today research has made great strides in this field, but it is only recently that the use of hybrid methods is systematically crossing the doors of new disciplines and/or applications. Figure 22 shows a beautiful example of application of hybrid modelling, (Stefanaki et al., 2015). On the left of Figure 22a it is reported a schematization of the soil-foundation-building system modelled with the hybrid approach. On the right of Figure 22a, instead, the hybrid model is depicted. The building, representing the NS, is supposed to be virtualized, while the soil and foundation, representing the PS, is reproduced in laboratory as the theory behind

the structural behaviour of granular materials, like soil materials, tends to be less determined than that one developed for cohesively solids. In addition, the interaction between the foundation and the soil it is known to be a rather complex problem for which mathematical models are easy to fail.

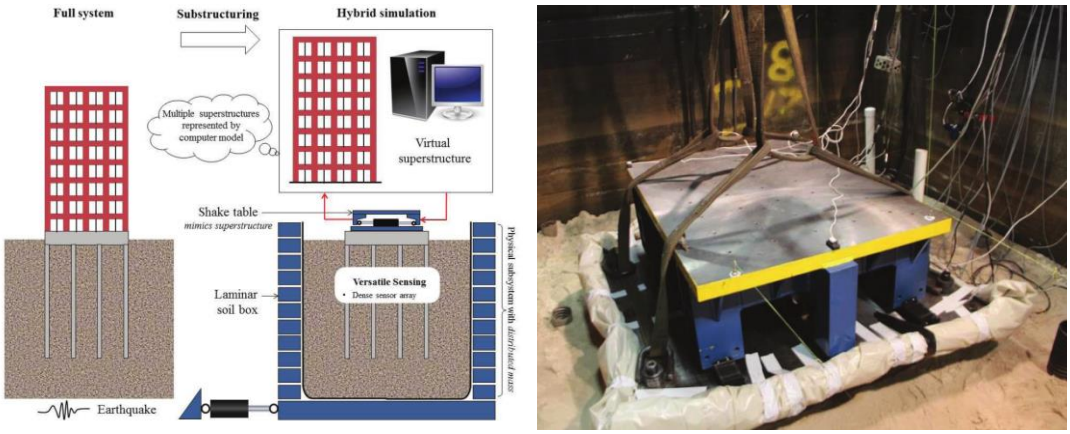

(a) (b)

Figure 22: Hybrid model of a soil structure system, (Stefanaki et al., 2015): (a) hybrid model schematization; and (b) physical substructure.

Figure 22b reports the PS tested in laboratory by (Stefanaki et al., 2015). Figure 23 instead reports another significant application of the hybrid modelling, (Bursi et al., 2014). In this case the hybrid model was used to perform several hybrid simulations testing on a typical full-scale industrial piping system endowed with critical components (e.g. elbows, etc.). The results of the hybrid simulations allowed to draw several conclusions on complex aspects of the piping performance.

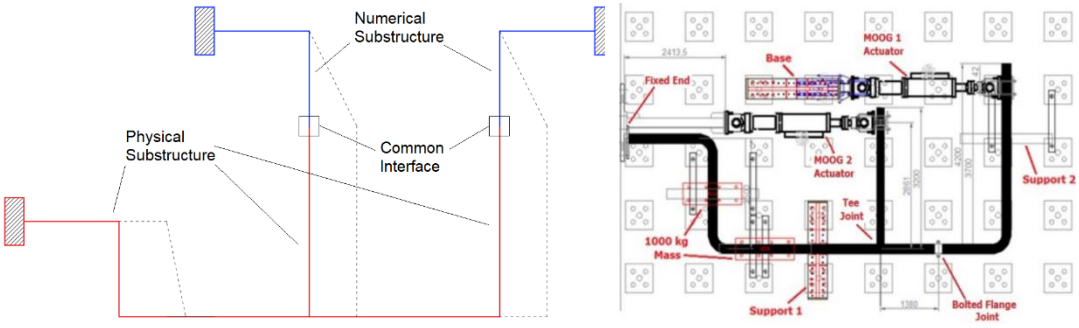

(a) (b)

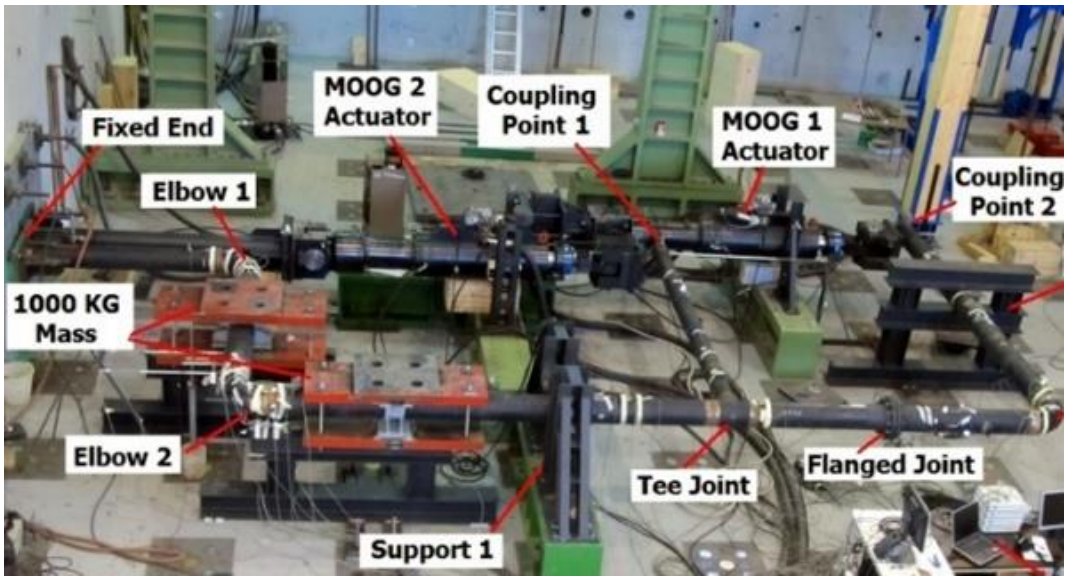

(c)

Figure 23: Hybrid model of a typical full-scale industrial piping system, (Bursi et al., 2014): (a) hybrid model schematization; (b) PS schematization; and (c) PS tested in laboratory.

Although hybrid modelling has been often used in civil and structural engineering field, the technique is also applied in other disciplines, such as mechanical and electrical engineering, where the PS usually describes critical electro-mechanical components of a distributed electric line, e.g. disconnected switch, or aerospace engineering, where hybrid simulation may be employed for the analysis and optimization of electronic control units of aircraft, e.g. quadcopters. In the specific work of (Hochrainer, M & Schattovich, 2017), the authors proposed hybrid simulations to optimize the control unit, which in this case represented the PS, by testing its effectiveness with the help of mathematical models (i.e. the NS) that simulated several flight dynamics scenarios (e.g. several trajectories, etc.). They concluded that hybrid simulation was useful to determine, during the simulated flights, the effects of different inertia measurement unit sensors, with specific noise characteristics on the overall flight dynamics, finding in this way the reasons for rarely occurring engine failures.

The last frontier of hybrid modelling is represented, in its most general conception, by (*spatially*) *distributed hybrid modelling*. Conceptually, there are no differences with classical hybrid modelling. However, when modelling is distributed, the physical model is not univocal. In this case, in fact, there are numerous physical models, built in different laboratories (or even in the same laboratory), used to emulate different parts of the system. All the physical models are then combined, in the hybrid distributed model, through a virtual model. Physical models and the virtual model exchange information through what in the real system would be the common interface areas. Obviously, having available a greater number of physical models, the need to resort to unreliable abstractions of the structural behaviour decreases, thus increasing the potential of the hybrid

(distributed) model and making the simulations even more consistent with reality. Today the applications of this modality are truly sporadic, and absent in the field of architectural heritage, mostly due to a lack of experts in this new sector.

In conclusion, in the specific case of architectural heritage structures, hybrid modelling would allow to estimate the overall response of the structure even in extreme collapse conditions, without the need to resort to unreliable virtualization, or real-scale tests of the system, which are impossible to apply to structures belonging the architectural heritage, avoiding in addition an excessively reduced physical modelling. On the other hand, hybrid models and testing are inherently non-destructive and non-invasive for the investigated piece and are in full compliance with the deontological guidelines on testing on cultural heritage, including the ICOMOS-ISCARSAH ones, (Icomos-Iscarsah, 2003).

1.6. References chapter 1

Bertolesi, E., Adam, J. M., Rinaudo, P., & Calderón, P. A. (2019). Research and practice on masonry cross vaults–A review. Engineering Structures, 180, 67-88.

Bursi, O. S., Abbiati, G., & Reza, M. S. (2014). A novel hybrid testing approach for piping systems of industrial plants. Smart Structures and Systems, 14(6), 1005-1030.

Cavallari Murat, A. (1982). Come carena viva Scritti sparsi, vol II. Bottega d'Erasmo, Torino. (In Italian).

Ceravolo, R., De Lucia, G., Miraglia, G., Pecorelli, M.L. (2019). Thermo-elastic finite element model updating with application to monumental buildings. Computer-Aided Civil and Infrastructure Engineering, CACAIE. (Submitted).

Cerone, M., Croci, G., & Viskovic, A. (2000, October). The structural behaviour of Colosseum over the centuries. In International congres More than two thousand years in the history of architecture, Bethlehem.

Chiorino, M.A. (2017). Reduced scale mechanical models in 20th century structural architecture: Guido Oberti (1907-2004) and Pier Luigi Nervi (1891-1979) A very special relationship. Spring School on Structural Health monitoring of architectural heritage, Columbia Univeristy/Politecnico di Torino, Vicoforte, Italy, June 15-16.

Croci, G. (2006, September). Seismic behavior of masonry domes and vaults of Hagia Sophia in Istanbul and St. Francis in Assisi. In Proceedings of the First European Conference on Earthquake Engineering and Seismology—

A Joint Event of the 13th ECEE & 30th General Assembly of the ESC (pp. 3-8).

Cundall, P. A., & Strack, O. D. (1979). A discrete numerical model for granular assemblies. geotechnique, 29(1), 47-65.

El Saddik, A. (2018). Digital twins: the convergence of multimedia technologies. IEEE MultiMedia, 25(2), 87-92.

Haddad, H., Guessasma, M., & Fortin, J. (2016). A DEM–FEM coupling based approach simulating thermomechanical behaviour of frictional bodies with interface layer. International Journal of Solids and Structures, 81, 203-218.

Hakuno, M., Shidawara, M., and Hara, T. (1969). Dynamic destructive test of a cantilever beam, controlled by an analog-computer. 土 木 学 会 論 文 報 告 集, 第171号 ・1969年11月.

Hesse, M.B. (1980). Modelli e analogie nella scienza. Feltrinelli, Milano. (In Italian).

Hildebrand, S., & Bergmann, E. (2015). Form-finding, form-shaping, designing architecture. Mendrisio Academy Press.

Hochrainer, M. J., & Schattovich, P. (2017). Real-Time Hybrid Simulation of an Unmanned Aerial Vehicle. In Dynamics of Coupled Structures, Volume 4 (pp. 41-48). Springer, Cham.

Icomos-Iscarsah. (2003). ICOMOS Charter—Principles for the analysis, conservation and structural restoration of architectural heritage. Proceedings of the ICOMOS 14th General Assembly and Scientific Symposium, Victoria Falls, Zimbabwe, 2731.

Iori, T., Poretti, S. (a cure of) (2007). Rassegna di Architettura e Urbanistica. Anno XII-n. 121/122, Kappa, Roma. (In Italian).

Lengyel, G. (2017). Discrete element analysis of gothic masonry vaults for self-weight and horizontal support displacement. Engineering Structures, 148, 195-209.

Marchis, V. (1988). Modelli esperimenti di simulazione al personal computer. *SEI*, Torino. (In Italian).

Marchis, V. (a cure of) (2009). Disegnare Progettare Costruire 150 anni di arte e scienza nelle collezioni del Politecnico di Torino. Fondazione Cassa di Risparmio di Torino, Torino. (In Italian).

Novello, G. (2013). Modelli per i beni culturali, ovvero, un'arte per governare la complessità. Corso di III livello, Conoscenza strutturale geotecnica e sismica dei beni culturali e tecniche di intervento per il recupero di strutture in legno e in muratura, Giugno, 2013, Italia, Torino, Politecnico di Torino. (In Italian).

Oberti, G. (1967). Corso di Tecnica delle Costruzioni, Levrotto&Bella, Torino. (In Italian).

Okada et al. (1980). Bidirectional Response of RC Column, 7WCEE, India.

Pecorelli, M. L., Ceravolo, R., & Epicoco, R. (2018). An Automatic Modal Identification Procedure for the Permanent Dynamic Monitoring of the Sanctuary of Vicoforte. International Journal of Architectural Heritage, 1-15.

Politecnico di Torino (1989). Capolavori di minuseria al servizio della Scienza delle Costruzioni: La collezione ottocentesca di modelli di Costruzioni della R. Scuola di Applicazioni per Ingegneri in Torino. CELID, Torino. (In Italian).

Ruocci, G. (2010). Application of the SHM methodologies to the protection of masonry arch bridges from scour. (Doctoral dissertation, PhD Thesis, Department of Structural and Geotechnical Engineering).

Ruocci, G., Ceravolo, R., & De Stefano, A. (2009). Modal identification of an experimental model of masonry arch bridge. In Key Engineering Materials (Vol. 413, pp. 707-714). Trans Tech Publications.

Stefanaki, A., Sivaselvan, M. V., Tessari, A., & Whittaker, A. (2015). Soil-Foundation-Structure Interaction Investigations using Hybrid Simulation. Structural Mechanics in Reactor Technology SMiRT23. Manchester, UK.

Tang, G. (2013). Timber gridshells: beyond the drawing board. Proceedings of the Institution of Civil Engineers. Construction Materials, 166(6), 390-402.

Zienkiewicz, O. C., Taylor, R. L., & Zhu, J. Z. (2005). The finite element method: its basis and fundamentals. Elsevier.

Chapter 2

Corroboration of numerical models for architectural heritage structures

This chapter covers different aspects concerning the corroboration of models for architectural heritage structures. First, the discussion focuses on actions that should be undertaken to reach a right knowledge of a building belonging the architectural heritage, such as historical knowledge, construction phases, geometry, construction details, material properties, foundations etc. The theme of soil-structure interaction is also briefly addressed in this chapter. Then, several ways corroborated models can contribute to the preservation of heritage structures are differentiated according to the specific aim of the simulations. The discussion continues with an excursus on linear and nonlinear model updating techniques, which are reviewed for numerical models. Finally, examples of the use of physical replicas for corroborating models in hybrid simulation schemes are reported.

2.1. Data collection

The building technologies for historical constructions are countless. This, in addition to the variety of their characteristics, results in an impossibility to define a general classification of the historical architectures. For this reasons, the analysis of an historic structure requires precise guidelines, (Icomos-Iscarsah, 2003). In light of that, the concept of the so-called *path of knowledge* is introduced as: *[...] a serious of standardised actions and aspects which have to interact in order to achieve the desired level of knowledge of the building [...]*.

One of the main aspects of the path of knowledge regards the data collection. This consists in the retrieval of information and in the more and more deepening

of investigations regarding to historic events and building transformations, geometric survey, constructive details and material properties and soil and foundations state. The information can be acquired through cognitive surveys and direct analyses of the artefact. Archive documentations and analysis of the sources are useful together with direct analyses to define the material constructive texture, the building dimensions, the state of preservation, the transformation interventions, the health state, the crack patterns and possible (local or global) mechanisms of collapse. Then, the deepening of this knowledge consists in determining the strength of the materials by means of experimental tests.

2.1.1. Historical analysis

The historical analysis of a cultural heritage building represents the first step towards a full understanding of its structural state. The time needed to complete the analysis of an historical building is usually much greater than the time required to complete that of a modern structure. Thus, any historical building experienced countless types of construction techniques that contributed to complicate its actual state. In addition, over the years a region can exhibit several mutations, including those not directly related to its physical characteristics (e.g. climate or geomorphological changes, etc.). These are rather anthropological changes or changes related to the society, which for its nature is prone to adapt itself in function of inevitable historical facts (e.g. wars, etc.). Furthermore, due to the long time required for the completion of the structures, some raw materials (such as quarry stones) could run out. Then, the changes in the economy could lead manufacturers to move towards cheaper materials. The knowledge of the historical, social and anthropic evolution of the place in which a historical building is located is therefore fundamental for discarding unreliable hypotheses on the material and morphological constitution of the building.

Long construction times bring also possible changes in the physical conditions of the place hosting the buildings. One of these is the condition of the soil, the change of which could lead to disruptions of the structure already in the construction phase, and therefore, to changes in the constructive approach that could result from a simple change of construction technologies, to the change of the operating techniques, up to the drastic decision to change the original project of the building. In this sense, if one makes an analogy between the completion of a building and the birth of a child, we could infer that while for modern structures birth represents a closed process, with rules established a priori and difficult to change, the birth of a historical building is a process affected by innumerable mutations, a process where there were no absolute rules, but rather the rules adapted to the history of a place.

A modern building comes to light following the construction process, and the transition between *gestation* and *life* is clear. On the contrary, in a historical building the transition between the gestation phase and the life is doubtful, and in some cases completely absent (e.g. Sagrada Família). This makes a historic

building tremendously more complex to understand than a traditional building, as it is the nature of the events that defined the rules that determined its state. That is exactly the opposite of what happens for traditional buildings for which there are (abstractly speaking), immutable rules that define the structural constitution.

Historical analysis is therefore a fundamental step to retrace the feedback process that generated historical architectures, and this process cannot be generalized, because of the inevitable absence of immutable and univocally identifiable construction rules. Nothing prevents, however, that in the future, buildings constructed nowadays (intended with *nowadays*, buildings that are being built during the writing of this thesis) can become difficult to conceive. In fact, even for modern buildings there is actually a feedback process, however, this process turns out to be much less complex than the processes implemented for the realization of historical architectures. In addition, nowadays there are specific documents that trace all the life phases of a structure, starting from its conception, moving from the gestation phase up to the birth, to arrive at the monitoring of its life until its final disappearance.

2.1.2. Geometry

The geometric data represent fundamental quantities for the definition of a model capable of representing the real structure in an acceptable way. Today there are countless technologies to support in situ investigations aimed at collecting geometric data. In a broad sense, we can classify geometric data as follows:

- Spatial geometric dimensions of structural and non-structural elements, such as: masonry walls, vaults, floors, columns, etc.;
- Presence of niches or voids directly and not directly found in the elements constituting the building;
- Estimates for loads on all structural elements;
- Identification of the type, shape and size of the foundations;
- Definition of the possible crack pattern (in terms of the size of the cracks and the typology) and of the existing failures or of evident deformation conditions that may arouse suspicion or represent pathological conditions for structure;
- Etc.

The collection of these data must always be accompanied by a visual inspection in situ. During data gathering, it is worth to remember that from a structural point of view the accuracy of the survey should not be too high. In such a case, one would risk introducing too much meaningless information, which would actually result in adding noise to the survey rather than an increase of the level of knowledge. This is also true because mechanical models are computationally intensive, thus, the geometric model should avoid adding not very useful data to the solution of the mechanical analysis (e.g. architectural

details). Among the countless available technologies/techniques for the geometric data gathering, some worth of mentioning are:

- *Laser scanner 3D* (LIDAR), it allows the collection of a points cloud in which each point provided of its spatial coordinates respect to a known reference system. The distance between two points can be as small as it is necessary, however for the global assessment of a structure belonging to the cultural heritage, arduousness can rise in the modelling phase if the distance between two points became less than about 0.1 m. In the opposite, for local assessment of crucial parts of the structure, minor distances between the cloud's points can improve moderately the accuracy of a model;
- *Thermography*, useful to detect possible holes in the structural elements, e.g. chimneys, etc.

2.1.3. Construction details

The acquisition of the right knowledge of construction and structural details is of paramount importance for the definition a reliable structural model. The details commonly represent very sensitive parts of the structure with particular characteristics, and a little variation in the nature of these characteristics commonly bring to an important variation of the model prediction capability. Among the countless of details that can be collected one should always focus his attention on:

- nature and quality of the connection between vertical-vertical and vertical-horizontal structural components;
- type of masonry and construction characteristics;
- presence of elements with high vulnerability;
- presence of interventions capable to decrease the vulnerability of the structure or of its parts.

2.1.4. Materials

The characterization of the materials strongly depends by the level of knowledge that one wants to achieve. Based on the aim of the model, the experimental campaigns for the material characterization may concern all or some of the following investigations tasks:

- characterization of masonry blocks;
- characterization of the mortar and the type used;
- characterization of the texture;
- assessment of the presence of transversal connections (e.g. diatones);
- etc.

2.1.5. Soil and structure interaction

Although having been neglected for years, the problem of the soil-structure interaction of buildings belonging to the architectural heritage should always be considered, at least to quantify its effect. Following a preliminary assessment, it will therefore be possible to state whether the problem of soil-structure interaction can be overlooked or must be taken into consideration in the definition of the model. In fact, in the general case, to build a good model, the first step to undertake is to recognize the *system* from the external *environment*, because the modelling phase should consider just the characteristics of the system, being the environment the collection of all the possible causes (input) that determine a change in any response (output) of the system. The change can be then temporary or permanent. In case of a temporary change of the output, the system remains unchanged, on the opposite, if a permanent change of the output is detected while the environment changes temporarily, it means that the system has changed its state, and the modelling phase should be retraced in some way.

However, if one mistakes to define the system, a clear distinction between permanent or temporary changes in the output cannot be achieved. Sometime, the soil is part of the system, and some other time it can be classified as belonging to the environment surrounding the system. To understand in which case one is collocated, an adequate level of knowledge of the soil characteristics should be achieved, this allowing for accurate analyses of the soil-structure interaction. Starting from this premise, some authors (Lancellotta, 2004, Kramer, 1996) state that the first step for the soil characterization is the collection of data concerning the stratigraphy (in terms of geometry), the water table level and the classification of the soil (in terms of materials) underneath the analysed structure. This can be done by using different established techniques, including:

- Standard Penetration Test (SPT);
- DownHole test (DH);
- CrossHole test (CH):
- Seismic refraction of shear Horizontal waves (SH);
- Multichannel Analysis of Surface Waves (MASW);
- etc.

Once the data gathering on the building and the soil is accomplished, the interaction of the two systems can be analysed and discussed to conclude if the final system to be modelled should concern only the building or a mixed soil-structure system.

2.2. The use of collected data for the modelling of architectural heritage

In the previous section it was highlighted how the data gathering for structures belonging the cultural heritage is relevant to the definition of a reliable mathematical model and how the accuracy of a chosen model is related to the quantity and quality of the collected information. However, the definition of a model is not only related to the type of available data. Another important factor that drives the definition of the mathematical model for a building is the scope for which that model is built. Figure 24 reports the conceptual map that should be followed when approaching the modelling of an historic building.

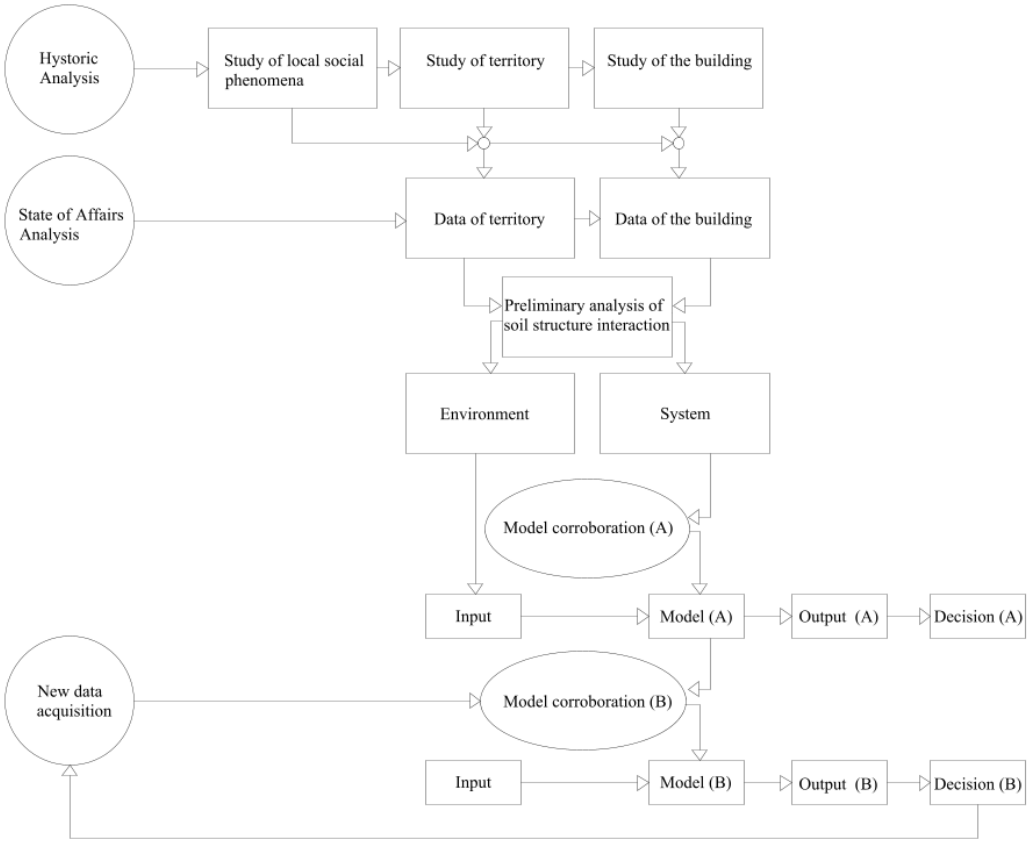

Figure 24: Conceptual map for the definition of mathematical models.

The first step regards the historical analysis from a social, environmental and structural point of view. Then, with the second step, the main data are collected for both the building and the territory surrounding it. These data regard the geometry, details, materials and other types of data, such as dynamic characteristics of both building and soil. Having this data, it is possible to carry out preliminary analyses to assess the presence of soil-structure interaction phenomena, this allowing for a clearer definition of the system that should be modelled, and the environment that will represent the collection of the inputs for the model. At this stage, it is important to understand what the quality and quantity of the collected data is. In addition, it is again important to have clear in

mind which will be the scope of the mathematical model. With these two important points in mind is then possible to select the type of model (e.g. scale, accuracy level, etc.). It will be conceived to predict one or more desired outputs, thanks to which specific decisions will be undertaken.

The last step for the definition of the model concerns the possibility to assimilate in it new data, of both dynamic and static nature. These new data should be incorporated in the model in order to obtain more accurate and reliable predictions. In this perspective, the model becomes evolutive, and if the new data are collected continuously of periodically, it will evolve for an indefinite time. The scope of this chapter is precisely to describe some model corroboration strategies.

2.2.1. Modelling to monitor the health of the structure

As stated before, the selection of a mathematical model will not only depend by the available data, but also on the type of decision one want to undertake. A very large field of research regards the definition of models able to provide information on the health state of a structure. Commonly, for this scope, the definition of a linear elastic constitutive laws for materials is enough to establish the mathematical model, this leading to some simplifications in the analysis. However, the effectiveness of the model remains still very high. In fact, for most of the time, a building is not subjected to any load, and thus its static or dynamic behaviour is related to a serviceability limit state, where the materials exhibit a linear elastic behaviour.

Once the model is corroborated with the experimental data, it can be used to predict any desired output. This output can be compared with the equivalent physical quantity monitored on the structure. A discrepancy between the model prediction and the actual outcome should indicate an anomalous behaviour of the structure. Following the detection of anomalies, specific actions can be undetaken in order to check the actual presence of pathologies, and in that case, to plan the collection of new data in order to define models able to perform more sophisticated analysis (e.g. nonlinear modelling).

An impressive application of virtual modelling to monitor the health state of structures belonging to the architectural heritage is represented by the studies conducted in (Ferretti & Bažant, 2006a) and (Ferretti & Bažant, 2006b). In these works, the authors analyse the causes of the redistribution of stresses in multiple-leaf ancient masonry walls during long periods of time. For this purpose the authors analysed coupled processes of moisture diffusion, carbon dioxide diffusion and carbonation reaction. Thanks to Finite Element (FE) model analyses, the authors concluded that moisture diffusion in ancient multiple-leaf masonry walls influences carbonation, shrinkage, creep and microcracking. Thus, due to the occurrence of these processes, a redistribution of the stresses was observed by the authors from the concrete core to the external layer of the walls. Finally, the authors recognized that the time scale of the diffusion-reaction phenomena is compatible with the age at which some towers had problems. They

applied their methodologies on a case study, the collapsed Pavia Tower, see Figure 25.

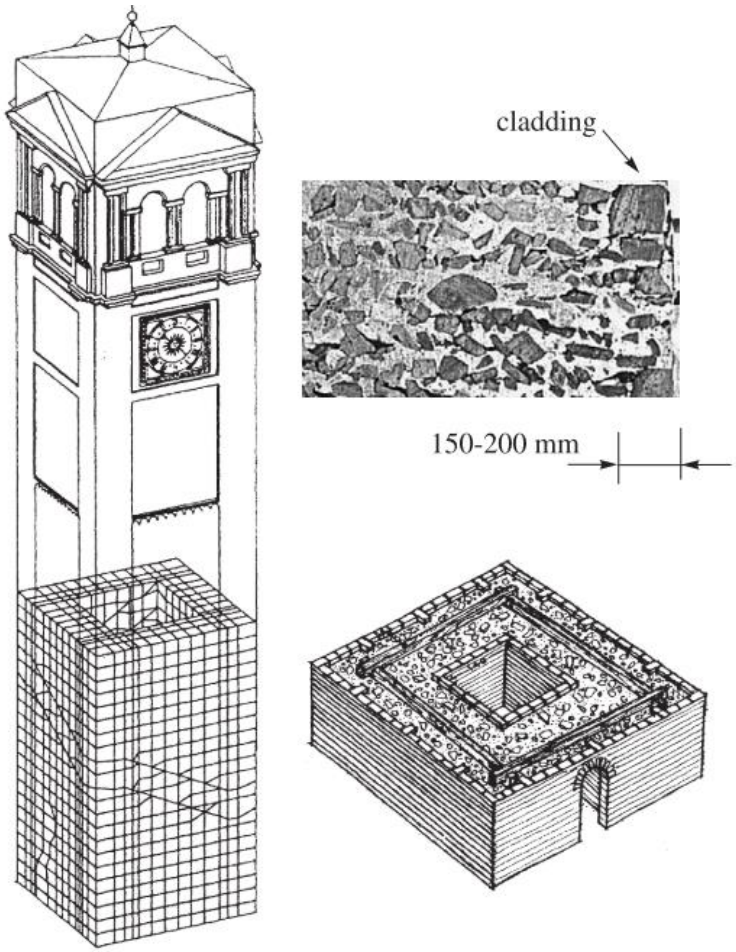

Figure 25: Ancient tower, (Ferretti & Bažant, 2006a): geometry and finite element mesh of the Civic Tower of Pavia, Italy, (on the left), typical cross section (on the bottom-right), and photo of the masonry wall of the Civic Tower of Pavia (on the upper-right).

2.2.2. Modelling to assess the safety condition of the structure or to evaluate retrofitting strategies

Another field of research regards models for assessing the safety condition of a structure when subjected to strong input forces. In this case, since the models must accomplish a wider range of variation of the input, they are commonly nonlinear. The nonlinearity can regard the geometry as well as the materials, and can be accompanyed, in almost all cases, by energy dissipation (e.g. plasticity). For building belonging to the cultural heritage, the most common geometric nonlinearity is represented by the existence of crack patterns or disconnection in the continuity of the structure. As regards materials, many types of nonlinearity can be recognized: softening, hardening, hysteretic, frictional nonlinearity due to degradation, etc. For this reason, the models used to describe nonlinear behaviours

of structures are characterized by a huge number of parameters, whose definition is commonly not as easy as the definition of linear elastic parameters. Sometimes, the exhibited behaviours are so complex that any analytical or numerical model fail to predict the actual output that one would obtain with experimental tests (in situ or in laboratory).

About this topic, (Portioli et al., 2011) reports a beautiful combination of virtual and physical models used to assess retrofitting interventions of the *Mustafa Pasha Mosque* in Skopje, see Figure 26.

(a) (b) (c)

Figure 26: Models of the Mustafa Pasha Mosque in Skopje, (Portioli et al., 2011): (a) physical model with strengthening; (b) distribution of plastic strains at the collapse in the minaret before, (left), and after, (right) the strengthening; and (c) distribution of plastic strains at the collapse in the mosque before, (left), and after, (right) the strengthening.

In their work the authors perform FE analyses to assess the use of a Carbon Fiber Reinforced Polymer (CFRP) based strengthening technique. The virtual

model used by the authors was preliminary calibrated thanks to shaking table experimental tests carried out on a large-scale physical reproduction of the architectural structures. To assess the retrofitting intervention respect to seismic loads, the authors performed dynamic and nonlinear static analyses before and after the strengthening, with the numerical as well as the physical model. The work was useful to conclude that the retrofitting intervention was able to bring a remarkable increase of the strength capacity of the structure under lateral loads.

Concluding, if a linear model can be used to predict the serviceability behaviour of a structure, a nonlinear model can push the prediction of the behaviour up to an ultimate limit state. But this is true just in case the building does not exhibit too complex behaviours that cannot be modelled.

2.3. Linear and Nonlinear model corroboration

Model corroboration is a vast field of research that includes any theory or technique useful to aid a mathematical model with data coming from experiments. In this framework, there is not a real net distinction between linear or nonlinear corroboration, as in many cases (but not always), the tools used for the latter can be also used for the first. One can classify the corroboration of models in two step, which can be very distinct or quite mixed together: (i) *Identification*; and (ii) *Updating*. In the identification, the aim is to obtain an estimate of some model parameters or laws directly coming from experimental data. In this case, the mathematical models that support the identification procedures are quite determined in their analytical or numerical form and generally do not require information on previous states of the system that is being identified. On the contrary, with updating one commonly refers to the action for which a predetermined state of a system, emulated with relative complicated virtual models, is modified thanks to new information obtained from identification procedures or directly from experimental data. In this case the virtual models are commonly undetermined, and advanced numerical and analytical laws are combined to get a comprehensive representation of the system being emulated. Thanks to this combination of laws, more information can be obtained respect to the identification tasks, (Marwala, 2010), (Friswell & Mottershead, 2013), (Ceravolo & Abbiati, 2013).

Another important distinction between identification and updating techniques is that with the first it is possible to obtain precious data about numerical values representing one or very few physical quantities. Instead, with updating techniques, the updated model is able to reproduce countless data about very different physical quantities, by interpolation actions. With these interpolation actions it is possible to obtain new information on the system, which could not have been obtained with identification processes only. Being the information obtained with interpolations just a deduction of values that are actually unknown from an experimental point of view, their comparison with *real* values is in fact

impossible. Thus, if on one hand the updating process leads to much more information than those obtainable with an identification process, it must always be remembered that (generalizing) the trust one can place in the results of an updating process is always lower than that can be put in an identification process. This is not surprising, because as the number of physical phenomena to be simulated grows, the uncertainties associated with the representation of these phenomena increase and therefore it is necessary to resort to more or less strong simplifications that can (without realizing it) compromise the accuracy of the emulated data. In the following, an excursus of the identification and updating methods used to corroborate linear and nonlinear models is reported.

Although some typical characteristics can be categorized for identification and updating processes, actually a clear distinction can be lost when these techniques are practically implemented. In this regard, (Noël & Kerschen, 2017), inserts the model updating in its classification of methods for the identification of nonlinear systems. In fact, *model updating* is nothing more than a method to identify unknown quantities starting from known data, and in this frame the definition of model updating as a particular case of system identification is extremely appropriate.

Linear corroboration is a field of mature research where research over the years has continued to find increasingly efficient and accurate solutions to real physical problems. The main assumption of linear corroboration is that the laws describing the system's behaviour are linear, thus a countless number of properties apply. The methods belonging this class of corroboration techniques owe their success also to their connection with the field of Structural Health Monitoring (SHM), (Limongelli & Çelebi, 2019), (Ceravolo et al., 2017). In particular, identification methods used to estimate the modal features of systems (i.e. natural frequencies, damping ratios and mode shapes) found a large number of applications for structures with very different characteristics and complexity, (Pecorelli et al., 2018), (Ewins, 2006), (Pintelon & Schoukens 2001), (Ewins, 2000), (Ljung, 1999), (Maia & Silva 1997), however difficultness exist when the system being analysed is characterized by very complex behaviours and uncertainties, (Ceravolo, De Lucia & Pecorelli, 2017). One important branch of linear identification methods among the countless number available (*time-domain*, *frequency-domain, time-frequency-domain* methods, etc.) is that one of *modal methods*. In general it is possible to define two big families for this type of linear identification methods:

- Input-Output methods, falling within the family of Experimental Modal Analysis (EMA) *tout court* when the parameters to be identified are modal features;
- Output-only methods, falling within the family of Operational Modal Analysis (OMA) when the parameters to be identified are modal features.

In the first case of EMA methods, the search of the unknown parameters of the modal model is performed thanks to the knowledge of the systems' input action and structure's output response. Conversely, OMA methods do not need any definition of the input, and to obtain the modal features just the recorded response is necessary. In this case, the input is commonly modelled as a stochastic process. In the field of civil engineering, two main algorithms have attracted the attention of researchers in the last years:

- Eigensystem Realization Algorithm, (ERA), (Juang & Pappa, 1985);
- Stochastic Subspace Identification, (SSI), (Van Overschee & De Moor, 1996).

Depending on the specific implementation, both methods can be used in presence of input (e.g. ERA with impulsive input or combined with Kalman filter Markov parameters, and SSI with deterministic component) or in its absence (e.g. NExT-ERA and classical SSI algorithm). For a better understanding of classical EMA methods, (Maia and Silva 1997), represents an excellent internationally accepted, reference. For the accuracy afforded by OMA techniques an effective synthesis can be found in (Ceravolo & Abbiati, 2013).

When talking about linear corroboration of models, the modal identification methods represent only a part of the corroboration process. The conclusion of the corroboration process comes with the *linear model updating*, whose goal is to estimate the structural model of a system, starting from the modal model estimated with the modal identification techniques. To do so, a mathematical, mostly numerical, model tries to emulate the identified modal model by changing its elastic mechanical and geometrical parameters. A distance between the identified modal features and the numerical modal features predicted by the model define the goodness of the updating. The mechanical and geometrical parameters of the numerical model are updated thank to specific optimization algorithms. One very huge branch of optimization algorithms used for this purpose is that one of *metaheuristic algorithms*, (Marwala, 2010). The main advantage of these methods is that they can deal with problems where the number of parameters to be updated can be small or extremely large, however they are intrinsically not robust and numerous of improved methods have been proposed to overcome this problem. Another big family of model updating techniques is that one of *sensitivity methods*, (Friswell & Mottershead, 2013), where a variation of the model parameters is analysed respect to a variation of the experimental data, trough out numerical gradient operators. Finally, in the last years, several algorithms belonging to the *machine learning* community are beginning proposed for this aim, (Binkhonain & Zhao, 2019), although they are finding a greater application in the nonlinear corroboration of the models by using Bayesian methods, (Beck & Katafygiotis, 1998), (Muto & Beck, 2008), (Green & Worden, 2015) and (Ebrahimian et al, 2015).

In this respect, following the classification of (Noël & Kerschen, 2017), it is possible to distinguish the following methods for the nonlinear corroboration of models:

- linearized methods;
- time-domain methods;
- frequency-domain methods;
- time–frequency methods;
- modal methods;
- black-box modelling;
- numerical model updating;
- etc.

Although this is a successful attempt to report a complete classification of the problem of model corroboration, as also reported by the authors, it cannot be comprehensive since the field of research on nonlinear corroboration of models is too vast to be summarized in a few pages.

However, following this classification the first method that is presented is that one of *linearized methods*. In these methods the linearization of the nonlinear behaviour of systems is performed around their most probable physiological conditions. However, method based on linearization processes have some minor drawbacks:

- They are valid just to represent the dynamic response due to forcing level close to that one used for the identification of the model parameters;
- Commonly, they are not adapted to model intrinsic nonlinear modal behaviours.

Although these minor drawbacks of the linearization methods, because their simplicity, research continued to focus on some specific aspects, in particular on choosing methods to derive the best linear model to approximates the nonlinear behaviour of systems. One very good solution for model linearization is represented by considering time-variant models, i.e. the mathematical laws used to describe the system change in time. The idea is based on the fact that, for very short time instants the system can be reasonably approximated by linear laws. Along this line (Sracic & Allen, 2011) moved their work, demonstrating its effectiveness using a single Degree of Freedom (DoF) system. Later, in 2014, the method was extended to multiple DoF systems, (Sracic & Allen, 2014).

The *time-domain methods* take their name from the nature of the experimental data being processed, i.e. time series data. Here, it is possible to distinguish 3 main techniques:

- Nonlinear AutoRegressive Moving Average with eXogenous inputs modelling (NARMAX);

- Restoring Force Surface (RFS), and;
- Time-domain Nonlinear Subspace Identification (TNSI).

With NARMAX techniques, the system behaviour is approximated with series expansions of nonlinear functions that consider input, output quantitates as well as the existence of errors in the time model formulation. Also in this case it is possible to recognize some drawback of the method, among them, NARMAX techniques involve the definition of countless model parameters, and thus their efficient application to large scale systems still remain a problem, (Peng et al., 2011).

RFS methods represent the earliest identification techniques, (Masri & Caughey, 1979). With these methods, the direct fitting of the equation of motions is performed through the use of least squares estimates. Although the method is restricted to systems with a low number of DoFs, it can be implemented to obtain qualitatively information on the shape of restoring force laws of complex structures. Several applications of these methods have been addressed in the past, among those one worth of noting one can recognize the work of (Worden et al., 2009), (Ceravolo et al., 2013), (Xu & Dyke, 2015) about the identification of nonlinearities due to complex damping.

The TNSI method was originally proposed by (Lacy & Bernstein, 2005) in the dynamic control theory, and it represents a generalization of the famous and widely applied time-domain Linear Subspace Identification Algorithms (VanOverschee & DeMoor, 1996). Since the TNSI method bases its formulation on very robust algorithms, such as the QR factorization or the Singular Value Decomposition (SVD) it represents a step forward in the time-domain identification, especially if compared with similar approaches as the NIFO, (Adams & Allemang, 1999) and CRP, (Richards & Singh, 1998), techniques.

Frequency-domain methods have the characteristic to be scalable to a large number of experimental data then time-domain methods. Three main frequency-domain methods have emerged as widely affirmed:

- Nonlinear Identification through Feedback of the Outputs, (NIFO), (Adams & Allemang, 1999);
- Conditioned Reverse Path (CRP), (Richards & Singh, 1998);
- Volterra series, (Schetzen, 1980).

The NIFO method is based on an identification formulation that uses a mechanism called output feedback. It simultaneously identifies the linear and non-linear parts of the system.

The CRP method is based instead on the construction of a set of unrelated answers in the frequency domain. If multiple inputs are available in different parts of the structure, and the outputs are recorded in the same points, it is possible to write a system of algebraic equations, one for each frequency. However, if this condition is no longer valid (output recorded in different positions with respect to

the positions in which the inputs are imposed), the CRP method cannot be applied directly, and needs further processing for the identification of the model parameters.

The Volterra series represent another common method for performing nonlinear identification of systems in the frequency domain, (Schetzen, 1980). High-order kernels are used within convolution processes to represent output as a function of input according to causal processes. As for the NARMAX methods, the Volterra series suffer from the high number of parameters necessary to conclude the identification process, however its definition in the field of non-linear identification has been fundamental, since it is thanks to them that the new Non-linear Response Function (NFRF) concept came to light, (Lang & Billings, 2005), (Peng et al., 2007), finding applications in both linear and nonlinear fields, (Peng, et al., 2008).

The importance of *time-frequency methods* lies in the fact that actually, systems, if taken in the nonlinear field exhibit a non-stationary behaviour with oscillations that are function, not only of a defined frequency value, but rather of a distribution of frequencies to which different energy values are associated. Among the noteworthy Time-Frequency methods it is possible to recall those of (Heller et al., 2009) and (Demarie et al., 2011) on the identification of backbone curves. Other techniques that consider the decomposition of multicomponent signals are:

- Empirical Mode Decomposition, (EMD), (Huang et al., 1998);
- Hilbert Vibration Decomposition, (HVD), (Feldman, 2006) and (Feldman, 2007);
- Time-Frequency Instantaneous estimators, (TFIE), (Ceravolo et al., 2013).

With EMD the original signal is represented by a sum of elemental functions, called Intrinsic Mode Functions (IMF), which are calculated by approximations with spline.

Instead, with the HVD method, the signal is decomposed into a series of quasi-harmonic signals. This method has been applied to identify two DoFs systems, (Feldman, 2007), however, applications to multi-DoFs systems are missing. Other applications of this method can be found in (Feldman, 2014).

As far as the TFIE method is concerned, it has recently been proposed in order to cope with nonlinear and hysteretic, time-varying systems. In this case, the experimental signals are transformed into a time-frequency domain, allowing the definition of an instantaneous cost function with which it is possible to obtain an instantaneous estimate of the values of the model parameters.

The *Modal methods* for nonlinear identification are really recent and very limited applications exist. Nowadays the methods are developing rapidly thanks to the emergence of very efficient algorithms, (Renson et al., 2016). The importance

of these methods lies in the fact that they are able to reliably describe each type of input in any range of values. Two noteworthy methods are:

- CONCERTO method;
- NLRDM method.

The CONCERTO method, (Carrella & Ewins, 2011), identifies an isolated nonlinear resonance based on stepped-sine data and adopts a linearized view of nonlinear modal identification, and defines *equivalent natural frequencies and damping ratios* which vary with the amplitude of motion.

On the opposite NLRDM methods perform the identification of multiple modes by introducing nonlinear coupling terms in linear modal-space models of the analysed system. This method is noted to be one of the most promising nonlinear modal identification technique (Kerschen et al., 2009). In addition the method has been validated with simply as well as very complex system, e.g. a 2 DoFs system, (Yang et al., 2006), a single bay panel, (Platten, et al., 2009) a complete transport aircraft, (Fuellekrug & Goege, 2012), etc.

The *Black-box methods* are based on the fact that it is extremely complicated to try to represent the nonlinear behaviour of real systems in a generalized way. Therefore, rather than referring to known physical processes, the system is described through mathematical constructs whose objective is to reconstruct the relationship between input and output as accurately as possible, without worrying about the reliability of the parameters of the model and its physical meaning. If the non-physical assumptions or approximations concern only a part of the model (the model maintains a physical sense in describing some behaviours), the method is called *Gray-box*.

A noteworthy Black-box method is the one proposed by (Paduart et al., 2010). It defines a model consisting of a multivariate polynomial combination of the state variables of a system and of input. An application of this method can be found in (Widanage et al., 2011), which in its work analyses an oil bath friction device. Nowadays numerous advanced numerical techniques that can be classified in this type of methods are those pertaining to the world of *machine learning*. See (Binkhonain & Zhao, 2019) and (Yassin et al., 2013) for reference.

Finally, in *nonlinear model updating* the aim is to modify a nonlinear model by changing its parameters, commonly in a recursive or iterative way. The methods to update numerical nonlinear models are very similar to those one used to update linear model, being the nonlinear parameters treated as the linear ones. Very limited application are presents nowadays in this field, especially for the high computational time needed to update complex structures. Several algorithms taken by the machine learning field are becoming very popular also for this type of corroboration methods.

In the following subsections, some emblematic examples are reported to show the importance of the aforementioned linear and nonlinear corroboration methods

on real world structures, especially focusing on buildings belonging to the architectural heritage.

2.3.1. Linear identification and model updating

One effective example of linear corroboration is that one reported in (Bursi et al., 2014). The authors propose a procedure for the modelling and simulation that relies on identification, model updating, and validation stages. They used the proposed procedure to analyse a complex twin-deck curved footbridge that it is prone to corrosion because the aggressive environment in which it is located, (see Figure 27). Due to the presence of uncertainties in FE modelling and due to structural changes during the construction of the bridge, the authors decided to corroborate the virtual model with data coming from an experimental system identification campaign:

- the sensors location was supported by a preliminary Finite Element (FE) model, then;
- modal characteristics of the footbridge were extracted from signals produced by ambient vibration via the SSI algorithm.
- after reducing the discrepancy between the numerical and experimental modal quantities (by using trust-region algorithms), the FE model was further updated in the modal domain, by changing both the stationary aerodynamic coefficients and the flutter derivatives of deck sections to consider the effects of the curved deck layout.

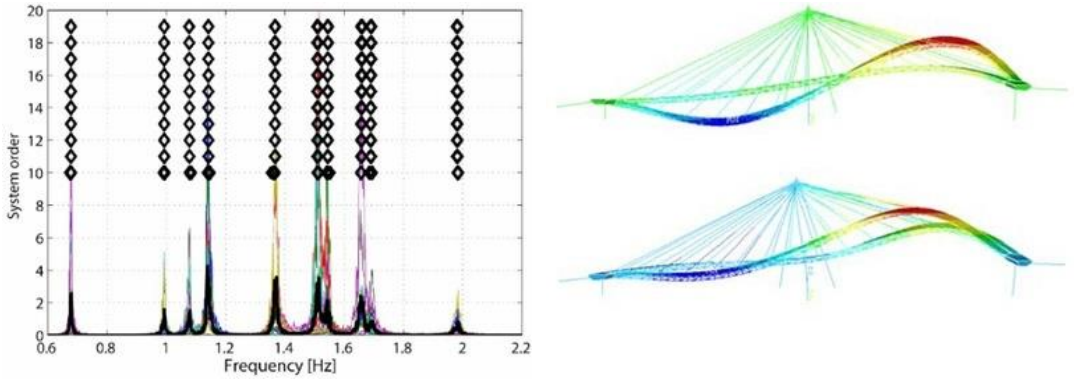

(a) (b)

Figure 27: *Ponte del Mare* footbridge, Pescara, Italy, (Bursi et al., 2014): (a) stabilization diagram; and (b) first two mode shapes.

The example shows in a very clear way the three main stages of the linear model corroboration, i.e. Optimal Sensor Placement, (OSP), identification, and model updating.

Another example worth of noting about the linear corroboration of models is that one reported in (Pecorelli et al., 2018) and (Ceravolo et al., 2019). In the first work the authors define the main steps followed for the definition of a robust

routine for the online Continuous Vibration-Based Structural Health Monitoring (CVB-SHM) of a large masonry oval dome, the dome of the Sanctuary in Vicoforte, (see Figure 28a). For the identification procedure, they used an output-only SSI technique complemented by an automatic procedure applied to the identification results which contemplates hierarchical clustering algorithms and stabilization diagrams detect spurious modes. On the sanctuary, in addition to the dynamic monitoring system constitutes by accelerometers, it is also installed a static monitoring system, which consists of temperature sensors, load cells, cracks meters, etc. In this respect, on Figure 28b a dispersion diagram of the first modal frequency vs the temperature recorded at the Sanctuary is reported. The figure is emblematic as it demonstrates the existence of a correlation between the two aforementioned physical quantities. This is important, because if a virtual model is used to assess the presence of damage in systems starting from modal quantities, such as frequencies, the model should consider the existence of this correlation.

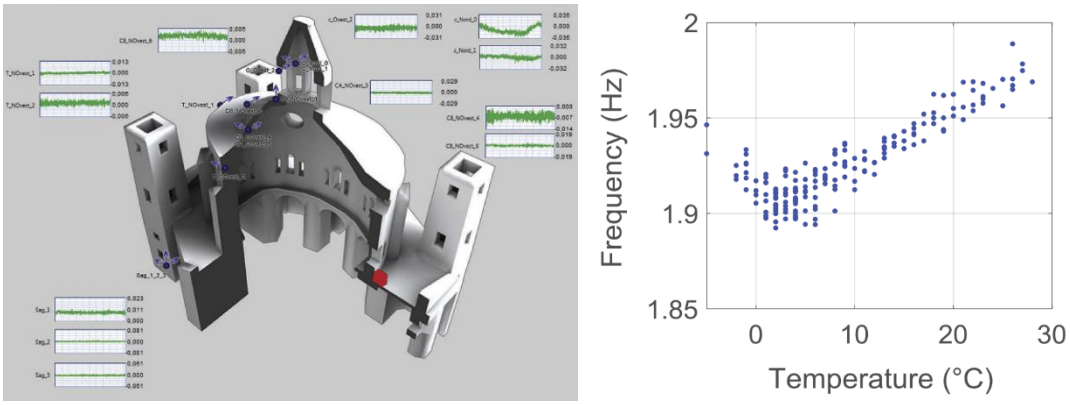

(a) (b)

Figure 28: Sanctuary in Vicoforte, (Pecorelli et al., 2018): (a) screenshot of a window of the monitoring system software; and (b) relation between frequency and temperature for the first mode of the sanctuary.

This fact prompted the authors to explore novel model updating methods based on *multiphysics techniques*, (Ceravolo et al., 2019). To do so, the authors propose to perform an uncoupled updating of the thermal and mechanical problem, (see Figure 29a), supposing a quasi-static variation of the temperature in time. The thermal model updating concerns the minimization of the difference between the temperature recorded in specific locations on the structure and the corresponding temperatures provided by the numerical model. Indeed, the mechanical model updating is represented by a classical modal updating technique. Then, thanks to the updated thermal model, a thermal analysis provides the thermal distribution on the entire, or on a subpart of the model that is analysed. The thermal distribution is applied to the virtual model and the corresponding forces that rise up due to the application of the thermal field are compared to those one recorded by means of load cells installed on the building.

Figure 29b reports an example of displacement field due to the application of a thermal distribution related to data recorded in winter.

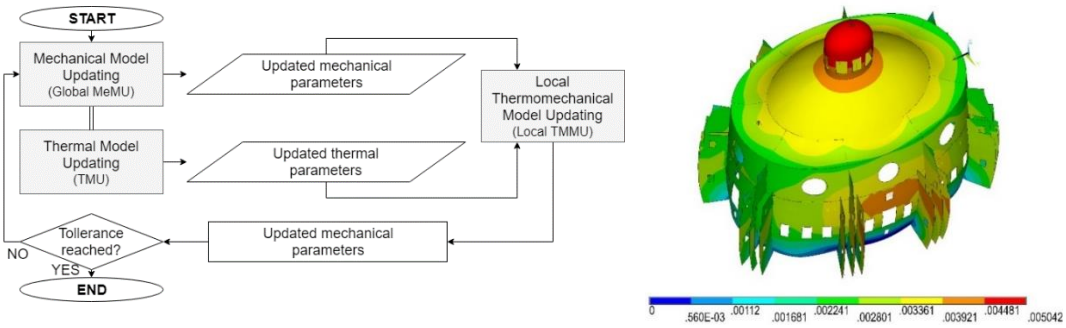

(a) (b)

Figure 29: Multiphysics Model Updating of Sanctuary in Vicoforte, (Ceravolo et al., 2019): (a) flowchart of the methodology; and (b) simulation of the temperature distribution inside the drum-dome-lantern subcomponent of the sanctuary.

Many times, differently from the case of the Sanctuary in Vicoforte, the data available for the model corroboration of real systems are limited. In these cases trying to calibrate too many model parameters with few experimental quantities can bring to updated models characterised by unphysical values of the updated mechanical parameters. In such cases, performing a *sensitivity analysis* is of paramount importance. Briefly, sensitivity analyses are methods to update model parameters by considering the variation that each parameter bring to the variation of some physical quantities predicted by the virtual model and that are compared with their corresponding experimental quantities (as for example identified natural frequencies). Commonly, indices of sensitivity summarize a measure of this variation. In their work, (Boscato et al., 2015), the authors explain as *global sensitivity* analysis allows model updating to be carried out even in the case of elevated uncertainty about the material characteristics. Architectural heritage structures deserve specific attention on account of their intrinsic geometrical complexity and heterogeneity. Thus in their work, the authors apply the concept of global sensitivity to a complex monumental structure, accompanying the study with more classical *local sensitivity* approaches. The main difference between global and local sensitivity analysis relies in the fact that local approaches are based on the calculation of partial derivates that bring information of the points in which they are evaluated, without considering the entire variation range of the model parameters. On the opposite, global approaches such as the *standardized regression coefficients* or the *variance-based methods* try to get information on the overall range of variation of the model parameters.

The system analysed by the authors is the church of *S. Maria del Suffragio* in L'Aquila, Italy, (see Figure 30), that was severely damaged by the 2009 earthquake. After the FE model updating, a dynamic analysis was performed in order to compare the model prediction, in terms of accelerations, with the acceleration responses recorded during the seismic event on the structure.

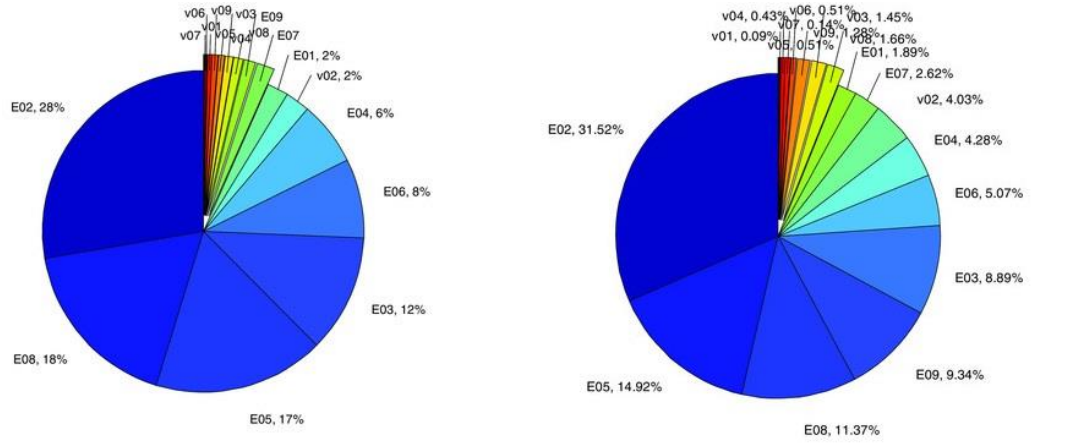

(a)

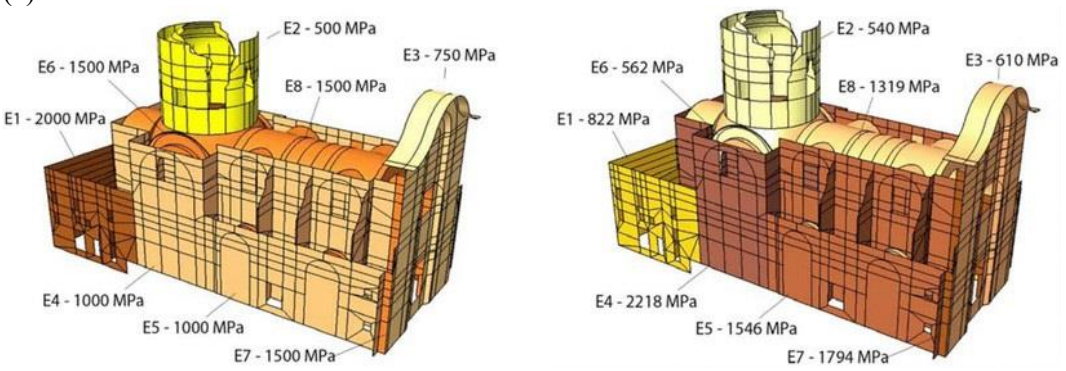

(b)

Figure 30: Sensitivity analyses for the FE model of *S. Maria del Suffragio*, (Boscato et al., 2015): (a) local and global sensitivity analysis indices; and (b) model parameters before, (left), and after, (right), the model updating performed by means of global sensitivity analysis.

2.3.2. Nonlinear identification and nonlinear model updating

Nonlinear corroboration of models is a very advanced field and applications on real systems are very limited. An admirable proposal for the nonlinear identification of multiple DoFs nonlinear systems is due to (Platten, et al., 2009). In their work the authors propose a novel identification method for large nonlinear systems. To do so, the authors apply the multi-exciter techniques in order to excite specific modes or DoF. The identification method is essentially a derivative of the RFS method and involves a nonlinear curve fit performed in modal space. To test the effectiveness of their work, the authors apply their proposed Nonlinear Resonant Decay Method (NLRDM) to a simulated 5 DoFs chain-like system, (see Figure 31a) and on an experimental clamped panel structure. The validation of their work is reported in Figure 31b for the 5 DoFs system, however the authors also performed a validation with experimental test on a plate structure.

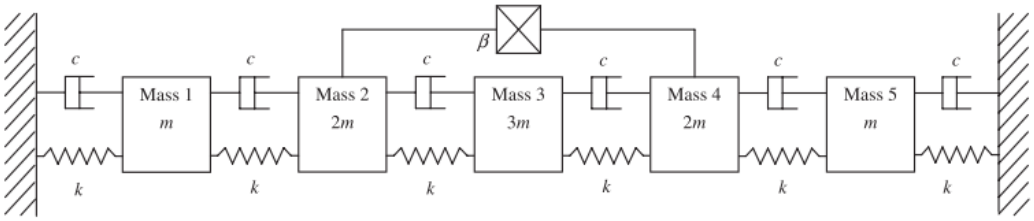

(a)

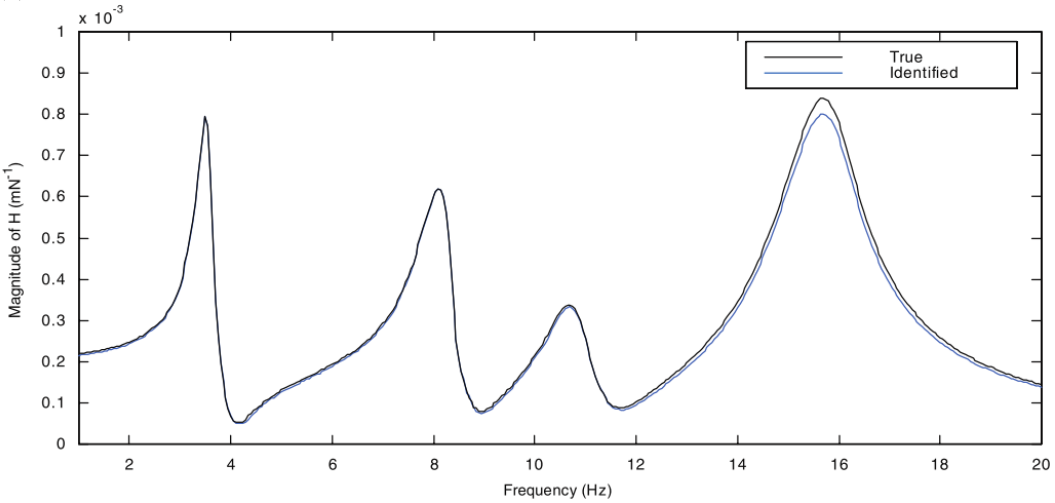

(b)

Figure 31: Nonlinear Resonant Decay Method (NLRDM) applied to a 5 DoFs system, (Platten, et al., 2009): (a) the 5 DoFs chain-like system; and (b) the comparison between the true, (black), and identified, (blue), Frequency Response Function (FRF).

In fact, validation of identification procedures with laboratory tests is a very common practice. In this respect, a particular application of the identification of nonlinear material parameters of a masonry model that was validated with experimental tests is reported in (Sarhosis & Sheng, 2014). In this work the authors developed a computational model for low bond strength masonry. Then, the material model parameters were identified from the results of load testing on large clay brick low bond strength masonry wall panels in the laboratory, avoiding in this way unreliable results that could be obtained with small sample tests. The authors initially modelled the prototype by means of a micro-modeling approach based on the Discrete Element (DE) method. For the minimization of the discrepance betwen the laboratory test results and the virtual model outcomes a procedure initially proposed by (Toropov & Garrity, 1998) was followed by the authors. The calibrated model was used to predict the response of another wall tested in laboratory, (see Figure 32a), which was used as validation case study. A good correlation between the calibrated model results (UDEC in Figure 32b) and the experimental results (DS1 in Figure 32b) was obtained by the authors as shown by in Figure 32.

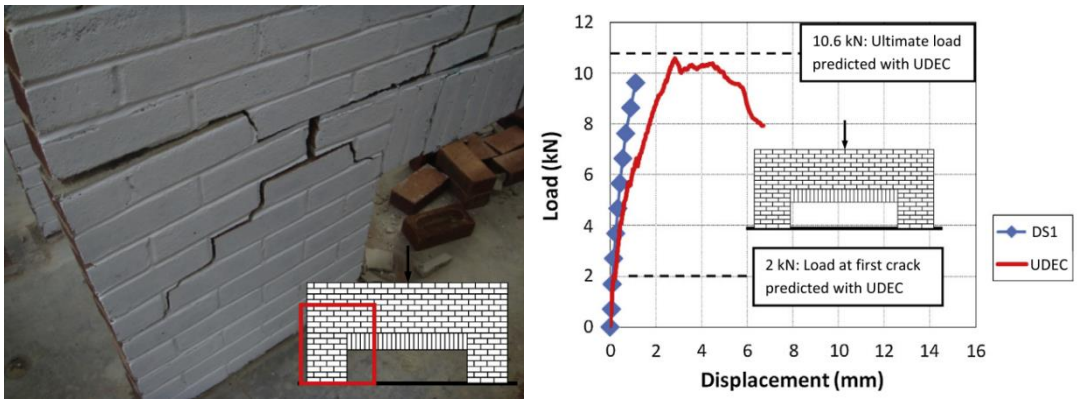

(a) (b)

Figure 32: Identification of the material parameters for masonry, (Sarhosis & Sheng, 2014): (a) picture of the experimental test; and (b) validation of the identification.

Another successful work in the nonlinear identification of systems is due to (Ceravolo et al., 2013). In their work the authors explore the instantaneous estimation of several, parametric and non-parametric, models to deal with problems encountered in the identification of full-scale structures subjected to strong excitations, such as earthquakes. Among these, one can recognize the need to deal with time-dependent behaviour of the structures (i.e. nonlinearity and non-stationarity). In fact, in presence of degradation or variation of any other structural characteristic, instantaneous identification certainly constitutes an enhancement of classical restoring force based techniques, and at the same time it may provide checks on the consistency of the assumed models by analysing the stability of the identified model parameters in the time. For example, Figure 33 reports the results of the application of the instantaneous method used by the authors to identify the instantaneous values of the parameters for a Bouc-Wen type 2 DoFs model. The method considers the use of pattern search algorithms to minimize a cost function defined by the summation of the difference between the Time Frequency Distributions (TFD) of the experimental records and the same distributions predicted by the virtual 2 DoFs model. As can be seen from Figure 33b, the analysed system presented a hysteretic degrading behaviour.

On the same line, the procedure reported in (Ceravolo et al., 2013) was also used in (Bursi et al., 2012) for the nonlinear identification of a multi-storey frame, having available data coming from pseudo dynamic tests. The technique is developed by means of a parametric approach, where a time-variant stiffness operator is coupled with a modified Bouc-Wen model, which allows both for slip and stiffness degradation. Strength deterioration was also indirectly considered.

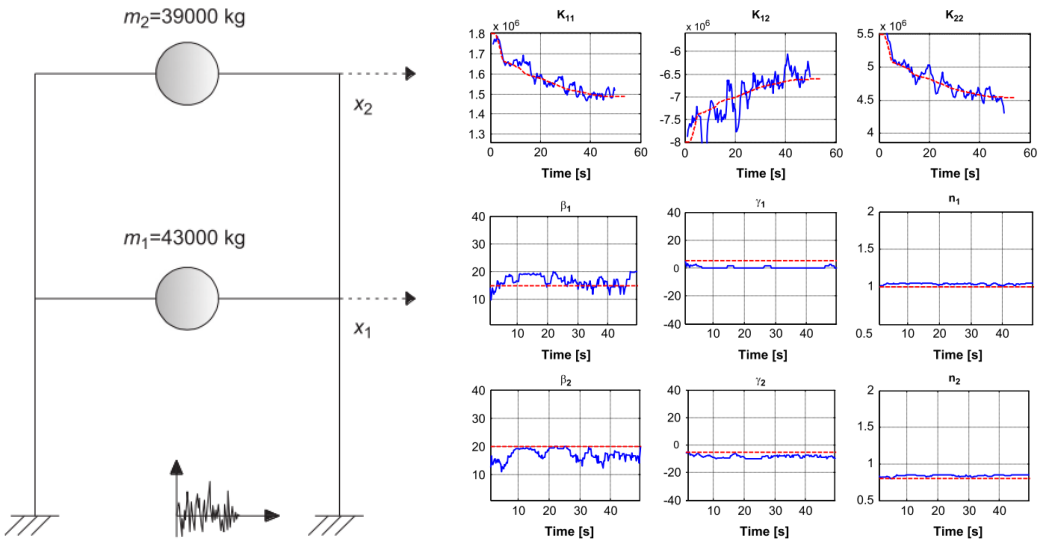

(a) (b)

Figure 33: Instantaneous estimation of a Bouc-Wen type model, (Ceravolo et al., 2013): (a) case study 2 DoFs system; and (b) instantaneous values of the identified parameters.

As regard nonlinear model updating, a very good attempt to introduce these methods to real world structures is represented by the work of (Muto & Beck, 2008). In this work, the nonlinear model updating is performed by means of Bayesian methods and model class selection using a recently developed stochastic simulation algorithm called Transitional Markov Chain Monte Carlo (TMCMC). In the paper the updating and model class selection is performed on a class of Masing hysteretic structural models. Finally, the authors give an example of the application of the method on synthetic dynamic data. The main outcome of the work, worth of noting, is that the proposed nonlinear updating method can identifies the hysteretic behaviour even in the case it is not directly contained in the acquired data, (e.g. local plasticization of the system and post plasticization behaviour of the entire system that remains apparently unchanged).

2.4. Towards the use of physical models for the simulation of architectural heritage structures

Identification and model updating techniques are fundamental to obtain a reliable virtual model. However, sometimes the corroboration of models is not possible because the lack of a reliable mathematical law able to simulate a specific physical behaviour. In this case the solution is to recall the concept of Hybrid Model (HM). With the hybrid modelling it is possible to upgrade the Numerical Substructure (NS) thanks to the information obtained from the Physical Substructure (PS) that is reproduced in laboratory. The model corroboration in this case passes through the fulfilment of Hybrid Simulations and Testing (HS/T) procedures. Generally, an HS/T procedure can be summarized as follow, see Figure 34:

- (i) The **NS** and **PS** are detached. The **NS** is simulated inside a numerical software, while the **PS** is tested in laboratory;
- (ii) An external action, **A**, is virtually applied to the **NS**, which possibly should be already calibrated with some methods described in the previous section. The restoring force, **F**, field is initialized inside the **NS** (for example with gravity loads);
- (iii) The values of the displacements, **D**, at the interface between the **PS** and **NS** obtained from the **NS** are applied to the tested specimen in laboratory, which represents the **PS**. **D** are obtained by solving the equations of motion;
- (iv) The values of the restoring forces, **F**, at the interface between the **PS** and **NS** obtained from the **PS** are applied to the **NS** inside the numerical software, simultaneously with the application of **A**. Here the equations of motion are solved for a subsequent time step compared to the point (iii). However, no models are needed to represent the restoring forces of the tested specimen, as they come from the experiment performed in laboratory;
- (v) The HS/T continues up to a desired time instant (end of action, collapse of the PS, etc.).

It is worth noting that the time of the simulation can differs from the time of the test carried out in laboratory.

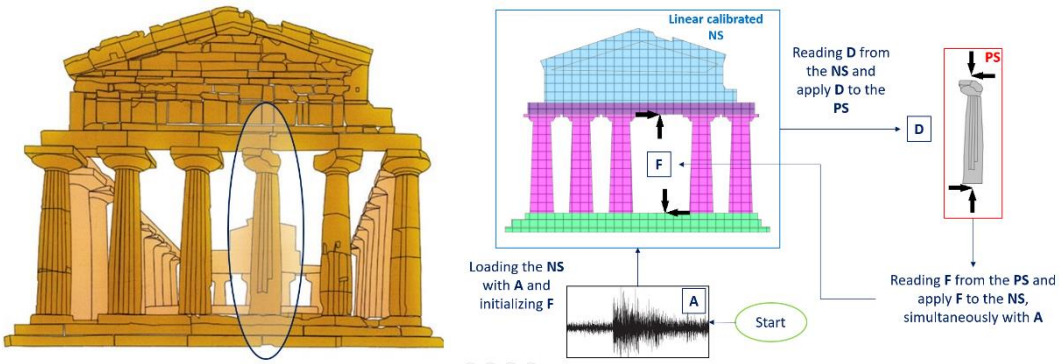

(a) (b)

Figure 34: Example of HS/T procedure: (a) system to be tested/simulated; and (b) steps of an HS/T procedure. Here the interface between NS and PS is considered to be concentrated (represented by a point).

The ratio between the time step with which the test in laboratory is performed and the time step used in the integration of the equations of motion within the numerical software is called *time-scale* and it is commonly referred to with the Greek letter, λ. Common values of the time-scale are limited by a value of 500. If the time-scale is 1, the hybrid simulation is known to be performed in *real time*. i.e. Real Time Test Hybrid Simulation (RTT-HS). On the opposite, if the time-scale differs from 1 (commons values are between 50 and 500) the test is referred as Pseudo Dynamic Test Hybrid Simulation (PDT-HS).

An effective advanced tool to corroborate virtual models by means of a physical model is the Online Model Updating in the Hybrid Simulation, (OMU-HS), framework. This techniques are useful to reduce modelling errors of the NS, especially when only a few critical components of a large system can be modelled as PS. With OMU-HS, the constitutive relations can be identified based on the data provided by the PS and the NS can be then updated with these data. Among the works on the corroboration of virtual models with physical models one worth of noting is the work done by (Mei et al., 2018). This work proposes a novel method to identify the constitutive parameters of a model by means of Unscented Kalman filter, (UKF). The method was validated with a monotonic loading test on a concrete column and real-time hybrid simulations of a reinforced concrete frame. The hybrid simulations were performed both in standard form and through the application of OMU-HS based on UKF.

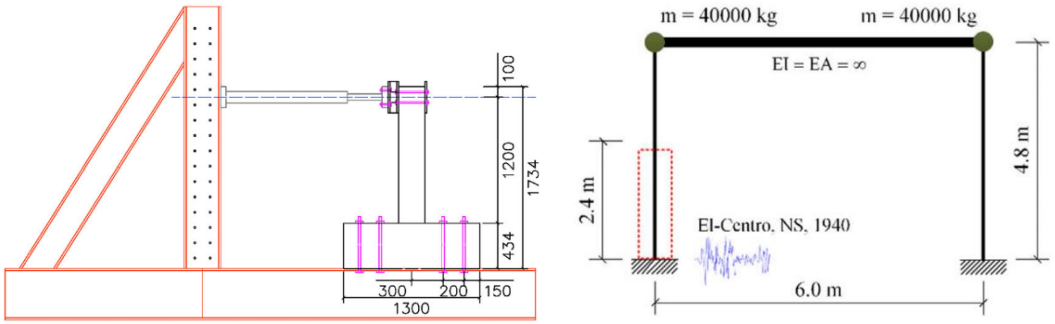

(a) (b)

Figure 35: Online Model Updating in the Hybrid Simulation, (OMU-HS), (Mei et al., 2018): (a) monotonic loading test setup of a reinforced concrete column performed to obtain the measurements for the nonlinear identification; and (b) hybrid simulation setup for the frame system, with the NS highlighted.

Another important application of virtual models aided with physical models can be found in (Abbiati et al., 2015) and (Abbiati et al., 2013). In their works the authors assessed the seismic performance of an old concrete viaduct, (Figure 36a). In particular, the attention was given to the complex behaviour of the isolation devices installed between the columns and the deck. In this case, hybrid simulation was conceived to simulate the dynamic response of the existing viaduct, both in the isolated and the non-isolated case. Hybrid numerical-physical time history analyses highlighted appreciable nonlinearities already under a serviceability limit state. For this reason, the authors decided to represent the NS with nonlinear laws. However, the nonlinear numerical model brought issues for performing efficient hybrid simulations. To overcome the problem, the NS was thus reduced with nonlinear techniques. Finally, in order to impose a consistent degradation of physical and numerical piers (see Figure 36b), during the hybrid simulation and testing, recursive identification and model updating sessions were performed.

(a)

(b)

Figure 36: Rio Torto viaduct, (Abbiati et al., 2013): (a) the real structure; and (b) the substructuring of the system in Numerical Substructure, (NS), and Physical Substructure, (PS).

In the previous examples, the interface between the NS and PS was always concentrated and assimilated by a point (e.g. connection between column and beam). However, architectural heritage structures are commonly referred to be mass distributed system with distributed interfaces between the subcomponents that constitutes the real system. In addition, also in the cases for which the interface can be recognized as a point, its mathematical approximation may not be consistent with actual conformation. Thus sometime there is the need to perform HS/T in presence of distributed interface. In this respect, Figure 37 represents the HS/T of the same system reported in Figure 34 performed with a distributed idealization of the interface. The thesis will find a solution for this type, such as for other type of problems related to masonry structures, under some assumptions.

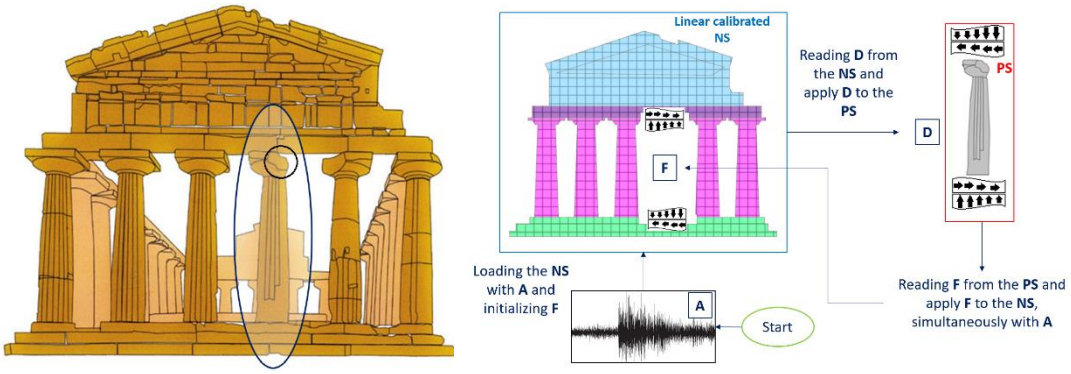

(a) (b)

Figure 37: Example of HS/T procedure: (a) system to be tested/simulated; and (b) steps of an HS/T procedure. Here the interface between NS and PS is considered to be distributed (represented by a line).

2.5. References chapter 2

Abbiati, G., Bursi, O. S., Cazzador, E., Ceravolo, R., Mei, Z., Paolacci, F., & Pegon, P. (2015). Pseudo-dynamic testing based on non-linear dynamic substructuring of a reinforced concrete bridge. In Experimental research in earthquake engineering (pp. 83-98). Springer, Cham.

Abbiati, G., Bursi, O. S., Cazzador, E., Ceravolo, R., Mei, Z., Paolacci, F., & Pegon, P. (2013). Pseudo-dynamic Testing with Non-linear Substructuring of a Reinforced Concrete Bridge Based on System Identification and Model Updating Techniques. SERIES Concluding Workshop, Joint Research Center, ISPRA, Italy, 28 May 2013.

Adams, D. E., & Allemang, R. J. (1999). A new derivation of the frequency response function matrix for vibrating non-linear systems. Journal of Sound and Vibration, 227(5), 1083-1108.

Beck, J. L., & Katafygiotis, L. S. (1998). Updating models and their uncertainties. I: Bayesian statistical framework. Journal of Engineering Mechanics, 124(4), 455-461.

Binkhonain, M., & Zhao, L. (2019). A Review of Machine Learning Algorithms for Identification and Classification of Non-Functional Requirements. Expert Systems with Applications.

Boscato, G., Russo, S., Ceravolo, R., & Fragonara, L. Z. (2015). Global sensitivity-based model updating for heritage structures. Computer-Aided Civil and Infrastructure Engineering, 30(8), 620-635.

Bursi, O. S., Ceravolo, R., Erlicher, S., & Zanotti Fragonara, L. (2012). Identification of the hysteretic behaviour of a partial-strength steel–concrete moment-resisting frame structure subject to pseudodynamic tests. Earthquake Engineering & Structural Dynamics, 41(14), 1883-1903.

Bursi, O. S., Kumar, A., Abbiati, G., & Ceravolo, R. (2014). Identification, model updating, and validation of a steel twin deck curved cable-stayed footbridge. Computer-Aided Civil and Infrastructure Engineering, 29(9), 703-722.

Carrella, A., & Ewins, D. J. (2011). Identifying and quantifying structural nonlinearities in engineering applications from measured frequency response functions. Mechanical Systems and Signal Processing, 25(3), 1011-1027.

Ceravolo, R., & Abbiati, G. (2013). Time Domain Identification of Structures: a Comparative Analysis of Output-Only Methods, In: JOURNAL OF ENGINEERING MECHANICS, pagine 537-544, ISSN: 0733-9399.

Ceravolo, R., De Lucia, G., & Pecorelli, M. L. (2017). Issues on the modal characterization of large monumental structures with complex dynamic interactions. Procedia Engineering, 199, 3344-3349.

Ceravolo, R., De Lucia, G., Miraglia, G., Pecorelli, M.L. (2019). Thermo-elastic finite element model updating with application to monumental buildings. Computer-Aided Civil and Infrastructure Engineering, CACAIE. (Submitted).

Ceravolo, R., De Marinis, A., Pecorelli, M. L., & Zanotti Fragonara, L. (2017). Monitoring of masonry historical constructions: 10 years of static monitoring of the world's largest oval dome. Structural Control and Health Monitoring, 24(10), e1988.

Ceravolo, R., Erlicher, S., & Fragonara, L. Z. (2013). Comparison of restoring force models for the identification of structures with hysteresis and degradation. Journal of Sound and Vibration, 332(26), 6982-6999.

Demarie, G. V., Ceravolo, R., Sabia, D., & Argoul, P. (2011). Experimental identification of beams with localized nonlinearities. Journal of Vibration and Control, 17(11), 1721-1732.

Ebrahimian, H., Astroza, R., & Conte, J. P. (2015). Extended Kalman filter for material parameter estimation in nonlinear structural finite element models using direct differentiation method. Earthquake Engineering & Structural Dynamics, 44(10), 1495-1522.

Ewins, D. J. (2000). Modal testing: theory, practice and application, 2000. Research Studies Press LTD., Baldock, Hertfordshire, England, 171, 415-437.

Ewins, D.J. (2006). A future for experimental structural dynamics, in: Proceedings of the International Conference on Noise and Vibration Engineering (ISMA), Leuven, Belgium, 2006.

Feldman, M. (2006). Time-varying vibration decomposition and analysis based on the Hilbert transform. Journal of Sound and Vibration, 295(3-5), 518-530.

Feldman, M. (2007). Considering high harmonics for identification of non-linear systems by Hilbert transform. Mechanical Systems and Signal Processing, 21(2), 943-958.

Feldman, M. (2014). Hilbert transform methods for nonparametric identification of nonlinear time varying vibration systems. Mechanical Systems and Signal Processing, 47(1-2), 66-77.

Ferretti, D., & Bažant, Z. P. (2006a). Stability of ancient masonry towers: Moisture diffusion, carbonation and size effect. Cement and Concrete Research, 36(7), 1379-1388.

Ferretti, D., & Bažant, Z. P. (2006b). Stability of ancient masonry towers: Stress redistribution due to drying, carbonation, and creep. Cement and Concrete Research, 36(7), 1389-1398.

Friswell, M., & Mottershead, J. E. (2013). Finite element model updating in structural dynamics (Vol. 38). Springer Science & Business Media.

Fuellekrug, U., & Goege, D. (2012). Identification of weak non-linearities within complex aerospace structures. Aerospace Science and Technology, 23(1), 53-62.

Green, P. L., & Worden, K. (2015). Bayesian and Markov chain Monte Carlo methods for identifying nonlinear systems in the presence of uncertainty. Philosophical Transactions of the Royal Society A: Mathematical, Physical and Engineering Sciences, 373(2051), 20140405.

Heller, L., Foltete, E., & Piranda, J. (2009). Experimental identification of nonlinear dynamic properties of built-up structures. Journal of Sound and Vibration, 327(1-2), 183-196.

Huang, N. E., Shen, Z., Long, S. R., Wu, M. C., Shih, H. H., Zheng, Q., ... & Liu, H. H. (1998). The empirical mode decomposition and the Hilbert spectrum for nonlinear and non-stationary time series analysis. Proceedings of the Royal Society of London. Series A: Mathematical, Physical and Engineering Sciences, 454(1971), 903-995.

Icomos-Iscarsah. (2003). ICOMOS Charter—Principles for the analysis, conservation and structural restoration of architectural heritage. Proceedings of the ICOMOS 14th General Assembly and Scientific Symposium, Victoria Falls, Zimbabwe, 2731.

Juang, J. N., & Pappa, R. S. (1985). An eigensystem realization algorithm for modal parameter identification and model reduction. Journal of guidance, control, and dynamics, 8(5), 620-627.

Kerschen, G., Peeters, M., Golinval, J. C., & Vakakis, A. F. (2009). Nonlinear normal modes, Part I: A useful framework for the structural dynamicist. Mechanical Systems and Signal Processing, 23(1), 170-194.

Kramer, S.L., (1996). Geotechnical Earthquake Engineering, Prentice-Hall.

Lacellotta, R., (2004). Geotecnica, Zanichelli, (In Italian).

Lacy, S. L., & Bernstein, D. S. (2005). Subspace identification for non-linear systems with measured-input non-linearities. International Journal of Control, 78(12), 906-926.

Lang, Z. Q., & Billings, S. A. (2005). Energy transfer properties of non-linear systems in the frequency domain. International Journal of Control, 78(5), 345-362.

Limongelli, M.P., and Çelebi, M. (2019). Seismic Structural Health Monitoring: From Theory to Successful Applications. Springer, Tracts in Civil Engineering, DOI: 10.1007/978-3-030-13976-6.

Ljung, L. (1999). System Identification – Theory for the User, Prentice Hall, Upper Saddle River, NY, USA.

Maia, N.M.M., Silva, J.M.M. (1997) "Theoretical and Experimental Modal Analysis".

Marwala, T. (2010). Finite element model updating using computational intelligence techniques: applications to structural dynamics. Springer Science & Business Media.

Masri, S. F., & Caughey, T. (1979). A nonparametric identification technique for nonlinear dynamic problems. Journal of Applied Mechanics, 46(2), 433-447.

Mei, Z., Wu, B., Bursi, O. S., Yang, G., & Wang, Z. (2018). Hybrid simulation of structural systems with online updating of concrete constitutive law parameters by unscented Kalman filter. Structural Control and Health Monitoring, 25(2), e2069.

Muto, M., & Beck, J. L. (2008). Bayesian updating and model class selection for hysteretic structural models using stochastic simulation. Journal of Vibration and Control, 14(1-2), 7-34.

Noël, J. P., & Kerschen, G. (2017). Nonlinear system identification in structural dynamics: 10 more years of progress. Mechanical Systems and Signal Processing, 83, 2-35.

Paduart, J., Lauwers, L., Swevers, J., Smolders, K., Schoukens, J., & Pintelon, R. (2010). Identification of nonlinear systems using polynomial nonlinear state space models. Automatica, 46(4), 647-656.

Pecorelli, M. L., Ceravolo, R., & Epicoco, R. (2018). An Automatic Modal Identification Procedure for the Permanent Dynamic Monitoring of the Sanctuary of Vicoforte. International Journal of Architectural Heritage, 1-15.

Peng, Z. K., Lang, Z. Q., & Billings, S. A. (2007). Linear parameter estimation for multi-degree-of-freedom nonlinear systems using nonlinear output

frequency-response functions. Mechanical Systems and Signal Processing, 21(8), 3108-3122.

Peng, Z. K., Lang, Z. Q., & Billings, S. A. (2008). Nonlinear parameter estimation for multi-degree-of-freedom nonlinear systems using nonlinear output frequency-response functions. Mechanical Systems and Signal Processing, 22(7), 1582-1594.

Peng, Z. K., Lang, Z. Q., Wolters, C., Billings, S. A., & Worden, K. (2011). Feasibility study of structural damage detection using NARMAX modelling and Nonlinear Output Frequency Response Function based analysis. Mechanical Systems and Signal Processing, 25(3), 1045-1061.

Pintelon, R., & Schoukens, J. (2001). System Identification: A Frequency Domain Approach IEEE Press. Piscataway, NJ.

Platten, M. F., Wright, J. R., Dimitriadis, G., & Cooper, J. E. (2009). Identification of multi-degree of freedom non-linear systems using an extended modal space model. Mechanical Systems and Signal Processing, 23(1), 8-29.

Portioli, F., Mammana, O., Landolfo, R., Mazzolani, F. M., Krstevska, L., Tashkov, L., & Gramatikov, K. (2011). Seismic retrofitting of Mustafa Pasha Mosque in Skopje: finite element analysis. Journal of Earthquake Engineering, 15(4), 620-639.

Renson, L., Gonzalez-Buelga, A., Barton, D. A. W., & Neild, S. A. (2016). Robust identification of backbone curves using control-based continuation. Journal of Sound and Vibration, 367, 145-158.

Richards, C. M., & Singh, R. (1998). Identification of multi-degree-of-freedom non-linear systems under random excitations by the “reverse path” spectral method. Journal of Sound and Vibration, 213(4), 673-708.

Sarhosis, V., & Sheng, Y. (2014). Identification of material parameters for low bond strength masonry. Engineering Structures, 60, 100-110.

Schetzen, M. (1980). The Volterra and Wiener theories of nonlinear systems.

Sracic, M. W., & Allen, M. S. (2011). Method for identifying models of nonlinear systems using linear time periodic approximations. Mechanical Systems and Signal Processing, 25(7), 2705-2721.

Sracic, M. W., & Allen, M. S. (2014). Identifying parameters of multi-degree-of-freedom nonlinear structural dynamic systems using linear time periodic

approximations. Mechanical Systems and Signal Processing, 46(2), 325-343.

Toropov, V.V., & Garrity, S.W. (1998). Material parameter identification for masonry constitutive models. In: Proceedings of the 8th Canadian masonry symposium. Alberta, Canada: Jasper; 1998. p. 551–62.

Van Overschee, P., De Moor, B. (1996). Subspace Identification for Linear Systems: Theory, Implementation and Applications, Kluwer Academic Publishers, Dordrecht, The Netherlands.

Widanage, W. D., Stoev, J., Van Mulders, A., Schoukens, J., & Pinte, G. (2011). Nonlinear system-identification of the filling phase of a wet-clutch system. Control Engineering Practice, 19(12), 1506-1516.

Worden, K., Hickey, D., Haroon, M., & Adams, D. E. (2009). Nonlinear system identification of automotive dampers: a time and frequency-domain analysis. Mechanical Systems and Signal Processing, 23(1), 104-126.

Xu, B., He, J., & Dyke, S. J. (2015). Model-free nonlinear restoring force identification for SMA dampers with double Chebyshev polynomials: approach and validation. Nonlinear dynamics, 82(3), 1507-1522.

Yang, Z., Dimitriadis, G., Vio, G. A., Cooper, J. E., & Wright, J. R. (2006). Identification of Structural Free-play Non-linearities using the Non-Linear Resonant Decay Method. In Proceedings of the 2006 International Conference on Noise and Vibration Engineering (pp. 2797-2809). Katholieke Universiteit Leuven.

Yassin, I. M., Taib, M. N., & Adnan, R. (2013). Recent advancements & methodologies in system identification: A review. Scientific Research Journal, 1(1), 14-33.

Chapter 3

Novel approaches to the model updating

In this chapter, rank aggregation strategies are introduced in the optimization framework to perform an Ensemble finite element Model Updating (EMU) of monitored masonry structures subjected to earthquakes. Ranking is used to obtain optimal results from several optimization solvers, establishing in this way a reference numerical model. For the model calibration, different solvers are employed (i.e. genetic, particle swarm, simulated annealing optimisation, etc.), which provide not unique definition of the model parameters. Then, through a combinatorial selection of the parameters, the best Finite Element (FE) model is defined among several optimal outcomes. To solve the ranking problem, a Plackett-Luce model-based strategy is pursued. The reason of using algorithms based on rank aggregation strategies in the optimization of complex systems lies in the fact that the outcomes of optimization in general are process dependent. Instead, the novel approach to optimization provides a ranking for the processes, which, thanks to the use of a Plackett-Luce model, supplies the most likely ranking. The outcomes of the process also correspond to the minimum variance over the solvers.

The chapter starts with a description of the combinatorial selection strategy, then to test its effectiveness, the strategy is applied to well-known optimization problems, as well as to a purely numerical benchmark model. The chapter continues with an overview of the Town Hall building of Pizzoli, the seismic events which occurred in 2016 in central Italy, and the installed monitoring system. After the processing of the experimental data, the strategy is applied to the structure of the Town Hall.

Part of the work described in this chapter was also previously exposed in conference.

3.1. Introduction

One of the most unresolved issue in the FE model calibration, concerns the reliability of the optimization process' outcomes. Although model updating is successfully used in vibration-based Structural Health Monitoring (SHM), see for example (Bassoli et al., 2018), (Boscato et al., 2015), (Bursi et al., 2014), (Ceravolo et al., 2016), (Hu et al., 2018), (Sun & Betti, 2015) and (Zhang et al., 2017), its applications to real problems can lead to a considerable number of results, i.e. model parameters, that fall within prefixed margins of error (not uniqueness of the solution). This means that different methodologies, or the same methodology applied with different settings, can lead to discrepant outcomes. A striking example can be found in the structural identification of modal parameters with ambient vibrations, where a change in the order of the system bring to obtain different identified modal parameters.

The proposed method tries to solve exactly these types of problems, by considering a synergic approach that considers the information coming from different methods, or from the same method set in different ways, ensuring in this way a unique reference result. The aim of this study is therefore the definition of a strategy that can reduce the uncertainties of the solution provided by current model updating techniques, and at the same time increases its reliability. It is not the intention of the authors to affirm that the result is unique in a broad sense, but rather to demonstrate that, starting from multiple solutions, the strategy leads to a reference solution which respects certain optimal characteristics. In this regard, the concept of the Rank Aggregation (RA) problem, (Yasutake et al, 2012), is introduced. The goal of a RA problem is to define a ranking list among several ranking lists expressed by voters. The ranking lists arrange a certain number of candidates in a specific order. Thus, the aim of an RA problem is to find the best ranking list among all the possible permutations of the candidates' order. The RA problem is a classic problem in social choice literature, (Yasutake et al, 2012), and has been applied to a wide variety of problems, i.e. to the ranking of documents, (Cao et al., 2007), to assess the potential demand of electric vehicles, (Beggs et al., 1981), for modelling electorates, (Gormley & Murphy, 2005), etc. In recent years, the problem has also been explored by the computer science community, (Dwork et al., 2001), (Fagin et al., 2003), (Andoni et al., 2008), in particular it has been addressed with efficient Bayesian methods for inferring the parameters of a specific ranking model, (Marden, 2014), such as the Plackett-Luce (PL) model, (Guiver & Snelson, 2009), (Plackett, 1975), (Luce, 2012). Inferring the parameters of the PL distribution is typically done by maximum likelihood estimation by means of the minimization/maximization (MM) algorithm, (Hunter, 2004). However, the Bayesian inference has proven to be very accurate and highly scalable to large real-world problems, (Minka, 2004), (Minka, 2005). Lately, the

RA problem has been addressed by using evolutionary algorithms, (Aledo et al., 2013), or other specific learners, (Aledo et al., 2017), in the machine learning community.

In this thesis, the RA problem is dealt with by using a PL model to select the permutation of the candidates which maximize the probability of being observed. In this regard, the candidates are supposed to be well-known optimization solvers. In other words, this work implements a "ranking" strategy to obtain optimal results from several optimization algorithms, such as Genetic Algorithm (GA), Particle Swarm Optimization (PSO), Pattern Search (PS), and Simulated Annealing (SA). Metaheuristics algorithms are useful for dealing with problems characterized by non-smooth and unknown cost functions (without a closed formulation). In addition, the calibration of very complex systems is often performed with these algorithms because of their ability to deal with problems characterized by a large number of parameters and uncertainties. These methods, however, present some disadvantages mainly related to the low precision of the results. Thus, different trials in the calibration process may lead to different results in the values of the updated parameters. This is true for metaheuristic as well as for a large number of other algorithms that try to solve an inverse problem. The use of a RA strategy helps in reducing this discrepancy in the results, by combining the outcomes of each algorithm and providing a learning phase.

This leads to a more reliable value of the parameters being updated, thanks to the information exchanged between the solvers. Last but not least, the motivation to use RA lies in combining many different rank orderings on the same model parameters to produce “best” compromise orderings. Later it is shown how to efficiently take any initial aggregated ordering, as resulting from different optimization algorithms, and produce a maximally consistent locally optimal solution.

3.2. Rank aggregation problem in the optimization framework

The problem of selecting the best result among several optimal results can be reduced to a ranking problem by means of *learning to rank* theory (Cao et al., 2007), (Joachims et al., 2007). Specifically, the RA problem, (Yasutake et al, 2012), aims to find the best ranking list of I candidates of an item q from several ranking lists provided by K voters. Among many models, the Plackett-Luce one has proved to be a very effective tool to solve the RA problem, (Guiver & Snelson, 2009). The Plackett-Luce distribution derives its name from independent works by Plackett and Luce. The Luce’s axiom governs the choice probabilities of a population choosing an item from a subset of a set of items. The axiom states that the choice probability ratio between two items is independent of any other items in the set. By using the Luce’s axiom, the Plackett model is easily extended to partial rankings, defining in this way the Plackett-Luce model. The PL model

applies when each observation provides either a complete ranking of all items, or a partial ranking of some of the items, or a ranking of the top few items. In more details, by means of this approach each voter k gives a score $w_{k,i}$ to the i-th candidate. The score represents the probability of picking the candidate i among the other candidates (Luce's axiom). In order to define who is the best candidate to be selected, it is necessary to follow some criteria. In this regard, the PL model aims to maximize the compound probability to observe some rankings, or permutations of the candidates, if both the voters and the candidates are independent. The total number of permutations is evaluated starting from the indices i which identify each candidate. Given the total number of candidates, I, it is possible to build the vector of the permutation indices, $\mathbf{t}$=1,2,..,i,..,I, that contains the positive natural numbers that go from 1 to I with step 1. The permutation matrix $\mathbf{C}$ containing all the P possible permutations is given by $\mathbf{C}$=perms($\mathbf{t}$), (Matlab, 2018), with $\mathbf{C} \in \mathbb{N}^{P \times R}$, R=I and P=I!

To explain how rank aggregation works, one can use an analogy by comparing the RA problem to a teacher-led work of a class. In a teacher-led work, teachers oversee and help students in accomplishing a specific project by providing explicit instructions, or explanations. The task entrusted by the teachers represents the optimal solution that the class must achieve. In a teacher-led work there is no competition in the classroom, but teachers help all the students to solve the assignment and to find the best solution accepted by everyone. In this type of problems, the teachers do not know the optimal solution of the work; they can just guide the students.

In this first phase of teacher-led work, each student must solve the assignment independently. Once all the students have completed the assignment, based only on their individual skills, they will deliver it to the teachers. This first phase is equivalent to reaching the optimum for each single algorithm, according to the convergence criterion adopted.

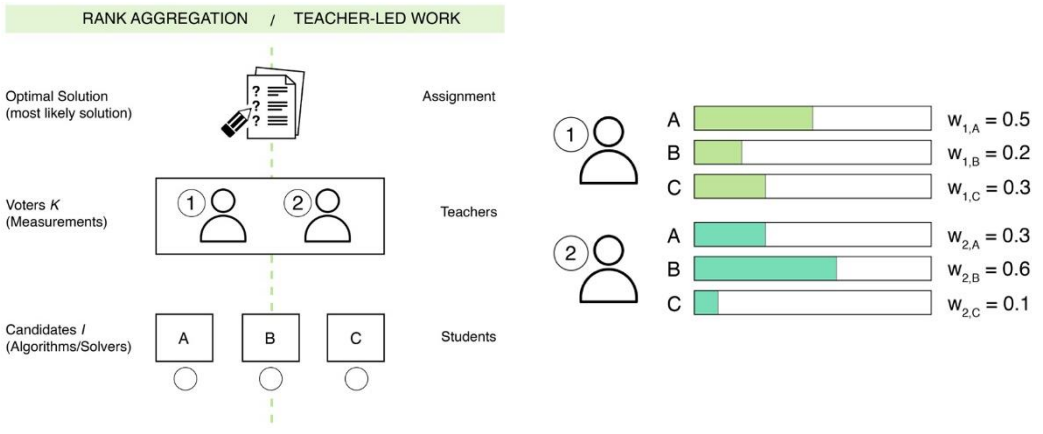

(a) (b)

Figure 38: Comparing RA problem with teacher-led work: (a) finding the optimum for each single algorithm; and (b) estimation of the scores.

If the task is extremely difficult, none of the students would be able to solve the assignment obtaining the 100% of the score; in other words, none of them would reach a satisfactory result.

This first phase is depicted in Figure 38a. After collecting all the completed assignments, teachers evaluate them independently by giving a score to each student. At this point, the problem arises about the best ranking to be adopted. In fact, as teachers do not know the exact solution, they might disagree about the score to assign to the students. For this reason, teachers need to use a decision-making method that help them to find a reference solution, represented by a ranking which classifies the assignments from the best to the worst one. This second phase, as depicted in Figure 38b, corresponds to the estimation of the score related to the difference between the experimental quantities and the numerical quantities provided by each algorithm.

Since teacher disagree about the classifications they have drawn up, they decide to question their own results. Therefore, they decide to analyse all the possible permutations of the assignments. In this way a finite number of ranking lists is generated and, consequently, a finite number of possible solutions to the problem. The solution of the RA aims to determine which list sorts the assignments, and therefore the students, from the best to the worst. This third step (see Figure 2) corresponds to the calculation of the permutation matrix, **C**, as described before.

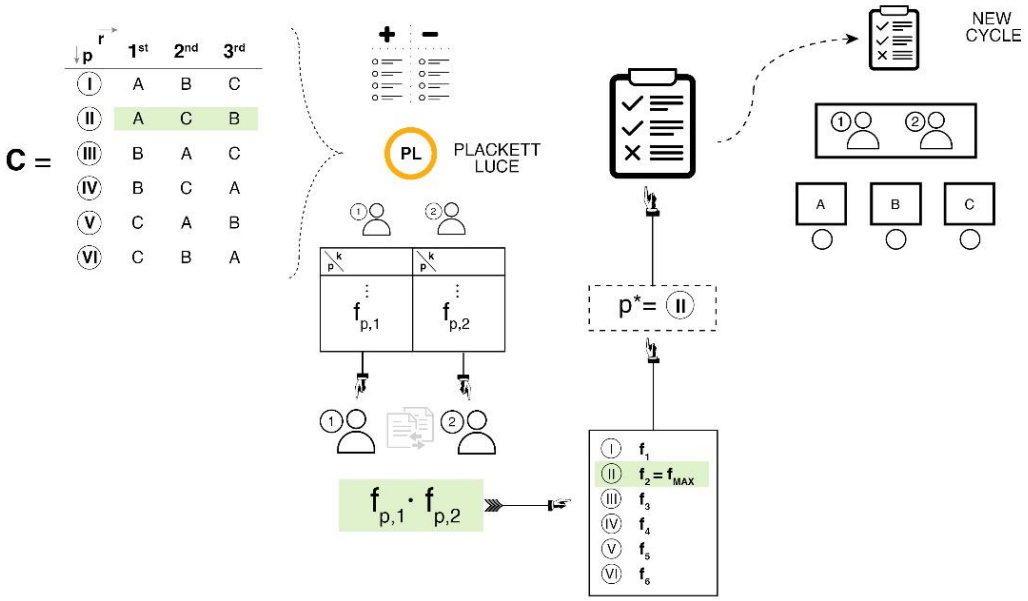

Figure 39: Comparing RA problem with teacher-led work: solving the problems with PL distribution.

3.2.1. Plackett-Luce model to solve the Rank Aggregation problem in the optimization framework

Having defined the permutation matrix, **C**, for the *p*-th permutation and for the *k*-th voter it is now possible to evaluate the probability of selecting a candidate instead of another one, having already selected a certain number of candidates:

$$f_{p,k} = \prod_{r=1}^{R} \frac{w_{k,C_{p,r}}}{\sum_{s=r}^{R} w_{k,C_{p,s}}} \tag{1}$$

where $w_{k,Cp,r}$ is the weight that the voter *k* gives to the candidate $C_{p,r}$, i.e. the *r*-th candidate of the *p*-th ranking obtained by permutation. Moreover, $R=I$, is the total number of candidates and *s* is an auxiliary variable; (1), which describes the Plackett-Luce model, can then be used to evaluate the probability observing a permutation set:

$$f_{p} = \prod_{k=1}^{K} \left(\prod_{r=1}^{R} \frac{w_{k,C_{p,r}}}{\sum_{s=r}^{R} w_{k,C_{p,s}}} \right) \tag{2}$$

The permutation that maximize (2) defines the best ranking list that should be selected, since it is related to the maximum probability of being observed (maximum likelihood). Indicating the selected ranking list with $a^*=C_{p^*,\forall r}$, a method (e.g. Mean Reciprocal Rank, etc.) can be chosen to define the optimal value of the analyzed item, among all the candidates ranked as established by a^* (p^* is the index of the row of **C** related to the permutation that maximize (2)).

For example, supposing to choose the first classified candidate, the optimal values of the analyzed items will be the ones related to the best candidate, according to the ranking list permuted as a^*. This means that the best candidate, i^*, is equal to $i^*=a_1^*=C_{p^*,1}$, and the optimal items are the ones related to the candidate i^*. In this study, the items are represented by the parameters obtained from the different optimization solvers, thus the candidates are chosen to be the optimization solvers, i.e. genetic algorithm, (Goldberg, 1989), pattern search, (Audet & Dennis, 2002), particle swarm optimization, (Kennedy & Eberhart, 1995), and simulated annealing, (Ingber, 2000). For reproducibility reasons, the default setting of the solvers has been maintained, (Matlab, 2018).

In a more general framework, the candidates could be represented by one or more solvers with different settings. The voters are instead chosen to be the normalized scatters between the numerical and experimental measurements but, in the general case, they can represent any objective. It is important to note that common problems in the calibration of engineering structures involve a minimization process. However, the RA is solved through a maximization process. For this reason, one need to move the minimization process of each algorithm in a maximization process for the PL model. Thus, for each solver *i* we

can define a normalized scatter, $\beta_{k,i}$, between the k-th numerical $z_{k,i}$, and the k-th experimental, $z_{k,e}$, measurements as:

$$\beta_{k,i} = \frac{|z_{k,e} - z_{k,i}|}{|z_{k,e}| + 1} \tag{3}$$

then, the scores, $w_{k,i}$, are assumed to be calculated starting from the scatters, $\beta_{k,i}$, using the Gaussian function of (4a):

$$w_{k,i}^{*} = exp\left[-\left(\frac{\beta_{k,i}}{\sigma_k}\right)^2\right] \tag{4a}$$

$$w_{k,i} = \frac{w_{k,i}^{*}}{\sum_{i=1}^{I} w_{k,i}^{*}} \tag{4b}$$

In (4a), σ_k is the standard deviation of the k-th scatter over the solvers. It is important to note that (4a) does not represent the probabilistic distribution of the scores, but just the relationship that allows the minimization to be converted into a maximization problem. As a matter of fact, in the present study the inference of the parameters of the probabilistic distribution of the scores is not undertaken.

To better explain the PL model, we will continue the analogy of the RA with the teacher-led work of a class. We are now in the fourth step of the RA problem. To decide which is the optimal ranking, the teachers decide to use a model of PL. With this model, each teacher calculates the probability of choosing one winning student instead of another, having already considered the scores of the other students. At this stage each teacher will use the score given in the previous phase. In this way, the teachers can assign a value to each permutation of the rankings; these values correspond to the probability of observing a certain ranking rather than another, based on the individual skills of the teachers. In fact, each teacher will obtain a result independently from the others. This phase corresponds to the use of (1), see Figure 39 for clarity.

Following the employment of the PL model, teachers compare their results and decide to combine the probabilities to observe a winning ranking rather than another one. Since both the grading processes have been carried out independently, teachers choose to multiply the probability values for each permutation, thus calculating the compound probability to observe a permutation rather than another one. In this way, a shared reference value of probability for each permutation is set. Teachers will determine which ranking permutation maximizes the probability to be observed, which is nothing but the most plausible ranking that orders the students (and therefore the assignments) from the best to the worst. This phase (see Figure 39 for clarity) corresponds to the application of (2) and, consequently, to the determination of the ranking that orders the algorithms from the one who provides the *best* result to the *worst*. After obtaining a list that ranks the assignments in the most plausible way, teachers will determine

if the best assignment is just the one in the first place, or a combination of the results of each individual assignment.

An example of combination is represented by the *mean reciprocal rank*, which would correspond to a mean value of the results of each assignment, weighted according to the position occupied by each assignment in the most plausible ranking. This phase corresponds to the calculation of the *mean reciprocal rank* value of each parameter updated by the various algorithms. The parameters that are defined optimal will correspond to the mean of the parameters of each single algorithm. Alternatively, the optimal parameters can be chosen as the parameters associated with the algorithm at the first place in the most likely ranking. In this last phase the teachers show the students a single reference assignment, explaining to them that it is the task that most likely corresponds to the optimal solution, and ask them to solve again the same problem. Therefore, the students must solve again the assignment, this time being aware that the most plausible solution, up to that point, is the one given by the teachers. The procedure continues until all the students (i.e. the algorithms) reach a common agreement, i.e. a common reference solution. The optimal result will not be the best in the broad sense (it does not necessarily correspond to a score of 100%), but it will rather be the most likely result, which at the same time maximizes the agreement between the different students. In this way, the whole class will reach a common solution.

This last phase (see Figure 39), corresponds to identifying the parameters (object of the calibration) that satisfy two conditions: (i) they are associated to the most plausible ranking list, in a sense that this list has the maximum probability of being observed (*maximum likelihood*); (ii) their values maximize the correspondence of the results obtained by the different algorithms (*minimum variance*). A pseudo-code of the proposed selection algorithm is reported in Table 1.

Table 1: Pseudo-code of the selection algorithm involving the PL model.

Having assumed I candidates (i.e. solvers setups) and K voters (i.e. objectives of the optimization) to calibrate Q items (i.e. model parameters), the following procedure applies:

A. Initialize the values for different items (i.e. model parameters)
   a. Set each candidate (i.e. solver) and perform an independent optimization with an assumed convergence criterion;
   b. Use the outcomes of each optimization (i.e. model predictions) and the available experimental quantities (i.e. measured quantities) to estimates the weights with (4a) based on the assumed objectives, e.g. (3);
   c. Calculate the permutation matrix of the rankings, $\mathbf{C}$=perms($\mathbf{t}$), where $\mathbf{t}$=1,2,..,*i*,..,*I*;
   d. Evaluate the probability of selecting a candidate instead of another one with (1);
   e. Evaluate the probability to observe a ranking from (2);
   f. Select the ranking that maximizes (2);
   g. Assume a method for estimating the new values of the items (i.e. model parameters). Use for example the items related to the first classified candidate or the "mean reciprocal rank" of the values of the items (i.e. model parameters) calculated

over the candidates.

B. Start again performing A in a recursive way up to convergence, i.e. until the variance of the values of the items (i.e. model parameters) calculated over all the candidates (i.e. solvers) is lower that a chosen tolerance.

3.3. Numerical tests

In this section the aforementioned methodology is applied to numerical problems in order to validate the effectiveness of the selection strategy.

3.3.1. Optimization of test functions

To assess the effectiveness of the proposed selection strategy, the RA problem is solved with the PL model applied recursively to a set of well-known optimization test functions, (Sun & Yuan, 2006), by choosing the first candidate classified of the selected permutation. The selected parameters are thus imposed as the initial condition for the next optimization (PS and SA), or as an individual (GA) or a swarm component (PSO). Among a vast number of test functions existing in the literature, it was decided to use six of them to test the strategy. The testing functions used in this study are shown in Figure 40 , and they are: Rosenbrock's function, Levi's function n.13, Eggholder function, Easom's function, Bukin's function n.6, and Cross-leg table function, with the optimum shifted to x_1=1, x_2=1 (see Figure 40 for clarity). While the first two functions are relatively simple problems, the last two are considered nearly impossible to minimize, (Mishra, 2006). All the test functions have been chosen in two dimensions in order to give a visual representation.

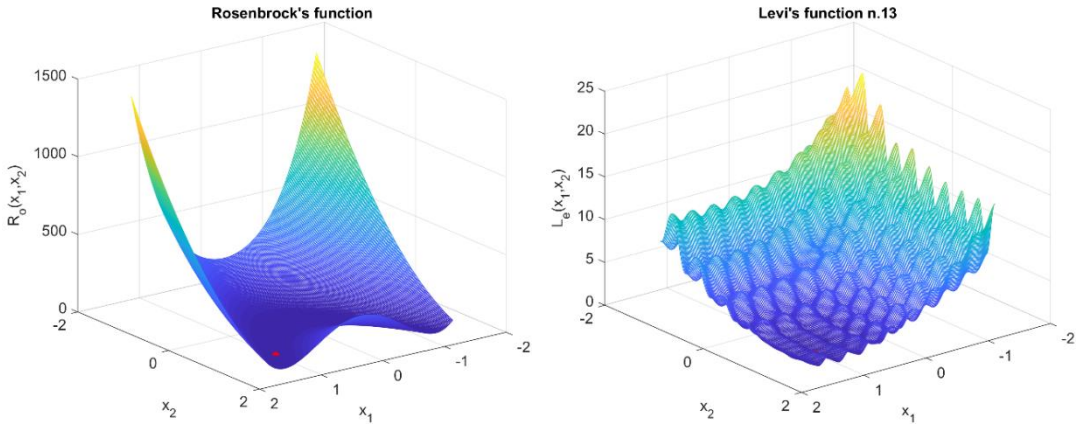

(a) (b)

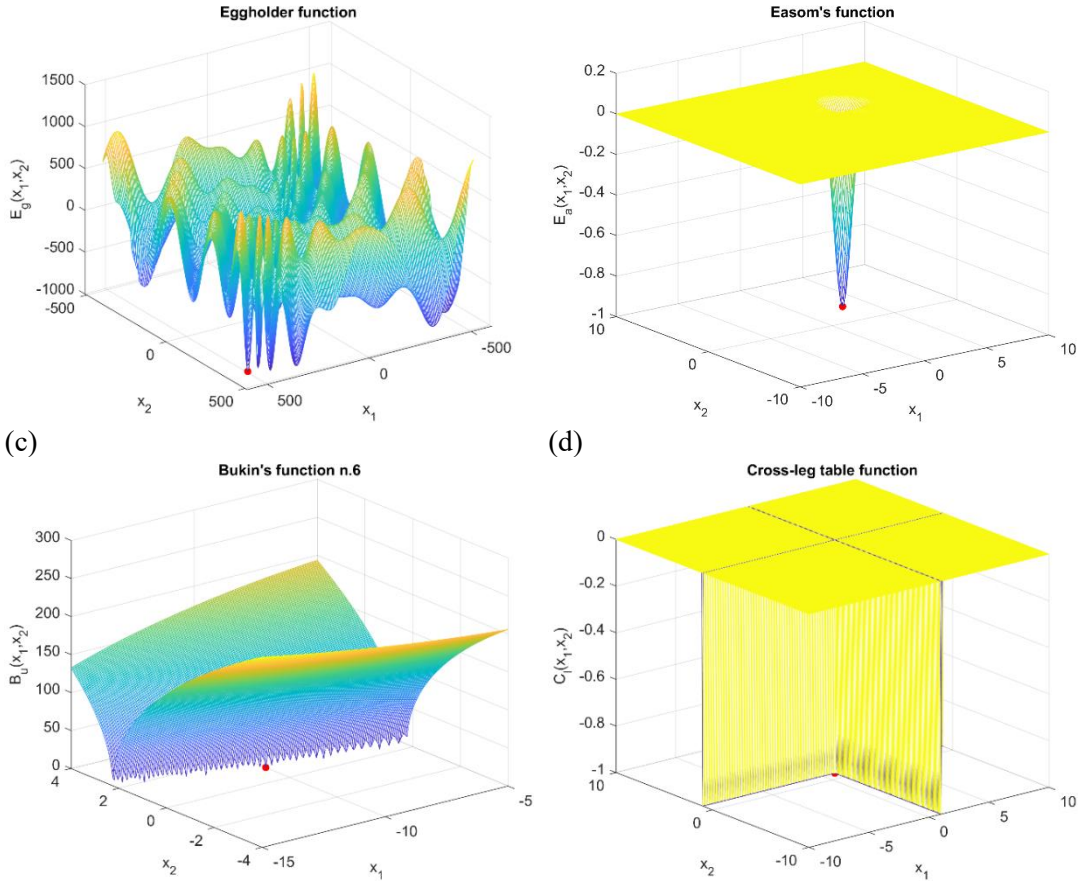

Figure 40: Optimization test functions. The global minimum is depicted by the dot.

Table 2: Optimization tests data.				
Test	$z_{1,e}$	$x_1, x_2\|_{true}$	$x_1, x_2\|_{min}$	$x_1, x_2\|_{max}$
Rosenbrock	0	1, 1	-10, -10	10, 10
Levi	0	1, 1	-10, -10	10, 10
Eggholder	-959.6407	512, 404.2319	-512, -512	512, 512
Easom	-1	π, π	-100, -100	100, 100
Bukin	0	-10, 1	-15, -3	-5, 3
Cross-leg table	-1	1, 1	-10, -10	10, 10

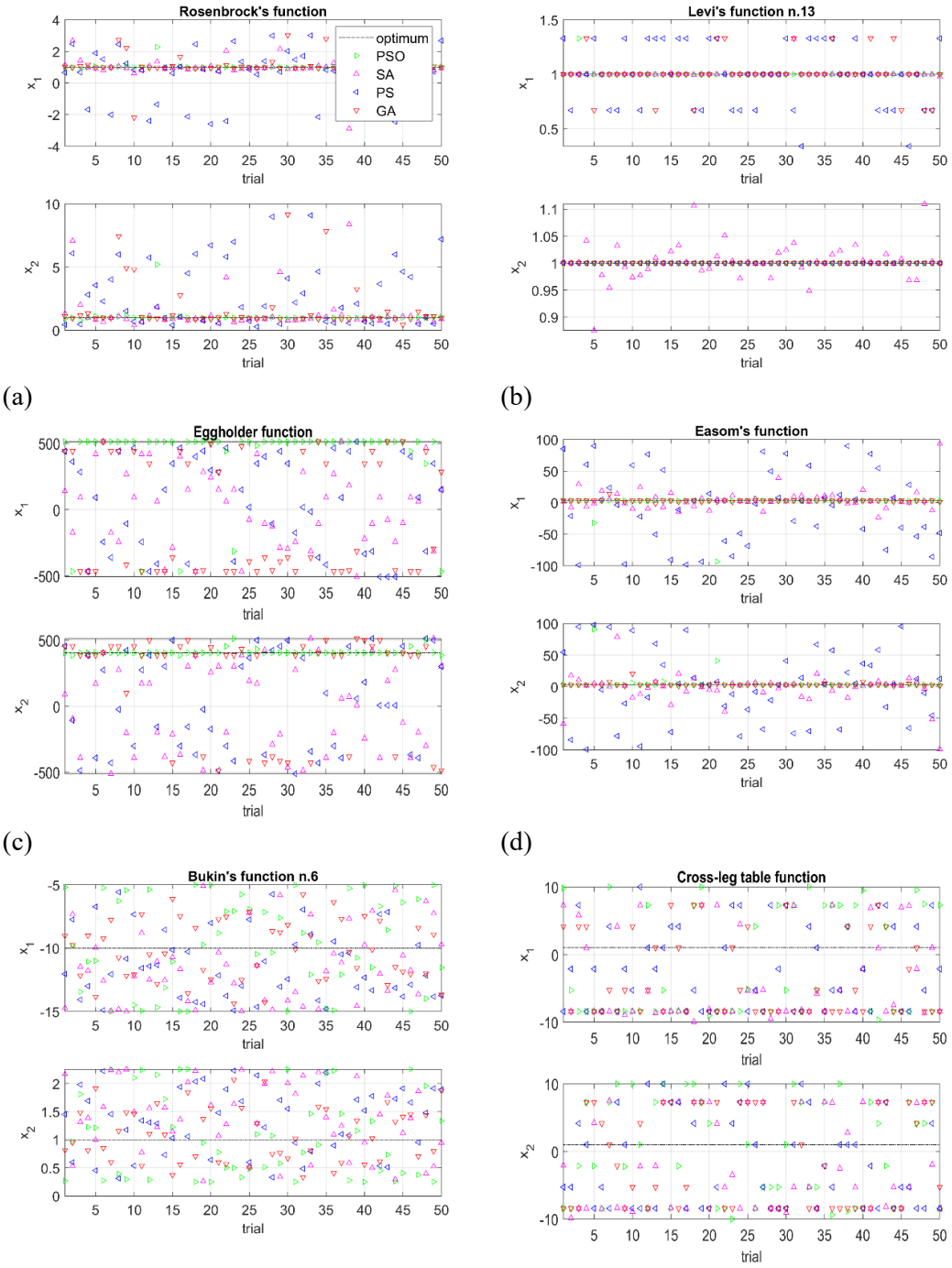

Figure 41: Test results without PL model; values of the parameters to be optimized.

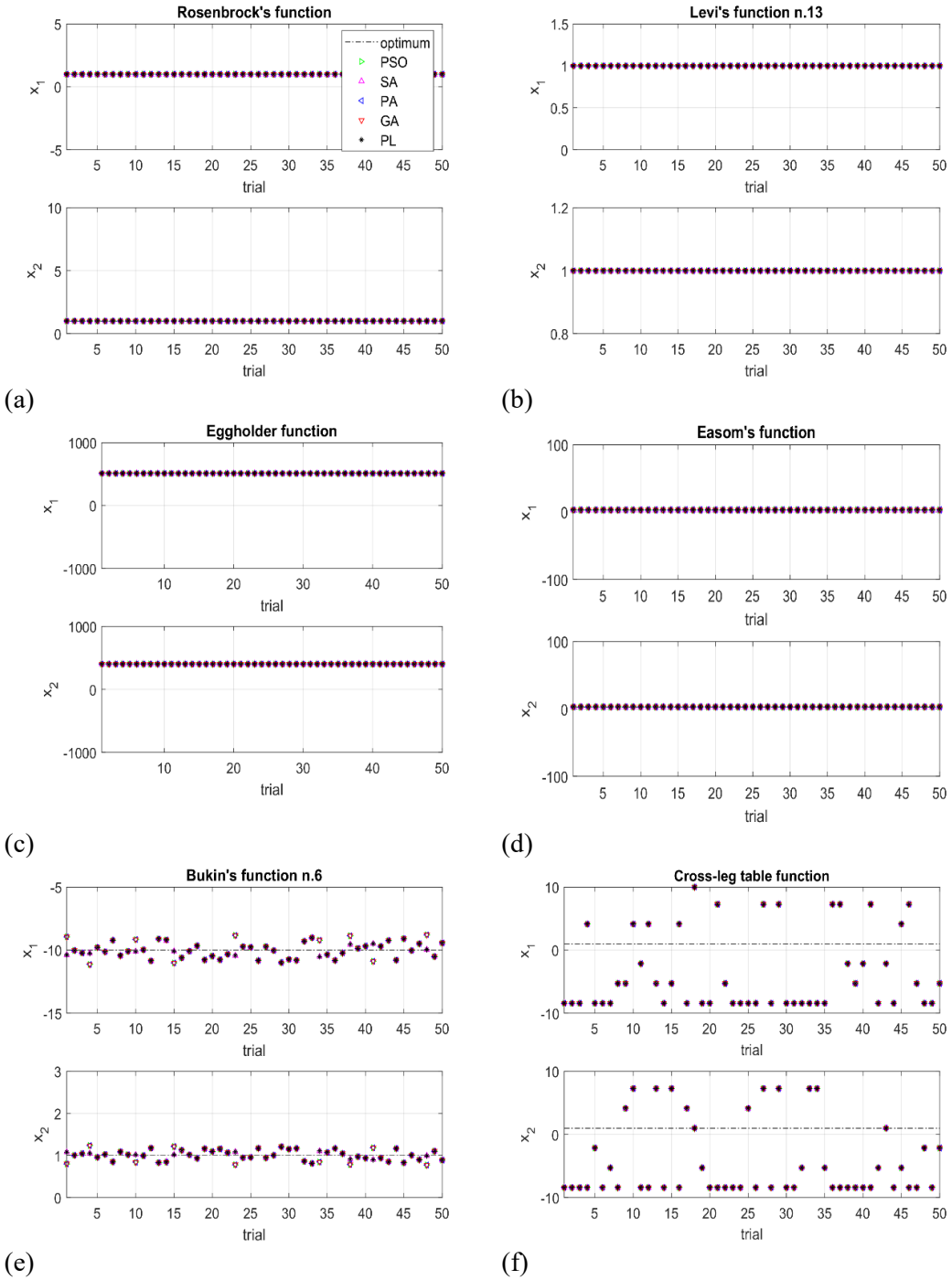

Figure 42: Test results with PL model: values of the parameters to be optimized.

The experimental measurements in this example are supposed to exactly correspond to the global minima of the functions, so that K=1, I=4, and the number of items (i.e. the parameters) is two, x_1 and x_2. For each test, Table 2 reports the experimental measurements (i.e. the global minimum) and the true values of the parameters with the respective searching space. For the optimization tests, the objective function of each solver i is the normalized scatter, $\beta_{k,i}$, between the k-th numerical $z_{k,i}$, and the k-th experimental, $z_{k,e}$, measurement. To compare the results of the optimization, a first study was performed in the absence of the

PL model. For each test function, 1000 trials with random starting points were evaluated. These results, in terms of parameter values are reported in Figure 41, where only the first 50 trials are shown, for brevity's sake. Subsequently, the optimization tests were repeated in the same conditions by introducing the PL model. The results of the optimizations obtained with the PL are reported in Figure 42. The numerical results in terms of efficiency (i.e. number of function evaluations), accuracy (i.e. average normalized scatter between the real and the best values of the parameters found by the solvers), and precision (i.e. standard deviation of the normalized scatter between the real and the best values of the parameters found by the solvers) are instead reported in Table 3, Table 4, Table 5, respectively. In these tables the results with and without the use of the PL model are shown. Specifically, when using the PL model, in addition to the results of each solver, the most likely result among the solvers, for each trial, is also obtained. This led to 1000 additional results from the trials. The column PL in Table 3, Table 4 and Table 5 contains the efficiency, accuracy and precision, respectively, for these 1000 additional results, which are available only in the case of optimization performed with the PL model. Thus, in Table 3, the column PL contains the sum of the values of the other columns, while for Table 4 and Table 5 the column PL does not necessarily contain the *best* results, but rather the accuracy and precision referred to the most likely results, i.e. those minimizing the discrepancies of the values obtained with different solvers, in accordance with the solution of the RA problem. In fact, not always the best result in terms of available experimental measurements reflects the true values of the parameters of a specific model (i.e. *overfitting*). This can also be inferred from Figure 43, where almost the same results in terms of modal data are obtained for very different values of model parameters.

Table 3: Efficiency (number of function evaluations); Average of 1000 trials. *Optimization stopped for a tolerance of the objective function equal to 1E-2 instead of the default value 1E-6.

Test	***Particle Swarm Optimization (PSO)***	***Simulated Annealing (SA)***	***Pattern Search (PS)***	***Genetic Algorithm (GA)***	***Plackett-Luce (PL)***
Without PL					
Rosenbrock	2488	2074	672	9580	
Levi	1094	1858	202	3919	
Eggholder	1077	1955	251	5630	
Easom	1198	1054	103	3713	
Bukin	2129	1823	132	5661	
Cross l-t	2550	1786	187	6026	
With PL					
Rosenbrock	3989	4335	1178	16044	25546
Levi	1517	2870	283	6476	11146
Eggholder	1857	3572	377	9712	15518
Easom	1715	2172	190	6098	10175

Bukin*	4851	9286	598	21538	36273
Cross l-t*	19157	37761	2903	99271	159092

Table 4: Accuracy [%]; Average of 1000 trials. *Optimization stopped at a tolerance of the objective function equal to 1E-2 instead of the default value 1E-6.

Test	***Particle Swarm Optimization (PSO)***	***Simulated Annealing (SA)***	***Pattern Search (PS)***	***Genetic Algorithm (GA)***	***Plackett-Luce (PL)***
Without PL					
Rosenbrock	6.46e0	4.87e1	1.94e2	5.81e1	
Levi	1.65e-1	1.57e0	9.74e0	5.95e0	
Eggholder	1.70e1	9.97e1	9.85e1	7.27e1	
Easom	6.79e1	3.68e2	1.37e3	4.12e1	
Bukin	4.72e1	4.67e1	3.94e1	3.56e1	
Cross l-t	7.43e2	6.84e2	5.98e2	6.77e2	
With PL					
Rosenbrock	5.96e-2	6.63e-2	6.38e-2	3.60e-2	3.20e-2
Levi	3.06e-4	1.24e-3	1.86e-4	1.94e-4	1.63e-4
Eggholder	1.47e-5	3.05e-5	1.17e-5	1.15e-5	1.16e-5
Easom	2.60e-4	2.72e-4	2.62e-4	1.05e-4	1.04e-4
Bukin*	8.78e0	6.79e0	8.78e0	8.78e0	6.79e0
Cross l-t*	7.14e2	7.14e2	7.14e2	7.14e2	7.14e2

Table 5: Precision [%]; Average of 1000 trials. *Optimization stopped at a tolerance of the objective function equal to 1E-2 instead of the default value 1E-6 for time reasons.

Test	***Particle Swarm Optimization (PSO)***	***Simulated Annealing (SA)***	***Pattern Search (PS)***	***Genetic Algorithm (GA)***	***Plackett-Luce (PL)***
Without PL					
Rosenbrock	2.89e1	9.81e1	1.80e2	1.07e2	
Levi	1.64e0	2.52e0	8.96e0	8.82e0	
Eggholder	3.64e1	4.70e1	5.55e1	6.19e1	
Easom	3.32e2	4.99e2	8.64e2	1.84e2	
Bukin	2.60e1	2.61e1	2.37e1	2.17e1	
Cross l-t	1.72e2	1.94e2	1.95e2	1.85e2	
With PL					
Rosenbrock	4.55e-2	4.88e-2	4.69e-2	3.96e-2	3.57e-2
Levi	5.74e-4	7.06e-3	1.51e-4	2.49e-4	2.01e-4
Eggholder	5.45e-5	1.20e-4	6.67e-8	1.18e-6	3.46e-6
Easom	4.24e-4	4.58e-4	4.06e-4	1.12e-4	1.10e-4
Bukin*	5.14e0	4.35e0	5.14e0	5.14e0	4.35e0
Cross l-t*	1.81e2	1.81e2	1.81e2	1.81e2	1.81e2

From the previous results it is possible to note that the use of PL improves the accuracy and the precision of the calibration and, consequently, leads to more reliable results, thanks to the information that each solver takes from the others. On the contrary, the efficiency decreases. However, a parallel session can re-

establish the efficiency (in terms of computational time) to produce values comparable to those of a single solver.

3.3.2. Benchmark FE model

In this subsection the proposed selection strategy is applied to a simple FE model, reported in Figure 43. The FE model is a linear elastic cantilever beam that implements the Timoshenko beam theory. It is discretized in 3 homogeneous portions of 1 m length, each discretized with 10 finite elements, (see Figure 43 for clarity). The cross section is a square section of 0.1x0.1 m. The Young's moduli, E, the densities, ρ, as well as Poisson ratios, υ, are reported in Figure 43. The best values of the objective function, J_i, of each solver i are also reported in Figure 43. J_i is assumed to be:

$$J_i = \frac{1}{K}\sum_{k=1}^{K}\left(z_{k,e} - z_{k,i}\right)^2 \tag{5}$$

where $z_{k,i}$, is the k-th numerical measurement related to the i-th solver, while $z_{k,e}$ is the k-th experimental measurements. For this benchmark problem the number of experimental measurements is K=4: namely the first two frequencies, f_1 and f_2, and the related ideal MAC (two unitary values) between the experimental and numerical modal shapes. The number of solvers is still I=4. The items are instead 3, namely the number of Young's moduli, E, of the FE model. It is assumed that the acceleration is recorded at two points of the model, i.e. the top point and the point at 1/3 of the total length (3 m). Clearly, a reliable optimization process should not involve too many parameters (e.g. Young's moduli) with respect to the number of available experimental data (e.g. number of modes). This is due to the risk of non-optimal solutions in the broadest sense, i.e. solutions that satisfy the experimental data, but with non-physical values of the calibration parameters. However, in order to consider some uncertainty in the calibration process, it is supposed that the experimental response of the point at 2/3 of the beam length is unknown. This leads to difficulty in finding the values of the Young's modulus of the second and third parts of the model (see Figure 43). The values taken as experimental measurements, together with the true values of the parameters and their searching space, are reported in Table 6 and Table 7. The optimization process was set to start from the values in the middle of the searching space. Finally, the scores are assumed to be in accordance with (3) and (4a). In this benchmark problem the optimization was first performed without the PL model. The resulting best values of the objective functions for this situation are reported in Figure 43.

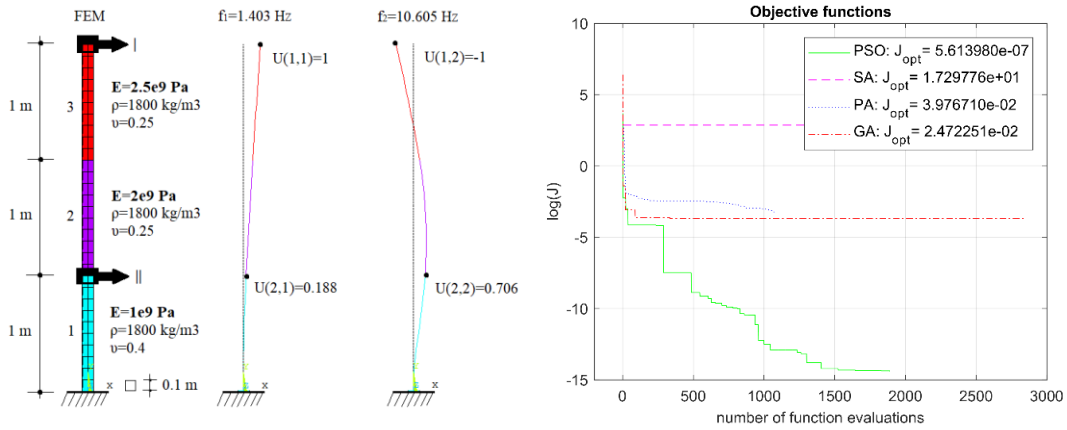

(a) (b)

Figure 43: The FE model: (a) modes that are assumed as experimentally measured; and (b) the objective functions of the solvers.

Table 6: FE benchmark model data: simulated experimental frequencies and MAC.	
K	$z_{k,e}$
1	1.403 [Hz]
2	10.605 [Hz]
3	1
4	1

Table 7: FE benchmark model data: assumed true Young's moduli and boundaries for the optimization.			
Q	$E_q\|_{true}$ ***[Pa]***	$E_q\|_{min}$ ***[Pa]***	$E_q\|_{max}$ ***[Pa]***
1	1e9	1e8	10e9
2	2e9	1e8	10e9
3	2.5e9	1e8	10e9

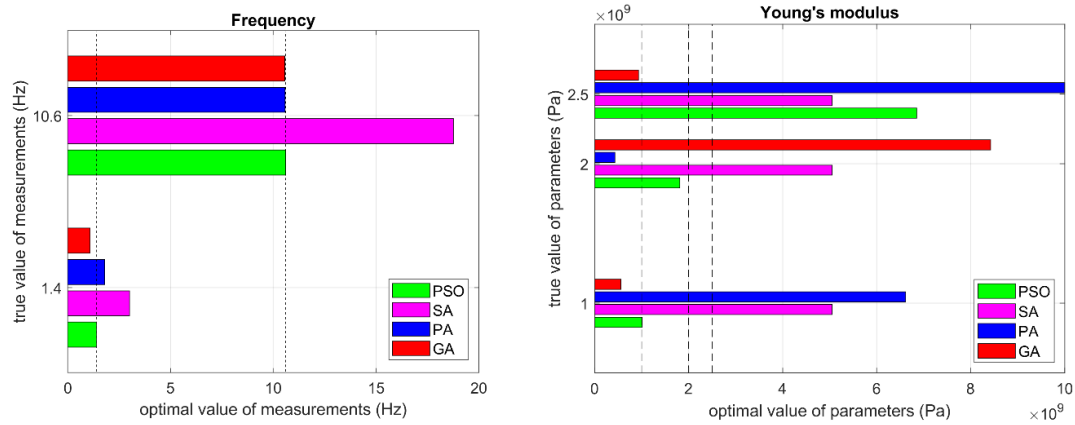

(a) (b)

Figure 44: Results of the calibration without PL model: (a) modal frequencies; and (b) Young's moduli.

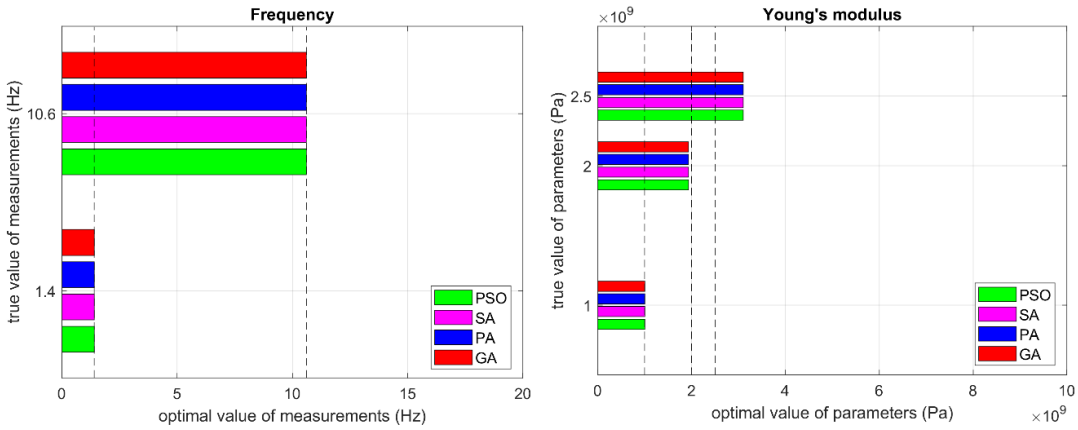

(a) (b)

Figure 45: Results of the calibration with PL model: (a) modal frequencies; and (b) Young's moduli.

Table 8: Numerical values found by the calibrations.

Quantity	***True value***		***PSO***		***SA***		***PS***		***GA***		***PL***
f_1 f_2 [Hz]	1.4	10.61	1.4	10.6	3.0	18.77	1.8	10.58	1.09	1.4	10.6
MAC	1	0.49	1	0.49	1	0.49	1	0.51	0.98	1	0.49
	0.49	1	0.49	1	0.45	1	0.56	0.99	0.62	0.47	1
E_1 [Pa]	1.000e9		1.008e9		5.049e9		6.616e9		0.557e9		1.002e9
E_2 [Pa]	2.000e9		1.814e9		5.049e9		0.429e9		8.423e9		1.938e9
E_3 [Pa]	2.500e9		6.852e9		5.049e9		9.999e9		0.935e9		3.105e9

The results in terms of frequency and Young's modulus without and with PL model are instead represented in Figure 44 and Figure 45, respectively, while the numerical values of the results are reported in Table 8. For the benchmark model, the PL selection was able to reduce the uncertainties of the results, increasing the reliability of the solution. As it can be noted from Figure 45, the third Young modulus still shows some discrepancies from the real value. This is due to the low sensitivity of the model with respect to that parameter. In fact, the middle portion of the model drives the upper one. In addition, it is possible to see that a small error affects the second Young modulus. The influence of this small error on the total cost is thus covered by a value of E_3 very different from the true one. This is the same problem that affects the optimization in absence of the PL model, but, as it can be noted by comparing Figure 44 and Figure 45, the RA strategy was able to reduce it, obtaining a more consistent result in terms of Young's moduli in presence of lack of data (e.g. acceleration response at 2 m from the base).

3.4. Pizzoli Town Hall building

Having established that the PL model can help increasing the reliability of the optimization, the proposed strategy is now applied to a real case study. The aim is to establish a numerical FE model in support of the existing monitoring system installed on the Town Hall building of Pizzoli. Once updated, the FE model can

be used to simulate the linear dynamic response of the building and, by defining some warning indicators, to assess the presence of pathological behaviors of the structure.

Figure 46: A historical postcard showing the Town Hall (on the left) and a current view of the building (on the right).

3.4.1. Description of the building

The Town Hall of Pizzoli is a two-story stone masonry building located northwest of the city of L'Aquila (Abruzzo), which is about 15 km away. The Town Hall, overlooking one of the main piazzas of the town, was built around 1920 and it formerly hosted a school (see Figure 46). The building presents a u-shaped regular plan, mainly distributed along one direction, and its elevations are characterized by regular openings. The building has three levels above the ground (the raised ground floor, the first floor and the under-roof floor) and a basement (see Figure 47 for clarity). The total area is about 770 m^2 while the volume is about 5000 m^3. The main dimensions of the building are reported in Figure 47. Previous investigations have highlighted that the Town Hall presents mixed masonry consisting of unsquared stone blocks, alternated with solid bricks strips. Over the years, the Town Hall has been subjected to various transformations.

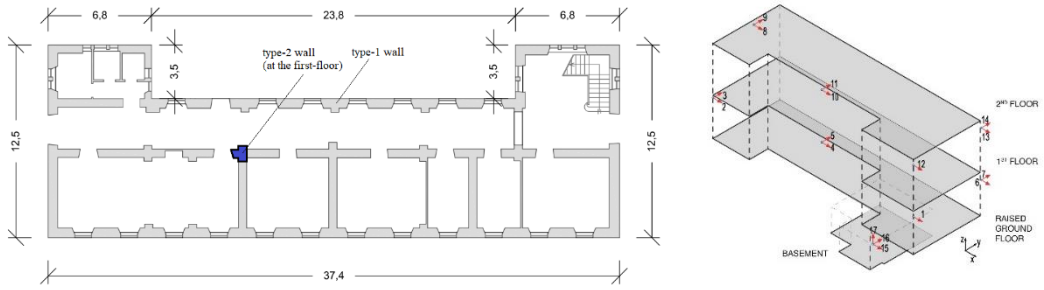

(a) (b)

Figure 47: Town Hall of Pizzoli: (a) the plan of the raised floor reporting the main dimensions (in meters); and (b) scheme of the accelerometers installed on the building (AQ).

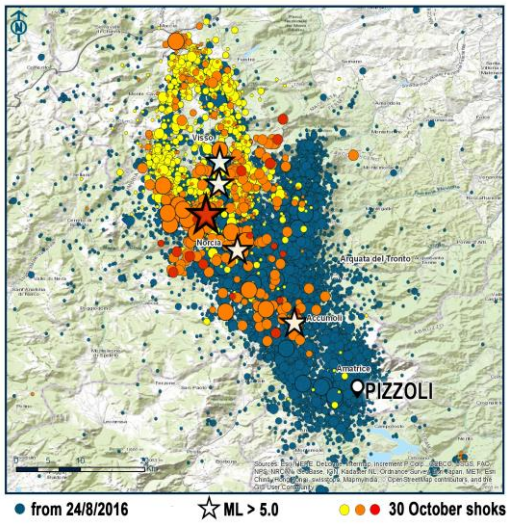

Date	*Time*	*Lat.*	*Lon.*	*ML*
24/08/2016	01:36	42.7	13.23	6
07/09/2016	03:29	42.68	13.29	1.6
26/10/2016	17:10	42.88	13.13	5.4
26/10/2016	19:10	42.91	13.13	5.9
30/10/2016	06:40	42.83	13.11	6.5

Figure 48: Seismic data from INGV.

The original wooden roof was replaced with a reinforced concrete roofing system. Then, an external elevator was attached to the north facade, and stairs in reinforced concrete were added.

The Town Hall of Pizzoli is part of the network of buildings monitored by the Seismic Observatory of Structures (OSS), (Dolce et al., 2017). The seismic acquisition system installed in this building was in operation during the sequence that struck central Italy in 2016. The OSS permanent monitoring system allowed the recording of the seismic response of the Pizzoli Town Hall before and during the recent earthquakes that struck central Italy in August-October 2016. The main shocks of this seismic swarm occurred on 24/8/2016 and 26-30/10/2016. Figure 48 reports the seismic swarm dated 30/10/2016; the star markers identify the epicenters of the main shocks that exceeded 5.0 ML. In the same figure, the main features of the recorded seismic data are summarized: date and time of occurrence, geographical coordinates of the epicenter and Richter magnitude (ML).

3.4.2. Monitoring system

The Town Hall of Pizzoli belongs to the network of strategic buildings monitored by the OSS, which is also responsible for the installed monitoring system. The OSS is a nationwide network founded in the 1990's by the Italian Department of Civil Protection (DPC). The aim of this network is to permanently monitor several strategic Italian buildings (Dolce et al., 2017), (Di Ludovico et al., 2017), (Ceravolo et al., 2017). Indeed, considering the intense seismic activity affecting the Italian territory and the earthquakes that periodically occur (e.g. Umbria-Marche 1997; L'Aquila 2009; Emilia Romagna 2012; Central Italy 2016), studies and investigations on the seismic behavior of civil buildings are

increasingly important. The buildings monitored by the OSS can be divided into two groups: the first group includes 300 buildings monitored by a simplified monitoring system composed of seven accelerometers; the second group, instead, comprises 105 strategic buildings (mainly schools, hospitals and city halls), 10 bridges, and a few dams all equipped with a dynamic permanent monitoring system of about 16-32 accelerometers each. The dynamic monitoring system installed on the Pizzoli Town Hall is composed of 17 accelerometers as can be noted by Figure 47.

3.4.3. Modal identification

This subsection reports the results of the modal identification of the stone masonry structure of the Pizzoli Town Hall. For its extensive use and proven validity, the identification method adopted for the case study is the Subspace State-Space System Identification implemented in the N4SID algorithm, (Van Overschee & De Moor, 1994), (Kim & Lynch, 2012).

Table 9: Identified damping ratio, frequency and modal shape from the records of 2015-July (first 4 modes).

Mode			***1***	***2***	***3***	***4***
ζ [%]			1.08	1.80	2.00	1.25
f [Hz]			4.827	5.835	7.013	9.260
	Channel	Direction				
	1	X	0.0434	0.0592	-0.2867	-0.2591
	2	X	-0.0642	0.1013	-0.2825	0.4018
	3	Y	-0.3629	-0.3631	0.0544	-0.6132
	4	X	0.0079	0.0490	-0.2883	-0.0055
	5	Y	-0.3238	0.0627	-0.0638	0.4341
	6	X	-0.0311	-0.0910	-0.3661	0.1966
U	7	Y	-0.2100	0.3681	-0.0095	-0.4154
	8	X	-0.0148	0.0121	-0.6200	0.1297
	9	Y	-0.5450	-0.4952	-0.0205	-0.7729
	10	X	0.0292	0.1563	-0.8433	0.0124
	11	Y	-1	0.2786	-0.2679	0.9469
	12	X	0.1594	0.1367	-0.8293	-0.7372
	13	X	-0.1204	-0.1424	-1	0.4308
	14	Y	-0.5770	1	-0.0591	-1

The structure is identified from the records of July 2015, thus acquired before the seismic events in central Italy. However, it is worth noting that, at that time, the structure had already been affected by the earthquake of L'Aquila (2009). For the case study, the state space model is estimated by varying the order of the system between 2 to 42 (order step equal to 2) in an input-output time domain identification. Channels 1-14 are used as output signals, while the 3 channels at the base of the building, 15-17, are used as input signals (see Figure 47 for clarity).

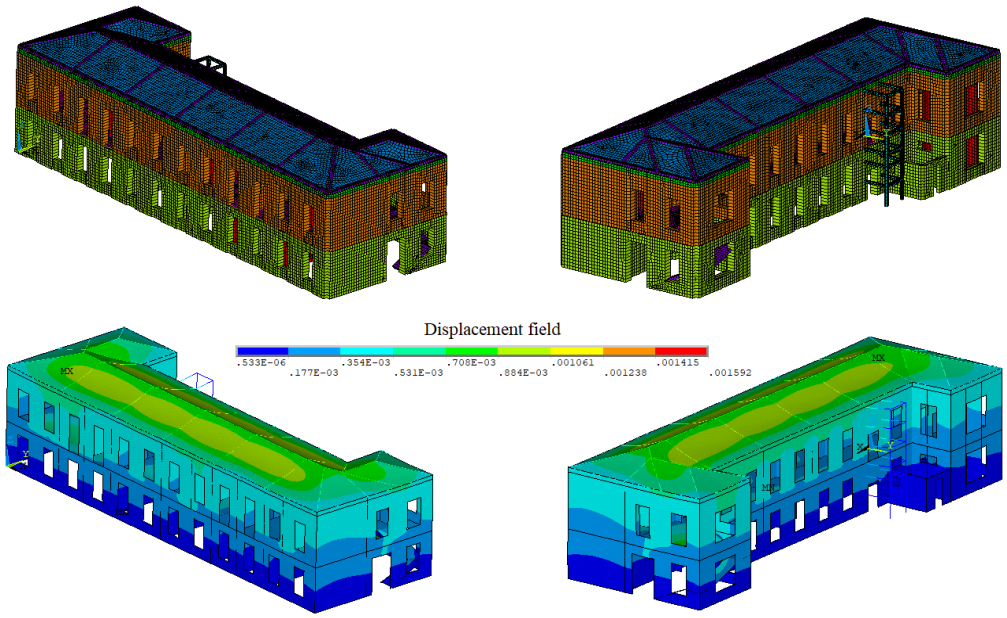

Figure 49: FE model of the Town Hall building of Pizzoli and linear elastic FE analysis considering gravity loads (displacement field in meters).

The modes are accepted only if the value of the estimated damping is within the limits 0.9-5.5 %. Then the optimal order, n=28, is selected through clustering operations in the frequency-damping plane. The identified values of the damping ratio, ζ, frequency, f, and modal shapes, **U**, are reported in Table 9 for the first 4 modes. The experimental frequencies and modal shapes are used to calibrate the FE model of the structure.

Table 10: Geometric quantities, between the center of the cross section of the component of the FE model (Town Hall of Pizzoli).

Description of the component	***Dimension [m]***
Height of the ground raised floor walls	4.00
Height of the first-floor walls	4.50
Upper height of the windows	3.30
Bottom height of the windows	0.85
Average width of the windows	1.20
Height of external doors	3.30
Average width of external doors	1.95
Upper height of the internal windows	1.85
Bottom height of the internal windows	0.85
Average height of internal doors	2.40
Average width of internal doors	1.15
Height of the first stairway landing	1.40
Height of the second stairway landing	2.70
Width of the stairway landings	1.30
Height of the under-roof floor walls	0.35
Height of the top truss of the roof	1.50
Height of the attached masonry room	2.60
Width of the attached masonry room: X / Y	2.95 / 3.50
Height of the 1st, 2nd, 4th, 5th, 6h “inter-story” of the elevator frame	1.50

Height of the 3rd “inter-story” of the elevator frame	1.00
Width of the elevator frame: X / Y	1.90 / 2.30
Height of the elevator doors and the attached masonry room door	2.20

3.4.4. FE model

For the FE modelling of the Town Hall building of Pizzoli (Figure 49), two element types are used: a 2-node beam element, which implements the Timoshenko theory, is used for the reinforced concrete beams and the steel beams of the elevator frame; a 4-node thick shell element with bilinear shape functions is used for the slabs and the masonry walls. A spring element is also used to model the uncertainties of the geometry and materials below the mezzanine floor (boundary conditions). The numerical model has 52369 nodes for a total number of 53919 elements. The average dimension of each element is about 0.25 m for both the shell and beam elements. For the raised ground floor, the average thickness of the external and internal walls can be set equal to 0.63 and 0.54 m, while for the first floor the same average quantities are 0.60 and 0.50 m, respectively. The actual values used for the simulation are set in accordance with the data obtained from a direct survey. The thickness of the portion of the walls located below the windows is 0.41 m (except for the area in which the stairs are situated, for which the thickness is equal to that of the wall above), while the thickness of the infill walls is set at 0.1 m. The cross-section dimensions are as follows: a rectangular section of 0.35x0.30 m (depth x width) for the reinforced concrete beams and a square hollow steel beam section of 0.18x0.18 m, 0.004 m thick, for the elevator frame. The stairs are modelled as 0.20 m thick plate. The equivalent thicknesses of the raised ground, first, under-roof floor, and the roof plate are assumed to be 0.22, 0.22, 0.16, 0.22 m, respectively, in accordance with the inspection. Other geometric quantities are reported in Table 10, while Table 11 contains the values initially assumed for the elastic parameters of the materials, in accordance with the data available from the survey. The static displacements field due to gravity loads is then illustrated in Figure 49.

Table 11: Initial linear elastic parameters of the FE model (Town Hall of Pizzoli). The values updated during the calibration are marked with an asterisk “*”.

Id.	***Description***	***E [Pa]***	***ρ [kg/m^3]***	***υ***
1	Steel	210e9	7850	0.27
2	Concrete	30e9	2500	0.25
3	Perforated bricks masonry (infill walls)	4.5e9	1500	0.30
4	Hollow blocks floor (roof)	13e9	1914	0.30
5	Hollow blocks floor with steel beam (under-roof)	25e9	2063	0.30
6	Full bricks masonry (type-2 and under-roof walls)	1.5e9	1800	0.30
7	Stone masonry (type-1 first floor)	2.8e9*	2200	0.30
8	Hollow blocks floor with steel beam (raised ground and first floor)	25e9	2082	0.30

9	Stone masonry (type-1 raised ground floor)	2.8e9*	2200	0.30
10	Spring in Y, imposed at the raised ground floor level	5e7*	K_Y [N/m]	
11	Spring in X, imposed at the raised ground floor level	5e7*	K_X [N/m]	

3.4.5. Selection of the best candidate

For the FE model updating of the Pizzoli Town Hall, the objective functions of the I=4 solvers are described by (5), where K=8 is the number of normalized scatters between the experimental and numerical frequencies and the number of ideal MAC between the experimental and numerical modal shapes. The scores are still modelled as described by (3) and (4a). In this first updating of the structure we are interested in the soil–structure interaction. In fact, while for the superstructure the availability of data from direct survey allows a certain level of confidence in the values assumed for the geometry and materials, for the portion of the structure connected to the ground some uncertainties remain.

The main uncertainty is related to the shape of the foundation and, thus, to the depth of the portion of the building under the raised ground floor, particularly for the inner walls of the building (the depth is in the range of 0.4-0.8 m for the external walls). To model these uncertainties two spring systems with different stiffnesses are imposed at the raised floor level, in the two horizontal directions (X and Y). In the vertical direction, Z, a rigid constraint is assumed. Since many uncertainties are present in the Young's modulus value of the stone masonry as well, in this updating the parameters of the optimization are assumed to be the Young's moduli of the raised ground and first floor walls of the building, as well as the stiffness of the two spring systems. This choice was also validated by performing a sensitivity analysis, which confirmed that the frequencies are very sensitive to a variation of the chosen moduli and stiffness. In this situation the number of items, Q, of the calibration is 4. The experimental measurements, together with the starting values of the parameters and their searching space are reported in Table 12 and Table 13. In Figure 50, instead, the first 4 updated numerical modal shapes are depicted, while the numerical values of the results in terms of frequencies (with the related errors), MAC and optimal values of the parameters are reported in Table 14.

Table 12: FE model updating; experimental frequencies and MAC.

k	$z_{k,e}$
1	4.827 [Hz]
2	5.835 [Hz]
3	7.013 [Hz]
4	9.260 [Hz]
5	1
6	1
7	1
8	1

Table 13: FE model updating data: starting values and boundaries for the optimization.			
q	***Starting values***	***Lower bound***	***Upper bound***
1, E_7	2.8e9 [Pa]	1.2e9 [Pa]	5e9 [Pa]
2, E_9	2.8e9 [Pa]	1.2e9 [Pa]	5e9 [Pa]
3, K_Y	5e7 [N/m]	1e7 [N/m]	9e7 [N/m]
4, K_X	5e7 [N/m]	1e7 [N/m]	9e7 [N/m]

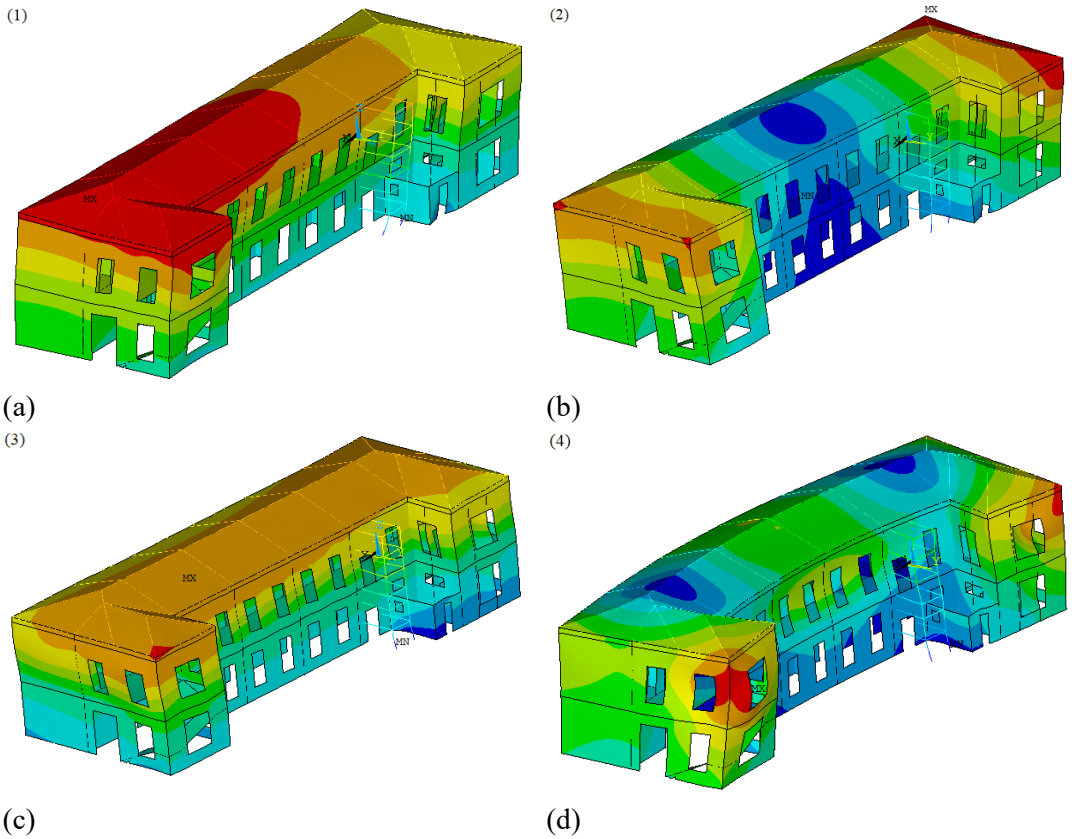

Figure 50: Updated numerical modal shapes: (a) 1st bending Y; (b) 1st torsional Z; (c) 1st bending X; and (d) 2nd torsional Z.

Table 14: Numerical results found by the calibrations with PL selection.												
Quantity	***Experimental values (exp.)***				***Numerical initial values (num.)***				***Numerical final values (num.)***			
$f_1\ f_2\ f_3\ f_4$ [Hz]	4.83	5.84	7.01	9.26	5.45	5.96	6.52	10.28	4.86	5.32	6.79	10.01
$\lvert f_{exp}-f_{num}\rvert / f_{exp}$	0	0	0	0	0.13	0.02	0.07	0.11	0.01	0.09	0.03	0.08
MAC	1.00	0.08	0.01	0.00	0.91	0.02	0.00	0.01	0.91	0.00	0.00	0.00
	0.08	1.00	0.02	0.02	0.14	0.78	0.08	0.02	0.03	0.89	0.02	0.02
	0.01	0.02	1.00	0.00	0.01	0.01	0.84	0.00	0.01	0.00	0.93	0.00
	0.00	0.02	0.00	1.00	0.05	0.01	0.00	0.90	0.05	0.02	0.00	0.93
E_7, E_9 [Pa] K_Y, K_X [N/m]	Unknowns				2.800e9, 2.800e9 5.000e7, 5.000e7				1.416e9, 4.435e9 2.559e7, 6.345e7			

The results of the application to the Town Hall building of Pizzoli can be summarized as follows:

- The overall modal quantities (i.e. frequencies and modal shapes) tend to satisfactorily approach the experimental values, with an average error of 5.25 % for the frequencies, and 8.50 % for the MAC, ensuring a more realistic response of the model in the case of dynamic analysis;
- The stiffness of the springs turned out to be higher in the X direction than in the Y direction, in accordance with the greater stiffness of the foundation walls in the X direction;
- The Young's modulus of the walls at the raised floor was attributed by PL a higher value than that of the higher floor. This may be due to: (i) a different composition of the masonry for the walls of the higher floor in comparison with the walls of the ground raised floor; (ii) the presence of damage in the first-floor walls (due to the 2009 earthquake of L'Aquila). In order to differentiate the two cases, records prior to the earthquake of L'Aquila (2009) would be required. Another explanation, which should be always considered in inverse problems, can be found in the challenge of properly representing the deformability and inertia of the basement level, challenge that is always present when dealing with structures like this Town Hall.

To conclude, in this chapter the use of combinatorial optimization methods has been investigated in order to establish a reference numerical model to support monitoring activities, as typically required by the seismic observatories of structures. In order to test the effectiveness of the combinatorial selection, based on a Plackett-Luce rank aggregation, the strategy was first applied to several well-known test functions, giving satisfactory results. The same procedure was then conducted on an FE benchmark problem. The PL selection has proven to be an effective tool to increase the accuracy and the precision of the solution, while at the same time producing more reliable results. In order to demonstrate the strategy on real dynamic monitoring data, the FE calibration of the Town Hall building of Pizzoli was carried out following 4 different optimization criteria: PSO, SA, PS and GA. The results of the optimization were recursively treated, using a combinatorial strategy, by solving the RA problem with the PL model. Because of the high uncertainty, the calibration involved soil-structure interaction parameters, representing the part of the structure below the raised floor, and the Young's moduli of the masonry walls. After the optimization and ranking procedure, the numerical modal quantities (i.e. frequencies and modal shapes) fit the experimental ones with an average error of 5.25 % for the frequencies, and 8.50 % for the MAC.

It is worth highlighting that the rank aggregation strategy can also be used in the selection of the best optimization parameters of a specific model updating algorithm,

a concept broadly known as meta-optimization, or even to perform multi-objective optimizations.

3.5. References chapter 3

Aledo, J. A., Gámez, J. A., & Molina, D. (2013). Tackling the rank aggregation problem with evolutionary algorithms. Applied Mathematics and Computation, 222, 632-644.

Aledo, J. A., Gámez, J. A., & Molina, D. (2017). Tackling the supervised label ranking problem by bagging weak learners. Information Fusion, 35, 38-50.

Andoni, A., Fagin, R., Kumar, R., Patrascu, M., & Sivakumar, D. (2008, June). Corrigendum to efficient similarity search and classification via rank aggregation by Ronald Fagin, Ravi Kumar and D. Sivakumar (proc. SIGMOD'03). In Proceedings of the 2008 ACM SIGMOD international conference on Management of data (pp. 1375-1376). ACM.

Audet, C., & Dennis Jr, J. E. (2002). Analysis of generalized pattern searches. SIAM Journal on optimization, 13(3), 889-903.

Bassoli, E., Vincenzi, L., D'Altri, A. M., de Miranda, S., Forghieri, M., & Castellazzi, G. (2018). Ambient vibration-based finite element model updating of an earthquake-damaged masonry tower. Structural Control and Health Monitoring, 25(5), e2150.

Beggs, S., Cardell, S., & Hausman, J. (1981). Assessing the potential demand for electric cars. Journal of econometrics, 17(1), 1-19.

Boscato, G., Russo, S., Ceravolo, R., & Fragonara, L. Z. (2015). Global sensitivity-based model updating for heritage structures. Computer-Aided Civil and Infrastructure Engineering, 30(8), 620-635.

Bursi*, O. S., Kumar, A., Abbiati, G., & Ceravolo, R. (2014). Identification, model updating, and validation of a steel twin deck curved cable-stayed footbridge. Computer-Aided Civil and Infrastructure Engineering, 29(9), 703-722.

Cao, Z., Qin, T., Liu, T. Y., Tsai, M. F., & Li, H. (2007, June). Learning to rank: from pairwise approach to listwise approach. In Proceedings of the 24th international conference on Machine learning (pp. 129-136). ACM.

Ceravolo, R., Matta, E., Quattrone, A., & Zanotti Fragonara, L. (2017). Amplitude dependence of equivalent modal parameters in monitored buildings during

earthquake swarms. Earthquake Engineering & Structural Dynamics, 46(14), 2399-2417.

Ceravolo, R., Pistone, G., Fragonara, L. Z., Massetto, S., & Abbiati, G. (2016). Vibration-based monitoring and diagnosis of cultural heritage: a methodological discussion in three examples. International Journal of Architectural Heritage, 10(4), 375-395.

Di Ludovico, M., Digrisolo, A., Graziotti, F., Moroni, C., Belleri, A., Caprili, S., ... & Ferracuti, B. (2017). The contribution of ReLUIS to the usability assessment of school buildings following the 2016 central Italy earthquake. Bollettino di Geofisica Teorica ed Applicata, 58(4).

Dolce, M., Nicoletti, M., De Sortis, A., Marchesini, S., Spina, D., & Talanas, F. (2017). Osservatorio sismico delle strutture: the Italian structural seismic monitoring network. Bulletin of Earthquake Engineering, 15(2), 621-641.

Dwork, C., Kumar, R., Naor, M., & Sivakumar, D. (2001, May). Rank aggregation methods for the web. In Proceedings of the 10th international conference on World Wide Web (pp. 613-622). ACM.

Fagin, R., Kumar, R., & Sivakumar, D. (2003, June). Efficient similarity search and classification via rank aggregation. In Proceedings of the 2003 ACM SIGMOD international conference on Management of data (pp. 301-312). ACM.

Goldberg, D. E. Genetic Algorithms in Search, Optimization, and Machine Learning, New York: Addison-Wesley, 1989.

Gormley, I. C., & Murphy, T. B. (2005). Exploring Irish election data: A mixture modelling approach. Technical Report 05/08.

Guiver, J., & Snelson, E. (2009, June). Bayesian inference for Plackett-Luce ranking models. In proceedings of the 26th annual international conference on machine learning (pp. 377-384). ACM.

Hu, J., Lam, H. F., & Yang, J. H. (2018). Operational modal identification and finite element model updating of a coupled building following Bayesian approach. Structural Control and Health Monitoring, 25(2), e2089.

Hunter, D. R. (2004). MM algorithms for generalized Bradley-Terry models. The annals of statistics, 32(1), 384-406.

Ingber, L. (2000). Adaptive simulated annealing (ASA): Lessons learned. arXiv preprint cs/0001018.

Joachims, T., Li, H., Liu, T.-Y. and Zhai, C. (2007). Learning to rank for information retrieval. in Acm Sigir Forum, vol. 41, pp. 58–62, ACM.

Kennedy, J. and Eberhart, R. (1995). Particle swarm optimization. In Proceedings of ICNN'95 - International Conference on Neural Networks, vol. 4, pp. 1942–1948 vol.4, Nov.

Kim, J., & Lynch, J. P. (2012). Subspace system identification of support-excited structures—part I: theory and black-box system identification. Earthquake engineering & structural dynamics, 41(15), 2235-2251.

Luce, R. D. (2012). Individual choice behavior: A theoretical analysis. Courier Corporation.

Marden, J. I. (2014). Analyzing and modeling rank data. Chapman and Hall/CRC.

Matlab (2018). The MathWorks, Natick, MA, USA2018a.

Minka, T. (2004). Power ep. Dep. Statistics, Carnegie Mellon University, Pittsburgh, PA, Tech. Rep.

Minka, T. (2005). Divergence measures and message passing. Technical report, Microsoft Research.

Mishra, S. K. (2006). Some new test functions for global optimization and performance of repulsive particle swarm method.

Plackett, R.L. (1975). The analysis of permutations. Applied Statistics, pp. 193–202.

Sun, H., & Betti, R. (2015). A hybrid optimization algorithm with Bayesian inference for probabilistic model updating. Computer-Aided Civil and Infrastructure Engineering, 30(8), 602-619.

Sun, W., & Yuan, Y. X. (2006). Optimization theory and methods: nonlinear programming (Vol. 1). Springer Science & Business Media.

Van Overschee, P., & De Moor, B. (1994). N4SID: Subspace algorithms for the identification of combined deterministic-stochastic systems. Automatica, 30(1), 75-93.

Yasutake, S., Hatano, K., Takimoto, E., & Takeda, M. (2012, November). Online rank aggregation. In Asian Conference on Machine Learning (pp. 539-553).

Zhang, F. L., Ni, Y. C., & Lam, H. F. (2017). Bayesian structural model updating using ambient vibration data collected by multiple setups. Structural Control and Health Monitoring, 24(12), e2023.

Chapter 4

Calibration of nonlinear and hysteretic models

In this chapter, the identification of a non-linear and hysteretic system is performed with the help of equivalent grey-box models. Firstly, the methodology for the estimate of the model parameters in time and frequency domain is described. The basis functions of in-series mass lumped Multi-DoFs (MDoFs) models with Bouc-Wen type behaviour are derived for an easy implementation both in time-frequency, time and scalar domain. An integral form of the derivate of the restoring force function is used for this purpose. The differential form (i.e. identification based on the jerk of the system) is instead reported in appendix. Then, to test the effectiveness of the tuning of the hysteretic laws, different optimization algorithms are explored, performing the optimization using time-frequency distribution of experimental records. The advantage in using time-frequency transforms lies in the fact that the optimization process can benefit from the joint representation in both time and frequency domains, making the calibration less inclined to local minima. In addition, these methods allow instantaneous estimates of the model parameters, enabling numerous actions such as the assessment of the parameter during seismic events, for example by the definition of damage indices, or assessing the stability of the parameter values in time, i.e. the feasibility of the use of a specific parameter in the chosen model. Moreover, time-frequency approaches applied in combination with quasi-direct methods are computationally efficient, which turns to be useful when dealing with large scale models as those for complex historical buildings. In this work, starting from the results of the calibration process a damage index based on the degrading stiffness of the system and the instantaneous frequencies has been defined.

4.1. Introduction

Masonry buildings are particularly affected by earthquakes even for low values of peak ground acceleration. However, huge masonry buildings can host, immediately after a seismic event, a big amount of people. Cleary this can be done just if the structure after the seismic event can be considered safe. For this reason, damage indicators can help to define the degree of damage in the structure allowing to make a quick decision on the use of a specific building immediately after the quake. The estimate of the damage can be done by identifying non-linear models that can be used to approximate the system behaviour. In this regard, the identification of hysteretic degrading systems subject to nonstationary loading is a fundamental topic, especially for masonry structures that commonly undergo nonlinear and nonstationary behaviour. Among several models that can be used to simulates hysteretic systems, the Bouc-Wen (BW) type models, e.g. (Bouc, 1971), (Wen, 1976) and (Baber & Wen, 1981) have proved to be very flexible in this, also even though they received some criticism regarding the ability to describe the phenomenon of hysteresis in a very accurate way (Ikhouane & Rodellar, 2005).

More in general, the identification methods for nonlinear systems can be classified in two big families: (i) parametric and (ii) non-parametric methods, (Worden, 2001). In parametric methods, like in the BW type models, the nonlinearities are modelled with a well-defined function, with parameters used to describe the system. For this reason, parametric models can be applied just to systems that approximately follow the chosen model. If this is true, they can be used also in presence of strong nonlinearities and complex behaviours. On the opposite, non-parametric methods, like polynomial models, do not require any assumption on the type of structural nonlinearity, but commonly, the identified quantities cannot be directly correlated to the equations of motion as in the case of parametric models. As regards the works on the identification of parametric models, (Chassiakos, 1995), (Smyth, 2000) and (Smyth, 2002) proposed a method in which the parameters of the BW model are identified through an adaptive procedure, based on the least square techniques, while, (Kyprianou, 2001) introduced a *differential evolutive* method. Instead, more recently, (Ashrafi, 2008), proposed an identification technique for hysteretic systems with degradation. As regard non-parametric models, the classical methods are based on the extensions of the restoring force surface method, (Masri, 1979), which, briefly, represents the system restoring force in terms of polynomial series. In this regard, (Benedettini, 1995), approximated the surface of the time derivative of the internal restoring force of a SDoF on a polynomial basis, by assuming as state variables the force itself and velocity. (Masri, 2004) extended this approach by proposing a polynomial base approximation of the restoring force for a SDoF as a function of velocity, displacement and the external excitation. Always in the frame of non-parametric approaches, (Pei, 2004), used a special type of neural

network, which showed good performances in the identification of hysteretic systems.

Another big classification of the identification methods for non-linear systems is based on the domain in which the identification is performed, i.e.: (i) time domain methods, and (ii) time-frequency domain methods, (Ceravolo, 2010), (Hammond, 1996) and (Carmona, 1998). The idea underlying time-frequency identification techniques is that, for certain classes of structural response signals, the availability of a limited number of experimental data can be partially obviated by taking into account the localization in time of the frequency components of the signals, see for example the work of (Ceravolo & Molinari, 2001), (Ceravolo, 2004), (Ceravolo & Erlicher, 2007), (Ceravolo, 2009) and (Pai & Langewisch, 2008). Both time, and time-frequency domain methods can be used to perform an instantaneous estimate of the parameters. This can help when a model is not able itself to reproduce the structural response (e.g. because the raised non-linearity can change the non-linear behaviour of the system). The instantaneous estimate of the parameters can be then used to check the consistency of a given model by assessing the stability of the parameters value in time, (Ceravolo, 2013). In this regard, when a structural system subject to earthquake loading exhibits degradation or behaves as time variant, instantaneous estimation techniques should be preferred. Among instantaneous-based identification techniques that operate in the time domain, works worth of noting are for example the approach of (Smyth, 1999), where an extended Kalman filter is applied to a state-space representation of the equations of motion. Along the same lines, (Wu & Smyth, 2008) employed the unscented Kalman filter technique, which can treat more general non-linearity. The idea behind the unscented Kalman filter is that it is easier to approximate a probability distribution than to approximate an arbitrary non-linear function or transformation. Similarly, (Spiridonakos, 2010) and (Du & Wang, 2010) employed families of autoregressive moving average models.

Despite the big amount of literature available about the non-linear identification, see for example the text of (Worden, 2001) for reference, seams that these works did not find their way into the realm of applications. In fact, there is a paucity of papers that apply these or similar techniques to full-scale Multi Degree of Freedom (MDoF) systems and/or scaled-down structures (Bursi, 2012). About this topic, (Bursi, 2009) tried to identify a full-scale two-story two-bay steel concrete composite structure. (Hernandez-Garcia, 2010) analysed a test specimen made of a 4-DoF system. (Loh, 2010) considered a one-story two-bay reinforced concrete frame. Finally, (Ma, 2006) studied wood joints made of plywood gusset plates.

In the present chapter, a quasi-direct instantaneous identification technique with Short (Fast) Fourier Transform (SFFT) of the records is adopted for the nonlinear identification. The choice of the time-frequency technique was made because of its robustness, that is, its capability to clearly identify both signal events that manifest during a short time interval (time localization) and signal

components, which are concentrated at frequencies, such as sinusoids (frequency localization). Instead, the choice of the quasi-direct method was made to reduce the number of parameters to be identified with algorithms, by restricting this estimate to just the exponential parameters of the Bouc-Wen type model of hysteresis. Starting from the evolution of the system's stiffness, an instantaneous damage index has been defined to provide promptly information about the health of the structure immediately after a seismic event, allowing to manage the post-event. The main point of this study is the definition of a procedure to perform an instantaneous hysteretic identification of MDoF systems, in order to provide information on the progressive health state degradation of monitored systems, with particular attention on architectural heritage buildings.

4.2. Method

In this section, the methodology used for the non-linear identification of the seismic damage in lumped mass systems is discussed. It is assumed for hypothesis that the responses in the two horizontal directions are uncoupled, allowing in this way an independent analysis in X and Y.

4.2.1. Nonlinear system identification using Time-Frequency Distribution (TFD)

We assume to approximate the experimental record, ${}^{d}\boldsymbol{n}_{e}(t)$, of a general Degree of Freedom (DoF) *d* in the following form:

$$ {}^{d}\boldsymbol{n}_{n}(t) = \sum_{i=1}^{{}^{d}I} {}^{d}p_{i} \cdot {}^{d}\boldsymbol{n}_{i}(t) \cong {}^{d}\boldsymbol{n}_{e}(t) \tag{6}$$

Where, ${}^{\boldsymbol{d}}\boldsymbol{n}_{\boldsymbol{n}}(\boldsymbol{t})$, is the numerical approximation of the record, ${}^{\boldsymbol{d}}\boldsymbol{p}_{\boldsymbol{i}}$ is the *i*-th system parameter to be identified, ${}^{\boldsymbol{d}}\boldsymbol{n}_{\boldsymbol{i}}(\boldsymbol{t})$, are basis functions and ${}^{\boldsymbol{d}}\boldsymbol{I}$ is the total number of basis functions used to approximate the *d*-th experimental record; finally *t* denotes the time. (6), likewise in (Masri, 2004), represents an expansion of the experimental records. The goal of this section is to find in an efficient way the parameters, ${}^{\boldsymbol{d}}\boldsymbol{p}_{\boldsymbol{i}}$, for a general DoF by using a linear TFD operator, $\boldsymbol{T}(\cdot)$, allowing in this way instantaneous estimate of their values. For this reason, can rewrite (6) as:

$$ T\left({}^{d}n_{n}(t)\right) \cong T\left({}^{d}n_{e}(t)\right) \tag{7}$$

$$ {}^{d}E(f,t;\,{}^{d}p) = T\left({}^{d}n_{n}(t)\right) - T\left({}^{d}n_{e}(t)\right) \tag{8}$$

In (8), ${}^{d}\boldsymbol{p}$, denotes the vector of the unknow parameters for the DoF d. Because the assumption of linear TFD one can write the TFD of the errors, ${}^{d}\boldsymbol{E}(f,t;\,{}^{d}\boldsymbol{p})$ as:

$$ {}^{d}\boldsymbol{E}(f,t;\,{}^{d}\boldsymbol{p}) = T\big({}^{d}\boldsymbol{n}_n(t) - {}^{d}\boldsymbol{n}_e(t)\big) \tag{9}$$

then:

$$ {}^{d}\boldsymbol{W}(f,t;\,{}^{d}\boldsymbol{p}) = \left\| {}^{d}\boldsymbol{E}(f,t;\,{}^{d}\boldsymbol{p})\right\|_2^2 = Re^2\big[{}^{d}\boldsymbol{E}(f,t;\,{}^{d}\boldsymbol{p})\big] + Im^2\big[{}^{d}\boldsymbol{E}(f,t;\,{}^{d}\boldsymbol{p})\big] \tag{10}$$

where ${}^{d}\boldsymbol{W}(f,t;\,{}^{d}\boldsymbol{p})$ is the norm-2 squared of the TDF of the errors that need to be minimised, for example using least-squares methods. Replacing (6) in (9) and recalling the linearity of $T(\cdot)$:

$$ {}^{d}\boldsymbol{E}\big(f,t;\,{}^{d}\boldsymbol{p}\big) = \sum_{i=1}^{d_I} {}^{d}p_i\, Re\big[T\big({}^{d}\boldsymbol{n}_i(t)\big)\big] - Re\big[T\big({}^{d}\boldsymbol{n}_e(t)\big)\big] + j\left\{\sum_{i=1}^{d_I} {}^{d}p_i\, Im\big[T\big({}^{d}\boldsymbol{n}_i(t)\big)\big] - Im\big[T\big({}^{d}\boldsymbol{n}_e(t)\big)\big]\right\} \tag{11}$$

where j denotes the imaginary operator. From (11) it is easy to see that:

$$ Re\big[{}^{d}\boldsymbol{E}(f,t;\,{}^{d}\boldsymbol{p})\big] = \sum_{i=1}^{d_I} {}^{d}p_i\, Re\big[T\big({}^{d}\boldsymbol{n}_i(t)\big)\big] - Re\big[T\big({}^{d}\boldsymbol{n}_e(t)\big)\big] \tag{12a}$$

$$ Im\big[{}^{d}\boldsymbol{E}(f,t;\,{}^{d}\boldsymbol{p})\big] = \sum_{i=1}^{d_I} {}^{d}p_i\, Im\big[T\big({}^{d}\boldsymbol{n}_i(t)\big)\big] - Im\big[T\big({}^{d}\boldsymbol{n}_e(t)\big)\big] \tag{12b}$$

one can now define:

$$ T_{Re}\big({}^{d}\boldsymbol{n}_i\big) = Re\big[T\big({}^{d}\boldsymbol{n}_i(t)\big)\big] \qquad T_{Re}\big({}^{d}\boldsymbol{n}_e\big) = Re\big[T\big({}^{d}\boldsymbol{n}_e(t)\big)\big] \tag{13a}$$

$$ T_{Im}\big({}^{d}\boldsymbol{n}_i\big) = Im\big[T\big({}^{d}\boldsymbol{n}_i(t)\big)\big] \qquad T_{RIm}\big({}^{d}\boldsymbol{n}_e\big) = Im\big[T\big({}^{d}\boldsymbol{n}_e(t)\big)\big] \tag{13b}$$

Introducing (13) in (12) and again the result in (10) it easy to demonstrate that:

$$ \begin{aligned} {}^{d}\boldsymbol{W}(f,t;\,{}^{d}\boldsymbol{p}) = \sum_{i=1}^{d_I} \Bigg\{ & {}^{d}p_i^2 \cdot \Big(T_{Re}{}^{\circ 2}\big({}^{d}\boldsymbol{n}_i\big) + T_{Im}{}^{\circ 2}\big({}^{d}\boldsymbol{n}_i\big)\Big) - \\ & 2\,{}^{d}p_i \cdot \Big(T_{Re}\big({}^{d}\boldsymbol{n}_i\big) \circ T_{Re}\big({}^{d}\boldsymbol{n}_e\big) + T_{Im}\big({}^{d}\boldsymbol{n}_i\big) \circ T_{Im}\big({}^{d}\boldsymbol{n}_e\big)\Big) + \\ & \sum_{\substack{k=1 \\ \forall k \neq i}}^{d_I} \Big[\, {}^{d}p_i\, {}^{d}p_k \cdot \Big(T_{Re}\big({}^{d}\boldsymbol{n}_i\big) \circ T_{Re}\big({}^{d}\boldsymbol{n}_k\big) + T_{Im}\big({}^{d}\boldsymbol{n}_i\big) \circ T_{Im}\big({}^{d}\boldsymbol{n}_k\big)\Big)\Big]\Bigg\} + \\ & \Big(T_{Re}{}^{\circ 2}\big({}^{d}\boldsymbol{n}_e\big) + T_{Im}{}^{\circ 2}\big({}^{d}\boldsymbol{n}_e\big)\Big) \end{aligned} \tag{14}$$

The previous equation, (14), can be written in a simpler form by defining the following quantities:

$$ {}^{d}\boldsymbol{Q}_{ik} = {}^{d}\boldsymbol{Q}_{ik}(f,t;\,{}^{d}\boldsymbol{p}) = T_{Re}\left({}^{d}\boldsymbol{n}_i\right)\circ T_{Re}\left({}^{d}\boldsymbol{n}_k\right) + T_{Im}\left({}^{d}\boldsymbol{n}_i\right)\circ T_{Im}\left({}^{d}\boldsymbol{n}_k\right) \tag{15a} $$

$$ {}^{d}\boldsymbol{Q}_{ie} = {}^{d}\boldsymbol{Q}_{ie}(f,t;\,{}^{d}\boldsymbol{p}) = T_{Re}\left({}^{d}\boldsymbol{n}_i\right)\circ T_{Re}\left({}^{d}\boldsymbol{n}_e\right) + T_{Im}\left({}^{d}\boldsymbol{n}_i\right)\circ T_{Im}\left({}^{d}\boldsymbol{n}_e\right) \tag{15b} $$

$$ {}^{d}\boldsymbol{Q}_{ee} = {}^{d}\boldsymbol{Q}_{ee}(f,t;\,{}^{d}\boldsymbol{p}) = T_{Re}\left({}^{d}\boldsymbol{n}_e\right)\circ T_{Re}\left({}^{d}\boldsymbol{n}_e\right) + T_{Im}\left({}^{d}\boldsymbol{n}_e\right)\circ T_{Im}\left({}^{d}\boldsymbol{n}_e\right) \tag{15c} $$

where the symbol (∘) denotes the Hadamard operator (i.e. Hadamard product, exponent, etc.). Replacing (15) in (14):

$$ {}^{d}\boldsymbol{W}(f,t;\,{}^{d}\boldsymbol{p}) = \sum_{i=1}^{{}^{d}I}\left\{ {}^{d}p_i^2\,{}^{d}\boldsymbol{Q}_{ii} - 2\,{}^{d}p_i\,{}^{d}\boldsymbol{Q}_{ie} + \sum_{\substack{k=1\\ \forall k\neq i}}^{{}^{d}I}\left[{}^{d}p_i\,{}^{d}p_k\,{}^{d}\boldsymbol{Q}_{ik}\right]\right\} + {}^{d}\boldsymbol{Q}_{ee} \tag{16} $$

Now it is possible to differentiate (16) respect to ${}^{d}p_i$, $\forall f, \forall t$:

$$ \frac{\partial\,{}^{d}W({}^{d}\boldsymbol{p})}{\partial\,{}^{d}p_i} = {}^{d}W_i({}^{d}\boldsymbol{p}) = 2\,{}^{d}p_i\,{}^{d}Q_{ii} - 2\,{}^{d}Q_{ie} + 2\sum_{\substack{k=1\\ \forall k\neq i}}^{{}^{d}I}\left[{}^{d}p_k\,{}^{d}Q_{ik}\right] \qquad \forall f, \forall t \tag{17} $$

while differentiating (17) respect to ${}^{d}p_k$ reads:

$$ \frac{\partial^2\,{}^{d}W({}^{d}\boldsymbol{p})}{\partial\,{}^{d}p_i\,\partial\,{}^{d}p_k} = {}^{d}W_{ik}\left({}^{d}\boldsymbol{p}\right) = {}^{d}H_{ik} = 2\,{}^{d}Q_{ik} \qquad \forall f, \forall t \tag{18} $$

The stationary points, ${}^{d}_{o}\boldsymbol{p}$, of ${}^{d}W({}^{d}\boldsymbol{p})$, $\forall f, \forall t$, can be found by analysing the system of equations ${}^{d}W_i({}^{d}\boldsymbol{p}) = 0$, $\forall f, \forall t$. The stationary points have global characteristics for ${}^{d}\boldsymbol{W}(f,t;\,{}^{d}\boldsymbol{p})$ because ${}^{d}\boldsymbol{H}$, which represents the Hessian matrix of ${}^{d}W({}^{d}\boldsymbol{p})$, $\forall f, \forall t$, is constant (and this comes from the quadratic form of ${}^{d}\boldsymbol{W}(f,t;\,{}^{d}\boldsymbol{p})$). In addition, because ${}^{d}H_{ik} = {}^{d}H_{ki}$, the Hessian matrix is symmetric and squared. Thus, all its eigenvalues are strictly positive if its determinant is different from zero. This mean that if $det\left({}^{d}\boldsymbol{H}\right) \neq 0$ the function ${}^{d}\boldsymbol{W}(f,t;\,{}^{d}\boldsymbol{p})$ is convex and the stationary points, ${}^{d}_{o}\boldsymbol{p}$, $\forall f, \forall t$ are global minimum of ${}^{d}\boldsymbol{W}(f,t;\,{}^{d}\boldsymbol{p})$. Clearly, the system of equations ${}^{d}W_i({}^{d}\boldsymbol{p}) = 0$ coincide to solve the following linear problem $\forall f, \forall t$, where ${}^{d}\boldsymbol{H}$ is symmetric and squared:

$$ {}^{d}\boldsymbol{H}\,{}^{d}\boldsymbol{p} = {}^{d}\boldsymbol{b} \qquad \forall f, \forall t \tag{19} $$

where ${}^{d}b_i = 2\,{}^{d}Q_{ie}$. The problem (19) can be solved by inverting ${}^{d}\boldsymbol{H}$ if $det\left({}^{d}\boldsymbol{H}\right) \neq 0$, and in this situation it is ensured that ${}^{d}_{o}\boldsymbol{p}$, $\forall f, \forall t$, represents the global minimum of ${}^{d}\boldsymbol{W}(f, t;\, {}^{d}\boldsymbol{p})$). For numerical reasons it is also possible to replace the inversion operation with the pseudo-inversion computed with the Singular Value Decomposition algorithm, that allow to reach a solution also in the case of conditioned Hessian matrices, thus the solution of (19) can be written as: ${}^{d}_{o}\boldsymbol{p} = {}^{d}\boldsymbol{H}^{\dagger}\,{}^{d}\boldsymbol{b}$, $\forall f, \forall t$. If one is not interested in a solution over the frequency values, the following problem can be set:

$$ \begin{cases} {}^{d}_{o}\boldsymbol{p} = {}^{d}\boldsymbol{H}^{\dagger}\,{}^{d}\boldsymbol{b} \qquad \forall t \\ {}^{d}H_{ik} = 2\int_0^t \left(\int_0^{f_s/2} {}^{d}\boldsymbol{Q}_{ik}(f, \tau;\, {}^{d}\boldsymbol{p}) df \right) d\tau \\ {}^{d}b_i = 2\int_0^t \left(\int_0^{f_s/2} {}^{d}\boldsymbol{Q}_{ie}(f, \tau;\, {}^{d}\boldsymbol{p}) df \right) d\tau \end{cases} \tag{20} $$

where f_s is the sampling frequency of the signal ${}^{d}\boldsymbol{n}_e(t)$. If the integral $\int_0^t (\cdot)\, d\tau$ in (20) is computed for $t = t_e$, where t_e is the length of the signal (in seconds) it is possible to get a scalar value of ${}^{d}_{o}\boldsymbol{p}$.

4.2.2. Basis functions for parameters identification of Bouc-Wen type oscillators in in-series mass lumped MDoFs systems

In this subsection the form of the basis functions ${}^{d}\boldsymbol{n}_i(t)$, as well as the form of the experimental record ${}^{d}\boldsymbol{n}_e(t)$ and the unknown parameters ${}^{d}p_i$, is reported if the dynamics of an in-series mass lumped Multi-DoFs (MDoFs) system is approximated with simple Bouc-Wen type oscillators. In general, the equations of motion for this type of systems subjected to the seismic action at the base can be written, for the *d*-th DoF and for an arbitrary direction (X or Y) as:

$$ m_d \ddot{\boldsymbol{u}}_d(t) + \boldsymbol{f}_d(t) = \boldsymbol{F}_d(t) = -m_d v_d \boldsymbol{a}(t) \tag{21} $$

Where $\boldsymbol{a}(t)$ is the input acceleration at the base of the structure, $v_d = 1$ is the *d*-th component of the drag vector in the analysed direction, m_d is the reduced lumped mass at the DoF *d*, $\ddot{\boldsymbol{u}}_d(t)$ is the acceleration response at the DoF *d*, while $\boldsymbol{f}_d(t)$ is the *d*-th restoring force. This can be written in differential form (ensuring causality) as:

$$ \frac{\partial \boldsymbol{f}_d(t)}{\partial t} = \dot{\boldsymbol{f}}_d(t) = \dot{\boldsymbol{f}}_{d,L}(t) + \dot{\boldsymbol{f}}_{d,NL}(t) \tag{22} $$

where $\dot{\boldsymbol{f}}_{d,L}(t)$ is a term proportional to the stiffness matrix components, while $\dot{\boldsymbol{f}}_{d,NL}(t)$ is a general non-linear term:

$$\dot{\boldsymbol{f}}_{d,L}(t) = \sum_{r=D}^{1} \boldsymbol{K}_{dr}(\boldsymbol{\varepsilon}_{dr}(t), t) \cdot \dot{\boldsymbol{u}}_r(t) \tag{23a}$$

$$\boldsymbol{K}_{dr}(\boldsymbol{\varepsilon}_{dr}(t), t) = K_{0,dr} \cdot \left(1 - \delta_{dr} \cdot \boldsymbol{\varepsilon}_{dr}(t)\right) = K_{0,dr} - K_{0,dr}\delta_{dr} \cdot \boldsymbol{\varepsilon}_{dr}(t) \tag{23b}$$

$$\begin{aligned}\dot{\boldsymbol{f}}_{d,NL}(t) = \beta_d\left(\dot{\boldsymbol{u}}_{d-1}(t) - \dot{\boldsymbol{u}}_d(t)\right)\left|\sum_{r=D}^{d} \boldsymbol{f}_d(t)\right|^{N_d} sign\left[\left(\dot{\boldsymbol{u}}_d(t) - \right.\right. \\ \left.\left.\dot{\boldsymbol{u}}_{d-1}(t)\right)\sum_{r=D}^{d} \boldsymbol{f}_d(t)\right] + \gamma_d\left(\dot{\boldsymbol{u}}_{d-1}(t) - \dot{\boldsymbol{u}}_d(t)\right)\left|\sum_{r=D}^{d} \boldsymbol{f}_d(t)\right|^{N_d} - \\ \dot{\boldsymbol{f}}_{d+1,NL}(t)\end{aligned} \tag{23c}$$

$$\boldsymbol{\varepsilon}_{rd}(t) := \int_0^t \boldsymbol{f}_d(\tau)\dot{\boldsymbol{u}}_r(\tau)d\tau \;\; \forall r \le d, \qquad \boldsymbol{\varepsilon}_{dr}(t) = -\boldsymbol{\varepsilon}_{rd}(t) \;\forall d \ne r \tag{23d}$$

with the conditions $\dot{\boldsymbol{u}}_0(t) = 0$, $\dot{\boldsymbol{f}}_{D+1,NL}(t) = 0$ and D total number of DoFs of the system in a specific direction (each one associated to a lumped mass m_d); r is a free parameter of the summation with step -1, $K_{0,dr} = K_{0,rd}$, $\boldsymbol{\varepsilon}_{dr}(t) = -\boldsymbol{\varepsilon}_{rd}(t)$, $\delta_{dr} = -\delta_{rd}$, $\forall d \ne r$, to enforce the symmetry of the stiffness matrix components $\boldsymbol{K}_{dr}(\boldsymbol{\varepsilon}_{dr}(t), t)$ at each time of the analysis. In (23) δ_{dr} are the elastic stiffness degradation parameters, $\boldsymbol{\varepsilon}_{dr}(t)$ are the energies dissipated by the system associated to the DoFs d and r, β_d and γ_d are the parameters of the Bouc-Wen type model of hysteresis, while N_d are the exponents parameters of the same Bouc-Wen type model. Thus, with (23b) it is assumed that the elastic stiffness matrix is linearly proportional to the dissipated energy, (Baber & Noori, 1985), (Babe, 1986). Because (23) define the derivate of the restoring force as a function linearly dependent on the state variable $\dot{\boldsymbol{u}}_d(t)$, the model has rate-independent characteristics. In addition, the presence of $\boldsymbol{f}_d(t)$ in the equations ensure memory. The equations of motion (21) can be rewritten as:

$$\boldsymbol{f}_d(t) = -\left(\boldsymbol{a}(t) + \ddot{\boldsymbol{u}}_d(t)\right)m_d = \boldsymbol{g}_d(t)m_d \tag{24a}$$

$$\boldsymbol{g}_d(t) = -\left(\boldsymbol{a}(t) + \ddot{\boldsymbol{u}}_d(t)\right) \tag{24b}$$

Now replacing (23) in (22):

$$\begin{aligned}\dot{\boldsymbol{f}}_d(t) = \sum_{r=D}^{1} K_{0,dr} \cdot \dot{\boldsymbol{u}}_r(t) + \sum_{r=D}^{1} -K_{0,dr}\delta_{dr} \cdot \boldsymbol{\varepsilon}_{dr}(t)\dot{\boldsymbol{u}}_r(t) + \\ \beta_d\left(\dot{\boldsymbol{u}}_{d-1}(t) - \dot{\boldsymbol{u}}_d(t)\right)\left|\sum_{r=D}^{d} \boldsymbol{f}_d(t)\right|^{N_d} sign\left[\left(\dot{\boldsymbol{u}}_d(t) - \right.\right. \\ \left.\left.\dot{\boldsymbol{u}}_{d-1}(t)\right)\sum_{r=D}^{d} \boldsymbol{f}_d(t)\right] + \gamma_d\left(\dot{\boldsymbol{u}}_{d-1}(t) - \dot{\boldsymbol{u}}_d(t)\right)\left|\sum_{r=D}^{d} \boldsymbol{f}_d(t)\right|^{N_d} - \\ \dot{\boldsymbol{f}}_{d+1,NL}(t)\end{aligned} \tag{25}$$

integrating (25) in time:

$$\boldsymbol{f}_d(t) = \sum_{r=D}^{1} K_{0,dr} \cdot \boldsymbol{u}_r(t) + \sum_{r=D}^{1} -K_{0,dr}\delta_{dr} \cdot \int_0^t \left(\boldsymbol{\varepsilon}_{dr}(\tau)\dot{\boldsymbol{u}}_r(\tau)\right) d\tau + \beta_d \cdot \int_0^t \left(\left(\dot{\boldsymbol{u}}_{d-1}(\tau) - \dot{\boldsymbol{u}}_d(\tau)\right) \left|\sum_{r=D}^{d} \boldsymbol{f}_d(\tau)\right|^{N_d} sign\left[\left(\dot{\boldsymbol{u}}_d(\tau) - \dot{\boldsymbol{u}}_{d-1}(\tau)\right) \sum_{r=D}^{d} \boldsymbol{f}_d(\tau)\right] \right) d\tau + \gamma_d \cdot \int_0^t \left(\left(\dot{\boldsymbol{u}}_{d-1}(\tau) - \dot{\boldsymbol{u}}_d(\tau)\right) \left|\sum_{r=D}^{d} \boldsymbol{f}_d(\tau)\right|^{N_d} \right) d\tau - \boldsymbol{f}_{d+1,NL}(t) \tag{26}$$

Then replacing (26) in (24a) and dividing by m_d, if N_d are supposed to be known, it is possible to obtain an equation in the form of (6:

$$\sum_{r=D}^{1} K_{0,dr} \cdot \frac{\boldsymbol{u}_r(t)}{m_d} + \sum_{r=D}^{1} K_{0,dr}\delta_{dr} \cdot \int_0^t -\left(\frac{\boldsymbol{\varepsilon}_{dr}(\tau)\dot{\boldsymbol{u}}_r(\tau)}{m_d}\right) d\tau + \beta_d \cdot \int_0^t \left(\frac{\left(\dot{\boldsymbol{u}}_{d-1}(\tau) - \dot{\boldsymbol{u}}_d(\tau)\right)}{m_d} \left|\sum_{r=D}^{d} \boldsymbol{f}_d(\tau)\right|^{N_d} sign\left[\left(\dot{\boldsymbol{u}}_d(\tau) - \dot{\boldsymbol{u}}_{d-1}(\tau)\right) \sum_{r=D}^{d} \boldsymbol{f}_d(\tau)\right] \right) d\tau + \gamma_d \cdot \int_0^t \left(\frac{\left(\dot{\boldsymbol{u}}_{d-1}(\tau) - \dot{\boldsymbol{u}}_d(\tau)\right)}{m_d} \left|\sum_{r=D}^{d} \boldsymbol{f}_d(\tau)\right|^{N_d} \right) d\tau \cong \boldsymbol{g}_d(t) + \frac{\boldsymbol{f}_{d+1,NL}(t)}{m_d} \tag{27}$$

where the equality has been substituted by the similarity because in this study the time dependent variables are supposed to be taken from experimental campaigns.

Instead of using an integral form of $\dot{\boldsymbol{f}}_d(t)$, nothing forbids to compare directly the derivate of (24) (proportional to the total jerk of the system) with $\dot{\boldsymbol{f}}_d(t)$. Also in this case the derivation brings to a form comparable with (6. A direct comparison between (27) and (6 allows to define the form of the basis functions ${}^d\boldsymbol{n}_i(t)$, as well as the form of the experimental record ${}^d\boldsymbol{n}_e(t)$ and the unknown parameters ${}^d p_i$. These quantities are defined as follow:

$${}^d p_i = \begin{cases} K_{0,dr}\ \forall r, & 1 \le i \le D\ \forall i\ \in \mathbb{N} \\ K_{0,dr}\delta_{dr}\ \forall r, & (D+1) \le i \le 2D\ \forall i\ \in \mathbb{N} \\ \beta_d, & i = 2D+1 \\ \gamma_d, & i = 2D+2 \end{cases} \tag{28}$$

$${}^d\boldsymbol{n}_i(t) = \begin{cases} \frac{\boldsymbol{u}_r(t)}{m_d}\ \forall r, & 1 \le i \le D\ \forall i\ \in \mathbb{N} \\ \int_0^t -\left(\frac{\boldsymbol{\varepsilon}_{dr}(\tau)\dot{\boldsymbol{u}}_r(\tau)}{m_d}\right) d\tau\ \forall r, & (D+1) \le i \le 2D\ \forall i\ \in \mathbb{N} \\ {}^d\boldsymbol{n}_{2D+1}(t), & i = 2D+1 \\ \int_0^t \left(\frac{\left(\dot{\boldsymbol{u}}_{d-1}(\tau) - \dot{\boldsymbol{u}}_d(\tau)\right)}{m_d} \left|\sum_{r=D}^{d} \boldsymbol{f}_d(\tau)\right|^{N_d}\right) d\tau, & i = 2D+2 \end{cases} \tag{29a}$$

$${}^d\boldsymbol{n}_{2D+1}(t) = \int_0^t \left(\frac{\left(\dot{\boldsymbol{u}}_{d-1}(\tau) - \dot{\boldsymbol{u}}_d(\tau)\right)}{m_d} \left|\sum_{r=D}^{d} \boldsymbol{f}_d(\tau)\right|^{N_d} \cdot sign\left[\left(\dot{\boldsymbol{u}}_d(\tau) - \right.\right.\right. \tag{29b}$$

$\dot{\boldsymbol{u}}_{d-1}(\tau)\big)\sum_{r=D}^{d}\boldsymbol{f}_d(\tau)\big]\Big)\,d\tau$

$$^{d}\boldsymbol{n}_e(t) = \boldsymbol{g}_d(t) + \frac{\boldsymbol{f}_{d+1,NL}(t)}{m_d} + \frac{\boldsymbol{f}_{d,KL}(t)}{m_d} \tag{30}$$

with the condition $\boldsymbol{f}_{D,KL}(t) = 0$. $\boldsymbol{f}_{d,KL}(t)$ is a known function that depend only by the symmetric parameter and functions already found (i.e. $K_{0,rd} = K_{0,dr}$, $\boldsymbol{\varepsilon}_{rd}(t) = -\boldsymbol{\varepsilon}_{dr}(t)$, $\delta_{rd} = -\delta_{dr}$, $\forall r \neq d$). Now the (28), (29), (30), the system (20) and (15) can be used to find the unknown parameters $^{d}p_i$ if the calibration process proceed in series starting from the highest DoF. If the calibration starts from d = D one obtains that $^{D}\boldsymbol{n}_e(t) = \boldsymbol{g}_D(t)$ and the parameters $^{D}p_i$ can be easily found. Then, continuing with d = *D-1* one gets $^{D-1}\boldsymbol{n}_e(t) = \boldsymbol{g}_{D-1}(t) + \frac{\boldsymbol{f}_{D,NL}(t)}{m_d} + \frac{\boldsymbol{f}_{D-1,KL}(t)}{m_d}$ where $\boldsymbol{f}_{D,NL}(t)$ is known because depend only by the Bouc-Wen parameter $^{D}p_i$ while $\boldsymbol{f}_{D-1,KL}(t)$ is known because the existence of the equality constraints between the symmetric parameters $K_{0,dr}$, $\boldsymbol{\varepsilon}_{dr}(t)$, δ_{dr}, $\forall r \neq d$). In this procedure we assumed that the parameters N_d are known, but this is not true. Despite of this, N_d can be found with optimization algorithms that try to minimize the following cost function:

$$^{d}J(^{d}_{o}\boldsymbol{p}; N_d) = \int_0^{t_e}\left(\int_0^{f_s/2} {}^{d}\boldsymbol{W}(f,\tau; {}^{d}_{o}\boldsymbol{p})df\right)d\tau \tag{31}$$

where for each tried value of N_d (starting from d = D and proceeding in decreasing order), $^{d}_{o}\boldsymbol{p}$ can be easily found and thus their values are known while calculating $^{d}J(^{d}_{o}\boldsymbol{p}; N_d)$ with (31). If in (31) the length of the signals, t_e, is replaced by a general variable t it is possible to obtain an estimate of N_d in the time. The only concern of the method is about the mass matrix components, m_d, that need to be known. If they are not known an estimate of their values can be used, e.g. values obtained by calibrated Finite Element (FE) model of the structure. If this estimate cannot be performed, m_d should be inserted in the unknown parameter $^{d}p_i$ instead of appearing in the basis functions $^{d}\boldsymbol{n}_i(t)$.

4.2.3. Nonlinear identification of the seismic damage

After the identification of the model parameters the values of $^{d}\boldsymbol{p}$ and N_d are known $\forall d$. Thus, it is possible to evaluate $\boldsymbol{K}_{dr}(\boldsymbol{\varepsilon}_{dr}(t), t) = K_{0,dr}\cdot\big(1 - \delta_{dr}\cdot\boldsymbol{\varepsilon}_{dr}(t)\big)$, where $\boldsymbol{K}_{dr}(\boldsymbol{\varepsilon}_{dr}(t), t)$ is the damaged stiffness matrix component as a function of the dissipated energy. If one supposes that the mass remains almost constant after the occurrence of damage (and this is true in civil engineer structures, because a sensitive reduction in the mass occurs only in very severe cases, where the assessment of the damage can be easily performed by visual inspection), the following time dependent eigen-problem can be solved $\forall t$:

$$(\boldsymbol{K}(t) - \boldsymbol{\omega}_s^2(t) \cdot \boldsymbol{m}) \cdot \boldsymbol{\phi}_s(t) = 0 \tag{32}$$

Thus, for each time instant we can evaluate the damaged pulsations of the system $\boldsymbol{\omega}_s(t)$, and the damaged eigenvectors $\boldsymbol{\phi}_s(t)$ for each mode, *s*, in the chosen direction of analysis. This provide the input for the evaluation of the instantaneous percentage of participation mass, $\boldsymbol{c}_s(t)$:

$$\boldsymbol{\Gamma}(t) = \boldsymbol{\phi}(t)^T \boldsymbol{m}\, \boldsymbol{v} \tag{33a}$$

$$\boldsymbol{c}_s(t) = \frac{\boldsymbol{\Gamma}_s^2(t)}{\sum_s \boldsymbol{\Gamma}_s^2(t)} \tag{33b}$$

where $\boldsymbol{v}$ is the unitary drag vector and $\boldsymbol{\Gamma}(t)$ is the vector of the modal participation factors. Then, $\boldsymbol{c}_s(t)$ can be used as a weighting factor for the damage index, $\boldsymbol{\iota}(t)$, defined as follow:

$$\boldsymbol{\alpha}_s(t) = 1 - \frac{\boldsymbol{\omega}_s(t)}{\boldsymbol{\omega}_s(0)} \tag{34a}$$

$$\boldsymbol{\iota}(t) := \boldsymbol{c}(t)^T \boldsymbol{\alpha}(t) \tag{34b}$$

where $\boldsymbol{\alpha}_s(t)$ it is the normalized difference of the pulsation for mode, *s*. The damage index defined in (34) depend only by the mass of the system and by the variation of the stiffness matrix during the seismic event, that again only depend by the energy dissipated by the system during the seismic event. Table 15 shows a pseudo-code of the proposed algorithm for the nonlinear identification of the seismic damage.

Table 15: Pseudo-code for the non-linear identification of the seismic damage.

Assume a direction of the seismic action and perform the following steps for this direction:

A) Initialize $d = D$.
   a. Assume a value of N_d
      i. Calculate the linear TFD of the quantities defined in (29) and (30), or (A9) and (A10), then apply (15) for *i* and *k* that go from 1 to ${}^{d}I$;
      ii. Solve the system of equations (20) subjected to the desired constraints and/or boundaries;
      iii. Evaluate the cost function with (31);
   b. Assume a new value of N_d and try to minimize (31) with a desired algorithm (following the steps i., ii. and iii.);
   c. Find $N_d = {}_{o}N_d$ that minimize (31);
   d. Find ${}_{o}^{d}p_i$ solving the system of equations (15) with $N_d = {}_{o}N_d$. Do it in time-frequency, time or scalar domain;

B) Start the identification for another DoF.
   a. Update the variable *d* as follow: $d = d\text{-}1$.
   b. Repeat the steps a., b., c. and d. of A) and a. of B) unless $d = 0$.

C) Evaluate the seismic damage.

a. Evaluate the damaged stiffness matrix with (23b): $$\boldsymbol{K}_{dr}(\boldsymbol{\varepsilon}_{dr}(t), t) = K_{0,dr} \cdot \left(1 - \delta_{dr} \cdot \boldsymbol{\varepsilon}_{dr}(t)\right)$$ b. Solve the time dependent eigen-problem of (32); c. Evaluate the instantaneous percentage of participation mass with (33); d. Evaluate the damage index $\boldsymbol{\iota}(t)$ with (34).
Perform steps A), B) and C) for another direction of the seismic actions.

4.3. Application

In this section the procedure described in Table 15 is applied to a real monitored masonry structure. The chosen masonry structure is the Town Hall of Pizzoli (AQ). The building is a two-storey stone masonry building located northwest of the city of L'Aquila (Abruzzo), which is about 15 km away. The Town Hall was built around 1920 and it presents a u-shaped regular plan, mainly distributed along one direction, and its elevations are characterized by various regular openings. The building has three levels above the ground (the raised floor, the first floor and the under-roof floor) and a basement. The total area is about 770 m^2 while the volume is about 5000 m^3. Previous investigations have highlighted that the Town Hall presents mixed masonry consisting of unsquared stone blocks, probably alternated with regular courses in solid bricks. Over the years, the Town Hall has been subjected to various transformations. Figure 51 shows the analysed structure.

Figure 51: A historical postcard showing the Town Hall (on the left), a current view of the building (on the right).

The OSS permanent monitoring system allowed the recording of the seismic response of the Pizzoli Town Hall before and during the recent earthquakes that struck central Italy in August-October 2016. The main shocks of this seismic swarm occurred on 24/8/2016 and 26-30/10/2016. In this study the records of the seismic event of 30/10/2016 are used for the non-linear identification of the damage occurred along the two horizontal directions of the building during that event.

4.3.1. Incomplete data set

The OSS permanent monitoring system allowed to record the acceleration signals of the first and second floor of the building and the input at the basement. However, the acceleration response of the first mass (associated to the raised floor) is missing. Thus the procedure described in Table 15 must be applied to an incomplete data set. For this purpose a grey-box identification is used to evaluate the response of a system reduced to the masses of the first, m_{ff}, and under-roof floor, m_{uf}, (see Figure 52 for clarity), while just a part of the mass of the raised floor, m_{rf}, is accounted.

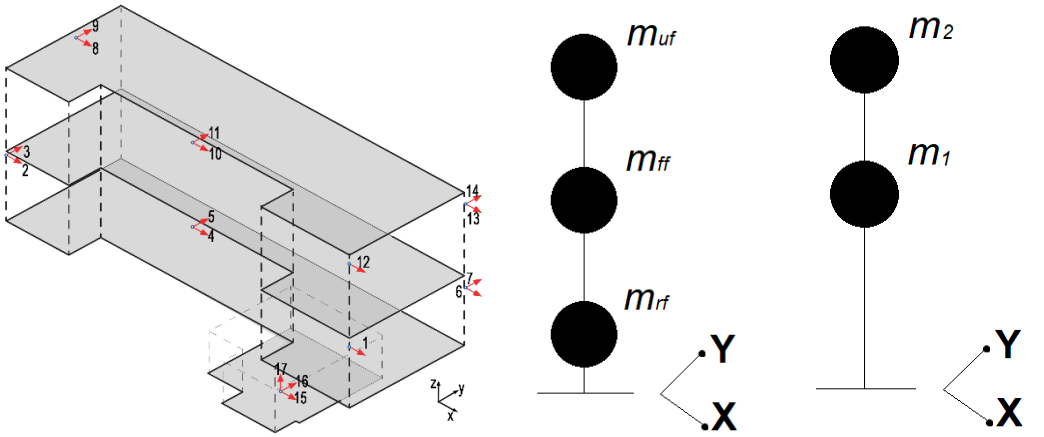

(a) (b) (c)

Figure 52: Town Hall of Pizzoli: (a) monitoring system installed on the building; (b) 3 lumped mass approximation; and (c) 2 lumped mass approximation.

An estimate of the structural masses is available from the linear calibrated FE model of the system described in Chapter 3. Thus the masses of the three floors, and the first frequency in each direction are known in an approximated form. The three lumped masses (see Figure 52 for clarity) and the calibrated frequencies of the FE model are reported in Table 16.

Table 16: Data from calibrated FE model.	
Mass [kg]	***Frequency [Hz]***
m_{rf} = 487300	6.79 in X direction (long) 4.86 in Y direction (short)
m_{ff} = 929430	
m_{uf} = 836370	

The lumped mass matrix reduced to the 2 DoFs system has been found by minimising the difference between the pulsations predicted by the entire FE model, $\omega_{FE,Y}$ and $\omega_{FE,X}$ (associated to the frequencies reported in Table 16) and those one predicted by the reduced system, $\omega_{red,Y}$ and $\omega_{red,X}$, with the two masses, m_1 and m_2 calculated as follow:

$$m_1 = \sigma_2\left[\left(m_{ff} + m_{uf}\right) + \sigma_1 m_{rf}\right] \tag{35a}$$

$$m_2 = (1 - \sigma_2)\left[\left(m_{ff} + m_{uf}\right) + \sigma_1 m_{rf}\right] \tag{35b}$$

The reduced stiffness matrix taken from the FE model in the two directions, $\boldsymbol{K}_{red,X}$ and $\boldsymbol{K}_{red,Y}$, allowed to solve the eigen-problem. In this way the following cost function has been minimized by exploring the parameters σ_1 and σ_2 from values between 0 and 1 with step 0.001:

$$J_m(\boldsymbol{\sigma}) = \left|\omega_{red,X} - \omega_{FE,X}\right| + \left|\omega_{red,Y} - \omega_{FE,Y}\right| \tag{36a}$$

$$\boldsymbol{K}_{red,X} = \begin{bmatrix} 7.8e9 & -3.1e9 \\ -3.1e9 & 3.1e9 \end{bmatrix} \qquad \boldsymbol{K}_{red,Y} = \begin{bmatrix} 4.9e9 & -2.2e9 \\ -2.2e9 & 2.2e9 \end{bmatrix} \tag{36b}$$

The optimal values of the parameters have been found to be: $\sigma_1 = 0.999$ and $\sigma_2 = 0.735$. Now it is possible to apply the procedure to the reduced system depicted in Figure 52c. To do this, the records $\ddot{\boldsymbol{u}}_d(t)$ of the channels 4, 10, 5, 11 have been used because more representative of the floor behaviour of the building, i.e. all the floor mass is supposed to be brought by those channels. Clearly this is not true, thus the estimates could be affected by this assumption, especially for the DoFs close to the ground where the boundary effects are stronger. The channels of the seismic input, $\boldsymbol{a}_X(t)$ and $\boldsymbol{a}_Y(t)$, have been selected accordingly, i.e. channels 15 in X direction and 16 in Y direction (see Figure 52a for clarity).

4.3.2. Definition of the problem for the 2 DoFs system

For the case study is easy to derive the basis functions, the unknow parameters and the experimental records for the two DoFs by applying (28), (29) and (30) in each direction, with *r* that takes the finite values 1 and 2 for the second DoF:

$$^2p_i = \begin{cases} K_{0,2r}\ r = [1,2], & 1 \le i \le 2\ \forall i\ \in \mathbb{N} \\ K_{0,2r}\delta_{2r}\ r = [1,2], & 3 \le i \le 4\ \forall i\ \in \mathbb{N} \\ \beta_2, & i = 5 \\ \gamma_2, & i = 6 \end{cases} \tag{37}$$

$$
{}^{2}\boldsymbol{n}_i(t) = \begin{cases} \frac{\boldsymbol{u}_r(t)}{m_2}\ r = [1,2], & 1 \le i \le 2\ \forall i\ \in \mathbb{N} \\ \int_0^t -\left(\frac{\boldsymbol{\varepsilon}_{2r}(\tau)\dot{\boldsymbol{u}}_r(\tau)}{m_2}\right) d\tau\ r = [1,2], & 3 \le i \le 4\ \forall i\ \in \mathbb{N} \\ {}^{2}\boldsymbol{n}_5(t), & i = 5 \\ \int_0^t \left(\frac{\left(\dot{\boldsymbol{u}}_1(\tau) - \dot{\boldsymbol{u}}_2(\tau)\right)}{m_2} |\boldsymbol{f}_2(\tau)|^{N_2}\right) d\tau, & i = 6 \end{cases} \tag{38a}
$$

$$
{}^{2}\boldsymbol{n}_5(t) = \int_0^t \left(\frac{\left(\dot{\boldsymbol{u}}_1(\tau) - \dot{\boldsymbol{u}}_2(\tau)\right)}{m_2} |\boldsymbol{f}_2(\tau)|^{N_2} \cdot sign\left[\left(\dot{\boldsymbol{u}}_2(\tau) - \dot{\boldsymbol{u}}_1(\tau)\right)\boldsymbol{f}_2(\tau)\right]\right) d\tau \tag{38b}
$$

$$
{}^{2}\boldsymbol{n}_e(t) = -\left(\boldsymbol{a}(t) + \ddot{\boldsymbol{u}}_2(t)\right) \tag{39}
$$

while for the first DoF we have that $K_{0,12} = K_{0,21}$, $\delta_{12} = -\delta_{21}$ and $\boldsymbol{\varepsilon}_{12}(t) = -\boldsymbol{\varepsilon}_{21}(t)$, thus in this case *r* takes just the value of 1:

$$
{}^{1}p_i = \begin{cases} K_{0,11}, & i = 1 \\ K_{0,11}\delta_{11}\ , & i = 2 \\ \beta_1, & i = 3 \\ \gamma_1, & i = 4 \end{cases} \tag{40}
$$

$$
{}^{1}\boldsymbol{n}_i(t) = \begin{cases} \frac{\boldsymbol{u}_1(t)}{m_1}, & i = 1 \\ \int_0^t -\left(\frac{\boldsymbol{\varepsilon}_{11}(\tau)\dot{\boldsymbol{u}}_1(\tau)}{m_1}\right) d\tau\ , & i = 2 \\ {}^{1}\boldsymbol{n}_3(t), & i = 3 \\ \int_0^t \left(\frac{\dot{\boldsymbol{u}}_1(\tau)}{m_1} |\boldsymbol{f}_2(\tau) + \boldsymbol{f}_1(\tau)|^{N_1}\right) d\tau, & i = 4 \end{cases} \tag{41a}
$$

$$
{}^{1}\boldsymbol{n}_3(t) = \int_0^t \left(\frac{\dot{\boldsymbol{u}}_1(\tau)}{m_1} |\boldsymbol{f}_2(\tau) + \boldsymbol{f}_1(\tau)|^{N_1} \cdot sign\left[\dot{\boldsymbol{u}}_1(\tau)\left(\boldsymbol{f}_2(\tau) + \boldsymbol{f}_1(\tau)\right)\right]\right) d\tau \tag{41b}
$$

$$
{}^{1}\boldsymbol{n}_e(t) = -\left(\boldsymbol{a}(t) + \ddot{\boldsymbol{u}}_1(t)\right) + \frac{\boldsymbol{f}_{2,NL}(t)}{m_1} + \frac{\boldsymbol{f}_{1,KL}(t)}{m_1} \tag{42}
$$

Recalling (23c) and integrating it easy to see that:

$$
\begin{aligned} \boldsymbol{f}_{2,NL}(t) = \beta_2 \cdot \int_0^t \left(\left(\dot{\boldsymbol{u}}_1(\tau) - \dot{\boldsymbol{u}}_2(\tau)\right)|\boldsymbol{f}_2(\tau)|^{N_2}\ sign\left[\left(\dot{\boldsymbol{u}}_2(\tau) - \right.\right.\right. \\ \left.\left.\left.\dot{\boldsymbol{u}}_1(\tau)\right)\boldsymbol{f}_2(\tau)\right]\right) d\tau + \gamma_2 \cdot \int_0^t \left(\left(\dot{\boldsymbol{u}}_1(\tau) - \dot{\boldsymbol{u}}_2(\tau)\right)|\boldsymbol{f}_2(\tau)|^{N_2}\right) d\tau \end{aligned} \tag{43}
$$

while $\boldsymbol{f}_{1,KL}(t)$ can be found from the symmetric parameters:

$$
\boldsymbol{f}_{1,KL}(t) = -K_{0,12}\frac{\boldsymbol{u}_2(t)}{m_1} + K_{0,12}\delta_{12}\int_0^t \left(\frac{\boldsymbol{\varepsilon}_{12}(\tau)\dot{\boldsymbol{u}}_2(\tau)}{m_1}\right) d\tau \tag{44}
$$

The dissipated energies for the case study are approximated with the sum of the kinetic and external energies:

$$\boldsymbol{\varepsilon}_{22}(t) = \int_0^t \left(\boldsymbol{f}_2(\tau)\dot{\boldsymbol{u}}_2(\tau)\right) d\tau \tag{45a}$$

$$\boldsymbol{\varepsilon}_{21}(t) = \int_0^t -\left(\boldsymbol{f}_2(\tau)\dot{\boldsymbol{u}}_1(\tau)\right) d\tau \qquad \boldsymbol{\varepsilon}_{12}(t) = -\boldsymbol{\varepsilon}_{21}(t) \tag{45b}$$

$$\boldsymbol{\varepsilon}_{11}(t) = \int_0^t \left(\boldsymbol{f}_1(\tau)\dot{\boldsymbol{u}}_1(\tau)\right) d\tau \tag{45c}$$

with the approximation coming from equation of motions (24a), that bring to:

$$\boldsymbol{f}_1(t) \cong -\left(\boldsymbol{a}(t) + \ddot{\boldsymbol{u}}_1(t)\right)m_1 \tag{46a}$$

$$\boldsymbol{f}_2(t) \cong -\left(\boldsymbol{a}(t) + \ddot{\boldsymbol{u}}_2(t)\right)m_2 \tag{46b}$$

To get the displacement and the velocity responses, the raw accelerations data (sampled at 250 Hz for a useful length of about 50 s) were filtered with a band-pass Butterworth filter of order 4 with cut-off frequencies equal to 0.5 and 20 Hz. Then the procedure described in Table 15 has been applied with several algorithms (i.e. interior points, minimax, genetic, pattern search, simulated annealing, and particle swarm optimization) to test the robustness of the identification; in addition, all the possible solutions of ${}^{d}J(N_d)$ have been evaluated with a precision of 0.001 on the values of N_d between 1 and 10. The chosen algorithms have been used to identify the exponential parameters of the Bouc-Wen model, N_d, for values that range between 1 and 10, while for the other parameters, ${}^{d}p_i$, the system of equations (20) has been solved searching the result in a subdomain of the parameters ${}^{d}p_i$ to deal with the existence of the following inequality constraints:

$$K_{0,dd} \geq 0 \tag{47a}$$

$$\beta_d \geq 0 \tag{47b}$$

$$-\beta_d \leq \gamma_d \leq \beta_d \tag{47c}$$

After solved the parameters identification, the nonlinear identification of the seismic damage has been performed using (34) for each analysed direction (i.e. X and Y).

4.4. Results

In this section the results of the study in the two analysed directions are reported. The TFDs assumed in this study were evaluated with a Short Time (Fast) Fourier Transform (SFFT) using a symmetric Hamming window.

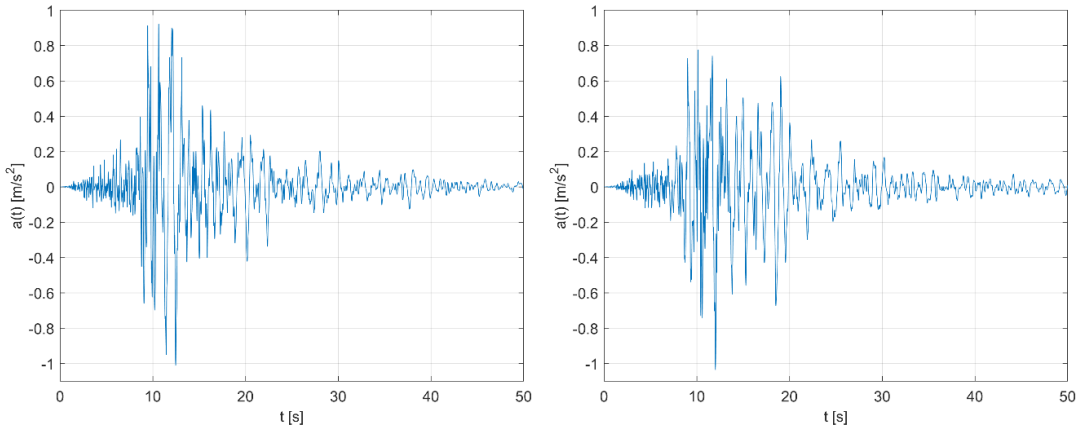

(a) (b)

Figure 53: Seismic acceleration at the basement: (a) X direction; and (b) Y direction.

The length of the window was chosen to minimize the difference between the time-points and frequency-points of the TFD. An overlapping of 50 % was then assumed. Figure 53 shows the ground motion in terms of accelerations associated to the selected input channels.

After the calculation of the TFDs of the quantities defined in (37)-(39), the overall procedure was followed for the second DoF, then by calculating the TFDs of the quantities described in (40)-(44), the procedure was applied to the first DoF. This was performed for each direction, X and Y. To test the robustness of the methodology the calibration was performed with 6 different optimization algorithms. The numerical values of the parameters obtained for the 2 DoFs system are reported in Table 17 and Table 18, with the values of the cost function and the time needed to reach the minimum.

Table 17: Identified scalar parameters: X direction (* gradient based algorithm).

Parameter	*Interior points**	*Minimax**	*Genetic*	*Pattern search*	*Simulated Annealing*	*Particle swarm*	*From all possible solutions*
N_1	2.00	1.17	1.18	1.18	1.18	1.18	1.18
N_2	1.00	1.03	1.03	1.03	1.03	1.03	1.03
β_1	0	0.17	0.17	0.17	0.17	0.17	0.17
β_2	0.93	0.81	0.69	0.69	0.69	0.69	0.69
γ_1	0	0.17	0.17	0.17	0.17	0.17	0.17
γ_2	-0.93	-0.81	-0.69	-0.69	-0.69	-0.69	-0.69
δ_{11}	2.845e4	2.114e-7	2.204e-7	2.204e-7	2.204e-7	2.204e-7	2.204e-7

δ_{12}	7.200e-7	7.175e-7	7.148e-7	7.147e-7	7.146e-7	7.149e-7	7.147e-7
δ_{22}	1.193e-6	1.190e-6	1.187e-6	1.187e-6	1.187e-6	1.187e-6	1.187e-6
$K_{0,11}$[N/m]	3.48e-17	3.093e9	3.093e9	3.093e9	3.094e9	3.093e9	3.093e9
$K_{0,12}$[N/m]	-2.142e9	-2.142e9	-2.142e9	-2.142e9	-2.142e9	-2.142e9	-2.142e9
$K_{0,22}$[N/m]	1.568e9	1.568e9	1.568e9	1.568e9	1.568e9	1.568e9	1.568e9
${}^{1}_{o}J$	7229.7	10.615	10.615	10.615	10.615	10.615	10.615
${}^{2}_{o}J$	1.4173	1.4168	1.4162	1.4162	1.4162	1.4162	1.4162
Time [s]	1.82	2.65	68.69	2.28	26.06	9.10	195

Table 18: Identified scalar parameters: Y direction (* gradient based algorithm).

Parameter	***Interior points****	***Minimax****	***Genetic***	***Pattern search***	***Simulated Annealing***	***Particle swarm***	***From all possible solutions***
N_1	1.99	1.00	1.00	1.00	1.00	1.00	1.00
N_2	1.99	1.00	1.00	1.00	1.00	1.00	1.00
β_1	0	0	0	0	0	0	0
β_2	0	35	35	35	35	35	35
γ_1	0	0	0	0	0	0	0
γ_2	0	-16.68	-16.68	-16.68	-16.68	-16.68	-16.68
δ_{11}	-2.326e4	1.455e-6	1.455e-6	1.455e-6	1.455e-6	1.455e-6	1.455e-6
δ_{12}	-1.772e4	7.940e-7	7.940e-7	7.940e-7	7.940e-7	7.940e-7	7.940e-7
δ_{22}	-2.096e4	1.812e-6	1.812e-6	1.812e-6	1.812e-6	1.812e-6	1.812e-6
$K_{0,11}$[N/m]	7.60e-20	1.838e9	1.838e9	1.838e9	1.838e9	1.838e9	1.838e9
$K_{0,12}$[N/m]	7.44e-17	-7.716e8	-7.716e8	-7.716e8	-7.716e8	-7.716e8	-7.716e8
$K_{0,22}$[N/m]	1.07e-16	5.735e8	5.735e8	5.735e8	5.735e8	5.735e8	5.735e8
${}^{1}_{o}J$	10.9726	15.637	15.637	15.637	15.637	15.637	15.637
${}^{2}_{o}J$	23.4984	1.2473	1.2473	1.2473	1.2473	1.2473	1.2473
Time [s]	1.15	1.28	86.72	1.48	11.85	4.57	195

From Table 17 and Table 18 is very easy to note that the parameters are very stable for different algorithms chosen for the optimization. The only exception is observed for the interior points algorithm. For this reason, the optimization was repeated for a narrower field of research of the parameter N_d (between 1 and 5 instead of 1 and 10) and in this latter case also the interior points algorithm provided the same results showed in Table 17 and Table 18 for the remaining algorithms. As well know, this is due to the gradient based search, that in presence

of not smooth cost functions is prone to be stuck in local minima. In fact, the cost function of (31) is not globally convex as the function of (16) because the presence of N_d as unknown parameter, and surely, ${}^{d}J(N_d)$, is not smooth (see Figure 54 and Figure 55 for the shape of ${}^{d}J(N_d)$, plotted between 0 and 10).

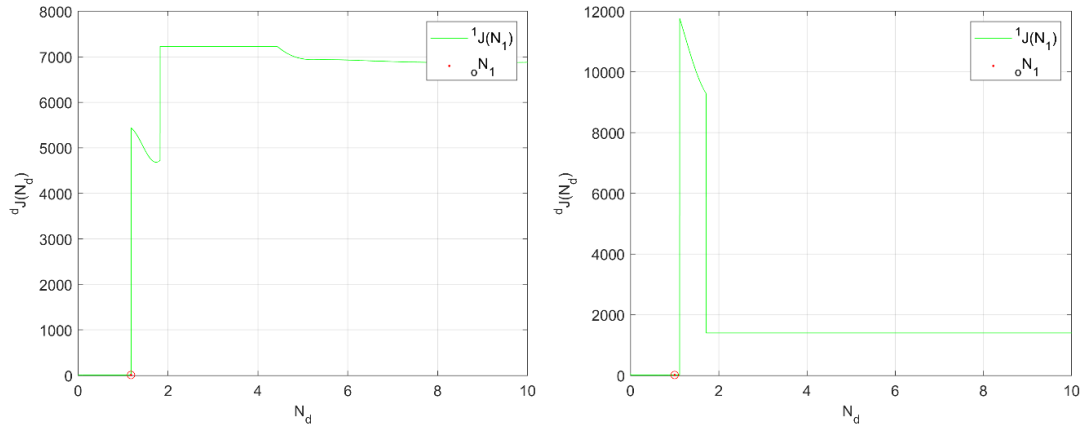

(a) (b)

Figure 54: Cost function for the first DoF, ${}^{1}J(N_1)$: (a) X direction; and (b) Y direction.

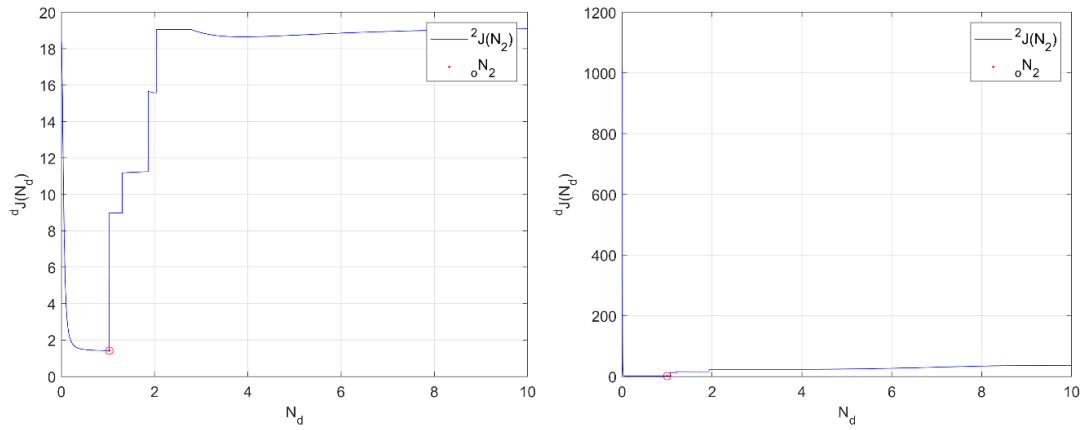

(a) (b)

Figure 55: Cost function for the second DoF, ${}^{2}J(N_2)$: (a) X direction; and (b) Y direction.

The reason of the good result of the minimax algorithm resides in the starting value of N_d, very close to the optimal solution. In fact, by changing the initial value of N_d, also the results of the minimax algorithm become not acceptable, while the remaining algorithms still provide satisfactory values of the parameters. From here on, we will refer to the results obtained with the pattern search algorithm as reference results. For brevity, Figure 56 and Figure 57 show the result in terms of β_2 and γ_2 as a function of time, while on the top of the figures the numerical values in the case of a scalar estimate is reported.

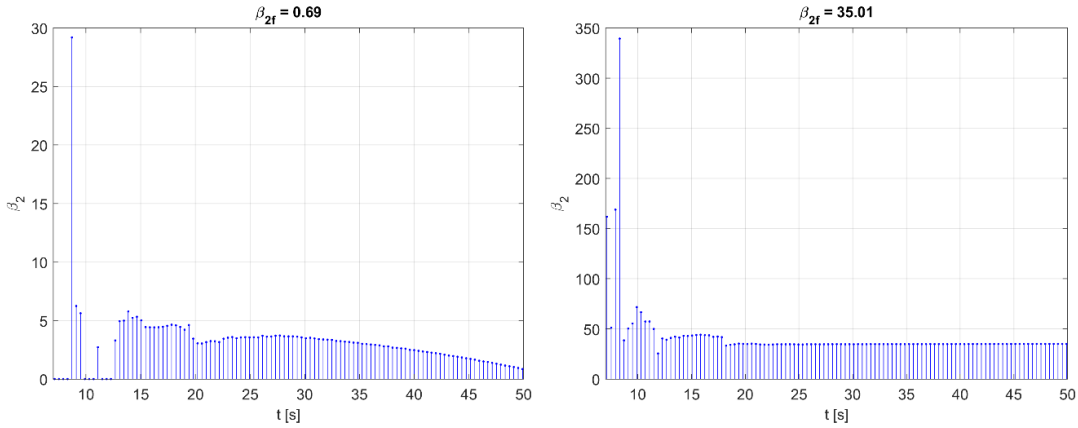

(a) (b)

Figure 56: Instantaneous $\boldsymbol{\beta_2}$ parameter: (a) X direction; and (b) Y direction.

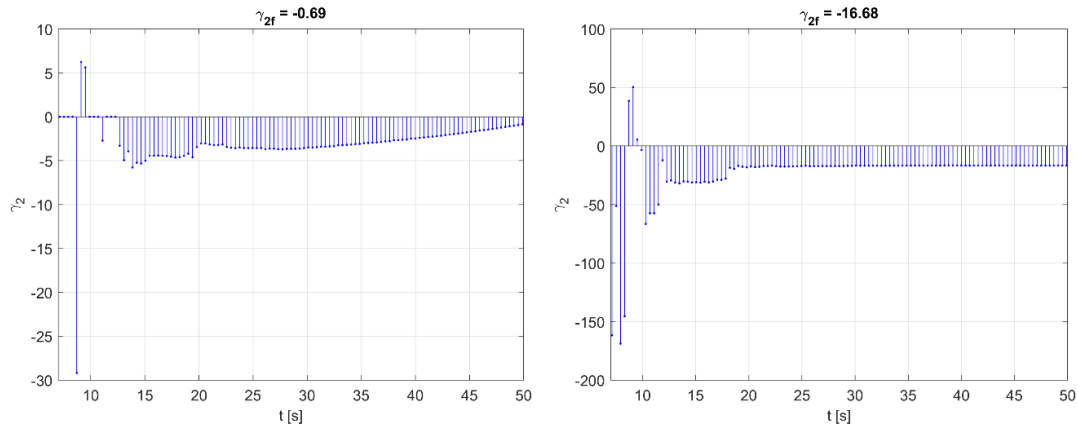

(a) (b)

Figure 57: Instantaneous $\boldsymbol{\gamma_2}$ parameter: (a) X direction; and (b) Y direction.

The instantaneous estimates of the parameters allowed to check the stability of the results. Before about 10 s, the values were highly instable because the not occurrence of a nonlinear behaviour in the structure, thus we avoided to plot them. This was expected as reported by (Ceravolo, 2013). There, it is showed that the parameters associated to a nonlinear behaviour can find a stability just in presence of high nonlinearity (e.g. damage). This is also demonstrated by the more stability of the parameters in Y direction, that as will be reported hereinafter, is associated to a higher damage respect to the X direction. For this reason, the stability along the time of the parameters (e.g. statistical variance) can be also used to check the feasibility of the use of a nonlinear model respect to another model (e.g. linear elastic, linear elastic with rate dependent capability, nonlinear model without hysteresis etc.). Then this choose can be also performed in a systematic way by moving the choosing of the best model in a Rank Aggregation (RA) problem, where in the present case the choice should be entrusted to the variance of the parameters along the time as objective of optimization together with the common objective dictated by the cost function. Figure 58 and Figure 59 show the fitted data, ${}^{d}\boldsymbol{n}_e(t)$, with the model described by ${}^{d}\boldsymbol{n}_n(t)$ for both the X and Y direction.

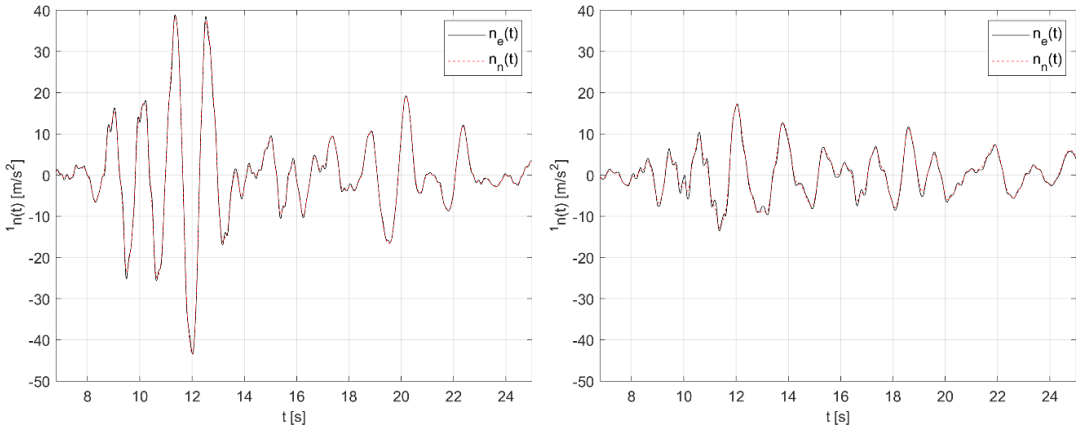

(a) (b)

Figure 58: Model fitting for the first DoF: (a) X direction; and (b) Y direction.

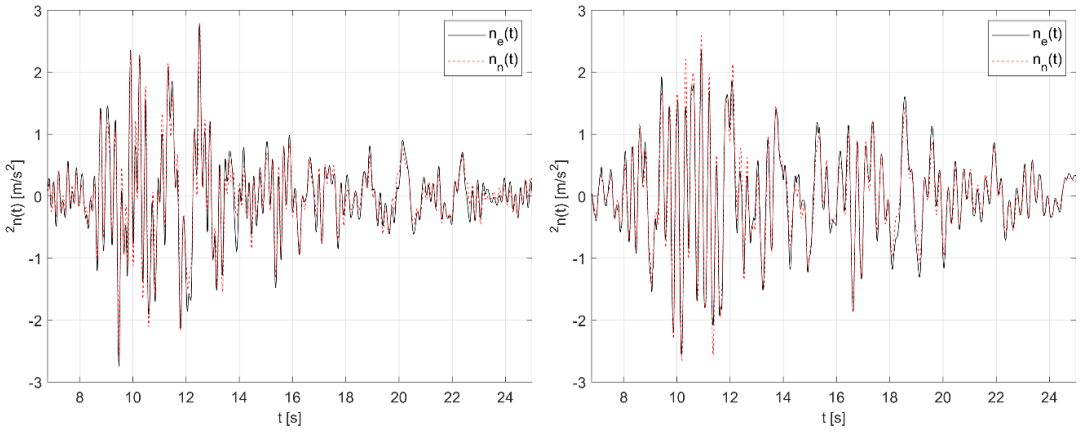

(a) (b)

Figure 59: Model fitting for the second DoF: (a) X direction; and (b) Y direction.

From the figures it is possible to see that the model replicates in an acceptable manner the provided data. The parameter used to perform the comparison are those one contained in Table 17 and Table 18 for the pattern search algorithm. However, identical results are obtained with the other solvers. Although the results are tempting, the goodness of the model should be verified by reproducing the dynamics of the system subjected to several actions. This is beyond the scope of this study, which instead will focus on the analysis of the system forced by the recorded seismic action. About that, Figure 60 and Figure 61 report the restoring force-displacement plot that compare the numerical restoring force predicted by the calibrated model, and the restoring force evaluated with the records. From the plots it is possible to denote that the fitting for the second DoF was able to catch not only the amplitude of the restoring force, but also its behaviour respect to the displacement responses, both in X and Y direction. Instead, for the first DoF, both the slope and the amplitude are replicated in a good manner for the X direction. In Y direction, a light overestimate of the amplitude is denoted, while the slope of the curve is still approximated in a satisfactory way.

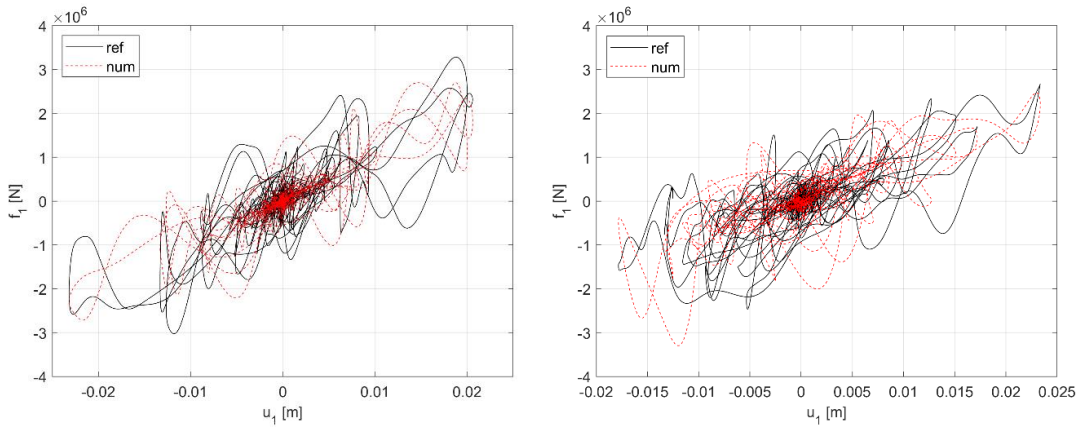

(a) (b)

Figure 60: Restoring force of the first DoF: (a) X direction; and (b) Y direction.

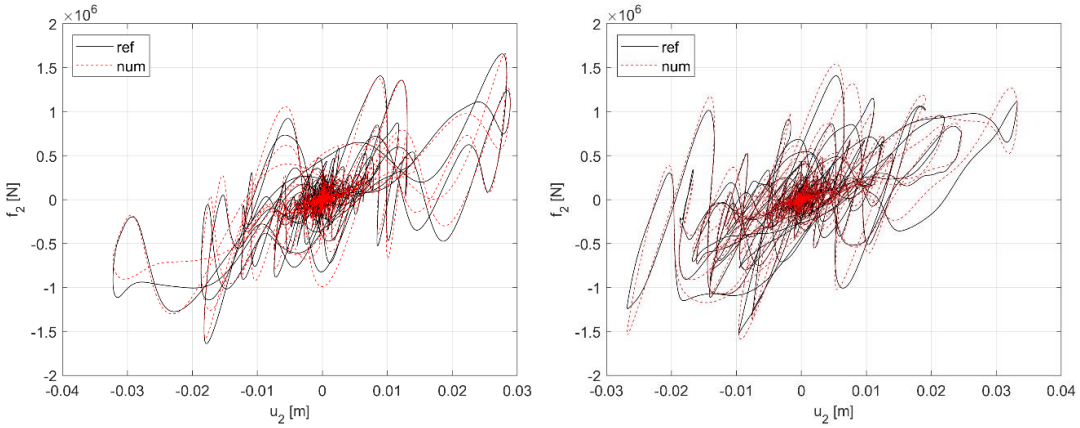

(a) (b)

Figure 61: Restoring force of the second DoF: (a) X direction; and (b) Y direction.

After the calibration of the model, the time dependent eigen-problem was solved to find the instantaneous frequencies and modal shapes. These were used to calculates the damage index defined in (34) and reported in Figure 62. The inter-floor drift, $\Delta \boldsymbol{u}(t)$, in the two directions is instead reported in Figure 63.

From these figures it is possible to note that as soon as the inter-floor drift increase in amplitude, the system starts to be damaged because the existence of a non-conservative term in the assumed model (e.g. hysteretic term). The loss of energy is then represented by (23b) in an alteration of the stiffness values, and thus in a modification of the system frequencies. From Figure 62 and Figure 63 it is also possible to see that the damage index reaches a stabilization after passing the high amplitude instants of the inter-floor drift. After the stabilization phase, the value of $\boldsymbol{\iota}(t)$ cannot decrease anymore because the existence of causal memory in the assumed model. The damage index at the end of the analysis can be thus accepted as an estimate of the damage occurred during the seismic event, providing timely information on the health of the structure. For the case study, following the assumed model, the main damage was detected in Y direction (along the short dimension of the building) and the value of the damage index is

about 10 %. Instead in X direction (long dimension of the building) the damage was more contained, approaching values of 2 %. The result is also consistent with the experimental observation reported in Figure 63, which shows that, even if the inter-floor amplitude is approximately the same in the two directions, in the Y direction the value is maintained for longer time. Thanks to the time-dependent definition of the damage index, it can also be used to correlate its value with a time-dependent quantity directly observable, such as the inter-floor displacement, velocity or acceleration.

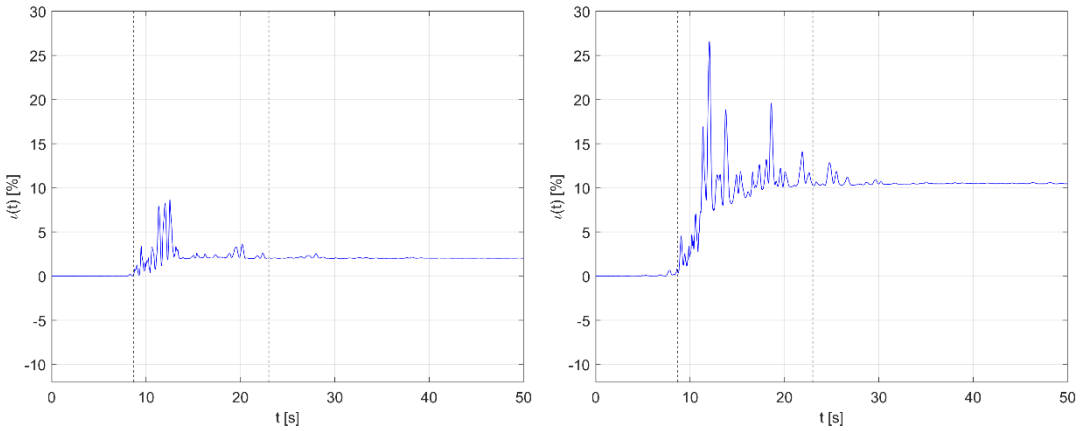

(a) (b)

Figure 62: Damage index: (a) X direction; and (b) Y direction.

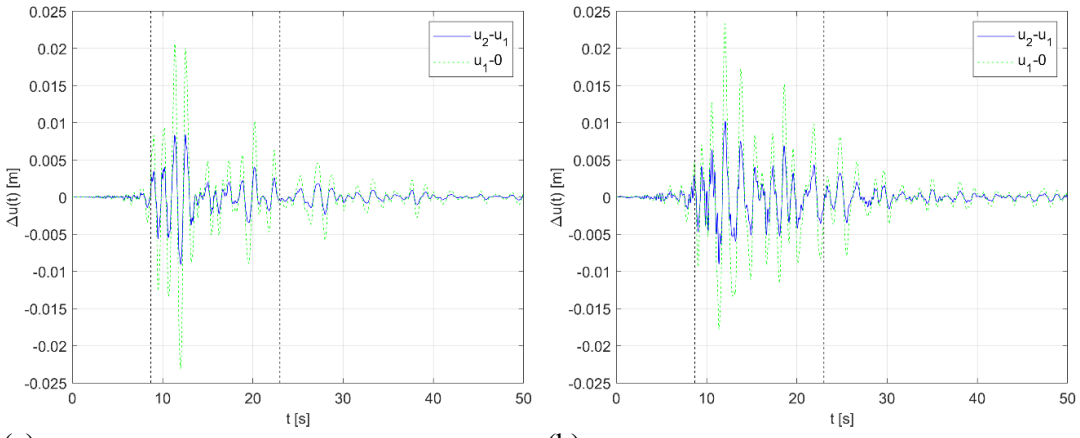

(a) (b)

Figure 63: Inter-floor drift of the first and second floor: (a) X direction; and (b) Y direction.

To conclude, in this chapter, the detection of the seismic damage occurred in a real monitored masonry building has been addressed by identifying the structural response of a grey-box model characterized by hysteretic Bouc-Wen type laws. This allowed the definition of two floor-laws that were used to define a damage index in each direction of the seismic action. The method described followed 3 main steps: (i) calculation of the TFD of the records and instantaneous identification of the model parameters; (ii) check of the identification results, and; (iii) estimate of the damage induced by the seismic event. It is worth mentioning

that mechanical nonlinearity of materials is not the only complex behavior encountered when working with masonry structures, especially heritage buildings. Other examples of very complex behaviors must be charged to the possibility to have different construction phases that characterize the building' materials, and/or the possibility of non-solidarity interactions between the different portions of the investigated structure, e.g. a poor connection between the subparts of systems (wall-wall, floor-wall, etc.). The presence of disconnections can affect the observed dynamic response, corrupting the identification processes if the mathematical models are not able to represent them. In this chapter the latters have not been considered, thus uncertainties in principle remain in the calibration outcomes. For the specific case of the Town Hall of Pizzoli, a global box-like behavior was supposed, also following the results of in situ inspections which led to the verification of the existing of good connections between wall-walls and floor-walls, before the occurrence of the seismic events.

4.5. Appendix 1: Derivation of the basis functions based on the total jerk of the system (differential form)

In this section we want to define the form of the basis functions ${}^{d}\boldsymbol{n}_i(t)$, as well as the form of the experimental record ${}^{d}\boldsymbol{n}_e(t)$ and the unknown parameters ${}^{d}p_i$ by following a differential approach, i.e. by fitting the total jerk of the system. The equations of motion for the analysed systems subjected to the seismic action at the base can be written, for the *d*-th DoF and for an arbitrary direction (X or Y) as:

$$m_d\ddot{\boldsymbol{u}}_d(t) + \boldsymbol{f}_d(t) = \boldsymbol{F}_d(t) = -m_d v_d \boldsymbol{a}(t) \tag{A1}$$

where $\boldsymbol{a}(t)$ is the input acceleration at the base of the structure, $v_d = 1$ is the *d*-th component of the drag vector in the analysed direction, m_d is the reduced lumped mass at the DoF *d*, $\ddot{\boldsymbol{u}}_d(t)$ is the acceleration response at the DoF *d*, while $\boldsymbol{f}_d(t)$ is the *d*-th restoring force. This can be written in differential form (ensuring causality) as:

$$\frac{\partial \boldsymbol{f}_d(t)}{\partial t} = \dot{\boldsymbol{f}}_d(t) = \dot{\boldsymbol{f}}_{d,L}(t) + \dot{\boldsymbol{f}}_{d,NL}(t) \tag{A2}$$

where $\dot{\boldsymbol{f}}_{d,L}(t)$ is a term proportional to the stiffness matrix components, while $\dot{\boldsymbol{f}}_{d,NL}(t)$ is a general nonlinear term:

$$\dot{\boldsymbol{f}}_{d,L}(t) = \sum_{r=D}^{1} \boldsymbol{K}_{dr}(\boldsymbol{\varepsilon}_{dr}(t), t) \cdot \dot{\boldsymbol{u}}_r(t) \tag{A3a}$$

$$\boldsymbol{K}_{dr}(\boldsymbol{\varepsilon}_{dr}(t),t) = K_{0,dr}\cdot\left(1-\delta_{dr}\cdot\boldsymbol{\varepsilon}_{dr}(t)\right) = K_{0,dr} - K_{0,dr}\delta_{dr}\cdot\boldsymbol{\varepsilon}_{dr}(t) \quad \text{(A3b)}$$

$$\dot{\boldsymbol{f}}_{d,NL}(t) = \beta_d\left(\dot{\boldsymbol{u}}_{d-1}(t)-\dot{\boldsymbol{u}}_d(t)\right)\left|\sum_{r=D}^{d}\boldsymbol{f}_d(t)\right|^{N_d} sign\left[\left(\dot{\boldsymbol{u}}_d(t)-\dot{\boldsymbol{u}}_{d-1}(t)\right)\sum_{r=D}^{d}\boldsymbol{f}_d(t)\right] + \gamma_d\left(\dot{\boldsymbol{u}}_{d-1}(t)-\dot{\boldsymbol{u}}_d(t)\right)\left|\sum_{r=D}^{d}\boldsymbol{f}_d(t)\right|^{N_d} - \dot{\boldsymbol{f}}_{d+1,NL}(t) \quad \text{(A3c)}$$

$$\boldsymbol{\varepsilon}_{rd}(t) := \int_0^t \boldsymbol{f}_d(\tau)\dot{\boldsymbol{u}}_r(\tau)d\tau \;\; \forall r \le d, \qquad \boldsymbol{\varepsilon}_{dr}(t) = -\boldsymbol{\varepsilon}_{rd}(t)\;\forall d \ne r \quad \text{(A3d)}$$

with the conditions $\dot{\boldsymbol{u}}_0(t)=0$, $\dot{\boldsymbol{f}}_{D+1,NL}(t)=0$ and D total number of DoFs of the system in a specific direction (each one associated to a lumped mass m_d); r is a free parameter of the summation with step -1, $K_{0,dr}=K_{0,rd}$, $\boldsymbol{\varepsilon}_{dr}(t) = -\boldsymbol{\varepsilon}_{rd}(t)$, $\delta_{dr}=-\delta_{rd}$, $\forall d\ne r$, to enforce the symmetry of the stiffness matrix components $\boldsymbol{K}_{dr}(\boldsymbol{\varepsilon}_{dr}(t),t)$ at each time of the analysis. In (A3) δ_{dr} are the elastic stiffness degradation parameters, $\boldsymbol{\varepsilon}_{dr}(t)$ are the energies dissipated by the system associated to the DoFs d and r, β_d and γ_d are the parameters of the Bouc-Wen type model of hysteresis, while N_d are the exponents parameters of the same Bouc-Wen type model. Thus, with (A3b) it is assumed that the stiffness matrix is linearly proportional to the dissipated energy. Because (A3) define the derivate of the restoring force as a function linearly dependent on the state variable $\dot{\boldsymbol{u}}_d(t)$, the model has rate-independent characteristics. In addition, the presence of $\boldsymbol{f}_d(t)$ in the equations ensure memory. The equations of motion (A1) can be then written as:

$$\boldsymbol{f}_d(t) = -\left(\boldsymbol{a}(t)+\ddot{\boldsymbol{u}}_d(t)\right)m_d = \boldsymbol{g}_d(t)m_d \quad \text{(A4a)}$$

$$\boldsymbol{g}_d(t) = -\left(\boldsymbol{a}(t)+\ddot{\boldsymbol{u}}_d(t)\right) \quad \text{(A4b)}$$

and deriving in time the equations reads:

$$\dot{\boldsymbol{f}}_d(t) = -\left(\dot{\boldsymbol{a}}(t)+\dddot{\boldsymbol{u}}_d(t)\right)m_d = \dot{\boldsymbol{g}}_d(t)m_d \quad \text{(A5a)}$$

$$\dot{\boldsymbol{g}}_d(t) = -\left(\dot{\boldsymbol{a}}(t)+\dddot{\boldsymbol{u}}_d(t)\right) \quad \text{(A5b)}$$

Here $\dot{\boldsymbol{g}}_d(t)$ is the total jerk of the system. Now replacing (A3) in (A2):

$$\dot{\boldsymbol{f}}_d(t) = \sum_{r=D}^{1} K_{0,dr}\cdot\dot{\boldsymbol{u}}_r(t) + \sum_{r=D}^{1} -K_{0,dr}\delta_{dr}\cdot\boldsymbol{\varepsilon}_{dr}(t)\dot{\boldsymbol{u}}_r(t) + \beta_d\left(\dot{\boldsymbol{u}}_{d-1}(t)-\dot{\boldsymbol{u}}_d(t)\right)\left|\sum_{r=D}^{d}\boldsymbol{f}_d(t)\right|^{N_d} sign\left[\left(\dot{\boldsymbol{u}}_d(t)-\dot{\boldsymbol{u}}_{d-1}(t)\right)\sum_{r=D}^{d}\boldsymbol{f}_d(t)\right] + \gamma_d\left(\dot{\boldsymbol{u}}_{d-1}(t)-\dot{\boldsymbol{u}}_d(t)\right)\left|\sum_{r=D}^{d}\boldsymbol{f}_d(t)\right|^{N_d} - \dot{\boldsymbol{f}}_{d+1,NL}(t) \quad \text{(A6)}$$

then, replacing (A6) in (A5a) and dividing by m_d, if N_d are supposed to be known, it is possible to obtain an equation in the form of (6):

$$\sum_{r=D}^{1} K_{0,dr} \cdot \dot{\boldsymbol{u}}_r(t) + \sum_{r=D}^{1} -K_{0,dr}\delta_{dr} \cdot \boldsymbol{\varepsilon}_{dr}(t)\dot{\boldsymbol{u}}_r(t) + \beta_d\big(\dot{\boldsymbol{u}}_{d-1}(t) - \dot{\boldsymbol{u}}_d(t)\big)\Big|\sum_{r=D}^{d} \boldsymbol{f}_d(t)\Big|^{N_d} sign\Big[\big(\dot{\boldsymbol{u}}_d(t) - \dot{\boldsymbol{u}}_{d-1}(t)\big)\sum_{r=D}^{d} \boldsymbol{f}_d(t)\Big] + \gamma_d\big(\dot{\boldsymbol{u}}_{d-1}(t) - \dot{\boldsymbol{u}}_d(t)\big)\Big|\sum_{r=D}^{d} \boldsymbol{f}_d(t)\Big|^{N_d} \cong \dot{\boldsymbol{g}}_d(t) + \frac{\dot{\boldsymbol{f}}_{d+1,NL}(t)}{m_d} \tag{A7}$$

Where the equality has been substituted by the similarity because in this study the time dependent variables are supposed to be taken from experimental campaigns. A direct comparison between (A7) and (6 allows to define the form of the basis functions ${}^{d}\boldsymbol{n}_i(t)$, as well as the form of the experimental record ${}^{d}\boldsymbol{n}_e(t)$ and the unknown parameters ${}^{d}p_i$. These quantities are defined as follow:

$${}^{d}p_i = \begin{cases} K_{0,dr}\ \forall r, & 1 \le i \le D\ \forall i\ \in \mathbb{N} \\ K_{0,dr}\delta_{dr}\ \forall r, & (D+1) \le i \le 2D\ \forall i\ \in \mathbb{N} \\ \beta_d, & i = 2D+1 \\ \gamma_d, & i = 2D+2 \end{cases} \tag{A8}$$

$${}^{d}\boldsymbol{n}_i(t) = \begin{cases} \frac{\dot{\boldsymbol{u}}_r(t)}{m_d}\ \forall r, & 1 \le i \le D\ \forall i\ \in \mathbb{N} \\ \frac{\boldsymbol{\varepsilon}_{dr}(\tau)\dot{\boldsymbol{u}}_r(\tau)}{m_d}\ \forall r, & (D+1) \le i \le 2D\ \forall i\ \in \mathbb{N} \\ {}^{d}\boldsymbol{n}_{2D+1}(t), & i = 2D+1 \\ \frac{\left(\dot{\boldsymbol{u}}_{d-1}(\tau) - \dot{\boldsymbol{u}}_d(\tau)\right)}{m_d}\Big|\sum_{r=D}^{d} \boldsymbol{f}_d(\tau)\Big|^{N_d}, & i = 2D+2 \end{cases} \tag{A9a}$$

$${}^{d}\boldsymbol{n}_{2D+1}(t) = \frac{\left(\dot{\boldsymbol{u}}_{d-1}(\tau) - \dot{\boldsymbol{u}}_d(\tau)\right)}{m_d}\Big|\sum_{r=D}^{d} \boldsymbol{f}_d(\tau)\Big|^{N_d} \cdot sign\Big[\big(\dot{\boldsymbol{u}}_d(\tau) - \dot{\boldsymbol{u}}_{d-1}(\tau)\big)\sum_{r=D}^{d} \boldsymbol{f}_d(\tau)\Big] \tag{A9b}$$

$${}^{d}\boldsymbol{n}_e(t) = \dot{\boldsymbol{g}}_d(t) + \frac{\dot{\boldsymbol{f}}_{d+1,NL}(t)}{m_d} + \frac{\dot{\boldsymbol{f}}_{d,KL}(t)}{m_d} \tag{A10}$$

with the condition $\dot{\boldsymbol{f}}_{D,KL}(t) = 0$. $\dot{\boldsymbol{f}}_{d,KL}(t)$ is a known function that depend only by the symmetric parameter and functions already found (i.e. $K_{0,rd} = K_{0,dr}$, $\boldsymbol{\varepsilon}_{rd}(t) = -\boldsymbol{\varepsilon}_{dr}(t)$, $\delta_{rd} = -\delta_{dr}$, $\forall r \neq d$).

4.6. References chapter 4

Ashrafi, S. S. (2008). Adaptive parametric identification scheme for a class of nondeteriorating and deteriorating nonlinear hysteretic behavior.

Baber, T. N. (1986). Modeling general hysteresis behaviour and random vibration applications. Journal of Vibration Acoustics Stress and Reliability in Design, 108, 411-420.

Baber, T., & Noori, M. (1985). Random vibration of degrading pinching systems. Journal of Engineering Mechanics ASCE, 111, 1010-1026.

Baber, T., & Wen, Y.-K. (1981). Random vibrations of hysteretic, degrading systems. J. Eng. Mech. Div. ASCE, 107, 1069–1087.

Benedettini, F. C. (1995). Identification of hysteretic oscillators under earthquake loading by nonparametric models. J. Eng. Mech., 121, 606–612.

Bouc, R. (1971). Mode` le mathe´matique d'hyste´re´sis. Acustica, 24, 16–25.

Bursi, O. C. (2009). Identification of the damage evolution in a benchmark steel-concrete composite structure during Pseudo-Dynamic testing. CompDyn.

Bursi, O. C. (2012). Identification of the hysteretic behaviour of a partial-strength steel–concrete moment-resisting frame structure subject to pseudodynamic tests. Earthquake Engng Struct. Dyn., 41, 1883–1903.

Carmona, R. H. (1998). Practical Time-Frequency Analysis. Academic Press.

Ceravolo, R. (2004). Use of instantaneous estimators for the evaluation of structural damping. J. Sound Vib., 274, 385–401.

Ceravolo, R. (2009). Time-frequency analysis. Encyclopedia of Structural Health Monitoring, 503–524.

Ceravolo, R. D. (2010). Instantaneous identification of degrading hysteretic oscillators under earthquake excitation. Struct. Health Monitor., 9, 447–464.

Ceravolo, R. D., & Erlicher, S. (2007). Instantaneous identification of Bouc-Wen-type hysteretic systems from seismic response data. Key Eng. Mat., 347, 331–338.

Ceravolo, R. D., & Molinari, F. (2001). Developments and comparisons on the definition of an instantaneous damping estimator for structures under natural excitation. Key Eng. Mat., 231–240.

Ceravolo, R. E. (2013). Comparison of restoring force models for the identification of structures with hysteresis and degradation. Journal of Sound and Vibration, 332, 6982-6999.

Chassiakos, A. M. (1995). Adaptive methods for the identification of hysteretic structures. Proceedings ofthe American Control Conference, 2349–2353.

Du, X., & Wang, F. (2010). Modal identification based on Gaussian continuous time autoregressive moving average model. J. of Sound and Vib., 329, 4294–4312.

Hammond, J. W. (1996). The analysis of non-stationary signals using time-frequency methods. J. of Sound and Vib., 190, 419–447.

Hernandez-Garcia, M. M. (2010). An experimental investigation of change detection in uncertain chain-like systems. J. of Sound and Vib, 329, 2395–2409.

Ikhouane, F., & Rodellar, J. (2005). On the hysteretic Bouc–Wen model. Nonlinear Dynamics, 78, 42-63.

Kyprianou, A. W. (2001). Identification of hysteretic systems using differential evolution algorithm. J. Sound Vib., 248, 289–314.

Loh, C. M. (2010). System identification and damage evaluation of degrading hysteresis of reinforced concrete frames. Earthquake Engng. Struct. Dyn.

Ma, F. N. (2006). On system identification and response prediction of degrading structures. Structural Control and Health Monitoring, 13, 347–364.

Masri SF, C. T. (1979). A nonparametric identification technique for nonlinear dynamic problems. Journal of Applied Mechanics(46), 433–447.

Masri, S. C. (2004). Identification of the state equation in complex non-linear systems. Int. J. Nonlinear Mech., 39, 1111–1127.

Pai, P. H., & Langewisch, D. (2008). Time-frequency method for nonlinear system identification and damage detection. Struct. Health Monit., 7, 103–127.

Pei, J.-S. S. (2004). Analysis andmodification ofVolterra/Wiener neural networks for the adaptive identification of non-linear hysteretic dynamic systems. J. Sound Vib., 275, 693–718.

Smyth, A. K. (2000). Parametric and nonparametric adaptive identification of nonlinear structural systems. Proceedings of the American Control Conference, 978–998.

Smyth, A. M. (1999). On-line parametric identification of MDOF nonlinear hysteretic systems. ASCE Journal of Engineering Mechanics, 125, 133–142.

Smyth, A. M. (2002). Development of adaptive modelling techniques for non-linear hysteretic systems. Int. J. Nonlinear Mech., 37, 1435–1451.

Spiridonakos, M. P. (2010). Output-only identification and dynamic analysis of time-varying mechanical structures under random excitation: A comparative assessment of parametric methods. J. of Sound and Vib., 329, 768–785.

Wen, Y.-K. (1976). Method for random vibration of hysteretic systems. J. Eng. Mech. Div. ASCE, 102, 249–263.

Worden, K. T. (2001). Nonlinearity in structural dynamics: detection, identification, and modelling. Institute of Physics Publishing: Philadelphia.

Wu, M., & Smyth, A. (2008). Real-time parameter estimation for degrading and pinching hysteretic models. Int. J. of Non-Linear Mech, 43, 822–833.

Chapter 5

Hybrid simulation/testing of masonry structures: test design for distributed mass systems with distributed interfaces

Hybrid simulation has been extensively applied for seismic response history analysis of steel and concrete frame structures. For these systems, subdomain partitioning follows storey levels and nodal (punctual) joints among beam/column-like elements. However, in the case of masonry structures, distributed interfaces characterize system subdomains, and in principle, several actuators should be used to impose the correct boundary conditions to the tested specimen. This chapter presents a new substructuring method for distributed mass systems with distributed interfaces, which aims to reduce the number of actuators necessary to achieve a predetermined coupling accuracy between physical and numerical subdomains. With the proposed methodology, a linear interface between the numerical and physical subdomain is proposed to link the two substructures. Then, Principal Component Analysis (PCA) is employed to define master and slave degrees of freedom in the reduction process, which allows the definition of a testing setup for distributed systems. Master degree of freedoms will define the position and direction of actuators. The numerical validation of this procedure is illustrated for a masonry building facade system.

Part of the work described in this chapter was also previously exposed in conference.

5.1. Introduction

Hybrid Simulation (HS), which is also known as Hardware-in-the-Loop (HiL) testing, has been introduced in the 1970s to simulate the seismic response of civil structures (Takanashi et al., 1975), (Stojadinovic et al., 2006). The hybrid model of the emulated system combines Numerical and Physical Subdomains (NS and PS) and its dynamic response to a realistic excitation is simulated using a numerical time-stepping response history analysis. A computer-controlled system applies displacements to the PS using hydraulic/electric servo-actuators and corresponding restoring forces are measured from these Degrees of Freedoms (DoFs) using load cells and fed back to the hybrid model. Then the equations of motion are solved at the next time step. When the response of the PS does not depend on the rate of loading, a Pseudo Dynamic (PSD) HS can be performed at an extended time scale, typically in the broad range of 50-200 times slower than the actual earthquake, requiring inertia and damping forces to be modelled numerically. Real-time (RT) HS is a special case of PSD-HS when a unit time scale is applied. Lack of reliable mathematical models or strongly nonlinear responses justify the experimental substructuring of a system subcomponent, i.e. the PS, while well-known subparts are instantiated in a numerical simulation software, namely computational environment, as NS.

HS has been extensively applied for seismic response history analysis of steel and concrete frame structures. However, there is still a paucity of applications to masonry structures. About that, Paquette and Bruneau, (Paquette & Bruneau, 2003), (Paquette & Bruneau, 2006), used PSD-HS to understand the flexible-floor/rigid-unreinforced-wall interaction during earthquake and the effectiveness of the use of fiberglass strips for retrofitting purposes. Pinto and co-workers, (Pinto et al., 2001), performed PSD-HS of different historical constructions subjected to earthquake loading. The extreme sensitivity of friction-based analytic models with respect to assumed friction coefficients motivated Buonopane and White to simulate the seismic response of a frame infilled with masonry by means of PSD-HS, (Buonopane & White, 1999). Along the same line, (Mosalam et al., 1998), assessed the seismic performance of a multi-story infilled frame through PSD-HS and observed a strong correlation between wall damage and hysteretic energy dissipation.

In all these cases, an entire facade of a masonry building was substructured in the laboratory and treated as a frame with storey masses lumped at the corresponding levels. However, this is not possible, for example, when only a portion of the wall is substructured in the laboratory and distributed boundaries characterize subdomain interfaces. In this case, several actuators should be used to impose the correct boundary condition to the PS, (Hashemi & Mosqueda, 2014), (Bakhaty et al., 2016). This perspective motivated to develop, in the present chapter, a new substructuring method for distributed mass systems with distributed interfaces. The procedure is illustrated for a virtual case study

consisting on a simple Planar Masonry Facade System (PMFS) subjected to gravity and seismic loads. A portion of the PMFS is supposed to be substructured in the laboratory as floating PS while the remainder is treated as NS.

In common practice, a geometric transformations eliminate rigid body translations and rotations and the only deformational component of the PS displacement response is applied to the tested specimen, which is typically fixed to a loading frame. Accordingly, a Reference (R) Finite Element (FE) partitioned model of the structure is implemented in Matlab, (Matlab, 2016), and separated analyses of deformational components of the PS response owing to gravity and seismic loads support the determination of simplified coupling conditions. In order to impose piecewise affine displacement fields along subdomain boundaries and reduce the number of connected nodes, rigid Interface Super-elements (ISs) are introduced on both NS and PS boundaries. In detail, rigid beam and link elements forms the NS ISs while steel frames, anchors and connection rods form the PS interface ISs, which imposes simplified interface boundary conditions to the PS in the laboratory. A Modified FE (M-FE) partitioned model of the PMFS, which incorporates rigid ISs, is used to validate the proposed approach in pure numerical simulation. Finally, a possible experimental setup is illustrated, which is based on a typical three-actuator setup used for PSD-HS test of masonry walls.

5.2. Description of the case study

This section describes the Planar Masonry Facade System (PMFS) as well as the Reference Finite Element (R-FE) partitioned model used to validate the substructuring method.

5.2.1. Planar masonry facade system

A rectangular shape of 9.6 x 6.6 m size with three openings and a uniform wall thickness of equal to 0.6 m characterizes the geometry of the PMFS, which is reported in Figure 64a.

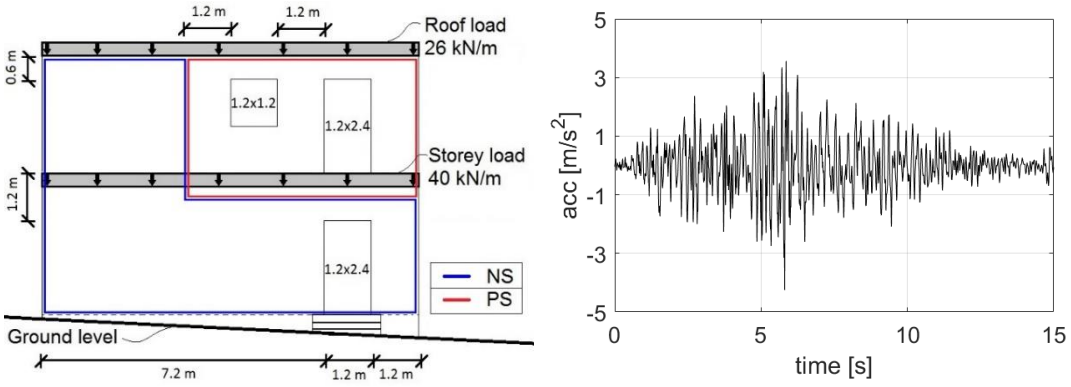

(a) (b)

Figure 64: Planar Masonry Facade System with applied loads: (a) geometry of the PMFS with static loads; and (b) record of Loma Prieta earthquake, 1989.

The PMFS carries gravity loads owing to self-weight and storey masses (equal to 40 kN/m and 26 kN/m for the first and last floor, respectively), and it is subjected to a transversal seismic excitation, which is represented by an accelerogram of the Loma Prieta earthquake of 1989 recorded from the UCSC station; see Figure 64b in this respect. In order to observe the crack pattern in the proximity of the upper openings, a portion of the PMFS is virtually substructured in the laboratory (PS) whilst the remaining portion of the PMFS is simulated in the computer (NS).

5.2.2. Numerical modelling

In order to simulate the hybrid physical/numerical substructuring of the PMFS a 196-nodes and 156-elements R-FE partitioned model was implemented in Matlab environment, (Matlab, 2016), according to partitioning scheme of Figure 64. To this end, a linear 4-node membrane element was coded in MATLAB and verified against Ansys' plane element, (Ansys, 2016), as reference benchmark. A uniform linear isotropic elastic material was assigned to the entire PMFS, which is characterized by Young elastic modulus E of 0.650 GPa, Poisson ratio υ equal to 0.35 and density ρ of 1900 kg/m^3. Figure 65 shows the R-FE partitioned model of the PMFS with NS and PS partitioning highlighted.

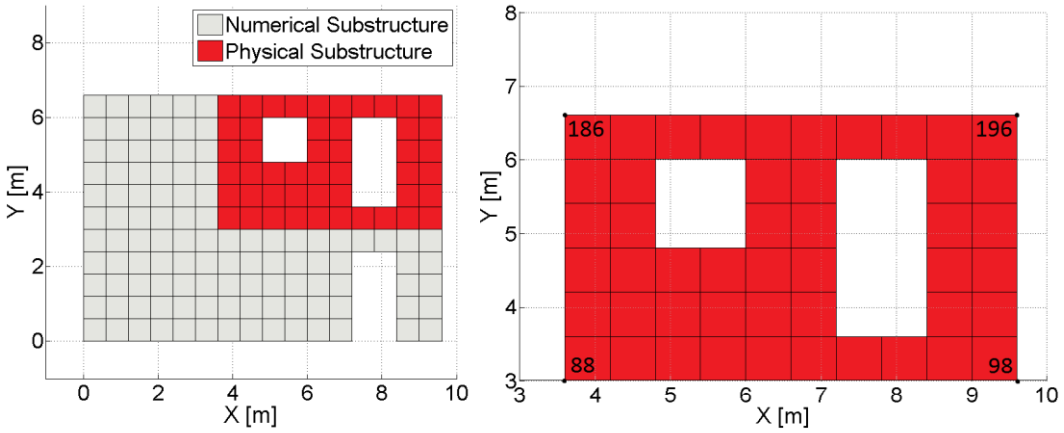

(a) (b)

Figure 65: R-FE partitioned model of the PMFS.

For the sake of clarity, a generic system DoF is indicated with the corresponding node number and direction of the displacement component, e.g. 196-X corresponds to the X displacement of node 196. In order to retain all substructure interface DoFs, a dual-assembly procedure based on Localized Lagrange Multipliers (LLM) was used to derive the coupled equations of motion, (Park, et al., 2000), which reads:

$$\begin{cases} \mathbf{M}^N\ddot{\mathbf{u}}^N + \mathbf{C}^N\dot{\mathbf{u}}^N + \mathbf{K}^N\mathbf{u}^N = \mathbf{L}^{N^T}\boldsymbol{\Lambda}^N + \mathbf{F}^N(t) \\ \mathbf{M}^P\ddot{\mathbf{u}}^P + \mathbf{C}^P\dot{\mathbf{u}}^P + \mathbf{K}^P\mathbf{u}^P = \mathbf{L}^{P^T}\boldsymbol{\Lambda}^P + \mathbf{F}^P(t) \end{cases} \quad (48a)$$

$$\begin{cases} \mathbf{L}^N\dot{\mathbf{u}}^N + \bar{\mathbf{L}}^N\dot{\mathbf{u}}_g = \mathbf{0} \\ \mathbf{L}^P\dot{\mathbf{u}}^P + \bar{\mathbf{L}}^P\dot{\mathbf{u}}_g = \mathbf{0} \end{cases} \quad (48b)$$

$$\bar{\mathbf{L}}^{N^T}\boldsymbol{\Lambda}^N + \bar{\mathbf{L}}^{P^T}\boldsymbol{\Lambda}^P = \mathbf{0} \quad (48c)$$

In this specific case, superscripts N and P refer to NS and PS subdomains, respectively. With regard to a generic subdomain l, $\mathbf{M}^{(l)}$, $\mathbf{C}^{(l)}$ and $\mathbf{K}^{(l)}$ are the mass, damping and stiffness matrices while $\ddot{\mathbf{u}}^{(l)}$, $\dot{\mathbf{u}}^{(l)}$ and $\mathbf{u}^{(l)}$ denote acceleration, velocity and displacement vectors. $\mathbf{L}^{(l)}$ and $\bar{\mathbf{L}}^{(l)}$ are Boolean signed matrices that collocates interface DoFs within the single subdomain and the reference DoF vector, respectively. Vector $\mathbf{F}^{(l)}(t)$ represents the external time-varying load. Lagrange multiplier vectors $\boldsymbol{\Lambda}^{(l)}$ represent interface force fields enforcing kinematic compatibility among subdomains and the reference DoF vector, $\mathbf{u}_g$. Figure 66 summarizes the main results of the modal analysis of the R-FE partitioned model.

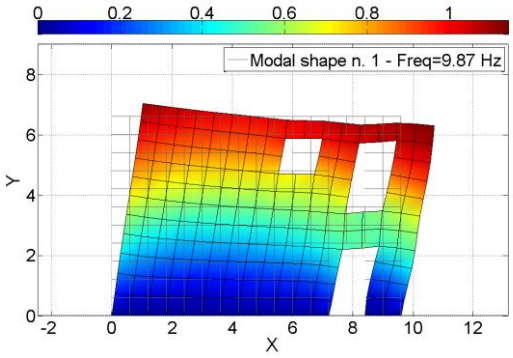

(a)

Mode	*Frequency [Hz]*
1	9.87
2	21.69
3	22.87
4	25.33
5	28.51

(b)

Figure 66: Modal analysis of the PMFS: (a) first modal shape; and (b) first five frequencies of the model.

As shown in Figure 66, the first mode is characterized by the global translation of the PMFS along the X direction.

5.3. Simplified coupling conditions

5.3.1. Deformational response of the physical substructure

In the common practice of HS, a geometric transformation compensates the rigid-body response the PS, which is constrained to a loading frame, and the sole deformational component of the PS response is applied to the tested specimen. Rigid body modes of the PS are defined as:

$$\boldsymbol{\Phi}^P = ker(\mathbf{K}^P) \quad (49)$$

where $ker(\cdot)$ is the kernel of a generic matrix $(\cdot)$. In order to extract the pure deformational component of the PS response, a specific number of DoFs equal to the number of rigid body modes is constrained. Figure 67 depicts the constraint setting of the PS.

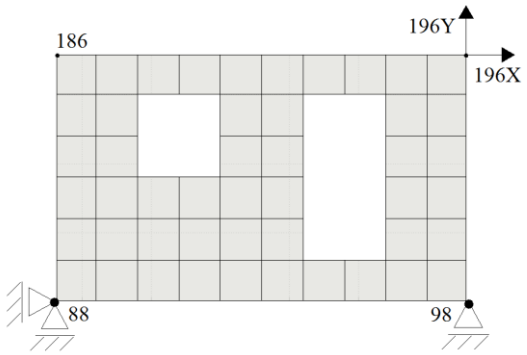

(a)

List of constrained DOFs	
Node	***Direction***
88	X
88	Y
89	Y

(b)

Figure 67: Constraint setting of the PS: (a) constrained PS; and (b) list of constrained DoFs.

The pure deformational component of the PS response, which is applied to the tested specimen, reads:

$$\tilde{\mathbf{u}}_k^{P,r} = \mathbf{u}_k^{P,r} + \boldsymbol{\Phi}^{P,r}\boldsymbol{\alpha}_k^P \tag{50}$$

where the rigid body response vector, $\boldsymbol{\alpha}_k^P$, is calculated as:

$$\boldsymbol{\alpha}_k^P = -\boldsymbol{\Phi}^{P,c^{-1}}\mathbf{u}_k^{P,c} \tag{51}$$

with:

$$\boldsymbol{\Phi}^P = \begin{bmatrix}\boldsymbol{\Phi}^{P,r}\\ \boldsymbol{\Phi}^{P,c}\end{bmatrix}, \mathbf{u}_k^P = \begin{bmatrix}\mathbf{u}_k^{P,r}\\ \mathbf{u}_k^{P,c}\end{bmatrix} \tag{52}$$

where superscripts r and c stand for retained and constrained DoFs, whilst subscript k represents a generic time step of the response history.

5.3.2. Static analysis considering gravity loads

The static analysis of the coupled system response is performed using a version of the algorithm proposed by Farhat and Roux, (Farhat & Roux, 1991), enhanced to the LLM framework, (Park et al., 2000). Accordingly, loading vectors $\mathbf{F}^N(t)$ and $\mathbf{F}^P(t)$ include gravity loads only.

$$\mathbf{F}^{(l)}(t) = -\mathbf{M}^{(l)}\mathbf{T}_g^{(l)}g \tag{53}$$

In (53) the subscripts, l, indicate a generic subdomain while $\mathbf{T}_g^{(l)}$ is a Boolean vector defined according to the direction of the gravity acceleration, g. Figure 68 depicts the pure deformational component of the displacement response of the PS subjected to gravity loads only.

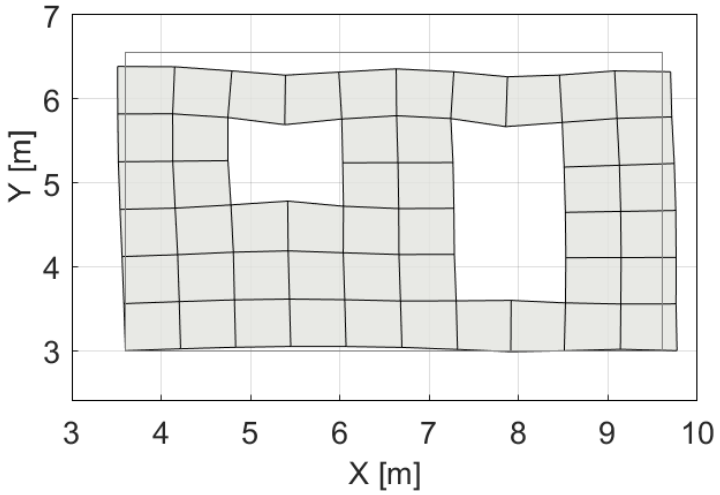

Figure 68: Deformed shape of the PS owing to gravity load.

As shown in Figure 68, the static analysis reveals an almost uniform lowering of the top of the wall.

5.3.3. Principal component analysis of the seismic response

A version of the time integration algorithm proposed by Gravouil and Combescure, (Gravouil & Combescure, 2001), enhanced to LLM framework, (Park et al., 2000), was used to simulate the dynamic response of the R-FE partitioned model subjected to seismic load. In this case, loading vectors $\mathbf{F}^N(t)$ and $\mathbf{F}^P(t)$ are defined as:

$$\mathbf{F}^{(l)}(t) = -\mathbf{M}^{(l)}\mathbf{T}_{a_g}^{(l)}a_g(t) \tag{54}$$

where the subscripts, l, indicate a generic subdomain, while $\mathbf{T}_{a_g}^{(l)}$ is a Boolean vector defined according to the direction of the seismic acceleration $a_g(t)$. Then, Principal Component Analysis (PCA) was applied to a dataset $\mathbf{X}$ corresponding to the deformational component of the PS calculated in with (50).

$$\mathbf{X} = \left[\tilde{\mathbf{u}}_1^{P,r} \quad \ldots \quad \tilde{\mathbf{u}}_n^{P,r}\right] \tag{55}$$

The key idea of PCA is to provide a separated representation of a certain number of correlated variables considering a smaller number of uncorrelated variables while preserving the overall process variance. An orthogonal transformation to the basis of the eigenvectors of the sample covariance matrix is

performed, and the data are projected onto the subspace spanned by the eigenvectors corresponding to eigenvalues sorted in descending order, (Kerschen et al., 2005). This transformation decorrelates the signal components and maximizes the preserved variance. In detail, for any real (m x n) matrix $\mathbf{X}$ there exists a real factorization called Singular Value Decomposition (SVD) that can be written as:

$$\mathbf{X} = \mathbf{U}\boldsymbol{\Sigma}\mathbf{V}^T \tag{56}$$

where $\mathbf{U}$ is an (m x m) orthonormal matrix whose columns $\mathbf{u}_i$, namely the left singular vectors, represents the Proper Orthogonal Modes (POMs) while $\mathbf{V}$ is an (n x n) orthonormal matrix, whose column vectors $\mathbf{v}_i$, namely the right singular vectors, represent the time modulation of the corresponding POMs. $\boldsymbol{\Sigma}$ is an (m x n) pseudo-diagonal and semi-positive definite matrix with singular values σ_i as diagonal entries. Singular values relate to the eigenvalues of the autocovariance matrix of the process $\mathbf{X}$ as:

$$\{\sigma_1^2 \quad \dots \quad \sigma_m^2\} = eig\left((\mathbf{X} - \boldsymbol{\mu}_\mathbf{X})(\mathbf{X} - \boldsymbol{\mu}_\mathbf{X})^T\right) \tag{57}$$

where $\boldsymbol{\mu}_\mathbf{X}$ is a matrix of repeated vectors of time averaged values of $\mathbf{X}$. Since gravity (constant) loads are excluded, $\boldsymbol{\mu}_\mathbf{X}$ is almost null and thus very small compared to $\mathbf{X}$. Accordingly, the original data set $\mathbf{X}$ can be reconstructed up to the desired degree of approximation by retaining a reduced number $q < m$ of POM:

$$\left(\widetilde{\mathbf{X}} - \boldsymbol{\mu}_\mathbf{X}\right) = \sum_{i=1}^{q} \sigma_i \mathbf{u}_i \mathbf{v}_i^T \tag{58}$$

The energy fraction carried by the i-th POM is defined as $E_i = \sigma_i^2 / E$, where E is total data energy $E = \sum_{i=1}^{m} \sigma_i^2$. Figure 69a reports the energy fraction of the first ten POMs.

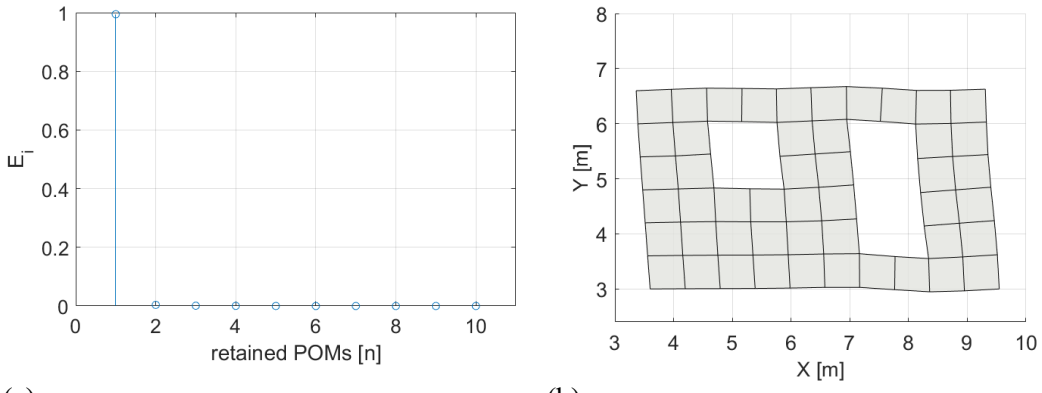

(a) (b)

Figure 69: Proper Orthogonal modes: (a) distribution of POM energy; and (b) first POM's deformed shape.

As can be appreciated from Figure 69a, the almost total energy of the deformational component of the displacement response of the PS is carried by the first POM, which is depicted in Figure 69b.

5.4. Validation of the substructuring method

In order to impose piecewise affine displacement fields along subdomain boundaries and reduce the number of connected nodes, rigid ISs are applied on both NS and PS boundaries. Figure 70 depicts the Modified (M)-FE partitioned model of the PMFS including ISs, which was used to validate the presented substructuring method.

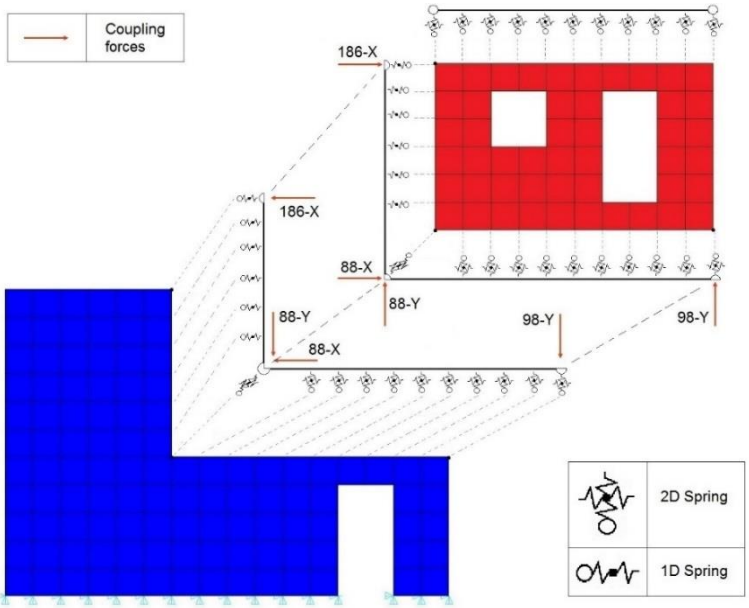

Figure 70: M-FE partitioned model of the PMFS.

As can be appreciated from Figure 70, both ISs are based on rigid spring and beam elements, which enforce affine displacement fields along PS and NS boundaries. In detail, simplified coupling conditions neglect continuity of vertical and horizontal shear along the vertical and horizontal edges of the PS interface, respectively. As a result, the number of coupled DoFs is reduced to 4. The system of coupled equations of motion of the M-FE partitioned model becomes:

$$\begin{cases} \mathbf{M}^{N,I}\ddot{\mathbf{u}}^{N,I} + \mathbf{C}^{N,I}\dot{\mathbf{u}}^{N,I} + \mathbf{K}^{N,I}\mathbf{u}^{N,I} = \mathbf{L}^{N,I^T}\boldsymbol{\Lambda}^{N,I} + \mathbf{F}^{N,I}(t) \\ \mathbf{M}^{N}\ddot{\mathbf{u}}^{N} + \mathbf{C}^{N}\dot{\mathbf{u}}^{N} + \mathbf{K}^{N}\mathbf{u}^{N} = \mathbf{L}^{N^T}\boldsymbol{\Lambda}^{N} + \mathbf{F}^{N}(t) \\ \mathbf{M}^{P,I}\ddot{\mathbf{u}}^{P,I} + \mathbf{C}^{P,I}\dot{\mathbf{u}}^{P,I} + \mathbf{K}^{P,I}\mathbf{u}^{P,I} = \mathbf{L}^{P,I^T}\boldsymbol{\Lambda}^{P,I} + \mathbf{F}^{P,I}(t) \\ \mathbf{M}^{P}\ddot{\mathbf{u}}^{P} + \mathbf{C}^{P}\dot{\mathbf{u}}^{P} + \mathbf{K}^{P}\mathbf{u}^{P} = \mathbf{L}^{P^T}\boldsymbol{\Lambda}^{P} + \mathbf{F}^{P}(t) \end{cases} \tag{59a}$$

$$\begin{cases} \mathbf{L}^{N,I}\dot{\mathbf{u}}^{N,I} + \bar{\mathbf{L}}^{N,I}\dot{\mathbf{u}}_g = \mathbf{0} \\ \mathbf{L}^{N}\dot{\mathbf{u}}^{N} + \bar{\mathbf{L}}^{N}\dot{\mathbf{u}}_g = \mathbf{0} \\ \mathbf{L}^{P,I}\dot{\mathbf{u}}^{P,I} + \bar{\mathbf{L}}^{P,I}\dot{\mathbf{u}}_g = \mathbf{0} \\ \mathbf{L}^{P}\dot{\mathbf{u}}^{P,D} + \bar{\mathbf{L}}^{P}\dot{\mathbf{u}}_g = \mathbf{0} \end{cases} \tag{59b}$$

$$\bar{\mathbf{L}}^{N,I^T}\boldsymbol{\Lambda}^{N,I} + \bar{\mathbf{L}}^{N^T}\boldsymbol{\Lambda}^{N} + \bar{\mathbf{L}}^{P,I^T}\boldsymbol{\Lambda}^{P,I} + \bar{\mathbf{L}}^{P^T}\boldsymbol{\Lambda}^{P} = \mathbf{0} \tag{59c}$$

where subscripts *N,I* and *P,I* refer to numerical and physical ISs, respectively. The static response of the modified partitioned model was calculated with a version of the FR algorithm, (Farhat & Roux, 1991), enhanced to LLM framework, while the following time history analysis was calculated with a version of (Gravouil & Combescure, 2014), enhanced to LLM framework. Figure 71 compares the displacement response of DoF 196-X and DoF 196-Y obtained from the R-FE and M-FE partitioned models.

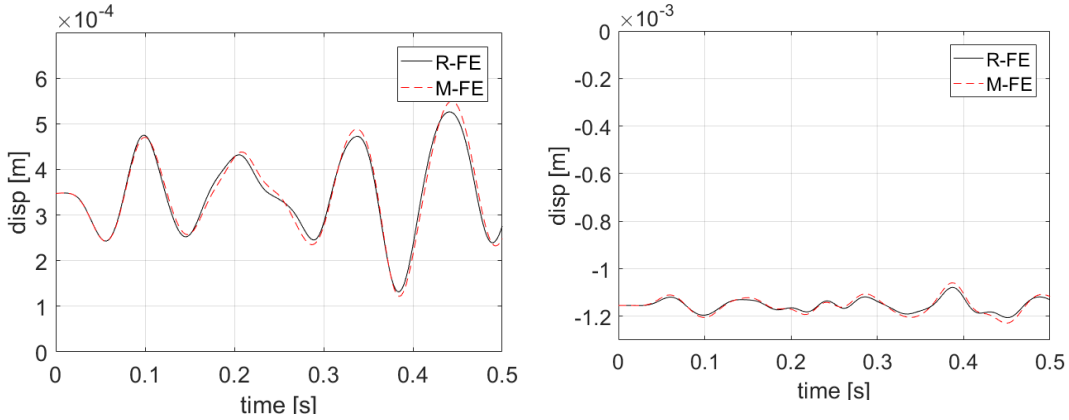

(a) (b)

Figure 71: Displacement response of the M-FE partitioned model: (a) DoF 196-X; and (b) DoF 196-Y.

As can be appreciated from Figure 71, the M-FE partitioned model accurately reproduces both horizontal and vertical displacement responses of the R-FE partitioned model. Figure 72 depicts a possible experimental setup for the PS.

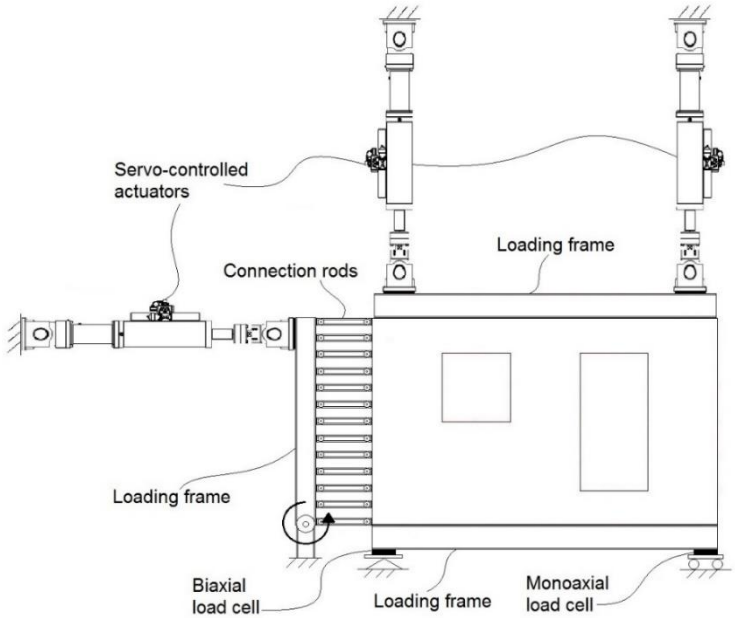

Figure 72: Experimental setup obtained with the proposed test design

procedure.

As shown in the figure, rigid frames, anchors and connecting rods form the physical IS and impose an affine interface displacement field to the PS, which is tested in statically determined configuration. Load cells installed on actuators and supports measure restoring force feedbacks.

To conclude, in this chapter a new substructuring method for performing hybrid simulation of masonry structures, which are characterized by distributed physical and numerical subdomain boundaries is proposed. The PS can be either floating or fixed. Rigid interface super-elements are introduced to impose affine displacement fields at subdomain boundaries with a reduced number of connection degrees-of-freedom, which allows for reducing the number of actuators of the relevant experimental setup. In detail, rigid beam and link elements forms the NS interface super-element while steel frames, anchors and connection rods form the PS interface super-element. The numerical validation of this procedure is illustrated for a planar masonry facade system, which is virtually substructured to allow an easy implementation of PSD-HS of structures constituted by masonry walls.

5.5. References chapter 5

Ansys, Ansys Academic Research, Release 16.2, 2016.

Bakhaty, A.A., Govindjee, S., and Mosalam, K.M. (2016). "Theoretical Evaluation of Hybrid Simulation Applied to Continuous Plate Structures." Journal of Engineering Mechanics, 142(12).

Buonopane, S.G. and White, R.N. (1999). "Pseudodynamic testing of masonry infilled reinforced concrete frame." J. Struct. Eng., ASCE 125, 578-589.

Farhat, C. and Roux, F.-X. (1991). "A method of finite element tearing and interconnecting and its parallel solution algorithm." Int J Num Meth Engng, 32, 1205-1227, doi: 10.1002/nme.1620320604.

Gravouil, A., Combescure, A. (2001). "Multi-time-step explicit – implicit method for non-linear structural dynamics." International Journal for Numerical Methods in Engineering, 199-225.

Hashemi, M.J., and Mosqueda, G. (2014). "Innovative substructuring technique for hybrid simulation of multistory buildings through collapse." Earthquake Engineering and Structural Dynamics, doi:10.1002/eqe.2427.

Kerschen, G., Golinval, J., Vakakis, A.F. and Bergman L. (2005). "The Method of Proper Orthogonal Decomposition for Dynamical Characterization and

Order Reduction of Mechanical Systems: An Overview." Nonlinear Dynamics, 41(1-3), 147–169, doi:10.1007/s11071-005-2803-2.

Matlab and Statistics Toolbox Release R2016b, The MathWorks, Inc., Natick, Massachusetts, United States.

Mosalam, K.M., White, R.N. and Ayala, G. (1998). "Response of infilled frames using pseudo-dynamic experimentation." Earthquake Engineering and Structural Dynamics, 27, 589-608.

Paquette, J. and Bruneau, M. (2003). "Pseudo-Dynamic Testing of Unreinforced Masonry Building with Flexible Diaphragm." M. ASCE2, DOI: 10.1061/~ASCE!0733-9445~2003!129:6~708!.

Paquette, J., Bruneau, M. (2006). "Pseudo-dynamic testing of unreinforced masonry building with flexible diaphragm and comparison with existing procedures." Construction and Building Materials, 20, 220-228.

Park K.C., Felippa C.A., Gumaste U.A. (2000). "A localized version of the method of Lagrange multipliers and its applications." Computational Mechanics, 24, 476-490.

Pinto, A., Molina, J., Pegon, P., Renda, V. (2001). "Protection of the cultural heritage at the ELSA Laboratory." ELSA, IPSC, Joint Research Centre, European Commission, I-21020 Ispra (VA), Italy.

Stojadinovic, B., Mosqueda, G. and Mahin S.A. (2006). "Event-Driven Control System for Geographically Distributed Hybrid Simulation." ASCE Journal of Structural Engineering, 132(1), 68-77.

Takanashi, K., Udagawa, K., Seki, M., Okada, T. and Tanaka, H. (1975). "Non-linear earthquake response analysis of structures by a computer-actuator on-line system." Bulletin of Earthquake Resistant Structure Research Center, Institute of Industrial Science, University of Tokyo, Tokyo.

Chapter 6

Laboratory test and validation of the hybrid simulation/testing procedure

In order to investigate the structural behaviour of unreinforced masonry structures under earthquake loading, usually, static cyclic tests are performed with the so called *three actuator setups*. In detail, two vertical servo-hydraulic actuators impose a specified level of precompression to the tested structure to simulate weight of upper parts. At the same time, a horizontal servo hydraulic actuator imposes a static cyclic displacement sequence to the top of the tested specimen. Mostly, two different boundary conditions are envisaged: cantilever and fixed-ends. In case of cantilever boundary condition, force controlled vertical actuators impose a constant vertical load to the specimen. The fixed ends boundary condition is obtained by combining a force and a displacement controlled vertical actuators to impose a constant vertical load while keeping null the rotation of the wall top.

However, neither of the two boundary conditions accounts for a realistic variation of vertical loading to which the lateral response of unreinforced masonry structures is very sensitive. From this standpoint, the procedure proposed in Chapter 5 is here applied in a real hybrid simulation/testing campaign in order to: (i) validate the procedure; and (ii) demonstrate that it is viable for investigating the structural behaviour of masonry structures, which are intrinsically sensitive to an alteration of vertical loading. For the latter purpose, advanced techniques for the model reduction, such as the Component Mode Synthesis (CMS), are implemented to derive reduced-order stiffness and mass matrices of both PS and NS so as to limit the frequency bandwidth of the prototype structure. This prevents the spurious excitation of higher frequency eigenmodes, which fall outside the frequency bandwidth of the actuators, where control tracking errors

are not negligible. To do that, a masonry facade case study is firstly described in the chapter. Then, the proposed CMS framework is outlined and reduced-order component models of both PS and NS are derived. Finally, both implementation and results of the PSD-HS campaign are presented and discussed.

6.1. Introduction

Despite being one of the oldest building concepts, masonry is still a widely used, extremely flexible and economical construction method with considerable potential for future developments. However, possibly due to the substantial empirical knowledge collected through several centuries of utilization of masonry as a structural material, the need for establishing a more modern basis for the design and assessment of masonry structures has not been properly appreciated. As a result, conventional masonry design practice is conservative, particularly in regard to the assessment of seismic resistance. Hence, the potential of masonry has not yet been exhausted and there is a clear need for better utilization. For example, the constitutive behaviour of masonry is known to be modified during a real seismic event. This is mainly due to the variation of vertical loads and stresses. Unfortunately this complex behaviour cannot be accurately predetermined. From this standpoint, Hybrid Simulation (HS) represents a viable approach for investigating the behaviour of UnReinforced Masonry (URM) structures accounting for variability of vertical loads.

It is important to stress that, in order to obtain an accurate time history response, the upper bound of the frequency bandwidth of the hybrid system, which corresponds to the frequency of the highest eigenmode of the prototype structure divided by the testing time scale, must lay within the frequency range where actuator control errors are negligible (Shing & Mahin, 1987). Commonly, 0-2 Hz represents an optimistic frequency range when standard equipment for civil structural testing is used whereas 0-10 Hz can be afforded for small displacements and forces with outstanding equipment and proper compensation of actuator dynamics. In general, members of frame structures experience almost constant axial load during seismic events. For this reason, in the current practice of HS, vertical Degrees of Freedom (DoFs) are excluded from the time integration loop and force-controlled hydraulic jacks impose constant gravity forces, e.g., (Bursi et al., 2017) and (Terzic & Stojadinovic, 2013). As a result, the frequency bandwidth of hybrid systems is limited to flexural modes, which are characterized by much smaller frequencies than those of eigenmodes entailing member axial deformation, and the experiment is feasible with a reasonable time scale.

In order to include vertical DoFs in the HS loop while keeping the frequency bandwidth of the hybrid system as small as possible, in this chapter a CMS algorithm, (Craig & Kurdila, 2006), is implemented to reduce the NS and PS. As a result, high frequency modes, which are not relevant for the prototype structure response but fall outside the bandwidth of the actuation system, are eliminated,

(Shing & Mahin, 1987). Thus, the proposed hybrid simulation/testing procedure is here aided with CMS reduction, for further improving the PSD-HS of masonry systems.

6.2. Description of the case study

The masonry facade case study emulated via HS consisted on a two storey wall structure of 2.70x5.20 m size and uniform thickness of 0.15 m. A door opening of 0.90x1.90m size was located at the ground floor while a window opening of 0.90x1.00 m size was located at the upper floor. The upper portion of the facade (NS) was simulated numerically while the lower portion (PS) of the facade was tested in the laboratory. A steel beam, which can be assumed infinitely stiff compared to the wall specimen, connected the tested specimen to the three servo-controlled actuators. As a result, the hybrid model of the emulated masonry facade was characterized by a rigid interface between NS and PS, as described in Chapter 5 on another case study.

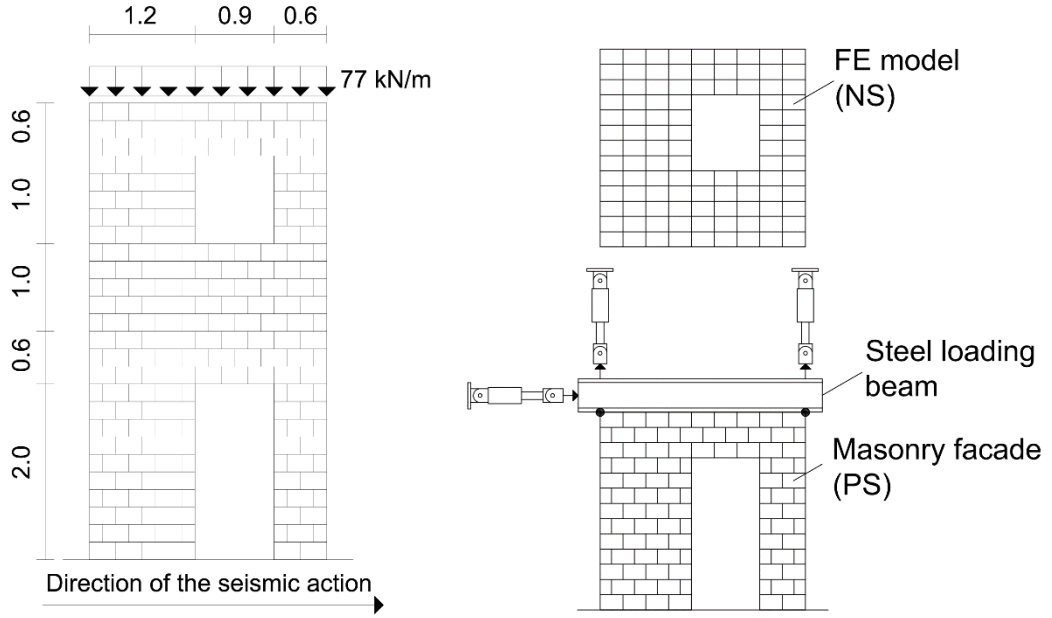

(a) (b)

Figure 73: The masonry facade case study: (a) schematic with main dimensions in meters; and (b) partitioning into PS and NS.

Figure 73 depicts the emulated masonry facade case study as well as the partitioning into NS and PS. The PS was made of calibrated Swiss K-Modul 15/19 clay blocks (type B according to SIA 266:2015, (SIA, 2005)) of nominal dimension 0.29x0.15x0.19 m and standard cement mortar. Average compressive strength, f_m=5.14 MPa and elastic modulus E=4.21 GPa of masonry were estimated on compressive tests of three wall samples of 0.59x0.15 m^2 cross-section and 1 m height, which were performed according SN EN 1052-1:1998, (E.CEN, 1998). Same material parameters were used to model the NS. The

masonry facade was subjected to a nominal vertical load of 208 kN, that corresponds to 10% of the compressive strength of masonry uniformly distributed over a cross section of 2.7x0.15 m. A record of the Montenegro earthquake (1979) was selected from the PEER Ground Motion Database (PEER), (P.PEERC, 2013), as seismic excitation and scaled to different values of Peak Ground Acceleration (PGA).

Figure 74 depicts both the selected seismic record and related acceleration response spectrum. In order to support the design of the experimental campaign and the derivation of both substructure matrices, two FE models of the masonry facade, namely Reference Model (RM) -1 and -2, were implemented in Matlab based on 4-node plate elements, (Matlab, 2010).

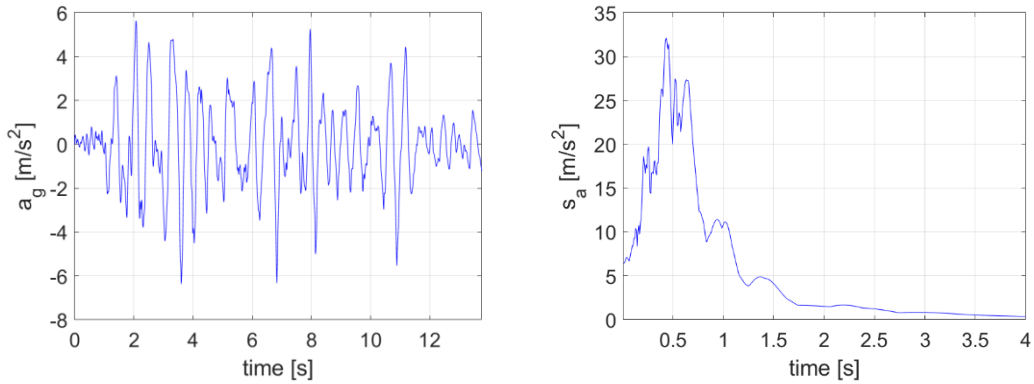

(a) (b)

Figure 74: The 1979 Montenegro earthquake: (a) ground motion record scaled to 6.36 m/s^2 PGA; and (b) corresponding acceleration response spectrum for 3.00 % viscous damping.

In detail, RM1 represents the idealized masonry facade while RM2 describes its hybrid model, which is characterized by a rigid interface between NS and PS. Both FE models are characterized by 468 DoFs but additional 2-nodes rigid beam elements enforce rigid behaviour at both substructure interfaces in RM2, as depicted in Figure 75.

Table 19 compares modal frequencies of RM1 and RM2 while Table 20 reports MAC values calculated for each pairs of corresponding deformational shapes, (Allemang & Brown, 1982). As can be appreciated, modal characteristics are almost unaltered up to mode 4. In order to testify that this was sufficient for preserving the seismic response of RM1, Figure 76 compares displacement response histories of RM1 and RM2 measured at Node 111 along X and Y directions. Time history analyses were performed with the Newmark algorithm, (Newmark, 1959), considering 3.00 % equivalent viscous damping and 1 msec time step. Accordingly, mass and stiffness matrices of both PS and NS were derived from RM2 as explained in the following section.

Table 19: Comparison of modal frequencies.

Mode	f_{RM1} ***[Hz]***	f_{RM2} ***[Hz]***

1	5.73	5.82
2	19.47	19.97
3	52.96	53.10
4	92.42	92.94
5	114.16	129.49

Table 20: MAC values between mode shapes.					
RM #2: / ***RM #1:***	***1***	***2***	***3***	***4***	***5***
1	1.00	0.14	0.00	0.29	0.11
2	0.12	1.00	0.00	0.08	0.04
3	0.00	0.00	1.00	0.00	0.00
4	0.26	0.08	0.00	1.00	0.01
5	0.44	0.40	0.00	0.00	0.52

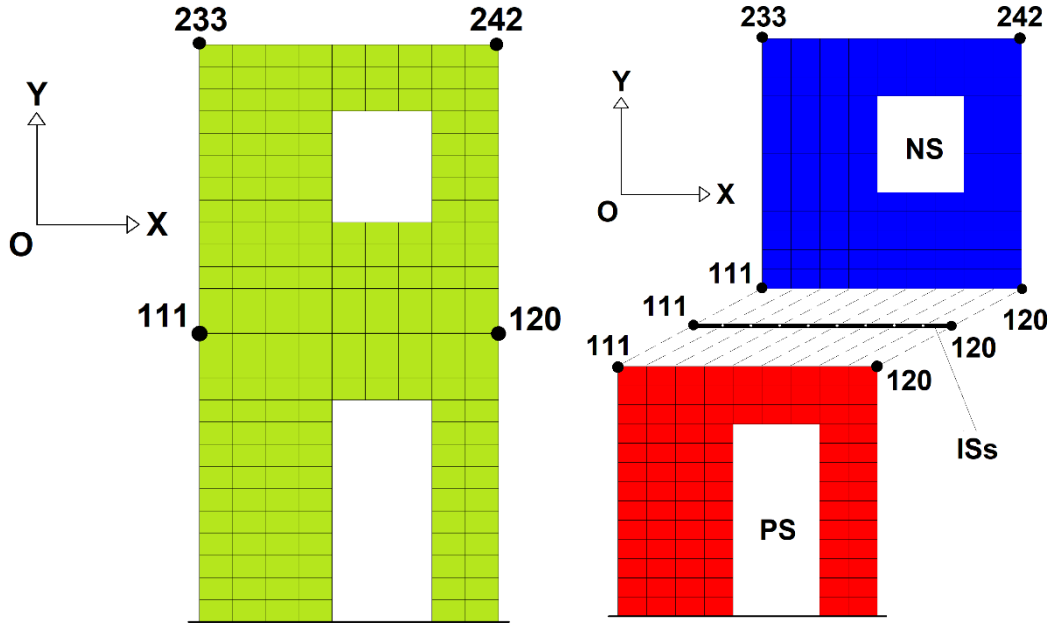

(a) (b)

Figure 75: FE modelling of the masonry facade case study: (a) RM1; and (b) RM2.

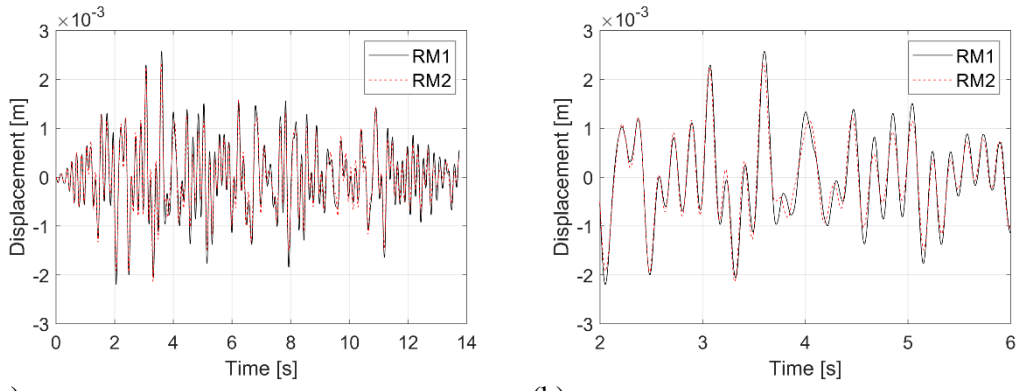

(a) (b)

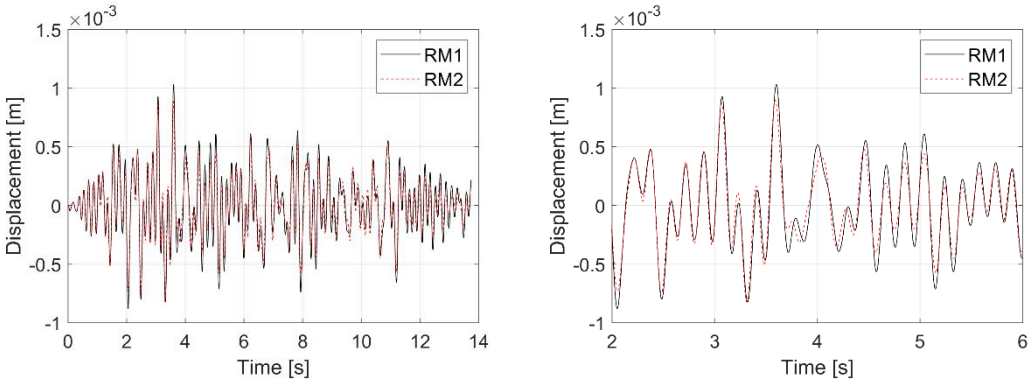

(c) (d)

Figure 76: Comparison of RM1 and RM2 response histories of DoFs: (a) 111-x; (b) 111-x zoom; (c) 111-y; and (d) 111-y zoom.

6.3. Dynamic substructuring with Component Mode Synthesis

The term *component mode* signifies Ritz vectors, or assumed modes, that are used as basis in describing the displacement of points within a substructure, or component, (Craig & Kurdila, 2006), (Klerk et al., 2008). Component Mode Synthesis (CMS) involves:

- Division of a structure into components (substructuring);
- Definition of sets of modes for these components (reduction);
- Assembling of the component modes to form a reduced-order system model (coupling).

The primary use of CMS is to reduce the computational cost of dynamic simulations by replacing a large FE model with the assembly of reduced order substructures. Here, CMS is used to:

- Formulate PS and NS reduced-order mass and stiffness matrices that are condensed to the set of DoFs controlled by the actuator's setup, which can be found applying the procedure proposed in Chapter 5;
- Provide a minimalistic reduced-order representation of the NS.

With reference to the last point, it is important to stress that the relatively coarse FE discretization of the NS of our case study entails already a large number of eigenmodes, which do not contribute to the overall system response. However, their spurious excitation due to actuator tracking errors may lead to dynamic instability, (Shing & Mahin, 1987). Accordingly, CMS is exploited to reduce the frequency bandwidth of the hybrid system. First, the Craig-Bampton CMS algorithm is revisited from the perspective of HS and, then the CMS of both NS and PS of the masonry case studies is performed.

6.3.1. Craig-Bampton algorithm

CMS relies on the definition of a component mode matrix, $\boldsymbol{\psi}$, that relates the displacement field $\hat{\mathbf{u}}$ of the reduced-order component model to a set of generalized coordinate vector $\mathbf{p}$ as:

$$\hat{\mathbf{u}} = \boldsymbol{\psi}\mathbf{p} \tag{60}$$

where $\hat{\mathbf{u}}$ approximates the displacement field $\mathbf{u}$ of the full component model. Accordingly, component matrices and vectors are condensed as:

$$\hat{\mathbf{k}} = \boldsymbol{\psi}^{\boldsymbol{T}}\mathbf{k}\boldsymbol{\psi} \tag{61a}$$
$$\hat{\mathbf{m}} = \boldsymbol{\psi}^{\boldsymbol{T}}\mathbf{m}\boldsymbol{\psi} \tag{61b}$$
$$\hat{\mathbf{f}} = \boldsymbol{\psi}^{\boldsymbol{T}}\mathbf{f} \tag{61c}$$
$$\hat{\mathbf{u}} \approx \mathbf{u} \tag{61d}$$

For the sake of clarity, the following matrix partitioning is used as reference for the derivation of the component-mode matrix of the Craig-Bampton method for an unconstrained component:

$$\mathbf{k} = \begin{bmatrix} \mathbf{k}_{ii} & \mathbf{k}_{ie} & \mathbf{k}_{ir} \\ \mathbf{k}_{ei} & \mathbf{k}_{ee} & \mathbf{k}_{er} \\ \mathbf{k}_{ri} & \mathbf{k}_{re} & \mathbf{k}_{rr} \end{bmatrix} \tag{62a}$$
$$\mathbf{m} = \begin{bmatrix} \mathbf{m}_{ii} & \mathbf{m}_{ie} & \mathbf{m}_{ir} \\ \mathbf{m}_{ei} & \mathbf{m}_{ee} & \mathbf{m}_{er} \\ \mathbf{m}_{ri} & \mathbf{m}_{re} & \mathbf{m}_{rr} \end{bmatrix} \tag{62b}$$
$$\mathbf{f} = \begin{bmatrix} \mathbf{f}_i \\ \mathbf{f}_e \\ \mathbf{f}_r \end{bmatrix} \tag{62c}$$
$$\mathbf{u} = \begin{bmatrix} \mathbf{u}_i \\ \mathbf{u}_e \\ \mathbf{u}_r \end{bmatrix} \tag{62d}$$

where subscripts *i*, *e* and *r* denote *interior*, *excess* and *rigid* body DoFs respectively. If constrained, *r*-DoFs must provide a statically determined configuration. Accordingly, the matrix of *rigid body modes*, $\boldsymbol{\psi}_{\boldsymbol{r}}$, is computed as:

$$\boldsymbol{\psi}_r = \begin{bmatrix} \boldsymbol{\psi}_{ir} \\ \boldsymbol{\psi}_{er} \\ \mathbf{I}_{rr} \end{bmatrix} = \begin{bmatrix} -\begin{bmatrix} \mathbf{k}_{ii} & \mathbf{k}_{ie} \\ \mathbf{k}_{ei} & \mathbf{k}_{ee} \end{bmatrix}^{-1} \begin{bmatrix} \mathbf{k}_{ir} \\ \mathbf{k}_{er} \end{bmatrix} \\ \mathbf{I}_{rr} \end{bmatrix} \tag{63}$$

On the other hand, *constraint modes* are computed by imposing a unit displacement on a single *e*-DoF while keeping other *e*-DoF zero, after constraining the set of *r*-DoF. The matrix of constraint modes $\boldsymbol{\psi}_e$ is defined as:

$$\boldsymbol{\psi}_e = \begin{bmatrix} \boldsymbol{\psi}_{ie} \\ \mathbf{I}_{ee} \\ \mathbf{0}_{re} \end{bmatrix} = \begin{bmatrix} -\mathbf{k}_{ii}^{-1}\mathbf{k}_{ie} \\ \mathbf{I}_{ee} \\ \mathbf{0}_{re} \end{bmatrix} \tag{64}$$

Finally, *fixed interface normal modes*, $\boldsymbol{\psi}_f$, are obtained from the eigenvalue analysis of the component after fixing both *e*-DoFs and *r*-DoFs:

$$\boldsymbol{\psi}_f = \begin{bmatrix} \boldsymbol{\psi}_{if} \\ \mathbf{0}_{ef} \\ \mathbf{0}_{rf} \end{bmatrix} \tag{65}$$

where ω_f^2 and $\boldsymbol{\psi}_{if}$ are frequency and modal shape of the component obtained after solving the following eigen-problem:

$$\left(\mathbf{k}_{ii} - \omega_f^2 \mathbf{m}_{ii}\right)\boldsymbol{\psi}_{if} = \mathbf{0} \tag{66}$$

The component-mode matrix of the Craig-Bampton method, $\boldsymbol{\psi}$, can include rigid body, constraint and fixed-interface normal modes and reads:

$$\begin{bmatrix} \hat{\mathbf{u}}_i \\ \hat{\mathbf{u}}_e \\ \hat{\mathbf{u}}_r \end{bmatrix} = \begin{bmatrix} \boldsymbol{\psi}_{if} & \boldsymbol{\psi}_{ie} & \boldsymbol{\psi}_{ir} \\ \mathbf{0}_{ef} & \mathbf{I}_{ee} & \boldsymbol{\psi}_{er} \\ \mathbf{0}_{rf} & \mathbf{0}_{re} & \mathbf{I}_{rr} \end{bmatrix} \begin{bmatrix} \mathbf{p}_f \\ \mathbf{p}_e \\ \mathbf{p}_r \end{bmatrix} \tag{67a}$$

$$\boldsymbol{\psi} = \begin{bmatrix} \boldsymbol{\psi}_{if} & \boldsymbol{\psi}_{ie} & \boldsymbol{\psi}_{ir} \\ \mathbf{0}_{ef} & \mathbf{I}_{ee} & \boldsymbol{\psi}_{er} \\ \mathbf{0}_{rf} & \mathbf{0}_{re} & \mathbf{I}_{rr} \end{bmatrix} \tag{67b}$$

where $\mathbf{p}_f$, $\mathbf{p}_e$ and $\mathbf{p}_r$ indicate corresponding fixed-interface normal mode, constraint mode and rigid body mode modal coordinates. Given stiffness and mass orthogonality of rigid body and fixed-interface normal modes, reduced-order matrices obtained with (61a) present the following block structure:

$$\hat{\mathbf{k}} = \begin{bmatrix} \hat{\mathbf{k}}_{ff} & \mathbf{0}_{fe} & \mathbf{0}_{fr} \\ \mathbf{0}_{ef} & \hat{\mathbf{k}}_{ee} & \mathbf{0}_{er} \\ \mathbf{0}_{rf} & \mathbf{0}_{re} & \mathbf{0}_{rr} \end{bmatrix} \tag{68a}$$

$$\hat{\mathbf{m}} = \begin{bmatrix} \hat{\mathbf{m}}_{if} & \hat{\mathbf{m}}_{fe} & \hat{\mathbf{m}}_{fr} \\ \hat{\mathbf{m}}_{ef} & \hat{\mathbf{m}}_{ee} & \hat{\mathbf{m}}_{er} \\ \hat{\mathbf{m}}_{rf} & \hat{\mathbf{m}}_{re} & \hat{\mathbf{m}}_{rr} \end{bmatrix} \tag{68b}$$

$$\hat{\mathbf{f}} = \begin{bmatrix} \hat{\mathbf{f}}_i \\ \hat{\mathbf{f}}_e \\ \hat{\mathbf{f}}_r \end{bmatrix} \tag{68c}$$

Accordingly, the component restoring force vector modal coordinates are defined as: $\hat{\mathbf{r}} = \hat{\mathbf{k}} \cdot \mathbf{p}$.

In order to achieve a deeper understanding of the Craig-Bampton method when applied to physically substructured components, some practical consideration needs to be done. First of all, fixed-interface normal mode coordinates $\mathbf{p}_f$, do not correspond to measurable quantities and cannot be imposed to the PS by means of servo-hydraulic actuators. Accordingly, fixed interface normal modes must be excluded when performing CMS of a PS (i.e. the number of fixed interface normal modes, $\mathbf{p}_f$, for the PS is zero). Moreover, also floating PS (i.e., PS no directly constrained to the ground in the prototype structure) are constrained to a reaction frame once tested in the laboratory. In order to avoid redundant geometric transformation, it is convenient to physically constraint the set of *r*-DoFs in the laboratory and to manipulate the set of *e*-DoFs with servo-hydraulic actuators. As a result, the displacement vector $\mathbf{p}_e$ can be imposed to the specimen without any additional coordinate transformation. It is important to stress that in PSD-HS, the PS is loaded quasi-statically and, therefore, PS inertia is simulated numerically. As a consequence, constraint modes, which describe the static deformation of the component when subjected to a linear combination of unit displacements applied to *e*-DoFs, provide a suitable basis for the reduction of the PS mass matrix. Accordingly, $\hat{\mathbf{r}}_e$ is the only non-zero component of the reduced restoring force vector, which is directly measured from actuator load cells.

6.3.2. CMS of the PS

As anticipated, when performing CMS of PS, it is very convenient to retain actuator controlled DoFs as *e*-DoFs while using related constraint modes as component-mode basis. With regard our masonry facade case study and according to Figure 73b, the two vertical servo-hydraulic actuators control the displacements of the upper corners of the PS along the Y direction while the horizontal actuator control the displacement of the same points along the X direction. Along this line, the reduced-order component model of the PS retains *e*-DoFs 111-x, 111-y and 120-y only. Figure 77 depicts corresponding constraint modes.

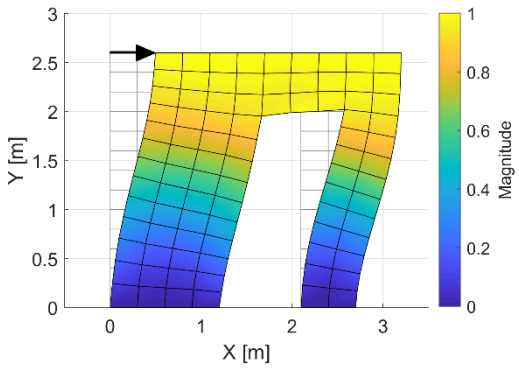

(a)

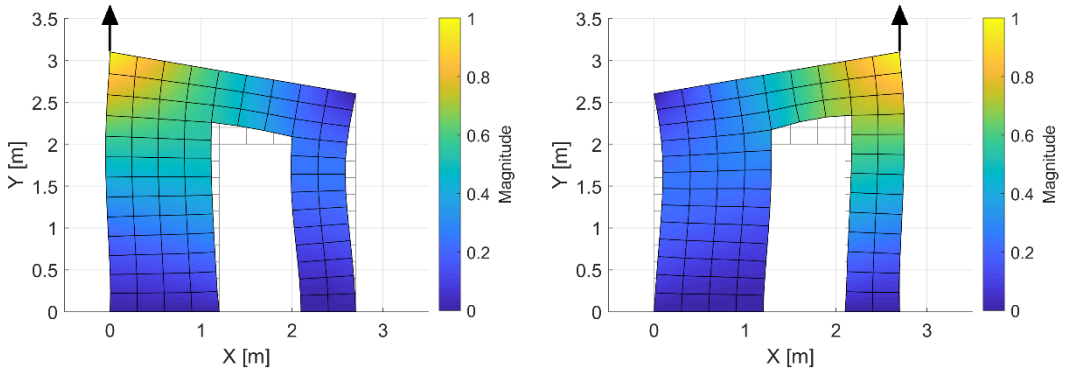

(b) (c)

Figure 77: Constraint modes of the PS related to DoFs: (a) 111-x; (b) 111-y; and (c) 120-y.

6.3.3. CMS of the NS

With regard to the NS, 4 and 7 DoFs reduced-order component models were developed. In order to be compatible, PS and NS matrices must share the same set of interface DoFs. Since the NS is floating, interface DoFs 111-x, 111-y and 120-y are retained as *r*-DoFs in both cases. With regard to the 4-DoFs NS, the first fixed-interface normal mode, is added to the component-mode basis depicted in Figure 78. With reference to the 7-DoFs NS, in addition to the same set of rigid-body modes of the 4-DoFs NS, constraint modes related to *e*-DoFS 233-x, 233-y and 242-y are included in the component-mode basis as well as the first fixed-interface normal mode, which is calculated after constraining both retained *r*- and *e*-DoFs. Figure 79 gathers all component-modes of the 7-DoFs except the rigid-body modes, which coincide to those reported in Figure 78 for the 4-DoFs NS case.

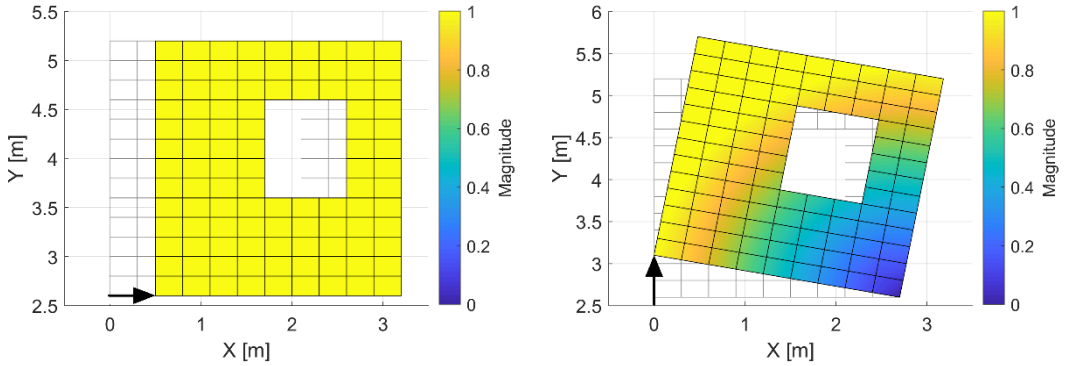

(a) (b)

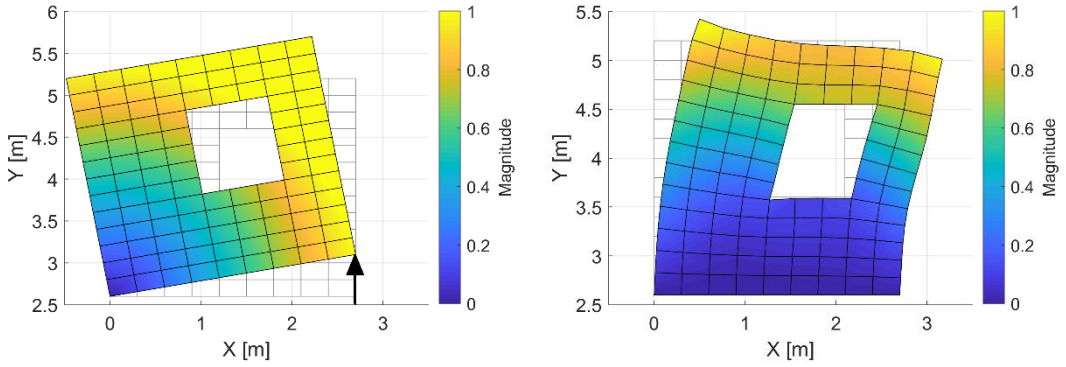

(c) (d)

Figure 78: Component-mode basis of the 4-DoFs NS; rigid body modes related to DoFs: (a) 111-x; (b) 111-y; (c) 120-y; and (d) first fixed-interface normal mode.

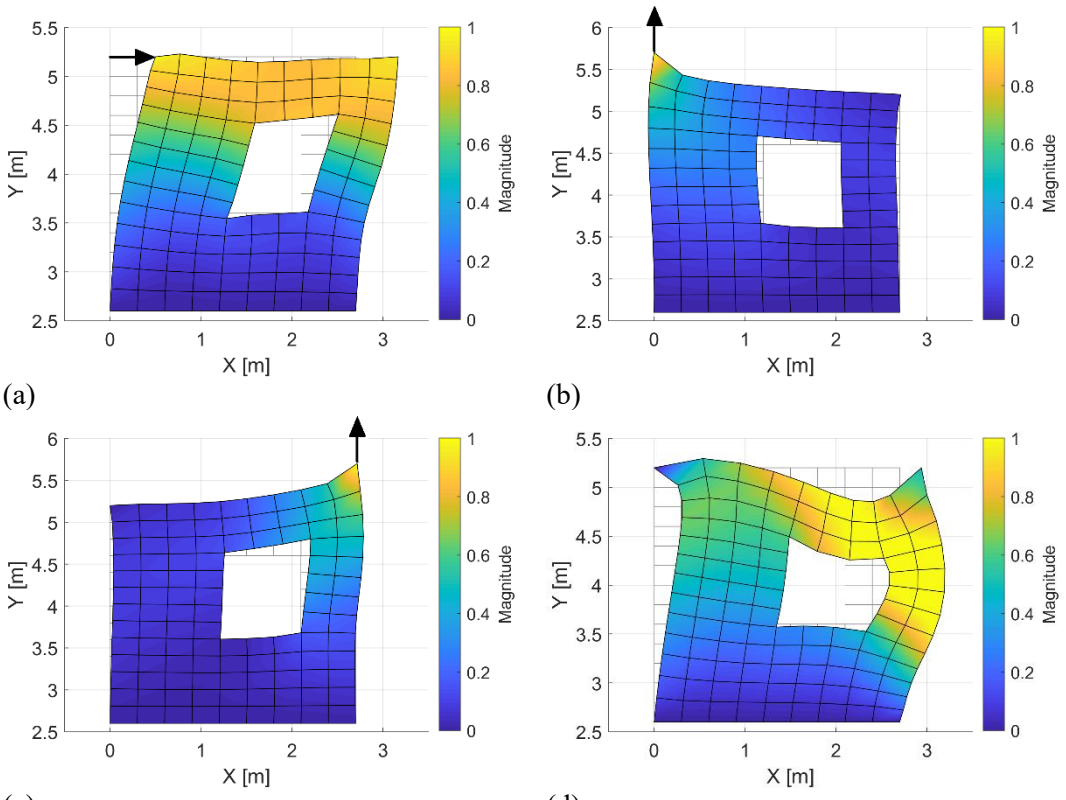

(a) (b)

(c) (d)

Figure 79: Component-mode basis of the 7-DoFs NS; constraint modes related to DoFs: (a) 233-x; (b) 233-y; (c) 242-y; and (d) first fixed-interface normal mode.

In order to validate the component models, two reduced-order substructured models of the masonry facade were assembled, namely SM1 and SM2, which represent the prototype structure emulated via PSD-HS. The former combines the 3-DoFs PS and the 4-DoFs NS, (SM1) while the latter combines the 3-DoFs PS and the 7-DoFs NS, (SM2). As can be appreciated from Table 21, which compares the modal frequencies of SM 1 and SM 2, the maximum frequency retained by SM2 is larger than twice the maximum frequency retained by SM1. Figure 80 compares the displacement responses of SM1 and SM2 measured at interface DoFs 111-x and 111-y to the reference solution provided by RM2, which

is reproduced by both substructured models with an extremely good degree of matching. The Newmark algorithm, (Newmark, 1959), was used to compute all time history responses of Figure 80 considering 3.00 % equivalent viscous damping and 1 msec time step.

Table 21: Modal frequencies of substructured models.		
Mode	f_{SM1} ***[Hz]***	f_{SM2} ***[Hz]***
1	5.82	5.82
2	19.99	19.98
3	57.30	55.58
4	113.77	99.10
5	-	157.24
6	-	203.65
7	-	276.83

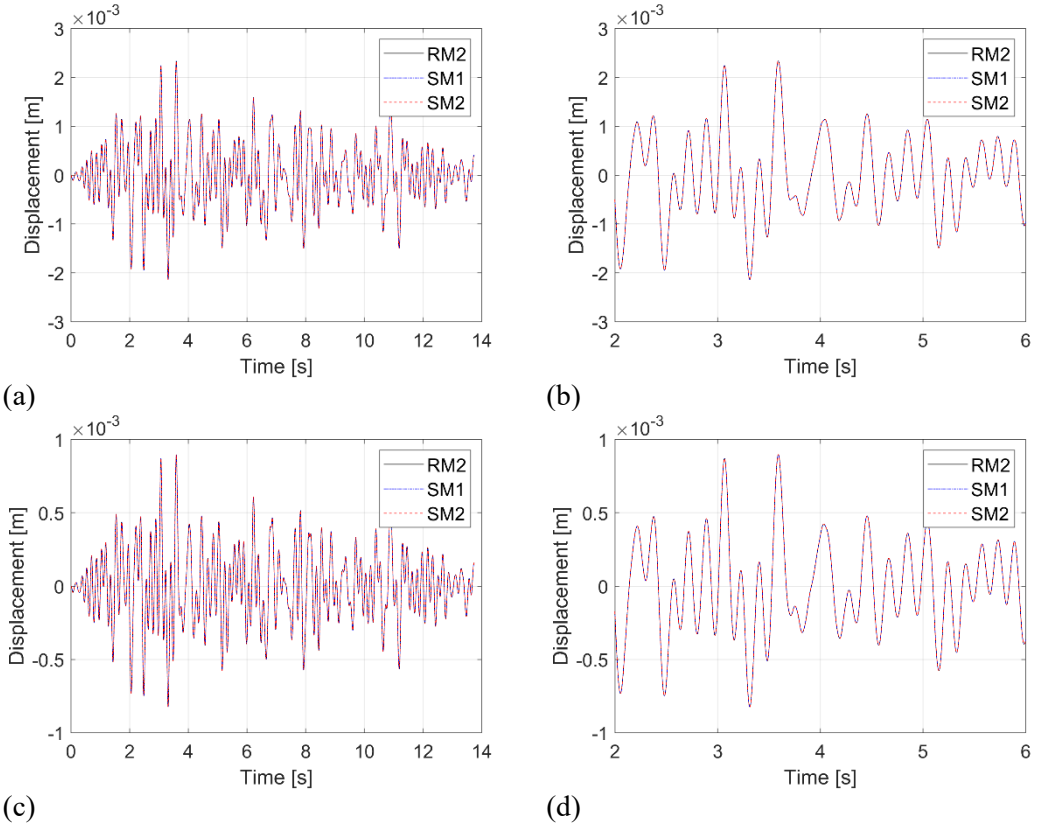

Figure 80: Displacement response histories of full and reduced-order model measured at DoFs: (a) 111-x; (b) 111-x zoom; (c) 111-y; and (d) 111-y zoom.

6.4. Hybrid simulation/testing campaign

This section provides a detailed description of the HS framework built at ETH Zürich to perform PSD-HS of the masonry facade case study.

In order to perform PSD-HS of the masonry facade case study, the actuator setup was interfaced to an INDEL GIN-SAM4 real-time computer via Ether CAT. Figure 81 provides an overview of the PSD-HS setup including locations of servo-

hydraulic actuators, sensors and a block diagram of the PSD-HS framework architecture. As can be appreciated from Figure 81, a steel beam interfaces three servo-hydraulic actuators of 1 MN capacity each to the wall specimen (PS) while eleven External Linear Variable Differential Transformers (LVDT) measure masonry deformation and relative sliding between specimen and reaction frame at multiple locations. During tests, a Digital Image Correlation (DIC) system acquires the in-plane displacement field of the wall specimen surface every 2 sec during tests. In detail, a NIKON D810 digital camera equipped with a 50 mm lens shoots planar Black & White (B&W) pictures of the wall surface, which is painted with a random speckle pattern. Two flash lights pointing the wall specimen guarantees a uniform illumination and optimal balance of images. The dot size of about 1±1.5 mm of the random speckle pattern was calibrated to obtain 3 ± 4 pixel size dots in digital images, which was proved to be an optimal setting for the target measurements, (Mojsilović & Salmanpour, 2016).

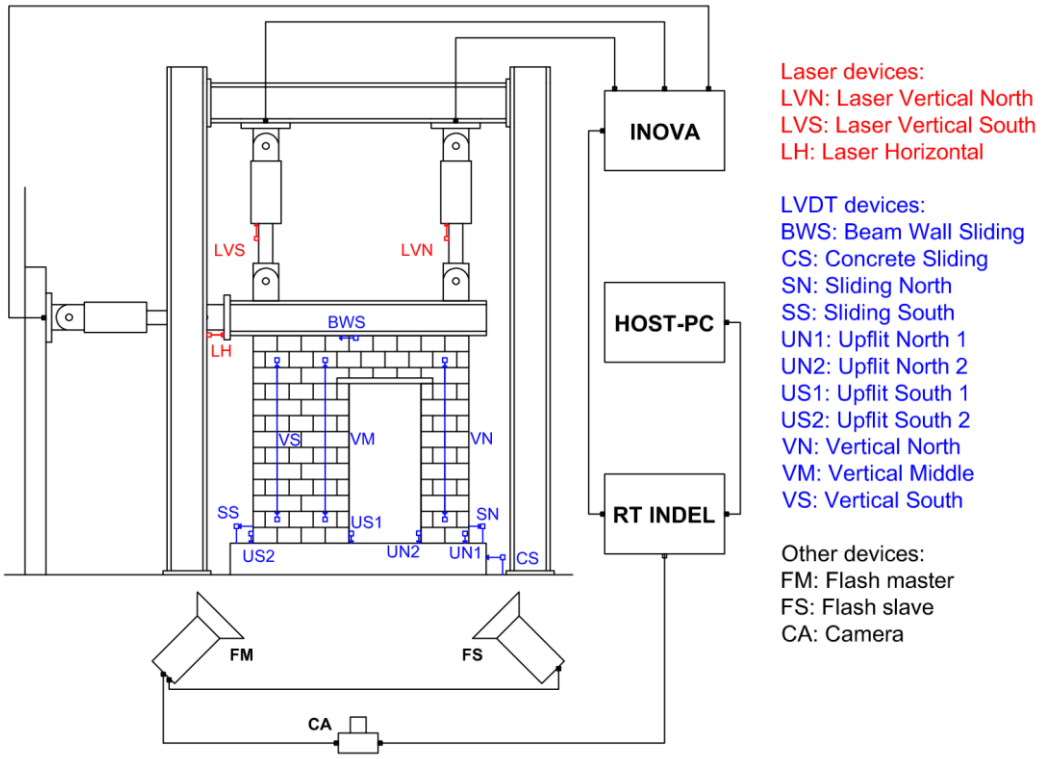

Figure 81: Architecture of the PSD-HS setup including DIC and LVDT measurement systems.

Figure 82 provides an overview of the DIC setup including a close-up view of the B&W random speckle pattern. Before starting the PSD-HS experiment, a vertical load ramp oriented downward and equally distributed between vertical actuators is imposed to the wall specimen up to 208 kN, which corresponds to the nominal vertical load of the case study. Then, the INDEL GIN-SAM4 real-time computer is engaged to coordinate the PSD-HS experiments. In detail, the INDEL executes the time integration algorithm and, via Ether-CAT, sends actuator

displacement commands to the INOVA controller and reads corresponding feedback forces measured with loads cells at each time step of the simulation. In order to synchronize testing and data acquisition, the INDEL real-time computer triggers DIC picture shooting and acquires LVDT sensors. A more detailed description of the time integration algorithm used in this testing campaign can be found in (Patterson et al., 2013), (Brun et al., 2014), (Bursi & Shing, 1996) and (Molina et al., 2011).

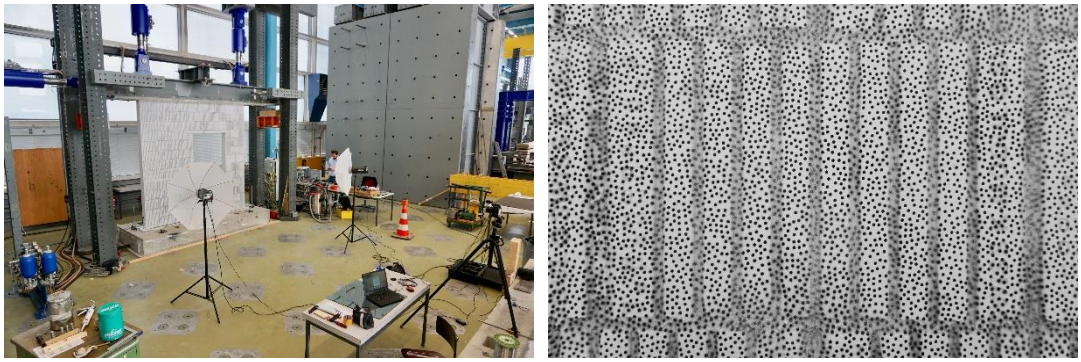

(a) (b)

Figure 82: Test setup for DIC: (a) DIC installation; and (b) speckle pattern applied to the masonry wall.

6.5. Results

This section reports and discusses the results of the experimental campaign. For the sake of comparison, all plots refer to simulation time, which corresponds to wall-clock time divided by testing time scale. Table 22 summarizes the list of experiments conducted on the same masonry facade specimen. The column *frequency bandwidth* reports the frequency bandwidth of the hybrid system, whose upper bound corresponds to the frequency of the highest eigenmode of the corresponding prototype structure reported in Table 21 divided by the testing time scale. As shown in Table 22, the first two experiments, namely Test #1a and #1b, were conducted considering SM2 as prototype structure, which is characterized by a 7-DoFs NS, and a PGA value sufficiently small to guarantee a linear response of the PS. The only difference between Test #1a and #1b was the testing time scale and, therefore, the frequency bandwidth of the hybrid system. As can be observed from Figure 83, which compares displacement, restoring force and corresponding hysteresis loop of the horizontal actuator, Test #1b was unstable and therefore it was stopped after about 1 sec. In order to prevent dynamic instability due to experimental errors, (Shing & Vannan, 1991), all following experiments were conducted assuming SM1 as prototype structure, which is characterized by a 4-DoFs NS and a testing time scale equal to 200. In this case, the frequency bandwidth of the hybrid system overlaps the frequency bandwidth of the actuation system where experimental errors are negligible.

Table 22: Test program.				
Test ID	***PGA [m/s²]***	***Time scale***	***Prototype structure***	***Frequency bandwidth [Hz]***
#1a	0.45	500	SM2 (7-DoFs NS)	0 ÷ 0.55
#1b	0.45	200	SM2 (7-DoFs NS)	0 ÷ 1.38
#2	1.82	200	SM1 (4-DoFs NS)	0 ÷ 0.56
#3	3.18	200	SM1 (4-DoFs NS)	0 ÷ 0.56
#4	3.18	200	SM1 (4-DoFs NS)	0 ÷ 0.56
#5	6.36	200	SM1 (4-DoFs NS)	0 ÷ 0.56

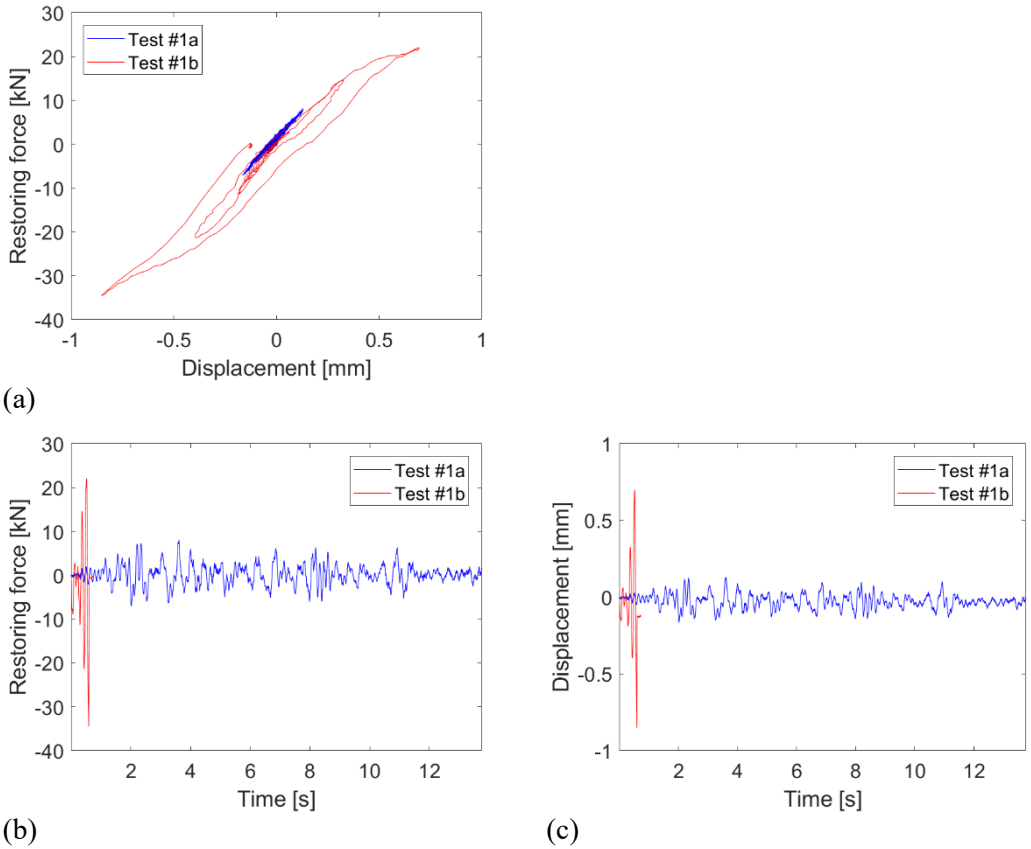

Figure 83: Comparison of Tests #1a and #1b: (a) hysteresis loop measured by the horizontal actuator; (b) related restoring force; and (c) related displacement.

A linear response was observed during Test #2 while slightly nonlinear responses characterized Tests #3 and #4. Finally, the collapse of the PS occurred during Test #5, which was stopped earlier than the duration of the ground motion.

All following discussions focus on Tests #3/#4 and Test #5. In this regards, Figure 84 compares hysteresis loop of actuator restoring forces measuring during Tests #3 and #4, which both were characterized by the same ground motion excitation. It is interesting to note that large oscillations around nominal gravity load characterized the response of vertical DoFs, which are included in the HS loop. The softening branches of hysteresis loops most likely indicate onset of rocking on both experiments. However, the good matching between Tests #3 and #4 testify that damage accumulation was very small. This is confirmed by the absence of visible cracks on the specimen surface after Test #4.

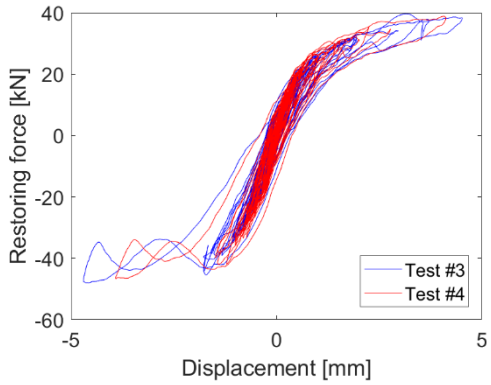

(a)

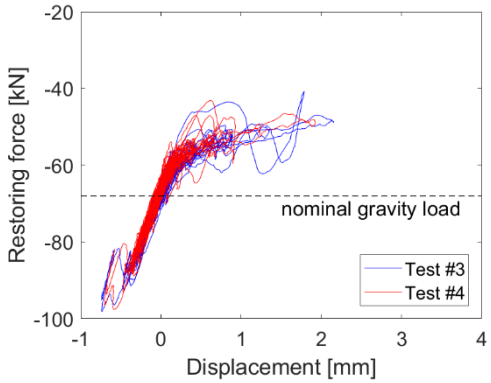

(b)

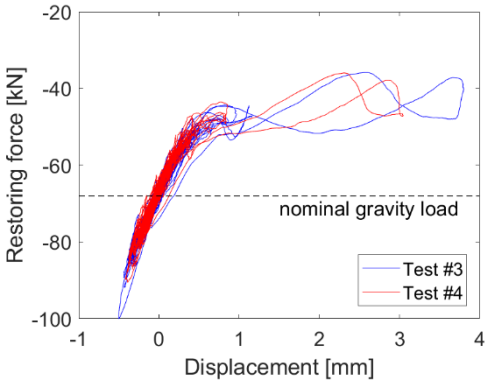

(c)

Figure 84: Hysteresis loops of restoring forces measured during Tests #3 and #4: (a) horizontal; (b) vertical south; and (c) vertical north actuators.

To demonstrate the effectiveness of the substructuring approach in the PSD-HS testing procedure, the Test #3 was compared with an additional test carried out in the same conditions of Test #3 but applying a constant vertical load. This was useful to shed light the role of vertical DoFs when included in the HS loop instead of imposing nominal vertical loads with force-controlled actuators.

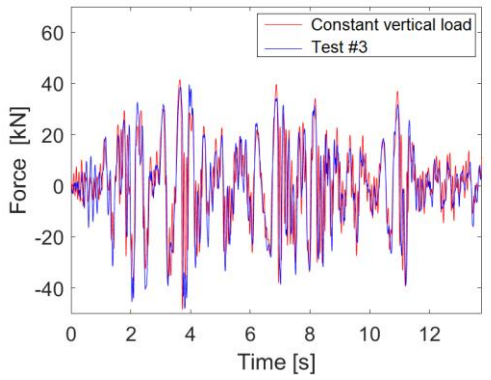

(a)

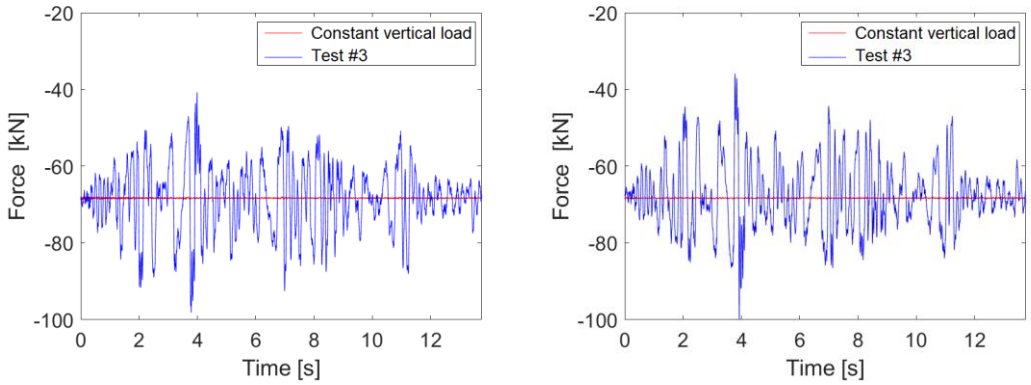

(b) (c)

Figure 85: Restoring force histories of: (a) horizontal; (b) vertical south; and (c) vertical north actuators, measured during Test #3 and during a test conducted in the same conditions of Test #3 but with constant (nominal) vertical load imposed at the PS (PS and NS modelled with 1, horizontal, DoF).

In order to evaluate the effect of including vertical DoFs into the HS loop, Figure 85 compares actuator restoring force histories measured during the hybrid tests. This figure highlights vertical force oscillations with amplitude peaks of about 50% of the average vertical load. This demonstrate as the neglecting of the vertical response (supposing a constant nominal value) during hybrid simulation testing can lead to too approximated results, and thus to possibly not correct conclusions (e.g. during calibration processes with HS), especially when working with masonry structures, which are intrinsically sensitive to variations of vertical loads and stresses.

Regarding the last test, Test #5, it was stopped after approximately 2.5 s of simulation time (500 s of wall-clock time). In this regard, Figure 86 gathers hysteresis loops of both horizontal and vertical restoring forces measured by actuators. For the sake of clarity, five milestones (T1, T2, T3, T4 and T5) are indicated on the figure to support the description of the specimen collapse.

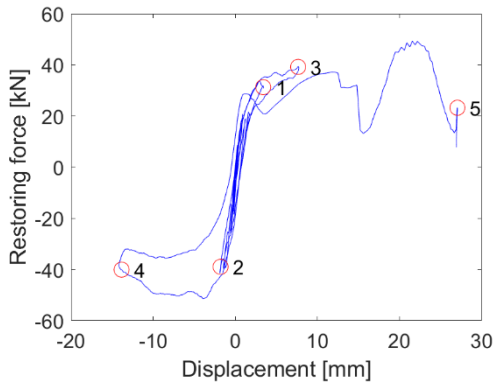

(a)

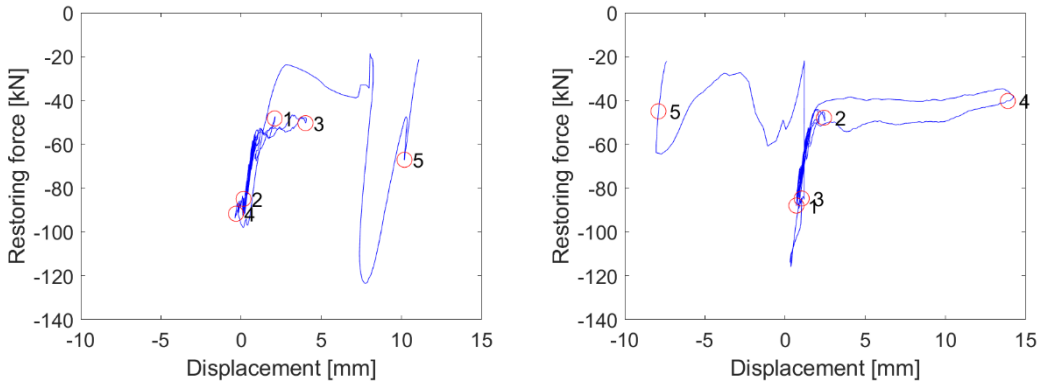

(b) (c)

Figure 86: Hysteresis loops of restoring forces measured during Test #5: (a) horizontal; (b) vertical south; and (c) vertical north actuators.

For these five milestones, Figure 87 shows the von Mises strain field, all measured via DIC. At T1 (about 1.2 s), von Mises strain concentrates at the lower mortar joint of the left wall bay and along a diagonal path following the mortar joints of the upper left part of the wall starting from the upper left corner of the opening. Such von Mises strain concentrations indicate joint opening, which allows relative rocking between wall subparts, (see Figure 87a). As can be appreciated from Figure 86, between T1 and T2 (about 1.45 s), the wall experience horizontal loading reversal, the lower left mortar joint closes and von Mises strain concentrations arise at both the lower and the upper levels of the thinner right wall bay, (see Figure 87b). At T3 (about 1.75 s), remarkable von Mises strain concentrations are visible on both left and right lower mortar joints as well as along a diagonal path that connects the upper left corner of the opening to the upper mortar joint. At this point, joint opening allows relative rocking of three facade blocks namely, left and right bays and the spandrel (see Figure 87c). Suddenly, at T4 (about 2.2 s), the thinner wall bay spits at the level of the upper mortar joint and detaches from the spandrel, which starts uplifting as depicted in Figure 87d.

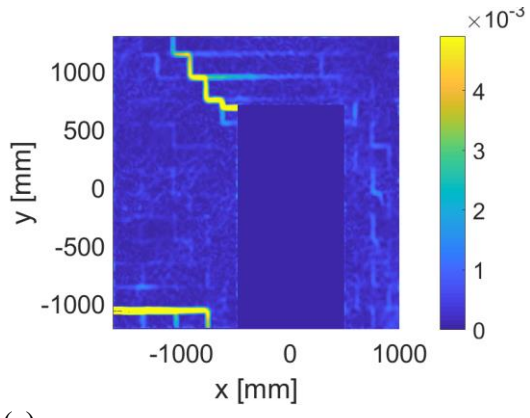

(a)

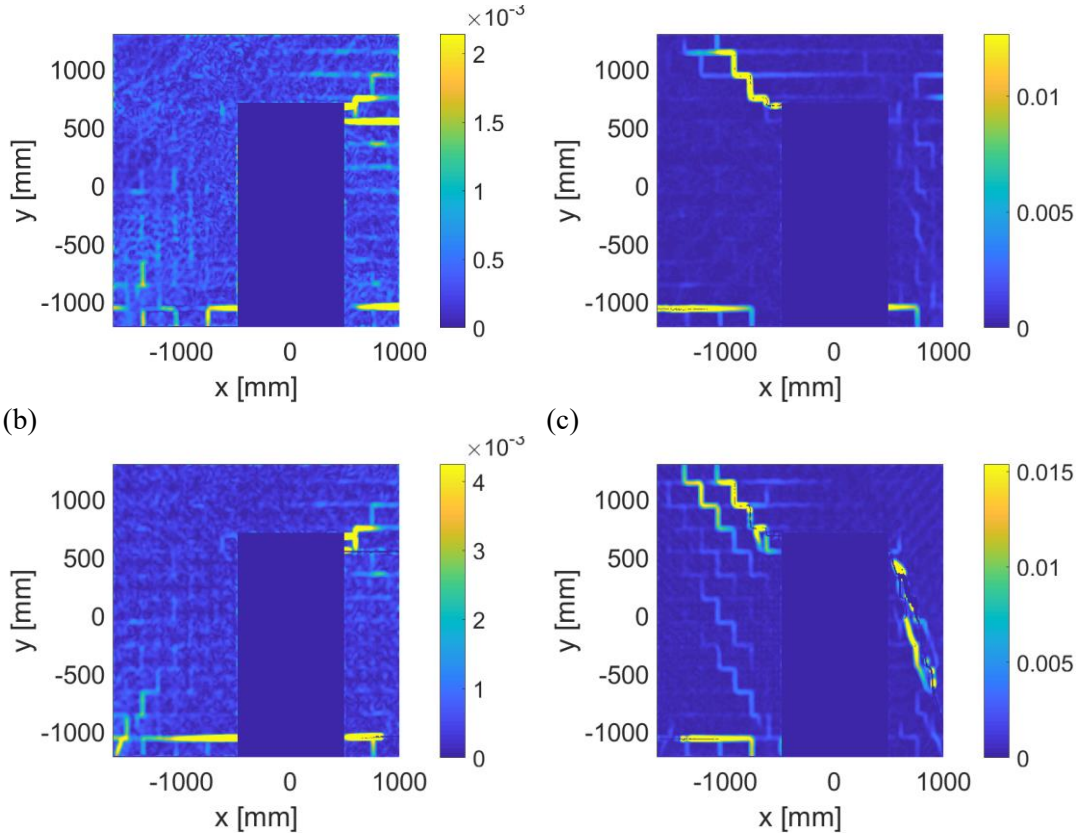

Figure 87: Von Mises strain field in [mm/mm] measured via DIC during Test #5 at milestones: (a) T1; (b) T2; (c) T3; (d) T4; and (e) T5.

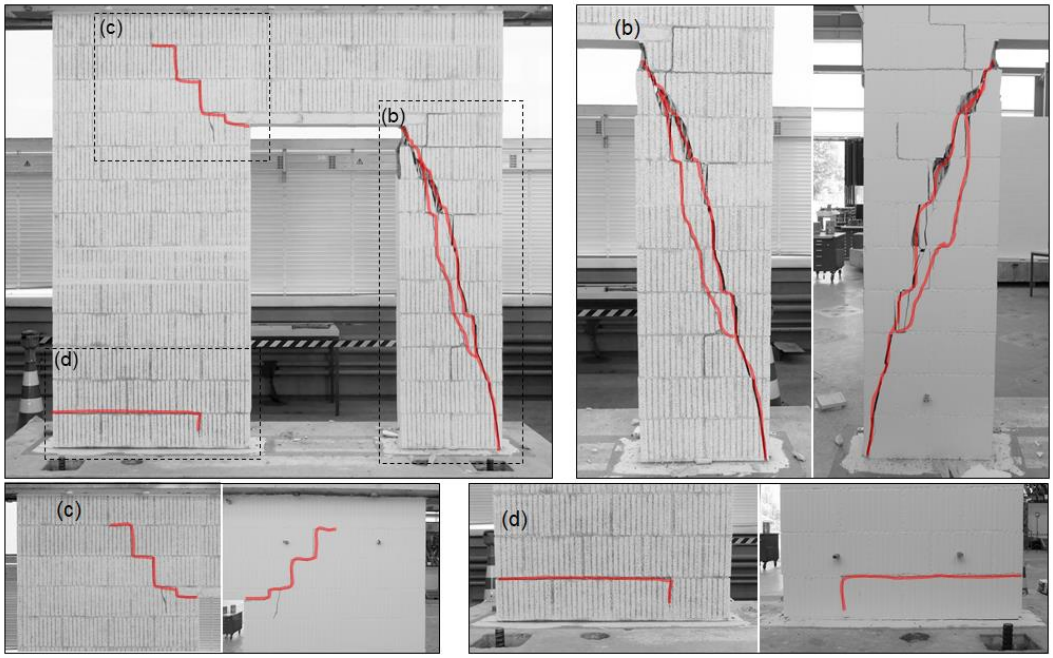

Figure 88: Overview of the wall specimen after Test #5: front view (upper left), right wall bay (upper right), left wall bay (bottom left) and bottom left corner (bottom right).

The right edge of the spandrel rotates in clock-wise between T4 and T5 (about 2.4s) and impacts the thinner wall bay, which crashes under compressive load as testified by the large diagonal crack visible at the end of the experiment, Figure 87e. The test stops immediately afterwards. Figure 88 provides an overview of the specimen after Test #5 including close-up views on regions where damage concentrated.

It is possible to conclude that the procedure proposed in Chapter 5 was able to allow to perform a PSD-HS of an unreinforced masonry wall case study, considering distributed interfaces, up to the collapse. Some errors during the integration of the coupled equation of motion was detected, mainly due to high eigenmodes that did not contribute to the response of the system but that produced instability in the control of the actuators. These problems were solved reducing the system with advanced CMS techniques. Thanks to the CMS used to reduce the system and combining it with the testing procedure, a realistic PSD-HS was performed including vertical DoFs so as to compute the time history response to vertical loading online.

6.6. References chapter 6

Allemang, R. J., & Brown, D. L. (1982, November). A correlation coefficient for modal vector analysis. In Proceedings of the 1st international modal analysis conference (Vol. 1, pp. 110-116). SEM Orlando.

Brun, M., Batti, A., Combescure, A., & Gravouil, A. (2014). External coupling software based on macro-and micro-time scales for explicit/implicit multi-time-step co-computations in structural dynamics. Finite Elements in Analysis and Design, 86, 101-119.

Bursi, O. S., & SHING, P. S. (1996). Evaluation of some implicit time-stepping algorithms for pseudodynamic tests. Earthquake engineering & structural dynamics, 25(4), 333-355.

Bursi, O. S., Abbiati, G., Cazzador, E., Pegon, P., & Molina, F. J. (2017). Nonlinear heterogeneous dynamic substructuring and partitioned FETI time integration for the development of low-discrepancy simulation models. International Journal for Numerical Methods in Engineering, 112(9), 1253-1291.

Craig, R. R., & Kurdila, A. J. (2006). Fundamentals of structural dynamics. John Wiley & Sons.

E.CEN. (1998). "1052-1–methods of test for masonry–part 1: Determination of compressive strength," European Committee for Standardization, Brussels.

Klerk, D. D., Rixen, D. J., & Voormeeren, S. N. (2008). General framework for dynamic substructuring: history, review and classification of techniques. AIAA journal, 46(5), 1169-1181.

Matlab. (2010). Version, Matlab 7.10. 0. The Mathworks, Natick Mass, USA.

Mojsilović, N., & Salmanpour, A. H. (2016). Masonry walls subjected to in-plane cyclic loading: application of digital image correlation for deformation field measurement. International Journal of Masonry Research and Innovation, 1(2), 165-187.

Molina, F. J., Magonette, G., Pegon, P., & Zapico, B. (2011). Monitoring damping in pseudo-dynamic tests. Journal of Earthquake Engineering, 15(6), 877-900.

Newmark, N. M. (1959, July). A method of computation for structural dynamics. American Society of Civil Engineers.

P.PEERC. (2013). "Peer ground motion database," Shallow Crustal Earthquakes in Active Tectonic Regimes, NGA-West2.

Patterson, M. A., Weinstein, M., & Rao, A. V. (2013). An efficient overloaded method for computing derivatives of mathematical functions in MATLAB. ACM Transactions on Mathematical Software (TOMS), 39(3), 17.

Shing, P. S. B., & Mahin, S. A. (1987). Cumulative experimental errors in pseudodynamic tests. Earthquake engineering & structural dynamics, 15(4), 409-424.

Shing, P. S. B., & Vannan, M. T. (1991). Implicit time integration for pseudodynamic tests: convergence and energy dissipation. Earthquake engineering & structural dynamics, 20(9), 809-819.

SIA, S. (2005). 266: Masonry. Swiss code, Swiss society of engineers and architects SIA, Zürich, Switzerland.

Terzic, V., & Stojadinovic, B. (2013). Hybrid simulation of bridge response to three-dimensional earthquake excitation followed by truck load. Journal of Structural Engineering, 140(8), A4014010.

Chapter 7

Application of the hybrid simulation/testing procedure to an emulated architectural heritage structure

With reference to the PDT-HS method, the present chapter reports an emulated application of an existing church of the procedure described in Chapter 5 and experimentally validated in Chapter 6. In this respect both NS and PS are simulated through the use of computers, imitating in this way the response of the PS, which would come from laboratory tests in a real hybrid simulation/testing. The *Regina Montis Regalis*, Sanctuary in Vicoforte, is selected as emblematic masonry case study of architectural heritage. A linear Finite Element (FE) model of the drum-dome system of the sanctuary is implemented, and a portion of the drum is supposed to be substructured in the laboratory as PS. To this end, a FE simulation software is coded in the Matlab environment in order to support future experimental implementations on real-time computers.

Part of the work described in this chapter was also previously exposed in conference.

7.1. Description of the *Regina Montis Regalis* case study

In order to demonstrate the effectiveness of the developed approach, the 25x35 m oval drum-dome system of the *Regina Montis Regalis*, Sanctuary in Vicoforte, is selected as reference case study. Such structural system suffered over the years from significant structural problems, partly due to settlements of the

building induced progressively by newly built masses. The tie-bars system consisting of three iron rings, which was embedded during the construction of the dome in 1734, testifies the critical structural health condition of the drum-dome system since the early stages of its construction. The continuity of such strengthening was tested by using an Impact Echo Scanner in 2004, (Aoki et al., 2004).

As shown in Figure 89, a widespread system of cracks encompasses various zones of the structure. The most important cracks cross the drum up to dome oval openings. Then, meridional cracks propagate downward from the buttresses beneath the drum evidencing and confining load paths converging to main base pillars, (Calderini et al., 2006). In order to limit the crack growth, a strengthening intervention was accomplished in 1987, when 56 active slightly tensioned steel 32 mm diameter tie-bars, for a total cross-section of 3200 mm^2, were placed within holes drilled in the masonry at the top of the drum along 14 tangents around the perimeter. Figure 90 offers a schematic view of the strengthening system.

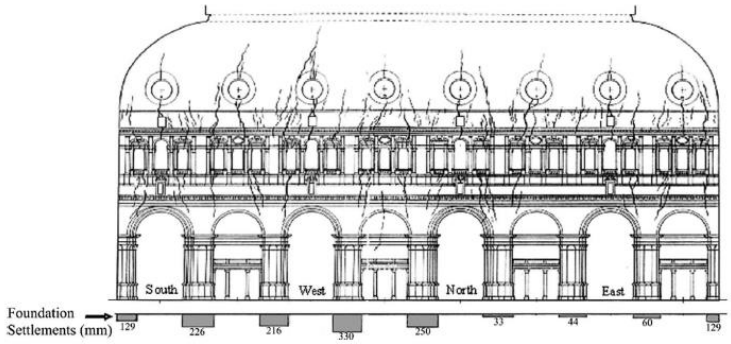

Figure 89: Schematic of crack patterns and foundation settlements, (Calderini et al., 2006).

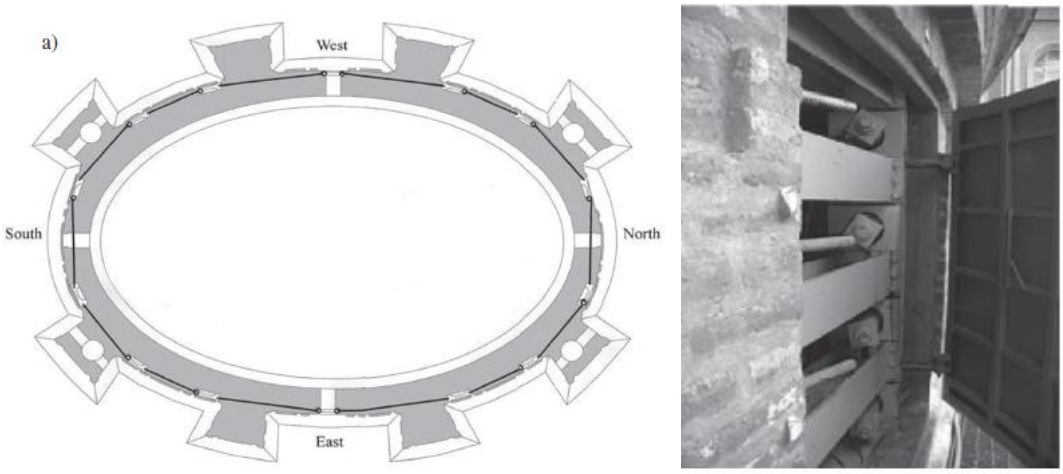

(a) (b)

Figure 90: Strengthening system based on slightly tensioned bars realized in 1987, (Calderini et al., 2006): (a) schematization of the system; and (b) reacting frame.

As shown in Figure 90, steel frames were interposed between each pair of bar segments to seam the drum structure. In 1997, bars were re-tensioned to compensate stress losses, (Chiorino et al., 2008). In general, a rigorous model-based evaluation of the effectiveness of masonry strengthening interventions is very often impracticable. The limited knowledge on force redistribution due to contact, friction and cracks, motivated to emulate the hybrid testing procedure on the sanctuary, distinguishing the NS from the PS, the latter supposed to be represented in this case by the area delimiting one of the 14 steel frames.

7.2. Finite Element model of the drum-dome system

An accurate FE model of the Basilica of Vicoforte has been created over the last decade, also thanks to an experimental testing campaigns and successive FE calibrations, based on both static and dynamic monitoring data, (Chiorino et al., 2011), (Ceravolo et al., 2017), (Pecorelli et al., 2018). On this basis, a 1231-nodes and 1230-elements FE model of the drum-dome system was derived to evince the proposed procedure.

The decision of manually code the FE model in Matlab environment was dictated by two strict requirements: (i) retrieving system matrices; and (ii) performing reasonably long-time history analyses with reduced memory storage. Moreover, developing finite elements can be easily adapted to a real-time computational environment for the purpose of conducting HS. The geometry of the dome approximates an ellipsoidal shape of axes of 37.15, 24.80 and 40.00 m, in X, Y and Z direction, respectively, and it is discretized in 82 sectors of 15 elements along the meridian direction. A uniform average thickness of 1.24 m is considered according to recent geo-radar scans. The size of the base ring elements approaches the dimension of the 1.20 m width, 2.00 m depth steel frames, which are represented by plate element of 0.015 m equivalent thickness.

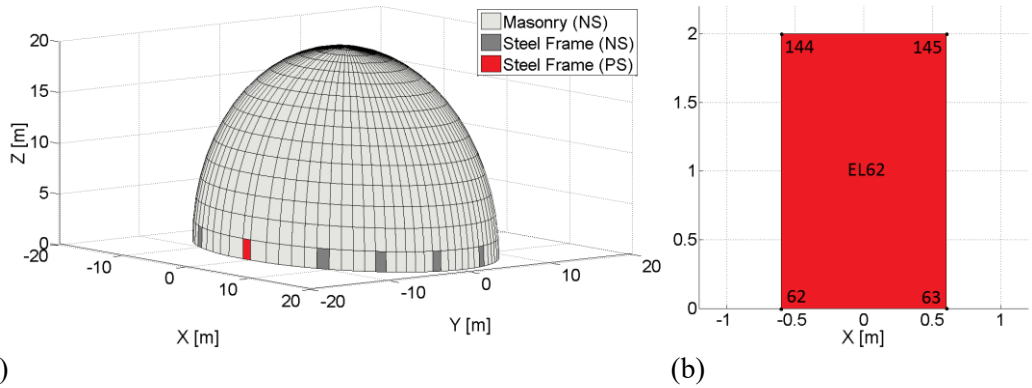

(a) (b)

Figure 91: Finite elements substructured mesh of the drum-dome system: (a) virtual model; and (b) emulated PS.

A 4-node finite element was used for all rings, except for the last level where 3-node elements were necessary. A set of multi-axial springs support the dome in

order to simulate the interaction with the remainder of the structure. The stiffnesses along the X, Y and Z directions were evaluated at approximately 3.4e7 N/m, 3.4e7 N/m and 3.8e7 N/m, respectively thanks to an available calibrated FE model. Figure 91 shows the implemented FE model with PS and NS partitioning highlighted. As can be appreciated from Figure 91, an area concerning a steel frame is supposed to be substructured in the laboratory as PS. For the sake of clarity, system DoFs are indicated with the number of the corresponding node and a displacement field component. For example, DOF 144-X corresponds to the X displacement of node 144. Table 23 summarizes the parameters of all materials, which are assumed to be linear elastic in this example.

Table 23: Material parameters.

Element	***E [GPa]***	***υ***	***ρ [kg/m^3]***
Masonry	5.9	0.35	1800
Steel	210	0.30	7800

Table 24 summarizes the first five eigenfrequencies of the structure while Figure 92 depicts the deformed shapes of the first two modes of the drum-dome system.

Table 24: Eigenfrequencies of the drum-dome system.

Mode	***Frequency [Hz]***
1	2.18
2	2.90
3	4.30
4	4.85
5	5.00

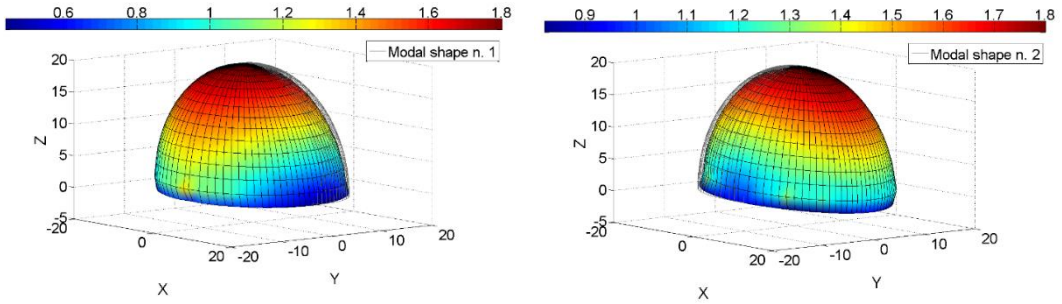

(a) (b)

Figure 92: Deformed shape of the drum-dome system of: (a) mode 1 at 2.18 Hz; and (b) mode 2 at 2.90 Hz.

The implementation of each single element as well as the overall model were validated with respect to solutions provided by the Ansys FE code, (Ansys, 2016).

7.3. Test design procedure applied to the drum-dome system

In this section some theoretical steps contained in Chapter 5 are briefly recalled for an easy reading of the application of the procedure to the case study.

7.3.1. Substructuring framework

The substructuring framework is introduced for the selected drum-dome system subjected to a seismic excitation, whose equation of motion reads:

$$\mathbf{M}\ddot{\mathbf{u}} + \mathbf{C}\dot{\mathbf{u}} + \mathbf{K}\mathbf{u} = -\mathbf{M}\mathbf{t}\ddot{u}_g \tag{69}$$

where, **M**, **C**, and **K** are mass, damping and stiffness matrices, respectively and **t** is a Boolean vector that project the seismic acceleration on the system DoFs. In line with the PDT-HS method, which splits the emulated system into PS and NS, (69) turns into:

$$\begin{cases} \left(\mathbf{M}^N + \mathbf{M}^P\right)\ddot{\mathbf{u}} + \left(\mathbf{C}^N + \mathbf{C}^P\right)\dot{\mathbf{u}} + \mathbf{K}^N\mathbf{u} = -\left(\mathbf{M}^N + \mathbf{M}^P\right)\mathbf{t}\ddot{u}_g - \mathbf{r}^P \\ \mathbf{r}^P = \mathbf{K}^P\mathbf{u} \end{cases} \tag{70}$$

In detail, superscript P and N refer to NS and PS and, $\mathbf{r}^P$ condenses the experimental response of the latter. Along the same criterion, the set of system DoFs can be partitioned on three disjoint subsets. One subset is restricted to interface DoFs connecting NS and PS while the other two gather pure numerical and physical DoFs,

$$\mathbf{u} = \begin{bmatrix} \mathbf{u}^N \\ \mathbf{u}^I \\ \mathbf{u}^P \end{bmatrix} \tag{71}$$

For brevity, the following simplified notation holds: N-DoFs, P-DoFs and I-DoFs, for pure numerical, pure physical and interface DoF, respectively. In this context, all matrices and vectors of (70) and (71) must be intended as expanded to the three DoF subsets. For the sake of clarity, the experimental displacement vector $\mathbf{u}^E$ is defined as:

$$\mathbf{u}^E = \begin{bmatrix} \mathbf{u}^I \\ \mathbf{u}^P \end{bmatrix} \tag{72}$$

It must be emphasized that the displacement response of the PS spans rigid body modes when the only constraint is provided by the connection to the NS. In

this respect, rigid rotations and translations define the kernel of the PS stiffness matrix:

$$\mathbf{R}^P = \ker\left(\mathbf{K}^P\right) \tag{73}$$

In the PDT-HS practice, the specimen is constrained to a reaction frame in a statically determined configuration and rigid body components are removed from the PS response to apply a pure deformation field to the specimen. This is of paramount importance for calculating all reaction forces, which are part of the restoring force vector, $\mathbf{r}^P$, and cannot be measured directly from actuator load cells. Both the experimental displacement vector $\mathbf{u}^E$ and the rigid body mode matrix $\mathbf{R}^P$ are partitioned according to retained or constrained experimental DoFs. At each time step k of the simulation, the rigid body response vector $\boldsymbol{\lambda}$ is calculated and purged from the PS response:

$$\begin{bmatrix}\mathbf{R}^{P,r}\\ \mathbf{R}^{P,c}\end{bmatrix}\boldsymbol{\lambda}_k + \begin{bmatrix}\mathbf{u}_k^{E,r}\\ \mathbf{u}_k^{E,c}\end{bmatrix} = \begin{bmatrix}\bar{\mathbf{u}}_k^{E,r}\\ \mathbf{0}\end{bmatrix} \tag{74}$$

where superscript r and c stand for retained and constrained DoFs and:

$$\boldsymbol{\lambda}_k = -\left(\mathbf{R}^{P,c}\right)^{-1}\mathbf{u}_k^{E,c} \tag{75}$$

As a result, the pure deformation component $\bar{\mathbf{u}}^{E,r}$ of the PS response is applied to the specimen, which is fixed to the reaction frame.

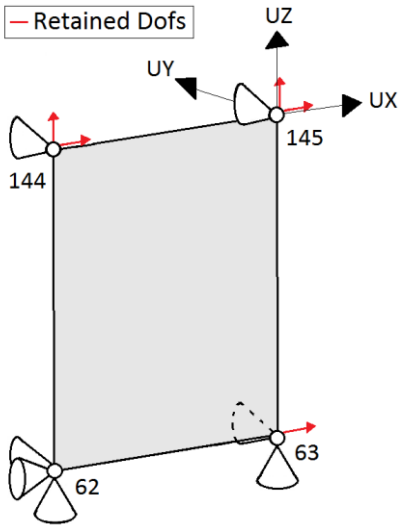

(a)

Node	*UX*	*UY*	*UZ*
62	Constrained	Constrained	Constrained
63	Retained	Constrained	Constrained
144	Retained	Constrained	Retained
145	Retained	Constrained	Retained

(b)

Figure 93: Constraint setting for the testing setup of the PS: (a) constraint representation; and (b) constrained and retained DoFs.

Restoring forces measured from load cells and calculated at constrained DoFs are fed back to the simulation environment that solves the equation of motion. Figure 93 depicts the constraint setting that was adopted for the substructured wall of the case study. As can be appreciated from Figure 93, seven displacements are constrained while the other five are retained by the experimental setup. According to the current PDT-HS practice, one actuator should handle each retained DoF so as to apply the deformation field to the tested specimen. Arguably, this represents a strong limitation for distributed parameter systems where several experimental DoFs are involved. Bursi and co-workers, (Bursi & Wagg, 2009), proposed a method to approximate the PS response with a smaller displacement vector. The basic idea was to optimize actuator placement in order to make specimen deformed configurations spanning the vector space defined by a corresponding reduction basis **T** over a reduced number of coordinates $\mathbf{u}^{E*}$:

$$\mathbf{u}^{E} \approx \mathbf{T}\mathbf{u}^{E*} \tag{76}$$

which allows for condensing PS matrices:

$$\tilde{\mathbf{K}}^{P} = \mathbf{T}^{T}\mathbf{K}^{P}\mathbf{T},\ \tilde{\mathbf{M}}^{P} = \mathbf{T}^{T}\mathbf{M}^{P}\mathbf{T},\ \tilde{\mathbf{f}}^{P} = \mathbf{T}^{T}\mathbf{f}^{P} \tag{77}$$

As a result, given the desired level of approximation, the test can be conducted with the minimum number of actuators. It is worth noting that, as reported in Chapter 5, the approach proposed by (Bursi & Wagg, 2009), here is extended to the case of floating PS. In this case, the reduction basis **T** operates on the sole deformation components of the PS displacement response, which is applied to the tested specimen:

$$\overline{\mathbf{u}}^{E,r} \approx \mathbf{T}\overline{\mathbf{u}}^{E*,r} \tag{78}$$

The following section describes how to formulate the reduction basis.

7.3.2. Selection of the reduction basis

As anticipated, the effectiveness of the testing setup relies on the optimal selection of the reduction basis **T**. In the following, the procedure proposed in Chapter 5 is applied. It is noteworthy that a robust testing design process should answer the two following questions:

- Which is the minimum rank of the reduction basis for a given level of approximation ?
- How to optimize the actuator placement to cover the reduction basis span ?

Principal Component Analysis (PCA) was proved of valuable help in answering to these questions, (Bursi et al., 2014). The key idea of PCA is to provide a separated representation of a huge number of correlated variables considering a smaller number of uncorrelated variables while preserving the overall process variance, (Kerschen, 2005). This transformation decorrelates the signal components and maximizes the preserved variance. In detail, for any real (m x n) matrix $\mathbf{X}$ there exists a real factorization called Singular Value Decomposition (SVD) that can be written as:

$$\mathbf{X} = \mathbf{U}\boldsymbol{\Sigma}\mathbf{V}^T \tag{79}$$

where $\mathbf{U}$ is an (m x m) orthonormal matrix whose columns $\mathbf{u}_i$, namely the left singular vectors, represents the Proper Orthogonal Modes (POMs) while $\mathbf{V}$ is an (n x n) orthonormal matrix, whose column vectors $\mathbf{v}_i$, namely the right singular vectors, represent the time modulation of the corresponding POMs. $\boldsymbol{\Sigma}$ is an (m x n) pseudo-diagonal and semi-positive definite matrix with singular values σ_i as diagonal entries. From a physical standpoint, singular values relate to the eigenvalues of the autocovariance matrix of the process $\mathbf{X}$ as:

$$\left\{\sigma_1^2 \quad \ldots \quad \sigma_m^2\right\} = eig\left(\left(\mathbf{X}-\boldsymbol{\mu}_\mathbf{X}\right)\left(\mathbf{X}-\boldsymbol{\mu}_\mathbf{X}\right)^T\right) \tag{80}$$

where $\boldsymbol{\mu}_X$ is a matrix of repeated vectors of time averaged values of $\mathbf{X}$. Accordingly, the original data set $\mathbf{X}$ can be reconstructed up to the desired degree of approximation by retaining a reduced number $q < m$ of POM:

$$\left(\tilde{\mathbf{X}}-\boldsymbol{\mu}_X\right) = \sum_{i=1}^{q}\sigma_i\mathbf{u}_i\mathbf{v}_i^T \tag{81}$$

Another important property of the Proper Orthogonal Decomposition (POD) is that it minimizes the root mean square error between the original signal $\mathbf{X}$ and its reduced separated representation, $\tilde{\mathbf{X}}$. In order to show how is possible to use PCA to optimize the design of the testing setup, the time history analysis of the FE model of the drum-dome system subjected to the Loma Prieta earthquake was simulated using the Newmark method, (Newmark, 1959), and a data set $\mathbf{X}$ was defined on the basis of the deformation response field of the PS:

$$\mathbf{X} = \left[\bar{\mathbf{u}}_1^{E,r} \quad \bar{\mathbf{u}}_2^{E,r} \quad \ldots \quad \bar{\mathbf{u}}_n^{E,r}\right] \tag{82}$$

Based on the total data variance $E = \sum_{i=1}^{m}\sigma_i^2$, it is defined $E_i = \sigma_i^2/E$ as the variance fraction carried by the i-th POM. The stem plot of Figure 94 compares the obtained values. As can be appreciated from Figure 94, the almost total variance of the deformation components of the displacement response of the PS is carried by the first POM.

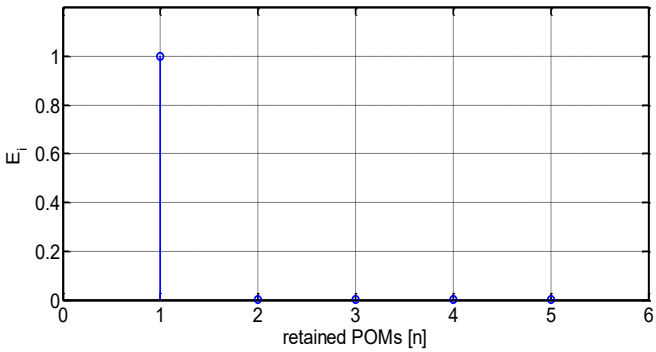

Figure 94: Fraction of data variance carried by the single POM.

In order to provide a more physical measure of the degree of approximation of the reconstructed response field, the following Weighted Normalized Root Mean Square Error (WNRMSE) score is introduced:

$$WNRMSE(\mathrm{X},\widetilde{\mathrm{X}}) = \frac{\sum_{i=1}^{m} NRMSE(\mathrm{x}_i,\tilde{\mathrm{x}}_i)\cdot max\left(\left|\mathrm{x}_i-\mu_{\mathrm{X}_i}\right|\right)}{\sum_{i=1}^{m} max\left(\left|\mathrm{x}_i-\mu_{\mathrm{X}_i}\right|\right)} \tag{83}$$

where:

$$NRMSE(\mathrm{x},\tilde{\mathrm{x}}) = \frac{\sqrt{\sum_{j=1}^{n}(x_j-\tilde{x}_j)^2/n}}{|max(\mathrm{x})-min(\mathrm{x})|} \tag{84}$$

and $\mathbf{x}_i$ represents the time history response of the single *i*-th retained DoF. As can be argued from (83) and (84), absolute displacement peaks weight the NRMSE average. Figure 95 depicts the trend of the WNRMSE up to the total number of POMs.

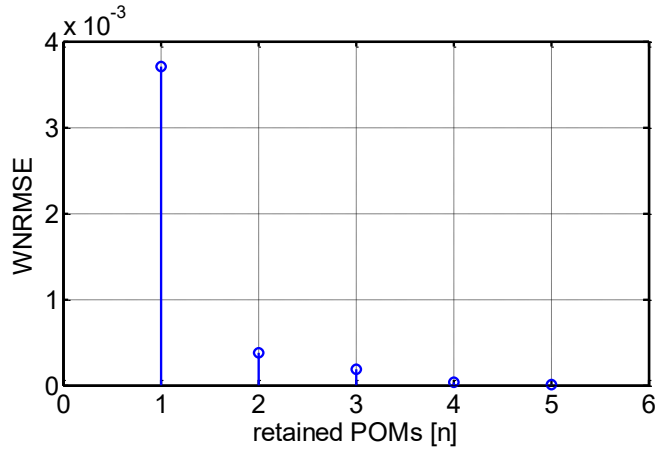

Figure 95: WNRMSE of the reconstructed deformation component of the PS response.

As can be appreciated from Figure 95, the first POM is arguably enough to capture the deformation response of the PS. This is confirmed by Figure 96 that

compares reference and reconstructed signals for DoF 144-X and 145-X, which showed dominant displacement peaks.

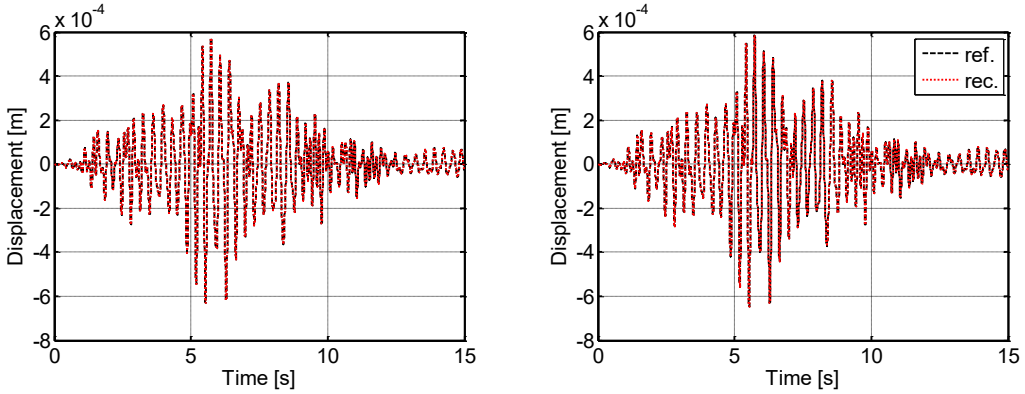

(a) (b)

Figure 96: Reference and reconstructed responses for: (a) DoF 144-X; and (b) DoF 145-X.

As can be observed from Figure 96, an almost exact signal reconstruction of the horizontal response is achieved by retaining the first POM only. Analogously, Figure 97 compare reconstructed signals corresponding to vertical displacements.

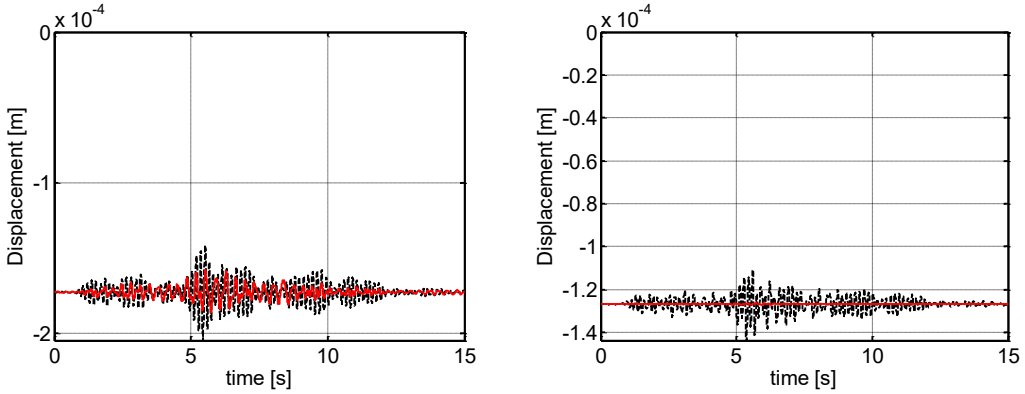

(a) (b)

Figure 97: Reference and reconstructed responses for: (a) DoF 144-Z; and (b) DoF 145-Z.

As can be appreciated from Figure 97, the retained POM does not capture the variability of vertical displacements, especially for DoF 145-Z, which is however negligible with respect to average values.

7.3.3. Actuator placement and validation of the setup

Based on the deformed shape of the retained POM, which is depicted in Figure 98a, the experimental setup layout of Figure 98b is obtained for testing the PS.

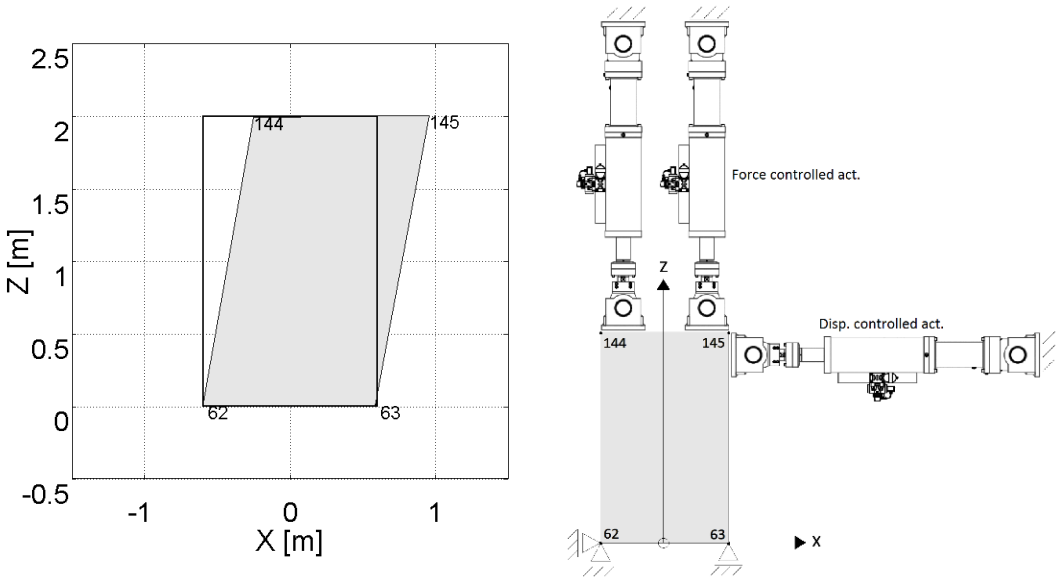

(a) (b)

Figure 98: Results of the testing design: (a) retained POM; and (b) experimental setup.

As shown by Figure 98a, the deformed shape of the retained POM indicates a shear deformation of the panel while the variance of the vertical displacements is negligible. Accordingly, a displacement controlled horizontal actuator pushes the top of the wall while two force controlled vertical actuators apply the gravity load coming from the dome. In order to validate the designed testing setup, a reduced order FE model of the drum-dome system was implemented. The reduction basis **T** operating on the PS DoFs was obtained by combining deformation modes preserved by the testing setup and rigid body modes, which describe rotations and translations of the floating domain. The Guyan, (Guyan, 1965), reduction was applied to obtain the deformation modes, $\mathbf{T}_d$, preserved by the setup:

$$\mathbf{T}_d = \begin{bmatrix} \mathbf{I} \\ -\mathbf{K}_{ss}^{P,r^{-1}} \mathbf{K}_{sm}^{P,r} \end{bmatrix} \tag{85}$$

where subscripts *s* and *m* stand for retained slave and master DoF subsets, respectively, and:

$$\mathbf{K}^{P,r} = \begin{bmatrix} \mathbf{K}_{mm}^{P,r} & \mathbf{K}_{ms}^{P,r} \\ \mathbf{K}_{sm}^{P,r} & \mathbf{K}_{ss}^{P,r} \end{bmatrix} \tag{86}$$

is the sub-block of the PS stiffness matrix retained by the experimental setup, after discarding DoFs that are physically constrained to the reaction frame in the idealized virtual laboratory. In this case, and according to Figure 98a, master DoFs are DoF 144-X, DoF 144-Z and DoF 145-Z while the slave DoF set includes DoF 145-X and DoF 63-X. It is noteworthy that the Guyan condensation assumes a static deformation of the domain in agreement with the slow

application of loads on the PS, as done in PDT-HS methods. Rigid rotations and translations were preserved by retaining corresponding rigid body modes. The resulting reduction basis **T** reads:

$$\mathbf{T} = \begin{bmatrix} \mathbf{T}_d & \mathbf{R}^{P,r} \\ \mathbf{0} & \mathbf{R}^{P,c} \end{bmatrix} \tag{87}$$

Figure 99 compares the displacement response of DoF 144-X and DoF 144-Z obtained from the reference and the reduced (emulated) models.

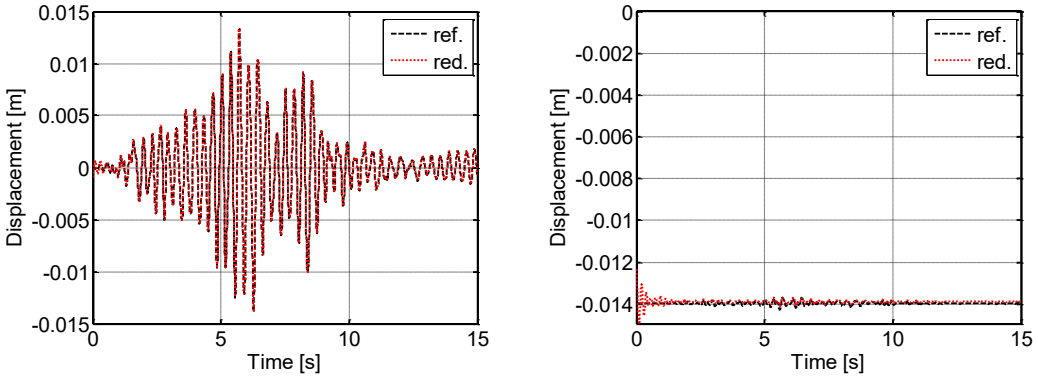

(a) (b)

Figure 99: Displacement response of: (a) DoF 144-X; and (b) DoF 144-Z.

As can be appreciated from Figure 99, the reduced model exactly reproduces the horizontal response obtained from the reference simulation. On the other hand, the small variability of the vertical load justifies the application of a nominal value for testing purpose. Such results corroborate the effectiveness of the test design procedure.

To recap this emblematic example, we can conclude that the proposed procedure is suitable for automatic implementations and the numerical validation highlighted its effectiveness. Masonry structures, which are inherently distributed parameter systems, can particularly benefit of the developed approach. A rigorous model-based evaluation of the effectiveness of strengthening interventions is very often impracticable due to the limited knowledge on force redistribution. In this context, hybrid simulation can be profitably used as virtualization paradigm with a potential great impact on cultural heritage conservation.

7.4. References chapter 7

Ansys, Ansys Academic Research, Release 16.2, 2016.

Aoki, T., Komiyama, T., Tanigawa, Y., Hatanaka, S., Yuasa, N., Hamasaki, H., & Roccati, R. (2004, July). Non-destructive testing of the Sanctuary of

Vicoforte. In Proceedings of 13th international brick and block masonry conference (Vol. 4, pp. 1109-1118).

Bursi, O. S., & Wagg, D. (Eds.). (2009). Modern testing techniques for structural systems: dynamics and control (Vol. 502). Springer Science & Business Media.

Bursi, O. S., Abbiati, G., & Reza, M. S. (2014). A novel hybrid testing approach for piping systems of industrial plants. Smart Structures and Systems, 14(6), 1005-1030.

Calderini C., Chiorino M. A., Roccati R., D'addato C., Aoki T., Spadafora A. (2006). Monitoring and Modeling Strategies for the World's Largest Elliptical Dome at Vicoforte, Structural Analysis of Historical Constructions, New Delhi.

Ceravolo, R., De Marinis, A., Pecorelli, M. L., & Zanotti Fragonara, L. (2017). Monitoring of masonry historical constructions: 10 years of static monitoring of the world's largest oval dome. Structural Control and Health Monitoring, 24(10), e1988.

Chiorino, M. A., Ceravolo, R., Spadafor, A., Zanotti Fragonara, L., & Abbiati, G. (2011). Dynamic characterization of complex masonry structures: the Sanctuary of Vicoforte. International Journal of Architectural Heritage, 5(3), 296-314.

Chiorino, M. A., Spadafora, A., Calderini, C., & Lagomarsino, S. (2008). Modeling strategies for the world's largest elliptical dome at Vicoforte. International Journal of Architectural Heritage, 2(3), 274-303.

Guyan, R. J. (1965). Reduction of stiffness and mass matrices. AIAA journal, 3(2), 380-380.

Kerschen, G., Golinval, J. C., Vakakis, A. F., & Bergman, L. A. (2005). The method of proper orthogonal decomposition for dynamical characterization and order reduction of mechanical systems: an overview. Nonlinear dynamics, 41(1-3), 147-169.

Newmark, N. M. (1959, July). A method of computation for structural dynamics. American Society of Civil Engineers.

Pecorelli, M. L., Ceravolo, R., & Epicoco, R. (2018). An Automatic Modal Identification Procedure for the Permanent Dynamic Monitoring of the Sanctuary of Vicoforte. International Journal of Architectural Heritage, 1-15.

Conclusions and perspectives

In order to extend the use of Hybrid Models to architectural heritage structures, this thesis has presented a new method that allows the Hybrid Simulation and testing of mass distributed systems with distributed interfaces between the Numerical and the Physical Subdomain. The proposed method also allows for the hybrid testing of physical subdomains that exhibit a floating behaviour, i.e. the physical subdomain, in the real system, is not directly connected to the ground, and thus, exhibits rigid body motions. Using advanced techniques for substructuring and reduction of the system's matrices, such as the Component Mode Synthesis, the method is extended to any general system, reducing the risk of control instability during the test. This is achieved going to reduce the frequency bandwidth of the test while keeping the time scale small enough.

In the thesis it is also proposed a novel technique to perform Ensemble Model Corroboration, i.e. a technique that point to a synergistic, and multi-objective, optimization of the model parameters going to combine not unique solutions of the calibration process. The synergistic effect lies in the fact that the solution of the optimization satisfies two conditions: (i) it is the most likely solution; and (ii) it is the solution that reduce the variance between the singles not unique solutions. In complex structural models, such as those of architectural heritage buildings, this helps to reduce overfitting risk, determining more reliable values of the model parameters, with an acceptable discrepancy between the model prediction and the experimental data. The technique can be applied to either linear or nonlinear corroboration of models.

For the latter case, in the thesis, the nonlinear model corroboration of a monitored masonry building has been addressed by the use of Time Frequency Distributions of the experimental records. The estimates of the model parameters of hysteretic and degrading laws results from an optimization in the joint time-frequency domain. While estimators for degrading systems can be naturally defined as time-varying (instantaneous estimators), instead of deterministic estimate of the model parameters for each time instant the method also allows for an instantaneous probabilistic distribution of the model parameters, thanks to the information coming from the frequency domain.

Once the model of an architectural heritage structure is corroborated (with or without preliminary hybrid simulations/testing), hybrid simulations can be carried out, also thanks the methods presented in the thesis, for different aims:

- to perform destructive tests on a physical model the represents a part or component of the architectural heritage structure, and thus investigate the effects on the global system behaviour, both in linear and nonlinear domain;
- to consider complex behaviours in the analysis and testing of architectural heritage structures, such as the effect of the vertical loads and stresses on the strength of materials, avoiding the modelling of physical behaviours that exhibit too many uncertainties (e.g. contact, etc.);
- to evaluate, in a more realistic way, the effects of retrofitting and strengthening interventions, before performing them on the real system;
- to assess the stability of overhanging elements, pinnacles, bell towers, gables, etc., which intrinsically exhibit a floating behaviour.

Finally, in its most general form, hybrid experimentation will allow for geographically distributed tests. In this distributed hybrid test numerous physical models, built in different laboratories (or even in the same laboratory), are used to emulate different parts of a complex structure. All the physical models are then combined, in the hybrid distributed model, through a virtual model. In the ideal case that all the subcomponents of the system are reproduced in laboratory, the virtual model would reduce to the mathematical laws that connect the physical substructures. When relying on a greater number of physical models, the need to resort to unreliable abstractions of the structural behaviour decreases, thus increasing the potential of the hybrid (distributed) model and making the simulations an accurate reflection of the reality.

References

Abbiati, G., Bursi, O. S., Cazzador, E., Ceravolo, R., Mei, Z., Paolacci, F., & Pegon, P. (2015). Pseudo-dynamic testing based on non-linear dynamic substructuring of a reinforced concrete bridge. In Experimental research in earthquake engineering (pp. 83-98). Springer, Cham.

Abbiati, G., Bursi, O. S., Cazzador, E., Ceravolo, R., Mei, Z., Paolacci, F., & Pegon, P. (2013). Pseudo-dynamic Testing with Non-linear Substructuring of a Reinforced Concrete Bridge Based on System Identification and Model Updating Techniques. SERIES Concluding Workshop, Joint Research Center, ISPRA, Italy, 28 May 2013.

Adams, D. E., & Allemang, R. J. (1999). A new derivation of the frequency response function matrix for vibrating non-linear systems. Journal of Sound and Vibration, 227(5), 1083-1108.

Aledo, J. A., Gámez, J. A., & Molina, D. (2013). Tackling the rank aggregation problem with evolutionary algorithms. Applied Mathematics and Computation, 222, 632-644.

Aledo, J. A., Gámez, J. A., & Molina, D. (2017). Tackling the supervised label ranking problem by bagging weak learners. Information Fusion, 35, 38-50.

Allemang, R. J., & Brown, D. L. (1982, November). A correlation coefficient for modal vector analysis. In Proceedings of the 1st international modal analysis conference (Vol. 1, pp. 110-116). SEM Orlando.

Andoni, A., Fagin, R., Kumar, R., Patrascu, M., & Sivakumar, D. (2008, June). Corrigendum to efficient similarity search and classification via rank aggregation by Ronald Fagin, Ravi Kumar and D. Sivakumar (proc. SIGMOD'03). In Proceedings of the 2008 ACM SIGMOD international conference on Management of data (pp. 1375-1376). ACM.

Ansys, Ansys Academic Research, Release 16.2, 2016.

Aoki, T., Komiyama, T., Tanigawa, Y., Hatanaka, S., Yuasa, N., Hamasaki, H., & Roccati, R. (2004, July). Non-destructive testing of the Sanctuary of Vicoforte. In Proceedings of 13th international brick and block masonry conference (Vol. 4, pp. 1109-1118).

Ashrafi, S. S. (2008). Adaptive parametric identification scheme for a class of nondeteriorating and deteriorating nonlinear hysteretic behavior.

Audet, C., & Dennis Jr, J. E. (2002). Analysis of generalized pattern searches. SIAM Journal on optimization, 13(3), 889-903.

Baber, T. N. (1986). Modeling general hysteresis behaviour and random vibration applications. Journal of Vibration Acoustics Stress and Reliability in Design, 108, 411-420.

Baber, T., & Noori, M. (1985). Random vibration of degrading pinching systems. Journal of Engineering Mechanics ASCE, 111, 1010-1026.

Baber, T., & Wen, Y.-K. (1981). Random vibrations of hysteretic, degrading systems. J. Eng. Mech. Div. ASCE, 107, 1069–1087.

Bakhaty, A.A., Govindjee, S., and Mosalam, K.M. (2016). "Theoretical Evaluation of Hybrid Simulation Applied to Continuous Plate Structures." Journal of Engineering Mechanics, 142(12).

Bassoli, E., Vincenzi, L., D'Altri, A. M., de Miranda, S., Forghieri, M., & Castellazzi, G. (2018). Ambient vibration-based finite element model updating of an earthquake-damaged masonry tower. Structural Control and Health Monitoring, 25(5), e2150.

Beck, J. L., & Katafygiotis, L. S. (1998). Updating models and their uncertainties. I: Bayesian statistical framework. Journal of Engineering Mechanics, 124(4), 455-461.

Beggs, S., Cardell, S., & Hausman, J. (1981). Assessing the potential demand for electric cars. Journal of econometrics, 17(1), 1-19.

Benedettini, F. C. (1995). Identification of hysteretic oscillators under earthquake loading by nonparametric models. J. Eng. Mech., 121, 606–612.

Bertolesi, E., Adam, J. M., Rinaudo, P., & Calderón, P. A. (2019). Research and practice on masonry cross vaults–A review. Engineering Structures, 180, 67-88.

Binkhonain, M., & Zhao, L. (2019). A Review of Machine Learning Algorithms for Identification and Classification of Non-Functional Requirements. Expert Systems with Applications.

Boscato, G., Russo, S., Ceravolo, R., & Fragonara, L. Z. (2015). Global sensitivity-based model updating for heritage structures. Computer-Aided Civil and Infrastructure Engineering, 30(8), 620-635.

Boscato, G., Russo, S., Ceravolo, R., & Fragonara, L. Z. (2015). Global sensitivity-based model updating for heritage structures. Computer-Aided Civil and Infrastructure Engineering, 30(8), 620-635.

Bouc, R. (1971). Mode` le mathe´matique d'hyste´re´sis. Acustica, 24, 16–25.

Brun, M., Batti, A., Combescure, A., & Gravouil, A. (2014). External coupling software based on macro-and micro-time scales for explicit/implicit multi-time-step co-computations in structural dynamics. Finite Elements in Analysis and Design, 86, 101-119.

Buonopane, S.G. and White, R.N. (1999). "Pseudodynamic testing of masonry infilled reinforced concrete frame." J. Struct. Eng., ASCE 125, 578-589.

Bursi*, O. S., Kumar, A., Abbiati, G., & Ceravolo, R. (2014). Identification, model updating, and validation of a steel twin deck curved cable-stayed footbridge. Computer-Aided Civil and Infrastructure Engineering, 29(9), 703-722.

Bursi, O. C. (2009). Identification of the damage evolution in a benchmark steel-concrete composite structure during Pseudo-Dynamic testing. CompDyn.

Bursi, O. C. (2012). Identification of the hysteretic behaviour of a partial-strength steel–concrete moment-resisting frame structure subject to pseudodynamic tests. Earthquake Engng Struct. Dyn., 41, 1883–1903.

Bursi, O. S., & SHING, P. S. (1996). Evaluation of some implicit time-stepping algorithms for pseudodynamic tests. Earthquake engineering & structural dynamics, 25(4), 333-355.

Bursi, O. S., & Wagg, D. (Eds.). (2009). Modern testing techniques for structural systems: dynamics and control (Vol. 502). Springer Science & Business Media.

Bursi, O. S., Abbiati, G., & Reza, M. S. (2014). A novel hybrid testing approach for piping systems of industrial plants. Smart Structures and Systems, 14(6), 1005-1030.

Bursi, O. S., Abbiati, G., & Reza, M. S. (2014). A novel hybrid testing approach for piping systems of industrial plants. Smart Structures and Systems, 14(6), 1005-1030.

Bursi, O. S., Abbiati, G., Cazzador, E., Pegon, P., & Molina, F. J. (2017). Nonlinear heterogeneous dynamic substructuring and partitioned FETI time integration for the development of low-discrepancy simulation

models. International Journal for Numerical Methods in Engineering, 112(9), 1253-1291.

Bursi, O. S., Ceravolo, R., Erlicher, S., & Zanotti Fragonara, L. (2012). Identification of the hysteretic behaviour of a partial-strength steel–concrete moment-resisting frame structure subject to pseudodynamic tests. Earthquake Engineering & Structural Dynamics, 41(14), 1883-1903.

Bursi, O. S., Kumar, A., Abbiati, G., & Ceravolo, R. (2014). Identification, model updating, and validation of a steel twin deck curved cable-stayed footbridge. Computer-Aided Civil and Infrastructure Engineering, 29(9), 703-722.

Calderini C., Chiorino M. A., Roccati R., D'addato C., Aoki T., Spadafora A. (2006). Monitoring and Modeling Strategies for the World's Largest Elliptical Dome at Vicoforte, Structural Analysis of Historical Constructions, New Delhi.

Cao, Z., Qin, T., Liu, T. Y., Tsai, M. F., & Li, H. (2007, June). Learning to rank: from pairwise approach to listwise approach. In Proceedings of the 24th international conference on Machine learning (pp. 129-136). ACM.

Carmona, R. H. (1998). Practical Time-Frequency Analysis. Academic Press.

Carrella, A., & Ewins, D. J. (2011). Identifying and quantifying structural nonlinearities in engineering applications from measured frequency response functions. Mechanical Systems and Signal Processing, 25(3), 1011-1027.

Cavallari Murat, A. (1982). Come carena viva Scritti sparsi, vol II. Bottega d'Erasmo, Torino. (In Italian).

Ceravolo, R. (2004). Use of instantaneous estimators for the evaluation of structural damping. J. Sound Vib., 274, 385–401.

Ceravolo, R. (2009). Time-frequency analysis. Encyclopedia of Structural Health Monitoring, 503–524.

Ceravolo, R. D. (2010). Instantaneous identification of degrading hysteretic oscillators under earthquake excitation. Struct. Health Monitor., 9, 447–464.

Ceravolo, R. D., & Erlicher, S. (2007). Instantaneous identification of Bouc-Wen-type hysteretic systems from seismic response data. Key Eng. Mat., 347, 331–338.

Ceravolo, R. D., & Molinari, F. (2001). Developments and comparisons on the definition of an instantaneous damping estimator for structures under natural excitation. Key Eng. Mat., 231–240.

Ceravolo, R. E. (2013). Comparison of restoring force models for the identification of structures with hysteresis and degradation. Journal of Sound and Vibration, 332, 6982-6999.

Ceravolo, R., & Abbiati, G. (2013). Time Domain Identification of Structures: a Comparative Analysis of Output-Only Methods, In: JOURNAL OF ENGINEERING MECHANICS, pagine 537-544, ISSN: 0733-9399.

Ceravolo, R., De Lucia, G., & Pecorelli, M. L. (2017). Issues on the modal characterization of large monumental structures with complex dynamic interactions. Procedia Engineering, 199, 3344-3349.

Ceravolo, R., De Lucia, G., Miraglia, G., Pecorelli, M.L. (2019). Thermo-elastic finite element model updating with application to monumental buildings. Computer-Aided Civil and Infrastructure Engineering, CACAIE. (Submitted).

Ceravolo, R., De Lucia, G., Miraglia, G., Pecorelli, M.L. (2019). Thermo-elastic finite element model updating with application to monumental buildings. Computer-Aided Civil and Infrastructure Engineering, CACAIE. (Submitted).

Ceravolo, R., De Marinis, A., Pecorelli, M. L., & Zanotti Fragonara, L. (2017). Monitoring of masonry historical constructions: 10 years of static monitoring of the world's largest oval dome. Structural Control and Health Monitoring, 24(10), e1988.

Ceravolo, R., De Marinis, A., Pecorelli, M. L., & Zanotti Fragonara, L. (2017). Monitoring of masonry historical constructions: 10 years of static monitoring of the world's largest oval dome. Structural Control and Health Monitoring, 24(10), e1988.

Ceravolo, R., Erlicher, S., & Fragonara, L. Z. (2013). Comparison of restoring force models for the identification of structures with hysteresis and degradation. Journal of Sound and Vibration, 332(26), 6982-6999.

Ceravolo, R., Matta, E., Quattrone, A., & Zanotti Fragonara, L. (2017). Amplitude dependence of equivalent modal parameters in monitored buildings during earthquake swarms. Earthquake Engineering & Structural Dynamics, 46(14), 2399-2417.

Ceravolo, R., Pistone, G., Fragonara, L. Z., Massetto, S., & Abbiati, G. (2016). Vibration-based monitoring and diagnosis of cultural heritage: a methodological discussion in three examples. International Journal of Architectural Heritage, 10(4), 375-395.

Cerone, M., Croci, G., & Viskovic, A. (2000, October). The structural behaviour of Colosseum over the centuries. In International congres More than two thousand years in the history of architecture, Bethlehem.

Chassiakos, A. M. (1995). Adaptive methods for the identification of hysteretic structures. Proceedings ofthe American Control Conference, 2349–2353.

Chiorino, M. A., Ceravolo, R., Spadafor, A., Zanotti Fragonara, L., & Abbiati, G. (2011). Dynamic characterization of complex masonry structures: the Sanctuary of Vicoforte. International Journal of Architectural Heritage, 5(3), 296-314.

Chiorino, M. A., Spadafora, A., Calderini, C., & Lagomarsino, S. (2008). Modeling strategies for the world's largest elliptical dome at Vicoforte. International Journal of Architectural Heritage, 2(3), 274-303.

Chiorino, M.A. (2017). Reduced scale mechanical models in 20th century structural architecture: Guido Oberti (1907-2004) and Pier Luigi Nervi (1891-1979) A very special relationship. Spring School on Structural Health monitoring of architectural heritage, Columbia Univeristy/Politecnico di Torino, Vicoforte, Italy, June 15-16.

Craig, R. R., & Kurdila, A. J. (2006). Fundamentals of structural dynamics. John Wiley & Sons.

Croci, G. (2006, September). Seismic behavior of masonry domes and vaults of Hagia Sophia in Istanbul and St. Francis in Assisi. In Proceedings of the First European Conference on Earthquake Engineering and Seismology—A Joint Event of the 13th ECEE & 30th General Assembly of the ESC (pp. 3-8).

Cundall, P. A., & Strack, O. D. (1979). A discrete numerical model for granular assemblies. geotechnique, 29(1), 47-65.

Demarie, G. V., Ceravolo, R., Sabia, D., & Argoul, P. (2011). Experimental identification of beams with localized nonlinearities. Journal of Vibration and Control, 17(11), 1721-1732.

Di Ludovico, M., Digrisolo, A., Graziotti, F., Moroni, C., Belleri, A., Caprili, S., ... & Ferracuti, B. (2017). The contribution of ReLUIS to the usability

assessment of school buildings following the 2016 central Italy earthquake. Bollettino di Geofisica Teorica ed Applicata, 58(4).

Dolce, M., Nicoletti, M., De Sortis, A., Marchesini, S., Spina, D., & Talanas, F. (2017). Osservatorio sismico delle strutture: the Italian structural seismic monitoring network. Bulletin of Earthquake Engineering, 15(2), 621-641.

Du, X., & Wang, F. (2010). Modal identification based on Gaussian continuous time autoregressive moving average model. J. of Sound and Vib., 329, 4294–4312.

Dwork, C., Kumar, R., Naor, M., & Sivakumar, D. (2001, May). Rank aggregation methods for the web. In Proceedings of the 10th international conference on World Wide Web (pp. 613-622). ACM.

E.CEN. (1998). "1052-1–methods of test for masonry–part 1: Determination of compressive strength," European Committee for Standardization, Brussels.

Ebrahimian, H., Astroza, R., & Conte, J. P. (2015). Extended Kalman filter for material parameter estimation in nonlinear structural finite element models using direct differentiation method. Earthquake Engineering & Structural Dynamics, 44(10), 1495-1522.

El Saddik, A. (2018). Digital twins: the convergence of multimedia technologies. IEEE MultiMedia, 25(2), 87-92.

Ewins, D. J. (2000). Modal testing: theory, practice and application, 2000. Research Studies Press LTD., Baldock, Hertfordshire, England, 171, 415-437.

Ewins, D.J. (2006). A future for experimental structural dynamics, in: Proceedings of the International Conference on Noise and Vibration Engineering (ISMA), Leuven, Belgium, 2006.

Fagin, R., Kumar, R., & Sivakumar, D. (2003, June). Efficient similarity search and classification via rank aggregation. In Proceedings of the 2003 ACM SIGMOD international conference on Management of data (pp. 301-312). ACM.

Farhat, C. and Roux, F.-X. (1991). "A method of finite element tearing and interconnecting and its parallel solution algorithm." Int J Num Meth Engng, 32, 1205-1227, doi: 10.1002/nme.1620320604.

Feldman, M. (2006). Time-varying vibration decomposition and analysis based on the Hilbert transform. Journal of Sound and Vibration, 295(3-5), 518-530.

Feldman, M. (2007). Considering high harmonics for identification of non-linear systems by Hilbert transform. Mechanical Systems and Signal Processing, 21(2), 943-958.

Feldman, M. (2014). Hilbert transform methods for nonparametric identification of nonlinear time varying vibration systems. Mechanical Systems and Signal Processing, 47(1-2), 66-77.

Ferretti, D., & Bažant, Z. P. (2006a). Stability of ancient masonry towers: Moisture diffusion, carbonation and size effect. Cement and Concrete Research, 36(7), 1379-1388.

Ferretti, D., & Bažant, Z. P. (2006b). Stability of ancient masonry towers: Stress redistribution due to drying, carbonation, and creep. Cement and Concrete Research, 36(7), 1389-1398.

Friswell, M., & Mottershead, J. E. (2013). Finite element model updating in structural dynamics (Vol. 38). Springer Science & Business Media.

Fuellekrug, U., & Goege, D. (2012). Identification of weak non-linearities within complex aerospace structures. Aerospace Science and Technology, 23(1), 53-62.

Goldberg, D. E. Genetic Algorithms in Search, Optimization, and Machine Learning, New York: Addison-Wesley, 1989.

Gormley, I. C., & Murphy, T. B. (2005). Exploring Irish election data: A mixture modelling approach. Technical Report 05/08.

Gravouil, A., Combescure, A. (2001). "Multi-time-step explicit – implicit method for non-linear structural dynamics." International Journal for Numerical Methods in Engineering, 199-225.

Green, P. L., & Worden, K. (2015). Bayesian and Markov chain Monte Carlo methods for identifying nonlinear systems in the presence of uncertainty. Philosophical Transactions of the Royal Society A: Mathematical, Physical and Engineering Sciences, 373(2051), 20140405.

Guiver, J., & Snelson, E. (2009, June). Bayesian inference for Plackett-Luce ranking models. In proceedings of the 26th annual international conference on machine learning (pp. 377-384). ACM.

Guyan, R. J. (1965). Reduction of stiffness and mass matrices. AIAA journal, 3(2), 380-380.

Haddad, H., Guessasma, M., & Fortin, J. (2016). A DEM–FEM coupling based approach simulating thermomechanical behaviour of frictional bodies with interface layer. International Journal of Solids and Structures, 81, 203-218.

Hakuno, M., Shidawara, M., and Hara, T. (1969). Dynamic destructive test of a cantilever beam, controlled by an analog-computer. 土木学会論文報告集, 第171号 ・1969年11月.

Hammond, J. W. (1996). The analysis of non-stationary signals using time-frequency methods. J. of Sound and Vib., 190, 419–447.

Hashemi, M.J., and Mosqueda, G. (2014). "Innovative substructuring technique for hybrid simulation of multistory buildings through collapse." Earthquake Engineering and Structural Dynamics, doi:10.1002/eqe.2427.

Heller, L., Foltete, E., & Piranda, J. (2009). Experimental identification of nonlinear dynamic properties of built-up structures. Journal of Sound and Vibration, 327(1-2), 183-196.

Hernandez-Garcia, M. M. (2010). An experimental investigation of change detection in uncertain chain-like systems. J. of Sound and Vib, 329, 2395–2409.

Hesse, M.B. (1980). Modelli e analogie nella scienza. Feltrinelli, Milano. (In Italian).

Hildebrand, S., & Bergmann, E. (2015). Form-finding, form-shaping, designing architecture. Mendrisio Academy Press.

Hochrainer, M. J., & Schattovich, P. (2017). Real-Time Hybrid Simulation of an Unmanned Aerial Vehicle. In Dynamics of Coupled Structures, Volume 4 (pp. 41-48). Springer, Cham.

Hu, J., Lam, H. F., & Yang, J. H. (2018). Operational modal identification and finite element model updating of a coupled building following Bayesian approach. Structural Control and Health Monitoring, 25(2), e2089.

Huang, N. E., Shen, Z., Long, S. R., Wu, M. C., Shih, H. H., Zheng, Q., ... & Liu, H. H. (1998). The empirical mode decomposition and the Hilbert spectrum for nonlinear and non-stationary time series analysis. Proceedings of the Royal Society of London. Series A: Mathematical, Physical and Engineering Sciences, 454(1971), 903-995.

Hunter, D. R. (2004). MM algorithms for generalized Bradley-Terry models. The annals of statistics, 32(1), 384-406.

Icomos-Iscarsah. (2003). ICOMOS Charter—Principles for the analysis, conservation and structural restoration of architectural heritage. Proceedings of the ICOMOS 14th General Assembly and Scientific Symposium, Victoria Falls, Zimbabwe, 2731.

Icomos-Iscarsah. (2003). ICOMOS Charter—Principles for the analysis, conservation and structural restoration of architectural heritage. Proceedings of the ICOMOS 14th General Assembly and Scientific Symposium, Victoria Falls, Zimbabwe, 2731.

Ikhouane, F., & Rodellar, J. (2005). On the hysteretic Bouc–Wen model. Nonlinear Dynamics, 78, 42-63.

Ingber, L. (2000). Adaptive simulated annealing (ASA): Lessons learned. arXiv preprint cs/0001018.

Iori, T., Poretti, S. (a cure of) (2007). Rassegna di Architettura e Urbanistica. Anno XII-n. 121/122, Kappa, Roma. (In Italian).

Joachims, T., Li, H., Liu, T.-Y. and Zhai, C. (2007). Learning to rank for information retrieval. in Acm Sigir Forum, vol. 41, pp. 58–62, ACM.

Juang, J. N., & Pappa, R. S. (1985). An eigensystem realization algorithm for modal parameter identification and model reduction. Journal of guidance, control, and dynamics, 8(5), 620-627.

Kennedy, J. and Eberhart, R. (1995). Particle swarm optimization. In Proceedings of ICNN'95 - International Conference on Neural Networks, vol. 4, pp. 1942–1948 vol.4, Nov.

Kerschen, G., Golinval, J. C., Vakakis, A. F., & Bergman, L. A. (2005). The method of proper orthogonal decomposition for dynamical characterization and order reduction of mechanical systems: an overview. Nonlinear dynamics, 41(1-3), 147-169.

Kerschen, G., Golinval, J., Vakakis, A.F. and Bergman L. (2005). "The Method of Proper Orthogonal Decomposition for Dynamical Characterization and Order Reduction of Mechanical Systems: An Overview." Nonlinear Dynamics, 41(1-3), 147–169, doi:10.1007/s11071-005-2803-2.

Kerschen, G., Peeters, M., Golinval, J. C., & Vakakis, A. F. (2009). Nonlinear normal modes, Part I: A useful framework for the structural dynamicist. Mechanical Systems and Signal Processing, 23(1), 170-194.

Kim, J., & Lynch, J. P. (2012). Subspace system identification of support-excited structures—part I: theory and black-box system identification. Earthquake engineering & structural dynamics, 41(15), 2235-2251.

Klerk, D. D., Rixen, D. J., & Voormeeren, S. N. (2008). General framework for dynamic substructuring: history, review and classification of techniques. AIAA journal, 46(5), 1169-1181.

Kramer, S.L., (1996). Geotechnical Earthquake Engineering, Prentice-Hall.

Kyprianou, A. W. (2001). Identification of hysteretic systems using differential evolution algorithm. J. Sound Vib., 248, 289–314.

Lacellotta, R., (2004). Geotecnica, Zanichelli, (In Italian).

Lacy, S. L., & Bernstein, D. S. (2005). Subspace identification for non-linear systems with measured-input non-linearities. International Journal of Control, 78(12), 906-926.

Lang, Z. Q., & Billings, S. A. (2005). Energy transfer properties of non-linear systems in the frequency domain. International Journal of Control, 78(5), 345-362.

Lengyel, G. (2017). Discrete element analysis of gothic masonry vaults for self-weight and horizontal support displacement. Engineering Structures, 148, 195-209.

Limongelli, M.P., and Çelebi, M. (2019). Seismic Structural Health Monitoring: From Theory to Successful Applications. Springer, Tracts in Civil Engineering, DOI: 10.1007/978-3-030-13976-6.

Ljung, L. (1999). System Identification – Theory for the User, Prentice Hall, Upper Saddle River, NY, USA.

Loh, C. M. (2010). System identification and damage evaluation of degrading hysteresis of reinforced concrete frames. Earthquake Engng. Struct. Dyn.

Luce, R. D. (2012). Individual choice behavior: A theoretical analysis. Courier Corporation.

Ma, F. N. (2006). On system identification and response prediction of degrading structures. Structural Control and Health Monitoring, 13, 347–364.

Maia, N.M.M., Silva, J.M.M. (1997) “Theoretical and Experimental Modal Analysis”.

Marchis, V. (1988). Modelli esperimenti di simulazione al personal computer. SEI, Torino. (In Italian).

Marchis, V. (a cure of) (2009). Disegnare Progettare Costruire 150 anni di arte e scienza nelle collezioni del Politecnico di Torino. Fondazione Cassa di Risparmio di Torino, Torino. (In Italian).

Marden, J. I. (2014). Analyzing and modeling rank data. Chapman and Hall/CRC.

Marwala, T. (2010). Finite element model updating using computational intelligence techniques: applications to structural dynamics. Springer Science & Business Media.

Masri SF, C. T. (1979). A nonparametric identification technique for nonlinear dynamic problems. Journal of Applied Mechanics(46), 433–447.

Masri, S. C. (2004). Identification of the state equation in complex non-linear systems. Int. J. Nonlinear Mech., 39, 1111–1127.

Masri, S. F., & Caughey, T. (1979). A nonparametric identification technique for nonlinear dynamic problems. Journal of Applied Mechanics, 46(2), 433-447.

Matlab (2018). The MathWorks, Natick, MA, USA2018a.

Matlab and Statistics Toolbox Release R2016b, The MathWorks, Inc., Natick, Massachusetts, United States.

Matlab. (2010). Version, Matlab 7.10. 0. The Mathworks, Natick Mass, USA.

Mei, Z., Wu, B., Bursi, O. S., Yang, G., & Wang, Z. (2018). Hybrid simulation of structural systems with online updating of concrete constitutive law parameters by unscented Kalman filter. Structural Control and Health Monitoring, 25(2), e2069.

Minka, T. (2004). Power ep. Dep. Statistics, Carnegie Mellon University, Pittsburgh, PA, Tech. Rep.

Minka, T. (2005). Divergence measures and message passing. Technical report, Microsoft Research.

Mishra, S. K. (2006). Some new test functions for global optimization and performance of repulsive particle swarm method.

Mojsilović, N., & Salmanpour, A. H. (2016). Masonry walls subjected to in-plane cyclic loading: application of digital image correlation for deformation

field measurement. International Journal of Masonry Research and Innovation, 1(2), 165-187.

Molina, F. J., Magonette, G., Pegon, P., & Zapico, B. (2011). Monitoring damping in pseudo-dynamic tests. Journal of Earthquake Engineering, 15(6), 877-900.

Mosalam, K.M., White, R.N. and Ayala, G. (1998). "Response of infilled frames using pseudo-dynamic experimentation." Earthquake Engineering and Structural Dynamics, 27, 589-608.

Muto, M., & Beck, J. L. (2008). Bayesian updating and model class selection for hysteretic structural models using stochastic simulation. Journal of Vibration and Control, 14(1-2), 7-34.

Newmark, N. M. (1959, July). A method of computation for structural dynamics. American Society of Civil Engineers.

Newmark, N. M. (1959, July). A method of computation for structural dynamics. American Society of Civil Engineers.

Noël, J. P., & Kerschen, G. (2017). Nonlinear system identification in structural dynamics: 10 more years of progress. Mechanical Systems and Signal Processing, 83, 2-35.

Novello, G. (2013). Modelli per i beni culturali, ovvero, un'arte per governare la complessità. Corso di III livello, Conoscenza strutturale geotecnica e sismica dei beni culturali e tecniche di intervento per il recupero di strutture in legno e in muratura, Giugno, 2013, Italia, Torino, Politecnico di Torino. (In Italian).

Oberti, G. (1967). Corso di Tecnica delle Costruzioni, Levrotto&Bella, Torino. (In Italian).

Okada et al. (1980). Bidirectional Response of RC Column, 7WCEE, India.

P.PEERC. (2013). "Peer ground motion database," Shallow Crustal Earthquakes in Active Tectonic Regimes, NGA-West2.

Paduart, J., Lauwers, L., Swevers, J., Smolders, K., Schoukens, J., & Pintelon, R. (2010). Identification of nonlinear systems using polynomial nonlinear state space models. Automatica, 46(4), 647-656.

Pai, P. H., & Langewisch, D. (2008). Time-frequency method for nonlinear system identification and damage detection. Struct. Health Monit., 7, 103–127.

Paquette, J. and Bruneau, M. (2003). "Pseudo-Dynamic Testing of Unreinforced Masonry Building with Flexible Diaphragm." M. ASCE2, DOI: 10.1061/~ASCE!0733-9445~2003!129:6~708!.

Paquette, J., Bruneau, M. (2006). "Pseudo-dynamic testing of unreinforced masonry building with flexible diaphragm and comparison with existing procedures." Construction and Building Materials, 20, 220-228.

Park K.C., Felippa C.A., Gumaste U.A. (2000). "A localized version of the method of Lagrange multipliers and its applications." Computational Mechanics, 24, 476-490.

Patterson, M. A., Weinstein, M., & Rao, A. V. (2013). An efficient overloaded method for computing derivatives of mathematical functions in MATLAB. ACM Transactions on Mathematical Software (TOMS), 39(3), 17.

Pecorelli, M. L., Ceravolo, R., & Epicoco, R. (2018). An Automatic Modal Identification Procedure for the Permanent Dynamic Monitoring of the Sanctuary of Vicoforte. International Journal of Architectural Heritage, 1-15.

Pecorelli, M. L., Ceravolo, R., & Epicoco, R. (2018). An Automatic Modal Identification Procedure for the Permanent Dynamic Monitoring of the Sanctuary of Vicoforte. International Journal of Architectural Heritage, 1-15.

Pecorelli, M. L., Ceravolo, R., & Epicoco, R. (2018). An Automatic Modal Identification Procedure for the Permanent Dynamic Monitoring of the Sanctuary of Vicoforte. International Journal of Architectural Heritage, 1-15.

Pei, J.-S. S. (2004). Analysis andmodification ofVolterra/Wiener neural networks for the adaptive identification of non-linear hysteretic dynamic systems. J. Sound Vib., 275, 693–718.

Peng, Z. K., Lang, Z. Q., & Billings, S. A. (2007). Linear parameter estimation for multi-degree-of-freedom nonlinear systems using nonlinear output frequency-response functions. Mechanical Systems and Signal Processing, 21(8), 3108-3122.

Peng, Z. K., Lang, Z. Q., & Billings, S. A. (2008). Nonlinear parameter estimation for multi-degree-of-freedom nonlinear systems using nonlinear output frequency-response functions. Mechanical Systems and Signal Processing, 22(7), 1582-1594.

Peng, Z. K., Lang, Z. Q., Wolters, C., Billings, S. A., & Worden, K. (2011). Feasibility study of structural damage detection using NARMAX modelling and Nonlinear Output Frequency Response Function based analysis. Mechanical Systems and Signal Processing, 25(3), 1045-1061.

Pintelon, R., & Schoukens, J. (2001). System Identification: A Frequency Domain Approach IEEE Press. Piscataway, NJ.

Pinto, A., Molina, J., Pegon, P., Renda, V. (2001). "Protection of the cultural heritage at the ELSA Laboratory." ELSA, IPSC, Joint Research Centre, European Commission, I-21020 Ispra (VA), Italy.

Plackett, R.L. (1975). The analysis of permutations. Applied Statistics, pp. 193–202.

Platten, M. F., Wright, J. R., Dimitriadis, G., & Cooper, J. E. (2009). Identification of multi-degree of freedom non-linear systems using an extended modal space model. Mechanical Systems and Signal Processing, 23(1), 8-29.

Politecnico di Torino (1989). Capolavori di minuseria al servizio della Scienza delle Costruzioni: La collezione ottocentesca di modelli di Costruzioni della R. Scuola di Applicazioni per Ingegneri in Torino. CELID, Torino. (In Italian).

Portioli, F., Mammana, O., Landolfo, R., Mazzolani, F. M., Krstevska, L., Tashkov, L., & Gramatikov, K. (2011). Seismic retrofitting of Mustafa Pasha Mosque in Skopje: finite element analysis. Journal of Earthquake Engineering, 15(4), 620-639.

Renson, L., Gonzalez-Buelga, A., Barton, D. A. W., & Neild, S. A. (2016). Robust identification of backbone curves using control-based continuation. Journal of Sound and Vibration, 367, 145-158.

Richards, C. M., & Singh, R. (1998). Identification of multi-degree-of-freedom non-linear systems under random excitations by the "reverse path" spectral method. Journal of Sound and Vibration, 213(4), 673-708.

Ruocci, G. (2010). Application of the SHM methodologies to the protection of masonry arch bridges from scour. (Doctoral dissertation, PhD Thesis, Department of Structural and Geotechnical Engineering).

Ruocci, G., Ceravolo, R., & De Stefano, A. (2009). Modal identification of an experimental model of masonry arch bridge. In Key Engineering Materials (Vol. 413, pp. 707-714). Trans Tech Publications.

Sarhosis, V., & Sheng, Y. (2014). Identification of material parameters for low bond strength masonry. Engineering Structures, 60, 100-110.

Schetzen, M. (1980). The Volterra and Wiener theories of nonlinear systems.

Shing, P. S. B., & Mahin, S. A. (1987). Cumulative experimental errors in pseudodynamic tests. Earthquake engineering & structural dynamics, 15(4), 409-424.

Shing, P. S. B., & Vannan, M. T. (1991). Implicit time integration for pseudodynamic tests: convergence and energy dissipation. Earthquake engineering & structural dynamics, 20(9), 809-819.

SIA, S. (2005). 266: Masonry. Swiss code, Swiss society of engineers and architects SIA, Zürich, Switzerland.

Smyth, A. K. (2000). Parametric and nonparametric adaptive identification of nonlinear structural systems. Proceedings of the American Control Conference, 978–998.

Smyth, A. M. (1999). On-line parametric identification of MDOF nonlinear hysteretic systems. ASCE Journal of Engineering Mechanics, 125, 133–142.

Smyth, A. M. (2002). Development of adaptive modelling techniques for non-linear hysteretic systems. Int. J. Nonlinear Mech., 37, 1435–1451.

Spiridonakos, M. P. (2010). Output-only identification and dynamic analysis of time-varying mechanical structures under random excitation: A comparative assessment of parametric methods. J. of Sound and Vib., 329, 768–785.

Sracic, M. W., & Allen, M. S. (2011). Method for identifying models of nonlinear systems using linear time periodic approximations. Mechanical Systems and Signal Processing, 25(7), 2705-2721.

Sracic, M. W., & Allen, M. S. (2014). Identifying parameters of multi-degree-of-freedom nonlinear structural dynamic systems using linear time periodic approximations. Mechanical Systems and Signal Processing, 46(2), 325-343.

Stefanaki, A., Sivaselvan, M. V., Tessari, A., & Whittaker, A. (2015). Soil-Foundation-Structure Interaction Investigations using Hybrid Simulation. Structural Mechanics in Reactor Technology SMiRT23. Manchester, UK.

Stojadinovic, B., Mosqueda, G. and Mahin S.A. (2006). "Event-Driven Control System for Geographically Distributed Hybrid Simulation." ASCE Journal of Structural Engineering, 132(1), 68-77.

Sun, H., & Betti, R. (2015). A hybrid optimization algorithm with Bayesian inference for probabilistic model updating. Computer-Aided Civil and Infrastructure Engineering, 30(8), 602-619.

Sun, W., & Yuan, Y. X. (2006). Optimization theory and methods: nonlinear programming (Vol. 1). Springer Science & Business Media.

Takanashi, K., Udagawa, K., Seki, M., Okada, T. and Tanaka, H. (1975). "Non-linear earthquake response analysis of structures by a computer-actuator on-line system." Bulletin of Earthquake Resistant Structure Research Center, Institute of Industrial Science, University of Tokyo, Tokyo.

Tang, G. (2013). Timber gridshells: beyond the drawing board. Proceedings of the Institution of Civil Engineers. Construction Materials, 166(6), 390-402.

Terzic, V., & Stojadinovic, B. (2013). Hybrid simulation of bridge response to three-dimensional earthquake excitation followed by truck load. Journal of Structural Engineering, 140(8), A4014010.

Toropov, V.V., & Garrity, S.W. (1998). Material parameter identification for masonry constitutive models. In: Proceedings of the 8th Canadian masonry symposium. Alberta, Canada: Jasper; 1998. p. 551–62.

Van Overschee, P., & De Moor, B. (1994). N4SID: Subspace algorithms for the identification of combined deterministic-stochastic systems. Automatica, 30(1), 75-93.

Van Overschee, P., De Moor, B. (1996). Subspace Identification for Linear Systems: Theory, Implementation and Applications, Kluwer Academic Publishers, Dordrecht, The Netherlands.

Wen, Y.-K. (1976). Method for random vibration of hysteretic systems. J. Eng. Mech. Div. ASCE, 102, 249–263.

Widanage, W. D., Stoev, J., Van Mulders, A., Schoukens, J., & Pinte, G. (2011). Nonlinear system-identification of the filling phase of a wet-clutch system. Control Engineering Practice, 19(12), 1506-1516.

Worden, K. T. (2001). Nonlinearity in structural dynamics: detection, identification, and modelling. Institute of Physics Publishing: Philadelphia.

Worden, K., Hickey, D., Haroon, M., & Adams, D. E. (2009). Nonlinear system identification of automotive dampers: a time and frequency-domain analysis. Mechanical Systems and Signal Processing, 23(1), 104-126.

Wu, M., & Smyth, A. (2008). Real-time parameter estimation for degrading and pinching hysteretic models. Int. J. of Non-Linear Mech, 43, 822–833. Ansys, Ansys Academic Research, Release 16.2, 2016.

Xu, B., He, J., & Dyke, S. J. (2015). Model-free nonlinear restoring force identification for SMA dampers with double Chebyshev polynomials: approach and validation. Nonlinear dynamics, 82(3), 1507-1522.

Yang, Z., Dimitriadis, G., Vio, G. A., Cooper, J. E., & Wright, J. R. (2006). Identification of Structural Free-play Non-linearities using the Non-Linear Resonant Decay Method. In Proceedings of the 2006 International Conference on Noise and Vibration Engineering (pp. 2797-2809). Katholieke Universiteit Leuven.

Yassin, I. M., Taib, M. N., & Adnan, R. (2013). Recent advancements & methodologies in system identification: A review. Scientific Research Journal, 1(1), 14-33.

Yasutake, S., Hatano, K., Takimoto, E., & Takeda, M. (2012, November). Online rank aggregation. In Asian Conference on Machine Learning (pp. 539-553).

Zhang, F. L., Ni, Y. C., & Lam, H. F. (2017). Bayesian structural model updating using ambient vibration data collected by multiple setups. Structural Control and Health Monitoring, 24(12), e2023.

Zienkiewicz, O. C., Taylor, R. L., & Zhu, J. Z. (2005). The finite element method: its basis and fundamentals. Elsevier.